

N° d'ordre : 41119

THÈSE

UNIVERSITE LILLE 1 – SCIENCES ET TECHNOLOGIES
ECOLE DOCTORALE SCIENCES DE LA MATIERE, DU RAYONNEMENT ET DE
L'ENVIRONNEMENT

présentée par

Alexia CORDOVA

pour l'obtention du

TITRE DE DOCTEUR EN MOLECULES ET MATIERE
CONDENSEE

intitulée

**SUPPORTED MOLYBDENUM AND TUNGSTEN BASED CATALYSTS FOR
THE DIRECT SYNTHESIS OF METHYLMERCAPTAN FROM SYNGAS**

Soutenance prévue le 24 Mai 2013

Directeurs de thèse: **Carole LAMONIER**, Professeur, Université Lille 1

Pascal BLANCHARD, Maître de Conférences, Université Lille 1

Rapporteurs: **Anne-Cécile ROGER**, Professeur, Université de Strasbourg

Pavel AFANASIEV, Chargé de Recherche, IRCELYON

Examineurs: **Franck DUMEIGNIL**, Professeur, Université Lille 1

Michel LACROIX, Directeur de Recherche, IRCELYON

Georges FREMY, Ingénieur de Recherche, Groupement de Recherches de
Lacq

N° d'ordre : 41119

THÈSE

UNIVERSITE LILLE 1 – SCIENCES ET TECHNOLOGIES
ECOLE DOCTORALE SCIENCES DE LA MATIERE, DU RAYONNEMENT ET DE
L'ENVIRONNEMENT

présentée par

Alexia CORDOVA

pour l'obtention du

TITRE DE DOCTEUR EN MOLECULES ET MATIERE
CONDENSEE

intitulée

**SUPPORTED MOLYBDENUM AND TUNGSTEN BASED CATALYSTS FOR
THE DIRECT SYNTHESIS OF METHYLMERCAPTAN FROM SYNGAS**

Soutenance prévue le 24 Mai 2013

Directeurs de thèse: **Carole LAMONIER**, Professeur, Université Lille 1

Pascal BLANCHARD, Maître de Conférences, Université Lille 1

Rapporteurs: **Anne-Cécile ROGER**, Professeur, Université de Strasbourg

Pavel AFANASIEV, Chargé de Recherche, IRCELYON

Examineurs: **Franck DUMEIGNIL**, Professeur, Université Lille 1

Michel LACROIX, Directeur de Recherche, IRCELYON

Georges FREMY, Ingénieur de Recherche, Groupement de Recherches de

Lacq

Remerciements

La recherche menant à tous les résultats inclus dans cette thèse a reçu un financement de la « European Union Seventh Framework Programme (FP7/2007-2013) under grant agreement n° 241718 EuroBioRef ».

C'est grâce au soutien d'un grand nombre de personnes dont l'intérêt manifestés tout au long de ma recherche, la générosité et la bonne humeur m'ont permis d'accomplir cet extraordinaire travail doctoral.

Je tiens tout d'abord à remercier grandement ma directrice de thèse, madame Carole Lamonier, une extraordinaire personne à tout point de vue. En premier lieu, merci pour m'avoir accueilli et m'avoir ouvert les portes de l'UCCS en acceptant m'encadrer dans ce travail doctoral, puis pour m'avoir guidé et conseillé et pour être toujours disponible et avoir consacré toutes ces heures à diriger cette recherche malgré ses nombreuses charges. Enfin je suis extrêmement heureuse d'avoir fait la connaissance d'une personne avec autant de qualités; gentillesse, générosité, patiente et amitié.

Mes remerciements vont également à monsieur Pascal Blanchard. Je vous remercie aussi bien par les discussions enrichissantes que j'ai eu la chance d'avoir avec lui comme par ses conseils, sa bonne humeur et son énorme qualité humaine. Il a été certainement agréable de travailler avec une personne si capable de qui j'ai appris tant de choses qui m'ont fait grandir personnel et professionnellement.

J'exprime tous mes remerciements à l'ensemble des membres de mon jury : madame Anne-Cécile Roger professeur de l'Université de Strasbourg; monsieur Pavel Afanasiev, chargé de Recherche à l'IRCELYON; monsieur Franck Dumeignil, professeur de l'Université Lille 1; monsieur Michel Lacroix, directeur de Recherche à l'IRCELYON et monsieur Georges Frémy, ingénieur de recherche du Groupement de Recherches de Lacq GRL.

Je pense ici en particulier au personnel du Groupement de Recherches de Lacq GRL. Merci à monsieur Georges Frémy pour m'avoir donné l'opportunité de réaliser un stage dans les installations du GRL. J'adresse aussi mes remerciements à monsieur Patrice Barré pour m'avoir appris, toujours dans la bonne humeur, tous les outils pour la réalisation des tests catalytiques. Je remercie également à madame Karine Sanchou pour toute sa collaboration dans la réalisation d'une grande partie de mon travail expérimental. Je souhaiterais aussi adresser ma gratitude aux autres membres du GRL, Chantal, Nicolas, Guillaume, Pierre, Manu pour sa gentillesse et pour m'avoir donné un accueil si chaleureuse.

Je souhaiterais aussi adresser ma gratitude à madame Josefina Scott, pour avoir été toujours comme une mère pour moi, pour m'avoir encouragé, conseillé et guidé pendant plusieurs années et surtout pour faire une partie importante de ma décision de venir en France à réaliser cette thèse.

Je passe ensuite une dédicace spéciale à l'ensemble du personnel scientifique, technique et administratif de l'UCCS : Christine Lancelot, Arnaud Beaurain, Olivier Gardoll, Jean-Charles Morin, Elise Berrier, Axel Löfberg, Laurence Burylo, Nora Djelal, Mickael Capron, Nicolas Nuns, Jean-Philippe Dacquin, Simon Desset, Jean-François Lamonier, Matine Trentesaux, Noëlla Brémard, Barbara Declerck-Boulangier, Sandrine Berton, Virginie Buchet et Arnaud Troupin, pour son aide et sa collaboration tout au long de mon séjour à l'UCCS.

J'adresse toute ma gratitude à tous mes collègues et amis du laboratoire et du bureau et ceux qui j'ai rencontré pendant mon séjour en France: Georgette, Silvia, Juliana, Jhon, Andres, Jérémy, Guillaume, Rémy, Minh-Tuan, Duy-Luan, Yihao, Lishil, Pam, Bianca, Diana, Yanina, Brenda, Fanny, Diego, José, Melesio, Luis Carlos et German. Je vous remercie tous pour les extraordinaires moments partagés pendant ces trois années, des moments qui resteront toujours marqués dans mon cœur.

Ma motivation, ma force, ma persévérance; toujours dans mon cœur malgré la distance. Le plus grand merci à ma famille, mami, papi, mes sœurs et frères Alejandra, Alexmar, Alejandro, Isaac, Marianelly, ma petite nièce Mariale, mes amies, Desi, Mari, Mayreli, Vane.. Merci pour le soutien et pour m'avoir accompagné depuis la distance pendant ces trois années. C'est à eux que je dédie cette thèse.

Finalement, mais non pour être moins important, mon copain, Manuel, mon amour. Merci pour ta compagnie, pour ton soutien, pour ta patience et compréhension et pour avoir été là, dans tout moment, pour moi. Sans toi cela n'aurait pas été possible. Je t'aime!

J'espère n'avoir oublié personne. Merci à tous qui ont cru en moi et qui m'ont permis d'arriver au bout de cette thèse.

GENERAL INTRODUCTION.....	1
CHAPTER 1. LITERATURE REVIEW.....	5
1.1. ORGANOSULFUR COMPOUNDS.....	7
1.1.1. Sulfides (Thioethers).....	10
1.1.2. Disulfides.....	11
1.1.3. Sulfoxides and sulfones.....	12
1.1.4. Thioacids.....	12
1.1.5. Mercaptans.....	13
1.2. METHYL MERCAPTAN.....	16
1.2.1. Methyl mercaptan: Markets, production and manufacturers.....	16
1.2.2. Uses of methyl mercaptan.....	18
1.2.2.1. Methionine.....	18
1.2.2.2. Dimethyl disulfide.....	21
1.2.2.3. Methanesulfonic acid.....	22
1.3. PROCESS FOR THE PRODUCTION OF METHYL MERCAPTAN.....	22
1.3.1. Synthesis of Methyl mercaptan from Methanol.....	23
1.3.1.1. Reaction conditions.....	23
1.3.1.2. Catalysts used in the thiolation of methanol.....	27
1.3.2. Synthesis of Methyl mercaptan from Syngas.....	45
1.3.2.1. Reaction conditions.....	45
1.3.2.2. Catalysts used in the reaction of syngas with hydrogen sulfide.....	51
1.4. SUMMARY AND OBJECTIVES.....	58
1.5. REFERENCES.....	61
CHAPTER 2. MATERIALS AND METHODS.....	71
2.1. CATALYSTS PREPARATION	73
2.1.1. Precursors preparation	73
2.1.2. Support preparation	76
2.1.3. Catalysts preparation.....	77
2.1.4. Reference catalysts	80

2.1.4.1. Monometallic catalysts.....	80
2.1.4.2. Bimetallic catalyst.....	81
2.1.4.3. Na based catalyst	81
2.2. EX SITU SULFIDATION OF CATALYSTS FOR CHARACTERIZATION	81
2.3. CHARACTERIZATION TECHNIQUES	83
2.3.1. Elemental Analysis	83
2.3.2. Specific Surface Area.....	84
2.3.3. X-Ray diffraction (XRD)	85
2.3.4. Laser Raman spectroscopy (LRS)	87
2.3.5. UV-Visible spectroscopy	88
2.3.6. Scanning electron microscopy (SEM).....	89
2.3.7. Transmission electron microscopy (TEM).....	90
2.3.8. X-Ray photoelectron spectroscopy (XPS).....	91
2.3.9. Electron probe microanalysis (EPMA)	96
2.3.10. Characterization techniques of acid-base properties of solids	97
2.3.10.1. Temperature programmed desorption (TPD).....	97
2.3.10.2. Isopropanol test reaction.....	98
2.4. EXPERIMENTAL SET-UP.....	100
2.4.1. Catalytic test procedure.....	100
2.4.2. Gas chromatograph GC.....	104
2.4.2.1. Experimental setup GRL.....	104
2.4.2.2. Experimental setup UCCS.....	105
2.4.3. Pretreatment of catalysts	110
2.4.4. Reaction conditions	112
2.4.5. Experimental procedure	112
2.4.6. Data analysis	113
2.5. VALIDATION OF UCCS CATALYTIC TEST.....	114
2.6. REFERENCES.....	115
CHAPTER 3. PRECURSORS, SUPPORTS AND FRESH CATALYSTS CHARACTERIZATION.....	117
3.1. CHARACTERIZATION OF PRECURSORS.....	119
3.1.1. UV-Vis spectroscopy.....	119
3.1.2. Laser Raman spectroscopy.....	121

3.1.3.	Wide angle powder XRD.....	122
3.2.	CHARACTERIZATION OF SUPPORTS.....	124
3.2.1.	Specific surface areas of supports.....	124
3.2.2.	Wide angle powder XRD.....	124
3.2.3.	Laser Raman spectroscopy.....	126
3.2.4.	Scanning electron microscopy (SEM).....	126
3.2.5.	Acid-base properties of solids.....	128
	3.2.5.1. <i>Temperature programmed desorption of ammonia and carbon dioxide</i>	128
	3.2.5.2. <i>Acid-base behavior determined by catalytic decomposition of isopropanol</i>	132
3.3.	CONCLUSIONS OF SECTION 3.1 AND 3.2.....	135
3.4.	CHARACTERIZATION OF Mo-BASED FRESH CATALYSTS.....	136
3.4.1.	Characterization of oxidic reference catalysts.....	136
	3.4.1.1. <i>Laser Raman spectroscopy</i>	136
	3.4.1.2. <i>X-Ray Photoelectron Spectroscopy (XPS)</i>	138
3.4.2.	Characterization of K ₂ MoO ₄ -based catalysts.....	140
	3.4.2.1. <i>Bulk composition and specific surface area</i>	140
	3.4.2.2. <i>Laser Raman Spectroscopy</i>	142
	3.4.2.3. <i>Wide angle powder XRD</i>	143
	3.4.2.4. <i>X-ray photoelectron spectroscopy (XPS)</i>	145
	3.4.2.5. <i>Scanning Electron Microscopy (SEM)</i>	147
	3.4.2.6. <i>Electron probe microanalysis (EPMA)</i>	148
3.4.3.	Characterization of K ₂ MoS ₄ -based catalysts.....	150
	3.4.3.1. <i>Bulk composition and specific surface area</i>	150
	3.4.3.2. <i>Laser Raman Spectroscopy</i>	151
	3.4.3.3. <i>Wide angle powder XRD</i>	152
	3.4.3.4. <i>X-ray photoelectron spectroscopy (XPS)</i>	154
	3.4.3.5. <i>Scanning Electron Microscopy (SEM)</i>	157
3.5.	CONCLUSION OF SECTION 3.4.....	158
3.6.	REFERENCES.....	159
CHAPTER 4.	Mo-based catalysts for the synthesis of MeSH from syngas/H₂S mixture.....	163
4.1.	SULFIDED REFERENCE CATALYSTS.....	166
4.1.1.	Catalytic test of sulfided reference results	166

4.1.1.1. Effect of the incorporation of potassium.....	168
4.1.1.2. Effect of the way of incorporation of molybdenum and potassium.....	171
4.1.1.3. Effect of the alkali promoter (K or Na) and the state of the precursor incorporated (oxidic or pre-sulfided).....	172
4.1.2. Characterization of sulfided reference catalysts. Comprehension and approach to the active phase.....	174
4.1.2.1. X-ray photoelectron spectroscopy (XPS)	174
4.1.2.2. High resolution transmission electron microscopy (HRTEM).....	185
4.2. K₂MoO₄-BASED CATALYSTS.....	190
4.2.1. Catalytic test of sulfided K ₂ MoO ₄ -based.....	190
4.2.2. Characterization of sulfided K ₂ MoO ₄ -based catalysts.....	191
4.2.2.1. Raman spectroscopy.....	192
4.2.2.2. High resolution transmission electron microscopy (HRTEM).....	194
4.2.2.3. X-ray photoelectron spectroscopy (XPS)	198
4.2.2.4. Correlation between catalytic performance and active K _x MoS ₂ phase.....	199
4.3. K₂MoS₄-BASED CATALYSTS.....	200
4.3.1. Catalytic test of sulfided K ₂ MoS ₄ -based catalysts.....	201
4.3.2. Characterization of sulfided K ₂ MoS ₄ -based catalysts.....	203
4.3.2.1. Raman spectroscopy.....	203
4.3.2.2. High resolution transmission electron microscopy (HRTEM).....	204
4.3.2.3. X-ray photoelectron spectroscopy (XPS)	205
4.3.2.4. Correlation between catalytic performance and active K _x MoS ₂ phase.....	206
4.4. EFFECT OF Mo LOADING OVER A SERIES OF ALUMINA-SUPPORTED CATALYSTS.....	207
4.5. EFFECT OF CATALYST PRETREATMENT OVER THE CATALYTIC ACTIVITY.....	209
4.5.1. Catalytic test.....	209
4.6. CONCLUSIONS.....	211
4.7. REFERENCES.....	213

CHAPTER 5. Synthesis of MeSH from syngas/H₂S mixture: Extension to tungsten based catalysts.....215

5.1. CHARACTERIZATION OF FRESH CATALYSTS.....	217
5.1.1. Characterization of K ₂ WO ₄ -based catalysts.....	217

5.1.1.1. Bulk composition and specific surface area.....	217
5.1.1.2. Raman spectroscopy.....	218
5.1.1.3. X-ray photoelectron spectroscopy (XPS)	219
5.1.2. Characterization of K ₂ WS ₄ -based catalysts.....	221
5.1.2.1. Bulk composition and specific surface area.....	221
5.1.2.2. Raman spectroscopy.....	221
5.1.2.3. Wide angle powder XRD.....	222
5.1.2.4. X- ray photoelectron spectroscopy (XPS).....	224
5.2. CATALYTIC TEST OF W-BASED SOLIDS.....	225
5.3. CHARACTERIZATION OF SULFIDED CATALYSTS.....	228
5.3.1.1. Raman spectroscopy.....	228
5.3.1.2. X-ray photoelectron spectroscopy (XPS)	229
5.4. CONCLUSIONS.....	233
5.5. REFERENCES.....	234
CONCLUSIONS AND PERSPECTIVES.....	236
ANEXXES.....	243

GENERAL INTRODUCTION

The amount of fossil fuels produced and consumed today is becoming increasingly less abundant, due to its fast-growing demand and because it seems that its extraction from the earth is at the present more difficult and expensive [1]. By this reason, it has become important to search for alternative means to produce fuels and chemicals. Among the renewable energy sources, biomass, according to the biorefinery approach, seems to be a unique renewable source able to satisfy both needs of providing feedstocks for biofuel and production, moving the market dependence away from fossil-based energy sources, which is the main purpose of EuroBioRef (European multilevel integrated biorefinery design for sustainable biomass processing), the European project (n° 241718) under which this thesis has been developed. The thesis was also performed in collaboration with GRL (Groupement de Recherches de Lacq, Arkema France).

Methyl mercaptan is a high added value material which may be obtained from syngas issued from biomass. Nowadays, methyl mercaptan is an industrially important chemical used as raw material for the production of valuable organosulfur compounds such as methionine (an important amino acid used as poultry feed supplement), dimethyl disulfide (sulfiding agent for hydrotreating catalysts) and methanesulfonic acid (acidic catalyst).

At the present, methyl mercaptan is manufactured at industrial scale by the reaction of methanol with hydrogen sulfide. Despite the fact that the production of methyl mercaptan *via* methanol/hydrogen sulfide route is an efficient process in terms of methanol conversion and methyl mercaptan yields, this route present the disadvantage that a multiple-step pathway for the synthesis of methanol is required ($\text{CH}_4 + \text{H}_2\text{O} \longrightarrow \text{Syngas} \longrightarrow \text{Methanol}$), which results in raised costs of production. This is the main reason why the development of a new route which may provide greater economies, by using a simple feedstock (syngas/hydrogen sulfide), is increasingly attractive in the industrial application. Early works disclosed that under the conditions of mixed alcohol synthesis using H_2S -containing syngas, the mixed alcohol of low carbon disappeared and methyl mercaptan was found to be the main product when the concentration of hydrogen sulfide in syngas was over 1.6 % [2]. The production of methyl mercaptan from the one-step reaction of syngas and hydrogen sulfide has been studied since 1980s and the K-Mo catalytic systems are the most frequently used.

The few researches done so far have mainly been focused on the improvement of catalytic performance but were less devoted to the comprehension of the nature of the active phase. The work developed in this thesis will be dedicated to both improvement of the catalytic performance and determination of the nature of the catalysts active phase.

The first part of this thesis deals with an extensive literature review concerning organosulfur compounds, mainly focused on methyl mercaptan. Production, manufacture and main uses of this compound are discussed. The two main routes of methyl mercaptan production, *via* methanol/H₂S and *via* syngas/H₂S, are willingly exposed taking into account that it is the first time that a thesis concerning the methyl mercaptan synthesis has been developed in our laboratory. In this regard, the involved reactions, the reaction conditions and the catalysts used for the production of methyl mercaptan by means of these two routes are discussed. Following this literature review the objectives of the thesis will be presented.

Chapter 2 is dedicated to the description of synthesis of precursors, supports and catalysts and the experimental techniques used in this work. An important part of this chapter concerns the set-up and put in operation of a new micro-pilot acquired for the production of methyl mercaptan in the UCCS (Unité de Catalyse de Chimie du Solide)-Université de Lille 1.

Chapter 3 is focused on the characterization of precursors, supports and Mo-based catalysts, promoted or not with potassium. Chapter 4 presents a complete study of the sulfided (K)(Na)Mo-based catalysts described in chapter 3. In a first part, the catalytic performance of reference (K)(Na)Mo-based solids in the reaction of syngas with hydrogen sulfide will be exposed; followed by the characterization of the sulfided catalysts with a major emphasis in the interpretation of the active phase which drives the catalytic performance. Several correlations between these two parameters are exposed. The second part of chapter 4 is dedicated to the synthesis of methyl mercaptan using two different catalytic systems (K₂MoO₄ and K₂MoS₄-based catalysts), searching improvement of catalytic performances. Characterizations of these catalytic systems are also exposed.

Chapter 5 is an extension of chapter 4 in which Mo will be substituted by W. The characterization of fresh and sulfided catalysts as well as the catalytic test and their

correlation with the active phase, will be exposed in this chapter.

REFERENCES

- [1] P. O'Connor, "The Role of Catalysis for the Sustainable Production of Bio-fuels. Chapter 1 – A General Introduction to Biomass Utilization Possibilities," <http://dx.doi.org/10.1016/B978-0-444-56330-9.00001-2>, pp. 1-25, 2013.
- [2] Y.-Q. Yang, Y.-Z. Yuan, S.-J. Dai, B. Wang, and H.-B. Zhang, "The catalytic properties of supported K₂MoS₄/SiO₂ catalyst for methanethiol synthesis from high H₂S-content syngas," *Catalysis letters*, vol. 54, pp. 65-68, 1998.

CHAPTER 1

Literature Review

Literature Review: Summary

1.1. ORGANOSULFUR COMPOUNDS	7
1.1.1. Sulfides (Thioethers).....	10
1.1.2. Disulfides	11
1.1.3. Sulfoxides and sulfones	12
1.1.4. Thioacids.....	12
1.1.5. Mercaptans	13
1.2. METHYL MERCAPTAN	16
1.2.1. Methyl mercaptan: Markets, production and manufacturers	16
1.2.2. Uses of methyl mercaptan.....	18
1.2.2.1. <i>Methionine</i>	18
1.2.2.2. <i>Dimethyl disulfide</i>	21
1.2.2.3. <i>Methanesulfonic acid</i>	22
1.3. PROCESS FOR THE PRODUCTION OF METHYL MERCAPTAN.....	22
1.3.1. Synthesis of Methyl mercaptan from Methanol.....	23
1.3.1.1. <i>Reaction conditions</i>	23
1.3.1.2. <i>Catalysts used in the thiolation of methanol</i>	27
1.3.2. Synthesis of Methyl mercaptan from Syngas	45
1.3.2.1. <i>Reaction conditions</i>	45
1.3.2.2. <i>Catalysts used in the reaction of syngas with hydrogen sulfide</i>	51
1.4. SUMMARY AND OBJECTIVES.....	58
1.5. REFERENCES	61

This chapter reports a systematic investigation of the literature about the most important organosulfur compounds doing a special focus in the organosulfur molecule mercaptan. Special emphasis is attributed to METHYL MERCAPTAN, the target compound under study in this work. Main uses of methyl mercaptan will be also discussed in this chapter. The larger part of the chapter is centered on the processes used for the production of methyl mercaptan and the catalytic systems used for it. Processes conditions (Temperature, pressure, GHSV, etc.) as well as the type of catalysts used for the synthesis of methyl mercaptan by reaction of hydrogen sulfide with either methanol or syngas are examined. Finally, the objectives of our work will be presented.

1.1. ORGANOSULFUR COMPOUNDS

Organosulfur compounds, a subclass of organic substances that contain sulfur [1], are known for their varied occurrence and unusual properties. They are frequently associated with disgusting odors; nevertheless many of the sweetest compounds known are organosulfur derivatives. These substances are used as defensive secretions by a variety of animal species and their unpleasant odors are associated with polluted air and water, particularly that resulting from the use of sulfur-rich fossil fuels. However, not all of these compounds are foul-smelling components, some types of organosulfur compounds found in foods as garlic, onion, broccoli, cabbage, radish, asparagus, mushroom, mustard, truffle, coffee, wine, nuts, cheddar cheese, chocolate and tropical fruit flavors [2] are sources of olfactory and gustatory delight. Many of these natural products also have important medicinal properties such as fighting cancer. They are found in diverse locations, including in interstellar space, inside hot acidic volcanoes, and deep within the oceans. Besides, organosulfur compounds occur in the bodies of all living creatures in the form of certain essential amino acids.

Compared to their analogs organic compounds of oxygen, some significant differences must be cited.

Table 1.1. Some dissociation energies

<i>Molecule</i>	<i>Dissociation Energy kcal/mol</i>	<i>Molecule</i>	<i>Dissociation Energy kcal/mol</i>
CH ₃ S --- SCH ₃	73	-O---O-	40 – 45
CH ₃ S --- CH ₃	73	CH ₃ O --- CH ₃	77
CH ₃ S --- H	89	CH ₃ O --- H	100
C = S	45	C = O	73

Whereas the O – O bond is relatively weak and may undergo homolysis already at moderate temperatures, the S – S bond is as strong as the C – S bond and only slightly weaker than the C – C linkage as can be seen in table 1.1 [3]. The S – H bond has a strength which is about equal to one-half the sum of the S – S and H – H dissociation energies.

Some values regarding the bond lengths of C, O and S are shown in table 1.2. This data suggest that there is a large difference between the lengths of bonds involving sulfur and the oxygen or carbon analogs, amounting from 0.3 to 0.5 Å units [3].

Table 1.2. Bond lengths of sulfur, oxygen and carbon atoms

<i>Bond</i>	<i>Bond length Å</i>	<i>Bond</i>	<i>Bond length Å</i>
C – S	1.82	C – O	1.43
S – S	1.8 – 2.1	C – C	1.53
S – H	1.33	O – H	0.96

Thiols are stronger acids than the corresponding alcohols because the S–H bond is weaker than the O–H bond and because the larger sulfur atom better disperses the resulting negative charge as compared with oxygen. Simultaneously, as a consequence of the weakness of S-H hydrogen bonding compared to O-H hydrogen bonding, thiols are more volatile and have lower boiling points than the corresponding alcohols. Disulfides are far more stable than peroxides, and sulfonium (R_3S^+) salts are much less reactive than oxonium salts; at the same time, simple thiocarbonyl (C=S) compounds are much more reactive than simple carbonyl (C=O) compounds. Sulfur also has the ability to form compounds in which atoms of these elements have higher valences; these compounds have no counterpart in oxygen chemistry. Some examples are sulfoxides (R_2SO), sulfones (R_2SO_2), sulfonic acids (RSO_3H), oxosulfonium salts ($R_3S^+=O$) and sulfates (SO_4^{2-}).

In chemical research, sulfur containing compounds are valued reagents widely used for synthesizing new compounds. For example, in the field of thiochemistry, the synthesis of a wide range of sulfur compounds such as, sulfides, disulfides, polysulfides, sulfoxides, thioacids and mercaptans is more and more important due to its increasing use in agrochemicals, petrochemicals, lubricants, cosmetics, pharmaceutical products and gas odorants [4].

Some of the most important organosulfur compounds are listed in the figure 1.1.

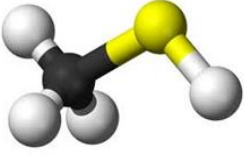
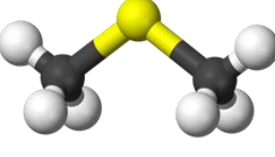
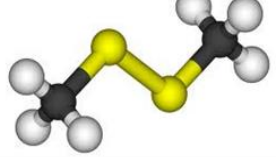
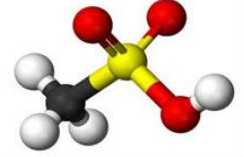
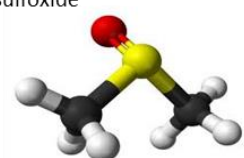
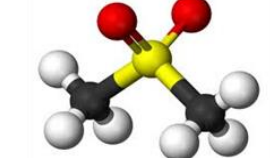
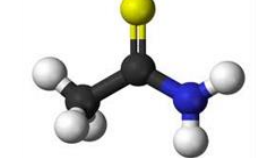
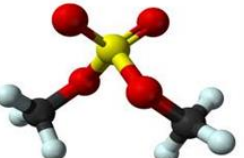





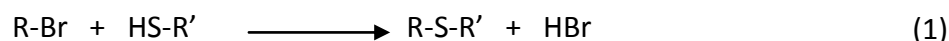
Structure: RSH	Structure: RSR	Structure: RSSR	Structure: RSO ₃ H
Name: Thiol	Name: Sulfide	Name: Disulfide	Name: Sulfonic acid
Example: Methanethiol	Example: Dimethyl sulfide	Example: Dimethyl disulfide	Example: Methanesulfonic acid
			
Structure: R ₂ S=O	Structure: R ₂ SO ₂	Structure: RC(S)NH ₂	Structure: (RO ₂)SO ₂
Name: Sulfoxide	Name: Sulfone	Name: Thioamide	Name: Sulfate ester
Example: Dimethyl sulfoxide	Example: Dimethyl sulfone	Example: Thioacetamide	Example: Dimethyl sulfate
			
Legend:  = Hydrogen,  = Carbon,  = Sulfur,  = Oxygen,  = Nitrogen			

Figure 1.1. Important organosulfur compounds

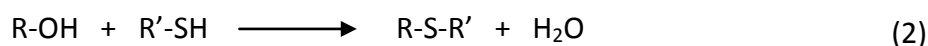
1.1.1. Sulfides (Thioethers)

Sulfides or thioethers, organosulfur compound with the connectivity R-S-R', are the sulfur counterpart of ethers. The replacement of oxygen with sulfur results in a compound with a low water solubility. In general, sulfide is considered to be a lipophilic functional group [5].

Thioethers are typically prepared by the alkylation of thiols in the presence of a base which converts the thiol into the more nucleophilic thiolate:

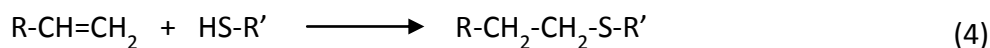


The reaction of thiols and alcohols (2) and the reaction of two molecules of thiol (3):





Alternatively, thioethers can be synthesized by the addition of a thiol to an alkene, catalyzed by free radicals:

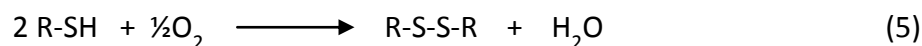


Among the more important reactions of thioethers can be cited the oxidation reaction. In this sense, thioethers may undergo a single oxidation to the sulfoxide or may be oxidized to the sulfone [5]. They are also readily alkylated to give stable sulfonium salts. Hydrogenolysis reaction is also carried out by thioethers in the presence of metal chlorides complexes [6], [7].

1.1.2. Disulfides

Another class of sulfur containing molecules is disulfides. The molecules have the generic formula R-S-S-R and are the corresponding sulfur analogs of peroxides. While still comparatively reactive, disulfides are much more stable than peroxides and are found in nature.

Disulfides are generally prepared by oxidation of thiols by the following reaction [8]:



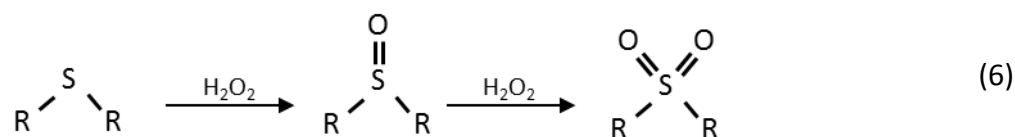
Alkyl, aryl and heteroaryl symmetrical disulfides can be easily obtained by heating the corresponding thiols for several hours at 80 °C with Et₃N in DMF under atmospheric oxygen [9]. Primary mercaptans oxidize more readily than secondary; tertiary mercaptans oxidize least readily. The oxidizing agents commonly used are O₂, sulfur, H₂O₂.

Some cyclic disulfides can be prepared by reaction of elemental sulfur with unsaturated compounds; for example, the reaction of acetylene with sulfur. The reaction of acetylene with sulfur was studied in more detail by Peel and Robinson, who determined that, below the boiling point of sulfur, acetylene reacts with it to give about a 5 per cent yield of thiophene, together with large amounts of carbon disulfide and hydrogen sulfide [10].

Among the most important reactions carried out by disulfides may be mentioned their reduction into thiols. Disulfides can be further oxidized to the thiosulfates, (R-S(O)S-R), thiosulfonates, (R-SO₂-S-R), disulfoxides and to sulfonic acids (RSO₃H).

1.1.3. Sulfoxides and sulfones

Two major groups of organosulfur compounds that have no counterparts among organic oxygen compounds are the sulfoxides (R-SO-R') and sulfones (R-S(O)₂-R').



Sulfoxides are easily prepared by oxidation of sulfides with such reagents as hydrogen peroxide (H₂O₂), sodium metaperiodate (NaIO₄) or nitrogen dioxide (NO₂). More-vigorous oxidation of sulfides or sulfoxides, for example, with potassium permanganate (KMnO₄) produces sulfones by following the reaction (6) described above. For example dimethyl sulfide is oxidized to dimethyl sulfoxide (DMSO) and then to dimethyl sulfone [11] [12].

1.1.4. Thioacids

Thioacids are a variety of other organosulfur compounds with structures of the types R-S(=O)-X, Y-S(=O)-X, R-S(=O)₂-X, and Y-S(=O)₂-X, in which X and Y are elements other than carbon, e.g., oxygen, nitrogen, or a halogen. Three types of organosulfur oxyacids are possible: sulfenic acids, R-S-OH; sulfinic acids, R-S(O)-OH; and sulfonic acids, R-S(O)₂-OH.

Sulfonic acids like methanesulfonic acid [13] and p-Toluenesulfonic acid are the most common of the sulfur-containing acids. They are very strong acids, are colourless and odourless acids and their salts are water soluble.

1.1.5. Mercaptans

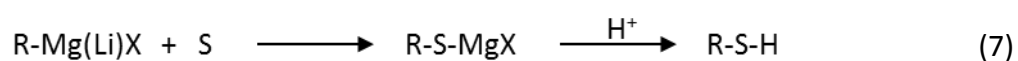
Among the organosulfur compounds, the most frequently used as starting materials for the syntheses of other important thio-compounds are mercaptans.

Mercaptans, often referred as thiols, are a class of organosulfur compounds characterized by the presence of one or more sulfhydryl (-SH) group. They are described by the general formula RSH, where R can be either an alkylic or an aromatic group. These sulfur compounds are commonly present both in natural gas and liquid fuels such as gasoline, kerosene, jet fuel, diesel and heating oils [14]. Mercaptans are the sulfur analogs of alcohols; indeed, there are many similarities in physical and chemical properties but there are also some notable differences. Replacement of the oxygen with the larger sulfur atom results in weaker association by hydrogen-bonding between the molecules. As aforementioned, this weaker intermolecular attraction is reflected in lower boiling points for the corresponding mercaptans, at least up to the six-carbon homologs, after which their boiling points become closely similar, because of the relatively smaller influence of the functional group. The bond strength between the hydrogen and the larger sulfur atom is weaker in the case of mercaptans (RSH) than the oxygen-hydrogen bond strength in alcohols (ROH). As a result, mercaptans are more reactive, more highly ionized and more acidic than alcohols. Like alcohols, the mercaptans react with carboxylic acids to form esters. Likewise, they react with aldehydes and ketones to form acetals and ketals. Unlike the alcohols, which upon oxidation produces aldehydes or ketones, the mercaptans are instead extremely easily oxidized to disulfides and under more vigorous conditions to thiosulfinates, thiosulfonates and finally, in the presence of water, yields to sulfinic and sulfonic acids. Water solubility of mercaptans is considerably lower than for the corresponding alcohols. Mercaptans form azeotropes with many hydrocarbons and the mercaptans above methyl and ethyl form azeotropes with their

corresponding alcohols.

Aliphatic mercaptans have been produced since many years. They can be synthesized by several procedures, including:

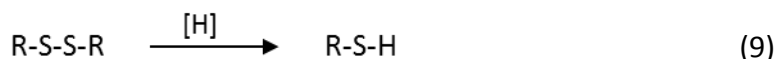
- a. Reaction of organomagnesium (RMgX) or organolithium (RLiX) compounds with elemental sulfur allows to form an intermediate susceptible to lead to a thiol in acid medium [1], [15].



- b. Reaction of an alkyl halide (RX, where X is a halogen) with the sulfur reagent thiourea, (NH₂)₂C=S, or with thiocyanate salts [1].



- c. Reduction of disulfides (RS-SR) to mercaptans (RS-H) by the action of one of the following reagents: NaBH₄, H₃PO₂, LiAlH₄, [1], [15].



- d. Aromatic thiols are frequently made from the reduction of arylsulfonyl chlorides.

Nevertheless, to industrial level, the most commonly starting compounds used for the synthesis of mercaptans (in general) are either n-alcohols or olefins [4], [16], [17] as shown in table 1.3. The choice of the starting compound depends upon the type of mercaptan wished (primary, secondary or tertiary mercaptans).

As can be seen, two routes may be followed to obtain primary mercaptans starting from hydrogen sulfide:

- a. Heterogeneous catalysis of n-alcohols.
- b. Photochemistry on α -olefins.

99% of purity in primary mercaptans is reached when starting from alcohols and hydrogen sulfide because of the high selectivity of catalytic substitution. On the other hand, only 92-93 % of primary mercaptans are obtained by photo-assisted addition of H₂S to olefins.

In the case of secondary and tertiary mercaptans, their production from alcohols leads to dehydration of the alcohol into an olefin as main product instead of the production of the corresponding mercaptan. When using olefins, the employment of acid catalysts is desired since the Markovnikov mechanism^(*) is selective for the secondary and tertiary mercaptans. Consequently, the addition of H₂S on the olefinic double bond by acid catalysis is preferred since the dehydration of the alcohol also produces undesired products.

Table 1.3. Industrially used routes for mercaptans manufacture

<i>Mercaptan</i>	<i>Primary</i>	<i>Secondary</i>	<i>Tertiary</i>
<i>Starting compound + H₂S</i>	R — SH	$\begin{matrix} R \\ \diagdown \\ \end{matrix} \text{SH}$	$\begin{matrix} R \\ \diagdown \\ R \\ \diagup \\ \end{matrix} \text{SH}$
<i>Alcohol</i>	Heterogeneous Catalysis	Heterogeneous Catalysis	Heterogeneous Catalysis
<i>Main product</i>	Mercaptan Purity 99%	Alcohol dehydration (Olefin)	Alcohol dehydration (Olefin)
<i>Olefin</i>	Photochemistry	Acid heterogeneous Catalysis	Acid heterogeneous Catalysis
<i>Main product</i>	Mercaptan Purity 92%	Mercaptan	Mercaptan

(*) Markovnikov mechanism predicts the regiochemistry of HX addition to unsymmetrically substituted alkenes. The halide component of HX is attached preferentially at the more highly substituted carbon, whereas the hydrogen prefers the carbon which already contains more hydrogen atoms.

In the following sections we will approach more in detail about the primary mercaptan **methyl mercaptan**, main character of this study.

1.2. METHYL MERCAPTAN

Methylmercaptan (MeSH), also known as methanethiol, is an organosulfur compound classified as a thiol. It is a colorless gas characterized by its obnoxious odor, its low boiling point (5,96 °C) and its highly flammable properties [18]. It is a natural substance found in the blood, brain, and animal and plant tissues. It is present in certain foods, such as some nuts and cheese as well as in the natural gas of certain and in some crude oils.

1.2.1. Methyl mercaptan: Markets, production and manufacturers

The main patents regarding the production of methyl mercaptan from methanol and hydrogen sulfide (Industrial route of production) belong to Elf Atochem North America, Inc. (Arkema), Phillips Petroleum Company (Chevron Phillips chemical Company), Pure Oil CO, Mobil Oil Corporation, American Oil Company, Rhone-Poulenc Animal Nutrition, Degussa AG and Evonik Degussa GmbH among others [19–32].

Nowadays, Methyl mercaptan is industrially manufactured by Arkema Inc. in Beaumont and Houston, Texas (EE.UU) as well as in industrial site of Lacq-Mourenx belonging to Arkema Company (FRANCE), being the last one the world leader in the field of thiochemistry [33]. The schema of manufacture of different products using as raw material hydrogen sulfide in industrial site of Lacq-Mourenx is shows in figure 1.2. The yellow dot-line highlights the process for the production of methyl mercaptan and the products manufactured from it.

By 1999, Phillips Chemical Company, a division of Phillips Petroleum Company, built a plant of methyl mercaptan in response to strong demand of this product. Company managers attribute the need for additional methyl mercaptan to rising demand of methionine, as a low cost supplement in animal feed [34].

In 2003, at the location Wesseling near Cologne (GERMANY), the business unit Feed Additives of Degussa AG, Düsseldorf, has established a methylmercaptan plant and successfully started up the production. The plant has an annual capacity of approximately

50,000 tons and is well matched to supply Degussa's methionine capacity in Wesseling and Antwerp. With the startup of methylmercaptan, the company is able to manufacture with its own process, all raw materials necessary for the production of DL-methionine [35].

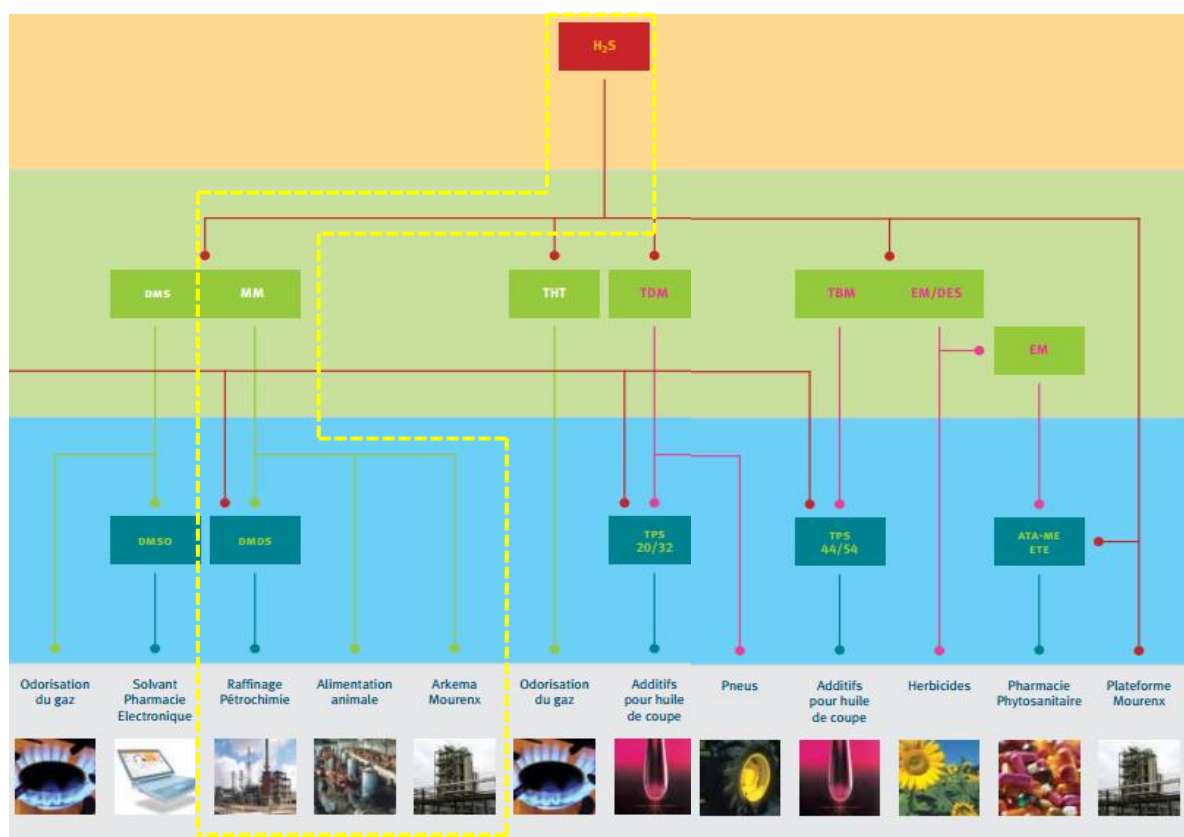


Figure 1.2. Production of methyl mercaptan (MM) and derivative products in the industrial site of Lacq-Mourenx (Arkema)

By 2011, CJ CheilJedang (CJ Group) and Arkema announced a project to build the world's first thiochemicals and bio-methionine platform in South East Asia (Malaysia). This project entails the construction of the world's first world-scale methyl mercaptan integrated bio-methionine plant, which will enable CJ to respond to strong demand for methionine, and Arkema to better serve its Asian customers from a new industrial platform. The project represents overall investments of \$400m split equally between both partners. According with the managing Director of Arkema's Thiochemicals Business Unit, with the construction of this plant, the company will have over 50,000 tons of new capacities for DMDS and mercaptans, primarily for the gas and petrochemicals markets. Last year (October 8th, 2012)

Arkema and CJ officially launch the start of the construction of their Bio-Methionine and Thiochemicals complex in Malaysia. The plant is scheduled to come on stream by end 2013 [36], [37].

1.2.2. Uses of methyl mercaptan

For many years, methylmercaptan was classified as an undesirable compound, particularly when present in petroleum fractions. In this sense, refiners started to develop processes for sweetening naphthas by conversion of the mercaptans to disulfides. Early, the main use for mercaptans was as an odorant for odorless gases [38], such as propane. Propane, as many sources of natural gas, is odorless by itself. Methanethiol is added for safety reasons, so the leaks are readily since methanethiol vaporizes readily and is odoriferous enough that only small quantities need be used.

Nowadays, methyl mercaptan is an industrially important chemical used as raw material for the production of valuable thio compounds such as methionine (the more important so far), dimethyl disulfide and methanesulfonic acid. Other indicated uses include the incorporation of methyl mercaptan in the synthesis of medicine, polymers, plastics, jet fuels, pesticides, fungicides, in agrochemical and pharmaceutical industry [38–42]. Similarly, methyl mercaptan may serve as the raw material for the synthesis of dimethyl sulfoxide, used as a solvent and in pharmaceutical production, through the intermediate dimethyl sulfide [38].

1.2.2.1. Methionine

As the building blocks of life, amino acids have long played an important role in both human and animal nutrition and health maintenance. There are nine (9) essential amino acids that humans and animals does not naturally produce, and so must be provided through our diet for normal growth and body functions [43]. One of those amino acids is methionine.

By far the single biggest use of methyl mercaptan is for production of synthetic methionine. Methionine, with the chemical formula $\text{CH}_3\text{-S-CH}_2\text{-CH}_2\text{-CH(NH}_2\text{)-COOH}$, is extensively used as

poultry food supplement and in feedstock industry. Its use in animal feed began in 1950s. As the methionine content in raw plant materials is insufficient, synthetic methionine complements must be added to animal feed. In animal diets it is the second limiting amino acid after lysine and in poultry it is even the first limiting one. The use of methionine has an indirect influence on humans. In this sense, some rare hereditary diseases like cystathioninuria and homocystinuria are caused by defective metabolism of methionine. Patients suffering from these diseases may exhibit one or more symptoms such as, mental retardation, seizures, thrombocytopenia, clubfoot, skeletal abnormalities, lens dislocation, and hearing defects. Dietary deficiency of methionine has also been linked to such ailments as toxemia, childhood rheumatic fever, muscle paralysis, hair loss, depression, schizophrenia, Parkinson's disease, liver deterioration, and impaired growth [44], [45]. Deficiencies can be overcome by supplementing the diet with methionine and, therefore, methionine is of significant interest.

In contrast with the other amino acids, methionine is biologically assimilable both in the dextrorotatory form (D or +) and in the laevorotatory form (L or -), which has allowed the development of chemical synthesis leading to the racemic product [46]. Thus, although several other amino acids such as lysine, threonine, isoleucine and histidine, are being produced successfully by biological means (fermentation), there are no reports about the commercial production of L-methionine by such method because microorganisms, either mutated or genetically engineered, have not produced sufficiently high concentrations of methionine. The bulk demand for methionine, about 350,000 tons annually across the globe, is met by the DL-methionine produced chemically. Most of the methionine demand comes from the poultry and animal feed industry and the remaining demand is due to the clinical and therapeutic use of L-methionine.

Chemical production of methionine involves the interaction of primary materials methyl mercaptan and acrolein along with various sources of ammonia and cyanide, in the presence of a catalyst [44]. It is proposed that acrolein and methyl mercaptan react leading to the intermediate methyl-mercaptopropionaldehyde (MMP) which after reaction with hydrogen cyanide or sodium cyanide leads finally to methionine [46]. At the present time, world's leading methionine producers are Evonik Industries, Adisseo, and Novus International. All

current methionine manufacturers have a similar production process, but the level of upstream integration varies.

The production site of Adisseo (currently Bluestar Adisseo) in Les Roches de Condrieu, south of Lyon (France) is the heart of the company's European methionine production and makes sulphur products (sulphuric acid and carbon disulfide) and Methionine MMP (methyl mercapto-propionaldehyde, the first intermediate in the synthesis of methionine). Figure 1.3 gives a schematic overview of the production of methionine and the materials involved. As can be seen, the basic products are derived from the petrochemical industry. Once MMP is established it is transported through an 11 kilometer long pipeline to a production plant in Roussillon where it is converted to DL-methionine [47].

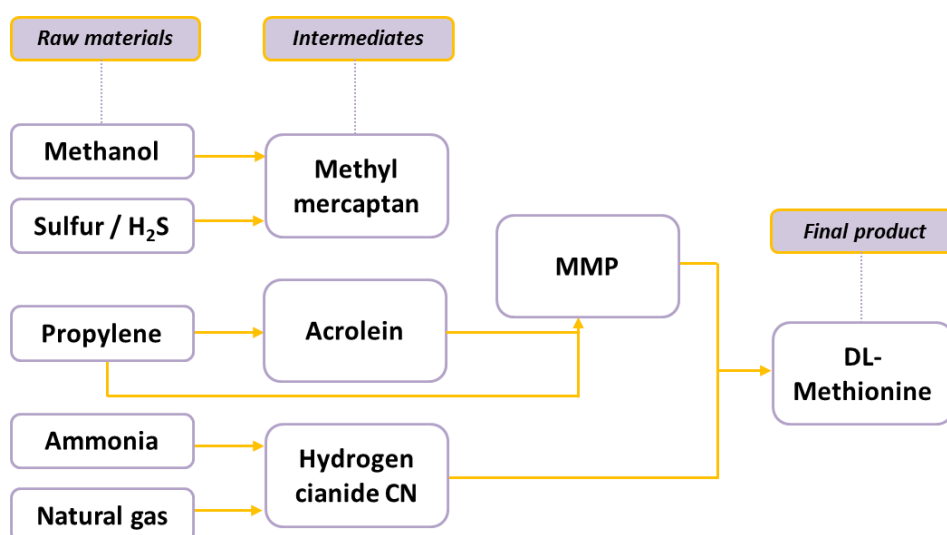


Figure 1.3. Simplified scheme of a complex methionine manufacturing process by Adisseo, Lyon (France)

On its part, Evonik Industries started to build a new methionine production complex in Jurong Island (Singapore) with an annual capacity of 150,000 metric tons. The new plant is scheduled to begin operating in the second half of 2014 and will employ several hundred persons. The main engineering and raw material contracts have already been awarded and preliminary work has already commenced. The new construction and the expansion of the four existing methionine production plants will raise Evonik's total annual capacity for this amino acid to 580,000 metric tons beginning in 2014 an increase of more than 60 percent in just five years (2010: 360,000 metric tons) [48].

As discussed in a previous section, CJ Group and Arkema also started de construction of world's first thiochemicals and bio-methionine platform in South East Asia (Malaysia). This plant will manufacture 80,000 tons of bio-methionine, which would be unique in the world.

The figure 1.4 below presents the estimated global methionine production capacities from 2009 to 2015.

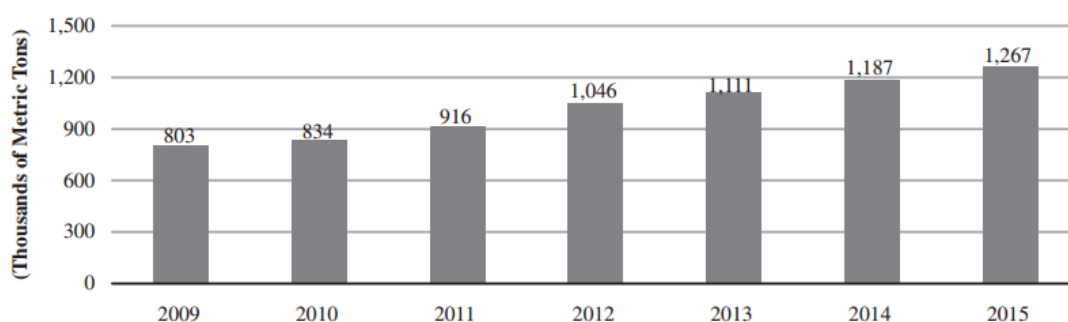


Figure 1.4. Methionine total capacities (2009 -2015)*

* Source: FA, based on companies' announcements.

1.2.2.2. Dimethyl disulfide

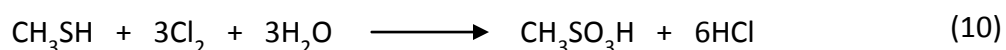
Dimethyl disulfide (DMDS), with chemical formula $\text{CH}_3\text{-S-S-CH}_3$, is volatile organic compound with a strong, pungent odour and highly flammable. Dimethyl disulfide is used in oil refining as a sulfiding agent to activate the catalysts of hydrotreating units and as additive for steam cracking, in petrochemicals for decoking operations and in metallurgy for its anticorrosion properties. Its great efficiency as a nematocide makes dimethyl disulfide a potential substitute for methyl bromide in agriculture. It is also used as a chemical intermediate in the manufacture of pesticides.

Its production may be made by the oxidative reaction of methyl mercaptan with dimethyl trisulfide in the presence of basic catalyst [49] and by the reaction of methyl mercaptan with sulfur [50].

1.2.2.3. Methanesulfonic acid

Methanesulfonic acid MSA (CH₃-SO₃-H) is the most common and simplest of the sulfur-containing acids. Because of its high acid strength (its kinetics are close to those obtained with sulfuric acid) and low molecular weight (it is the lowest molecular weight sulfonic acid commercially available), MSA is an excellent catalyst for esterification, alkylation and condensation reactions. Many esters prepared using MSA as the catalyst, are manufactured for the plasticizer, solvent and specialty chemicals markets.

Methanesulfonic acid is formed in the atmosphere from the chemical oxidation of atmospheric dimethyl sulfide (most of which is of biogenic origin) and deposited on the earth in rain and snow, and by dry deposition. Chemically, MSA is produced by the chemical oxidation of methyl mercaptan using a variety of oxidants such as chlorine gas, nitric acid or ozone. The current commercial process for its synthesis involves the chlorine oxidation of methyl mercaptan [13] and is called chloroxidation process (developed by Pennwalt Corporation in 1967-Currently Arkema [30]). It consists in the oxidation of methanethiol by chlorine to form methanesulfonyl chloride, which is then hydrolyzed to form MSA, with HCl as a by-product. The overall reaction of this synthesis is given below:





The increasing demand of methyl mercaptan is then directly related with the need of this important intermediary in the synthesis of new organosulfur compounds. Consequently, additionally to the current routes for the production of MeSH, new synthetic routes for methyl mercaptan production are to be developed, allowing, as far as possible, reduce costs and improve the production of such required product.

1.3. PROCESS FOR THE PRODUCTION OF METHYL MERCAPTAN

As a key material used for the production of important compounds in the field of medicine,

petrochemical, agriculture, pharmaceutical, among others, methyl mercaptan is currently prepared by two routes:

-  Methanol + H₂S (Industrial production as describe above)
-  Syngas + H₂S (micro-pilot / lab scale production)

1.3.1. Synthesis of Methyl mercaptan from Methanol

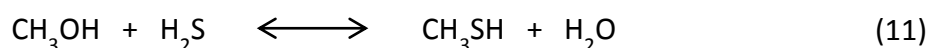
1.3.1.1. Reaction conditions

The reactions of alcohols with hydrogen sulfide for the formation of alkanethiols and dialkyl sulfides were first studied by 1910. Such reactions were studied using a solid catalyst of thorium dioxide, in the gas-phase at temperatures between 300 and 380 °C [51].

Later, in 1921, the same reaction was studied employing methanol and also butanol over a thoria catalyst, molar ratio CH₃OH:H₂S = 1:1 and temperatures of about 380 °C. Yields of MeSH around 30-50% were reported [52].

Since then, a large investigation regarding the production of MeSH, using the mixture methanol and hydrogen sulfide, has been made. From one to another, different parameters vary such as temperature, pressure, molar ratio between reagents, gas hourly space velocity (GHSV) and catalytic system, among others.

This route of synthesis is, in fact, the currently one used industrially for the manufacture of methyl mercaptan. The general reaction for producing methyl mercaptan by this process is as follows [22], [53].



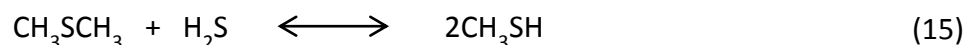
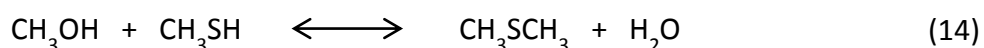
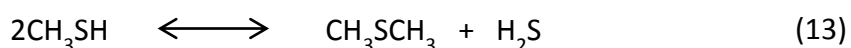
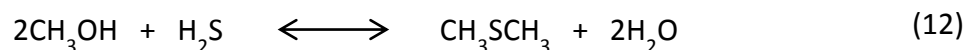
In practice, methyl mercaptan is synthesized in the following ranges of parameters [4], [38], [54]:

- Temperatures of 340-430 °C;
- Contact time 5-35 s depending on the temperature;
- Molar ratio H₂S: CH₃OH = 1.5-7.5;
- Overall pressure in the system as a rule not above 20 Bar.

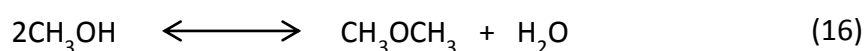
Depending on the different reaction conditions and catalysts employed, several side reactions may take place [4], [22], [38], [41], [53–65]. Nevertheless, by regulating the composition of catalysts and the reaction conditions, (temperature, pressure, contact time, molar ratio of hydrogen sulfide to methanol) it is possible to direct the process towards the formation of the desired product.

The most important sub-products of the reaction are dimethyl sulfide (DMS) and dimethyl ether (DME).

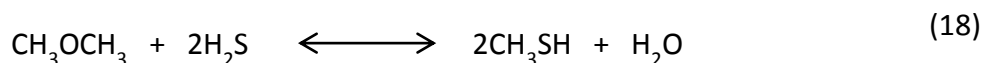
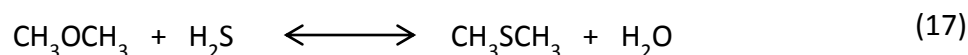
Reactions which may lead to the formation of dimethyl sulfide DMS or methyl mercaptan, depending upon rates and the position of equilibrium, may be represented as follows [38]:



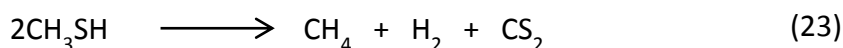
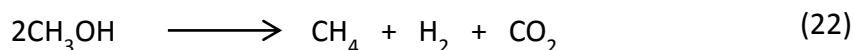
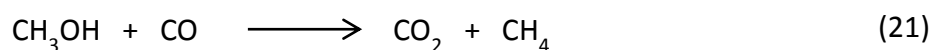
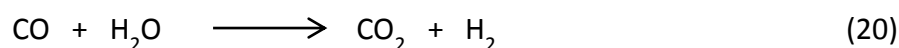
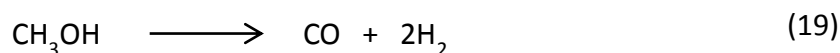
On its part, the primary oxygen-containing product DME may be formed by the methanol dehydration by the following reaction [38]:



If formed, DME may be converted to either DMS or MeSH according to the reactions:



In addition to the above reactions, other undesirable co-lateral reactions (decomposition reactions) occur to a greater or lesser extent. These reactions are relatively non reversible under the reaction conditions normally used [53], [55], [56].



i. Effect of temperature and pressure reaction

Dimethyl sulfide is principally produced by reaction (12) or (33) or (14). Activation energies of reactions (11), (12) and (14) decrease in the order (14) >> (12) > (11). Accordingly, lower the reaction temperature, higher the selectivity and conversion of methanol into methyl mercaptan [55]. On the other hand, the degree of methanol conversion increases by increasing temperature although at the cost of selectivity in favor of dimethyl sulfide [55], [56]. Concerning dimethyl ether, in order to prevent its formation, it is important to maintain a maximum temperature of above 315 °C [38].

It was reported by Doumani et al. [22] that reaction (14) proceeds extremely rapidly and goes essentially to achievement at temperatures above 315 °C in the absence of hydrogen sulfide. If H₂S is present, the reaction proceeds at a slower rate and there are more competing side reactions. Reaction (15) is found to be thermodynamically feasible only

about above 370 °C and in the presence of an absorbent catalyst. At lower temperatures, the equilibrium is too far to the left to obtain practically yields of mercaptan. Reaction (15) is somewhat slower than reaction (14).

Regarding decomposition reactions, at elevated temperatures, the initial methanol can decompose with formation of carbon oxides and methane, in agreement with reactions (19), (21) and (22) [54], [57]. Methane is also a product of the degradation of methanethiol and dimethyl sulfide according to the reaction (23) [54], [62].

No such importance has been given to the effect of the pressure in the reaction of methanol with hydrogen sulfide, however, has been reported that the rate of formation of dimethyl sulfide also increases with increase in the partial pressure of methanol and of the methanethiol formed from it [54].

ii. Effect of $\text{CH}_3\text{OH}:\text{H}_2\text{S}$ ratio

From reactions (11), (13), (15) and (17), it might be presumed that by employing an excess of H_2S in the reaction mixture $\text{CH}_3\text{OH}/\text{H}_2\text{S}$, side reactions leading to the formation of dimethyl sulfide could be repressed [53], [56], [58].

iii. Effect of the contact time

As well as temperature and pressure, the contact time plays also an important role in the direction of the possible reactions which may take place. In this regard, it has been reported that using a mixture $\text{CH}_3\text{OH}:\text{H}_2\text{S} = 1$, at a pressure of about 7 bar and temperatures around 400 °C, with catalysts composed basically for alumina and/or silica, high conversions and yields in MeSH were obtained, however, when the contact times were extended, the yields and conversions tended to drop off because of the increasing importance of the slower side reactions (reactions (19) to (22)) [22], [53]. Mashkin et al. [57] also reported that at the elevated temperature and high contact time, methane and carbon oxides are formed as well by decomposition of dimethyl ether and methanol in agree with reactions (19), (21) and (22). Similarly, Mashkina [54] reported that for a long contact time and at an elevated

temperature, methanethiol and dimethyl sulfide are partly decomposed with formation of methane and the deposition of coke on the surface.

1.3.1.2. Catalysts used in the thiolation of methanol

Among the parameters which play an important role in the selectivity toward the different products in the production of methyl mercaptan the catalyst choice is of critical importance, probably the most important parameter. In fact, many efforts have been concentrated on formulating catalyst compositions tailored which would be highly active for the conversion of methanol at high selectivity since certain of the above mentioned side reactions may be almost entirely repressed by the use of such specific catalysts.

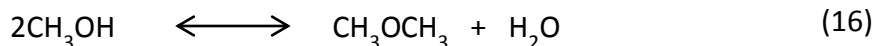
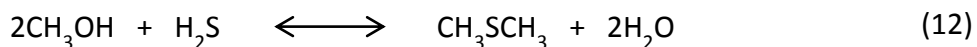
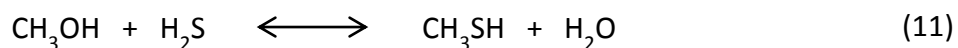
The conversion of alcohols into thiols occurs only in the presence of catalysts. As mentioned above, the active catalysts in thiolation of methanol are also active in competitive reactions leading to the formation of by-products, main reason by which the choice of the catalytic system become such an important parameter to control in the reaction.

Based on this argument, the reaction of methanol and hydrogen sulfide has been extensively studied over a vast variety of catalysts. In general, suitable catalysts consisted of alkali metal oxides, alkali metal carbonates, etc., or alkali metal salts of acids of Group VI metals on activated alumina or similar high surface area supports [20], [66], [67].

In order to better understand this section, a classification summarizing the most common and important catalytic formulation used for the production of MeSH when methanol reacts with hydrogen sulfide has been made.

i. Metal oxides

The reaction between methanol and hydrogen sulfide has been intensively studied first on various oxides and sulfides. This reaction leads to the formation of methanethiol and/or dimethyl sulfide as mainly products and also dimethyl ether according to reactions (11), (12) and (16) respectively.



Reactions (11) and (12) can proceed on a pair of Lewis acid–base sites or with the participation of Brønsted acid centres. The selectivity towards CH_3SH strongly depends on the nature of active sites. A low Brønsted acidity and a high basicity of catalysts favor the hydrosulfurization process. A decrease of acidity strength causes the growth of thiol and the decrease of sulfide formation. High strength of Brønsted acid sites leads to a high conversion of methanol to hydrocarbons (a competitive process) and low activity in the hydrosulfurization reaction [68].

Al_2O_3 was initially preferred as catalyst for the conversion of alcohols into thiols due to its high thermostability and because is relative readily available and cheap [54]. Catalytic results from literature established that such pairs of Lewis acid-base sites are present on alumina. Table 1.5 presents some examples of the conversion ($X\%$) of methanol with alumina catalysts and the selectivities ($S\%$) as a function of temperature, $\text{H}_2\text{S}:\text{CH}_3\text{OH}$ ratios and residence time (τ).

The high activity of Al_2O_3 in the reaction involving the conversion of methanol into the thiol has been explained by the presence in the oxide of paired acid - base centres promoting the activation of the reactants [69]. In the interaction of methanol with hydrogen sulfide in the presence of $\gamma\text{-Al}_2\text{O}_3$, a high rate of reaction per unit weight of catalyst is attained. As showed in table 1.4, the principal reaction products are methanethiol, dimethyl ether, and dimethyl sulfide and under severe conditions (high temperature and long contact time) carbon oxides and methane are also formed. With a deficit of hydrogen sulfide relative to methanol and at a high temperature, dimethyl sulfide is formed preferentially. Thus, in order to obtain methanethiol with a high selectivity, it is necessary that the $\text{H}_2\text{S}:\text{CH}_3\text{OH}$ ratio should be greater than 5 [38], [70].

Table 1.4. Performance of Al_2O_3 in the interaction of alcohols with hydrogen sulfide as a function of temperature, $H_2S:CH_3OH$ ratios and residence time

Author	T / °C	$H_2S:CH_3OH$	τ / s	X (%)	S (%)		
					CH_3SH	$(CH_3)_2O$	$(CH_3)_2S$
Calvino et al. [68]	300	2	-	100	34	0	63
Ziolek et al. [60]	350	1	-	99	11	0	88
Ziolek et al. [59]	350	2	6	99	46	0	53
Mashkina et al. [69]	360	1,6	0,06	86	40	24	35
Mashkina et al. [71]	360	0,6	0,2	85	6	12	81
Miki et al. [70]	370	1	3	100	37	0	63
Miki et al. [70]	370	10,8	3	100	88	0	12

Ziolek et al. [59] compared the activities of the Mg, Ti, Zr, Ce, and Al oxides in the reaction of methanol with hydrogen sulfide for $H_2S:CH_3OH$ ratio = 0.5 – 2.0, 350 °C and τ = 2-6 s. Table 1.5 reports activity and selectivity of the investigated samples for various $H_2S:CH_3OH$ molar ratios at the stationary state. It was found that the degree of conversion of methanol for all the catalysts, excepting MgO, was between 45 and 100 % when using an excess of hydrogen sulfide. The authors observed that by decreasing the $H_2S:CH_3OH$ molar ratio, from 2:1 to 1:1 and then from 1:1 to 1:2, the degree of conversion of the alcohol diminished.

A similar behavior was observed regarding the selectivities. By decreasing the $H_2S:CH_3OH$ molar ratio, the selectivity with respect to methanethiol falls, but the selectivity with respect to dimethyl sulfide increases. These two products (MeSH and DMS) were the main products formed. Methane was also produced on both titania samples, ceria, zirconia and alumina. For instance, for titania anatase, zirconia, ceria, and alumina, the selectivity toward dimethyl sulfide increases from the initial step to the stationary state using $H_2S:CH_3OH$ molar ratio of

1:1. This could be explained invoking first the formation of CH₃SH and next, transformation to (CH₃)₂S, according to Mashkina et al. [69], [71].

Table 1.5. Activity and selectivity of metal oxides in thiolation of methanol[59].

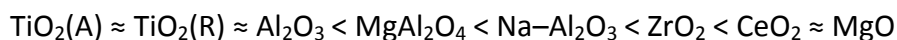
H ₂ S:CH ₃ OH	Catalyst					
	MgO	TiO ₂ (R)	TiO ₂ (A)	ZrO ₂	CeO ₂	Al ₂ O ₃
X_{CH₃OH} (%)						
2:1	2	45	91	72	68	99
1:1	3	25	52	34	59	99
1:2	2	15	32	16	42	43
S_{CH₃SH} (%)						
2:1	100	95	57	96	80	46
1:1	100	91	36	90	50	15
1:2	100	85	31	100	36	2
S_{(CH₃)₂S} (%)						
2:1	0	3	41	3	1	53
1:1	0	1	57	9	7	84
1:2	0	3	52	0	1	93
S_{CH₄} (%)						
2:1	0	2	2	1	19	0
1:1	0	8	7	1	43	1
1:2	0	12	17	0	63	5

Among the samples described, titania (anatase) and alumina show the highest selectivity toward dimethyl sulfide. Zirconia is a catalyst presenting a medium activity and very high selectivity toward methyl mercaptan and magnesia shows a complete selectivity towards methyl mercaptan despite its low activity. Ceria appears to be a very interesting catalyst since it produces the highest amount of methane and shows high selectivity toward methyl mercaptan.

The oxides investigated differ in their catalytic properties. Thus, the authors attribute the observed variations to the different acid-base characteristics of the above oxides.

Waqif et al. [72] studied the SO₂ adsorption on different metal oxides (MgO, CeO₂, Al₂O₃, ZrO₂, MgAl₂O₄, TiO₂-anatase, TiO₂-rutile, and Na-Al₂O₃) using various techniques

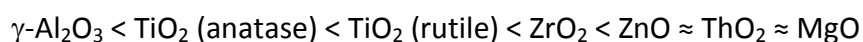
(thermogravimetry, temperature programmed desorption and IR spectroscopy). The authors reported the order given for the number of basic sites measured by SO₂ adsorption as follows:



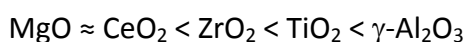
They observed that several types of species are formed. They discussed the results in terms of their thermal stability. On basic oxides, such as Na-Al₂O₃, SO₂ acts as an electron acceptor and adsorbs on either weakly basic O²⁻ sites or on the basic OH⁻ groups. In this latter case, the formation of hydrogen sulfite species is suggested. More strongly adsorbed species occur on all the oxides. These are characterized by strong absorption bands between 1100 and 800 cm⁻¹ and are due to sulfite species. Weakly adsorbed species can result from the coordination of SO₂ on Lewis acid sites such as Al₂O₃ and TiO₂, being such interactions quite weak.

The results achieved by Waqif are in good agreement with the selectivities' order observed by Zilolek et al. [59], in particular for a H₂S:CH₃OH molar ratio of 2:1. The rarer the basic sites, the higher the selectivity to dimethyl sulfide.

Others authors reported the strength of active sites for Lewis acidity and basicity, measured by adsorption microcalorimetry and/or transmission IR spectroscopy with different probe molecules [72–77]. They propose the following order for Lewis basicity, taking into account that this order is not precise since it is deduced from results obtained using various probe molecules



Concerning Lewis acid site strength, the following order can be proposed:



Comparing these order of basicity and acidity with the results achieved by Ziolek et al. [59] showed on table 1.6, the authors summarized:

- (i) The highest basicity of metal oxides (MgO) leads to the lowest activity and the highest selectivity to methanethiol.
- (ii) The presence of strong Lewis acid sites and medium basic sites ($\gamma\text{-Al}_2\text{O}_3$) implies the highest activity and the highest selectivity to dimethyl sulfide.
- (iii) The activity and selectivity of other samples do not bear a simple relationship to their basicity or acidity. This can be explained, considering the fact that they have pairs of Lewis acid and base centers which are involved in the reaction between methanol and hydrogen sulfide. Actually, the adsorption of both methanol and hydrogen sulfide requires oxygen and cation sites acting as Lewis base and acid centers.

These results confirm that methanol has to be chemisorbed in the form of methoxy groups to react with hydrogen sulfide and that methoxy species formation requires pairs of acidic-basic centers. As described in figure 1.5, on basic catalysts, the first step in the formation of methoxy species is methanol interaction with O^{2-} sites leading to H-bonded species; on acidic oxides, the first step is the formation of coordinated methanol species [78], [79]. However, the formation of methoxy species is not the only factor to consider since such species are formed on MgO and $\text{PO}_4^{3-}/\text{SiO}_2$, both oxides being inactive in the thiolation of methanol as observed in table 1.5. The strength of methanol chemisorption has also to be taken into account; if the methoxy species are too strongly held, they do not react with H_2S .

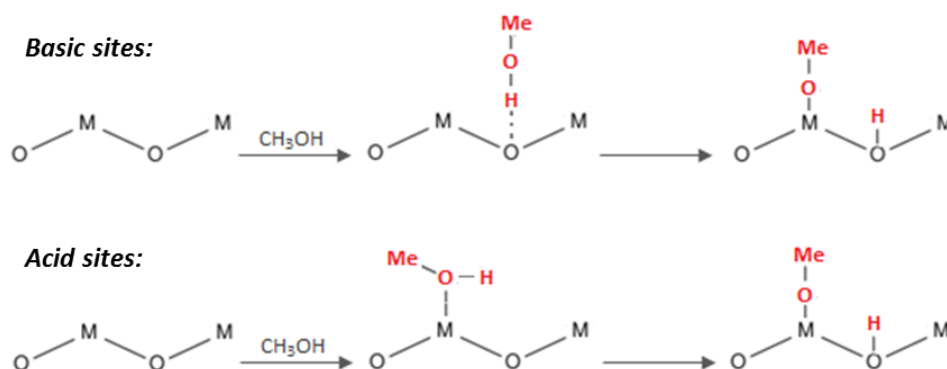


Figure 1.5. Adsorption of methanol and formation of methoxy groups over basic and acid sites.

The active form of adsorbed H_2S was not exposed by Ziolek et al. In this regard, several

papers deal with the mechanism of H₂S interaction with alumina [80–82]. For this oxide, two modes of H₂S adsorption were reported: i) undissociative adsorption (molecular adsorption) and ii) dissociative adsorption. Both forms of adsorption are represented in figure 1.6. Molecular adsorption occurs either on coordinately unsaturated cations with the formation of a coordinate bond (i.a) or via hydrogen bond to surface OH groups (i.b). Dissociative adsorption takes place on the strong Lewis acid-base pair sites and leads to appearance of acidic OH group and SH⁻ species (ii.a) or to S²⁻ ions and either two OH groups (reaction 24) or one water molecule (reaction 25) (ii.b) per every dissociated molecule of H₂S [82–84].

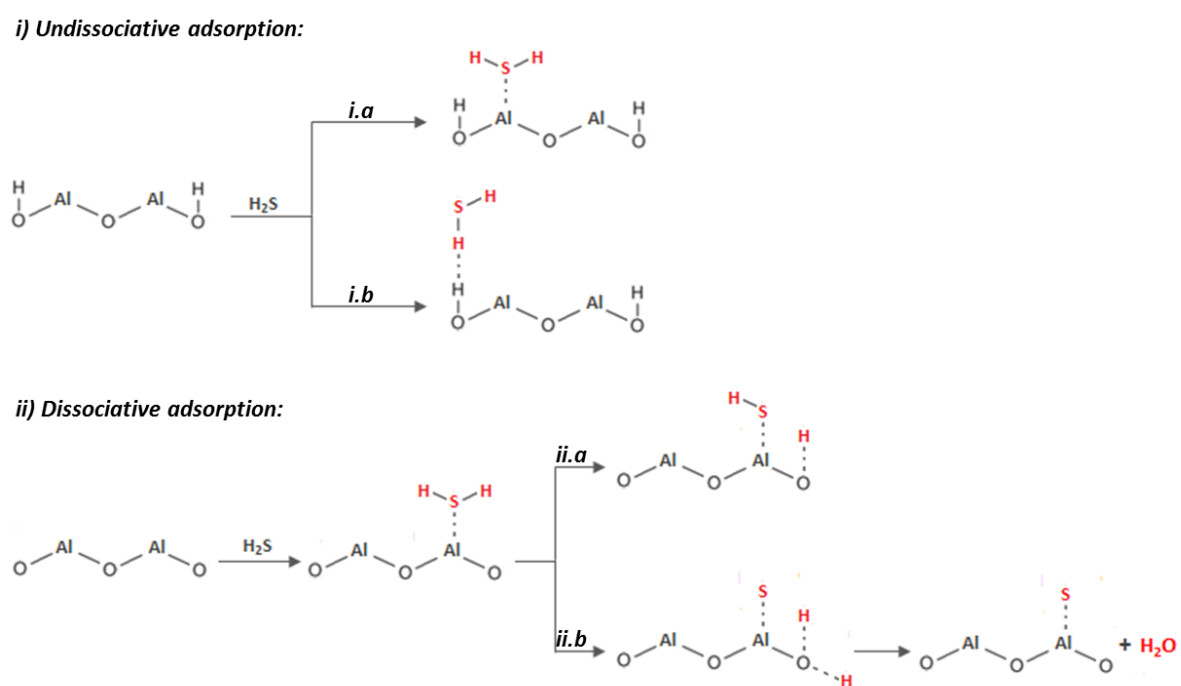
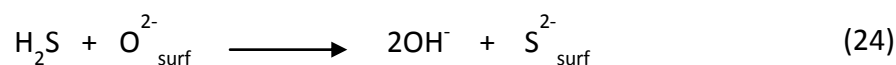
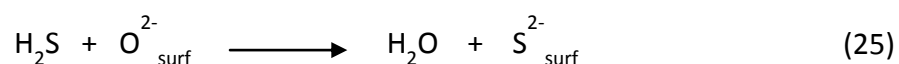


Figure 1.6. Forms of adsorption of H₂S over surface catalysts (e.g. Al₂O₃).

Mashkina et al. [69], [85] proposed that thiolation of methanol proceeds *via* the chemisorption of both methoxy and HS⁻ species, but after, they also suggest that H₂S molecules can react with methoxy groups. Others authors [86] show that H₂S adsorption on basic solids as MgO leads to the exchange of surface oxygen by sulfur according to the reaction 25.





Hydrogen sulfide appears to react first with the surface to form a water molecule in a configuration which immediately reacts to form hydroxyl groups; thionyl groups are not observed during the early stages of adsorption. The stability of methoxy species and the absence of HS^- formation explain the very weak activity of magnesia. By contrast, on alumina, the HS^- forms of H_2S chemisorbed is stable at high temperature, whereas methoxy groups are not too strongly held, thus explaining the highest activity of this oxide [80–82], [87].

Much less is known about H_2S adsorption on other oxides. On silica, H_2S only reversibly interact with surface silanol groups. On titania, hydrogen sulfide is mainly reversibly adsorbed undissociatively on both titania anatase and rutile, giving a coordinatively bonded species. In such a case, the hydrosulfurization reaction would occur between methoxy species and H_2S molecules [88], good activity is observed nevertheless. Water was observed when H_2S was adsorbed on the rutile form of titania [83]. On zirconia, H_2S adsorption leads to the formation of OH groups (observed by IR) suggesting the dissociative adsorption of H_2S . The absence of IR bands in SH region suggests that the second step of H_2S dissociation occurs ($\text{H}_2\text{S} \rightleftharpoons 2\text{H}^+ + \text{S}^{2-}$) which can lead to the replacement of oxygen by sulfur [59], [80], [83].

In conclusion, three possible sulfidation pathways can be considered when H_2S is adsorbed on metal oxides:

- (i) Coordinatively bonded hydrogen sulfide which can be a source of Brønsted acidity
- (ii) Dissociation of H_2S towards HS^- and H^+ , the latest forming hydroxyl groups on the catalyst surface
- (iii) Exchange of oxygen from metal oxide to sulfur

Pure silica is an example of an inert surface. Acidity of silanol sites in silica gel is so weak, with pK_a values in the range of 4 to 7, that the usual acid-catalyzed reactions do not proceed on SiO_2 [19]. There are neither strong basic sites. In recent studies, it has been shown that

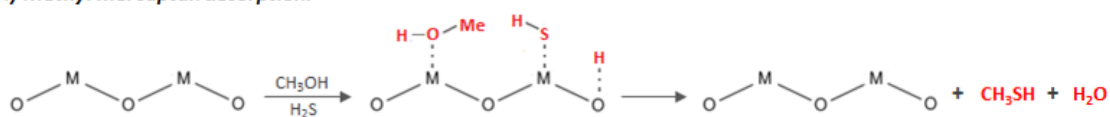
silica adsorbs little to no pyridine [20], ammonia or carbon dioxide [21]. Thus, silicon dioxide is relatively ineffective in the interaction of methanol with hydrogen sulfide. Mashkina et al. [69], [71] obtained yields of methyl mercaptan and dimethyl sulfide as low as 5 mol% and 1.2 mol% respectively (360 °C, $M = 0.6-1.6$, $\tau = 42$ s, $x \leq 20$ %).

Mashkina et al. [69] studied silica, silica-alumina, and alumina supports doped with transition metal oxides. They found that alumina-supported catalysts were an order of magnitude more active than silica-alumina-supported catalysts, which were themselves an order of magnitude more active than silica-supported catalysts. A conclusion from their results is that catalysts with Lewis centers of modest acid strength, such as alumina, are the most active for this reaction, while catalysts with either strong (silica-alumina) or weak (silica) Lewis centers are less active taking into account that pure silica cannot easily dissociate either methanol or H₂S [85], [89].

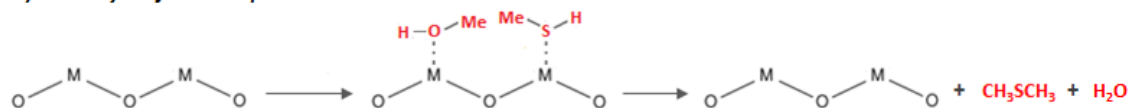
Several mechanisms have been proposed for the reactions between methanol and H₂S on metal oxide. As displayed in figure 1.7, Mashkina et al. [69] proposed a serial mechanism by which surface methoxy and bisulfide species on Lewis centers interact to form CH₃SH, which then desorbs (figure 1.7 (i)). CH₃SH also adsorbs on Lewis centers, reacting with a methoxy group to form (CH₃)₂S (figure 1.7 (ii)).

According to Mashkin et al. [57], the disproportionation of two molecules of CH₃SH to (CH₃)₂S and H₂S occurs on strong acid sites such as a pair of Lewis centers, and (CH₃)₂O is formed when surface methoxy species interact with each other (figure 1.7 (iii)) or with gas phase methanol. Other mechanisms suggest that (CH₃)₂S is formed by the reaction of surface methoxy species with gas phase H₂S [90], or the reaction of gas phase H₂S and (CH₃)₂O.

i) Methyl mercaptan desorption:



ii) Dimethyl sulfide desorption:



iii) Dimethyl ether desorption:

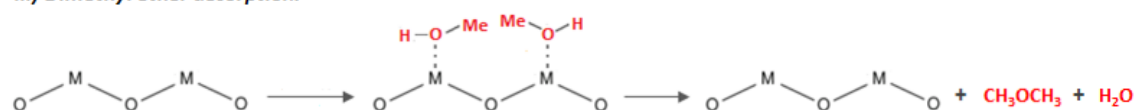


Figure 1.7. Representative scheme for the formation of (i) Methyl mercaptan, (ii) Dimethyl sulfide and (iii) Dimethyl ether

The mechanism proposed by Plaisance et al. [61] is exposed in figure 1.8. In this case M is a metal cation acting as a Lewis acid site. The authors postulate that the surface reaction pathway on alumina begins with the dissociative adsorption of methanol and H₂S onto LC/BC (Lewis acid–base) pairs. The resulting bisulfide (LC-SH) and methoxy (LC-Me) groups can then react according to several different paths as is shown. If a methyl with slight positive charge is adjacent to the bisulfide, the two can combine and desorb as MeSH (A), leaving a regenerated LC/BC pair. Alternatively, the bisulfide hydrogen can desorb by combining with a neighboring hydroxyl or methoxy group to form water or methanol, resulting in a sulfide (LC-S) and LC on the surface. The sulfide is expected to be more reactive than the bisulfide, and a neighboring methyl group can transfer to it to form a mercaptide species (B). The mercaptide (LC-S-Me) can then be protonated by a neighboring hydroxyl and desorb as MeSH (C). Once formed, MeSH dissociatively adsorbs onto LC/BC pairs in a way similar to H₂S and will react with other surface species. The adsorbed mercaptide can react with a neighboring methyl species and desorb as DMS (D). This reaction is expected to be first order in MeSH and irreversible. The disproportionation reaction will also occur to produce DMS and H₂S from MeSH. This reaction can occur when a methyl group is transferred from one surface mercaptide to another to desorb DMS (E), leaving a sulfide and LC on the surface.

This reaction is similar to (D), but should have a lower activation barrier, because the methyl group that is transferred is more weakly bound to sulfur than it is to oxygen. In a reaction similar to (E), a methyl group can transfer between two neighboring methoxy groups to desorb DME (F), this path being fast and reversible.

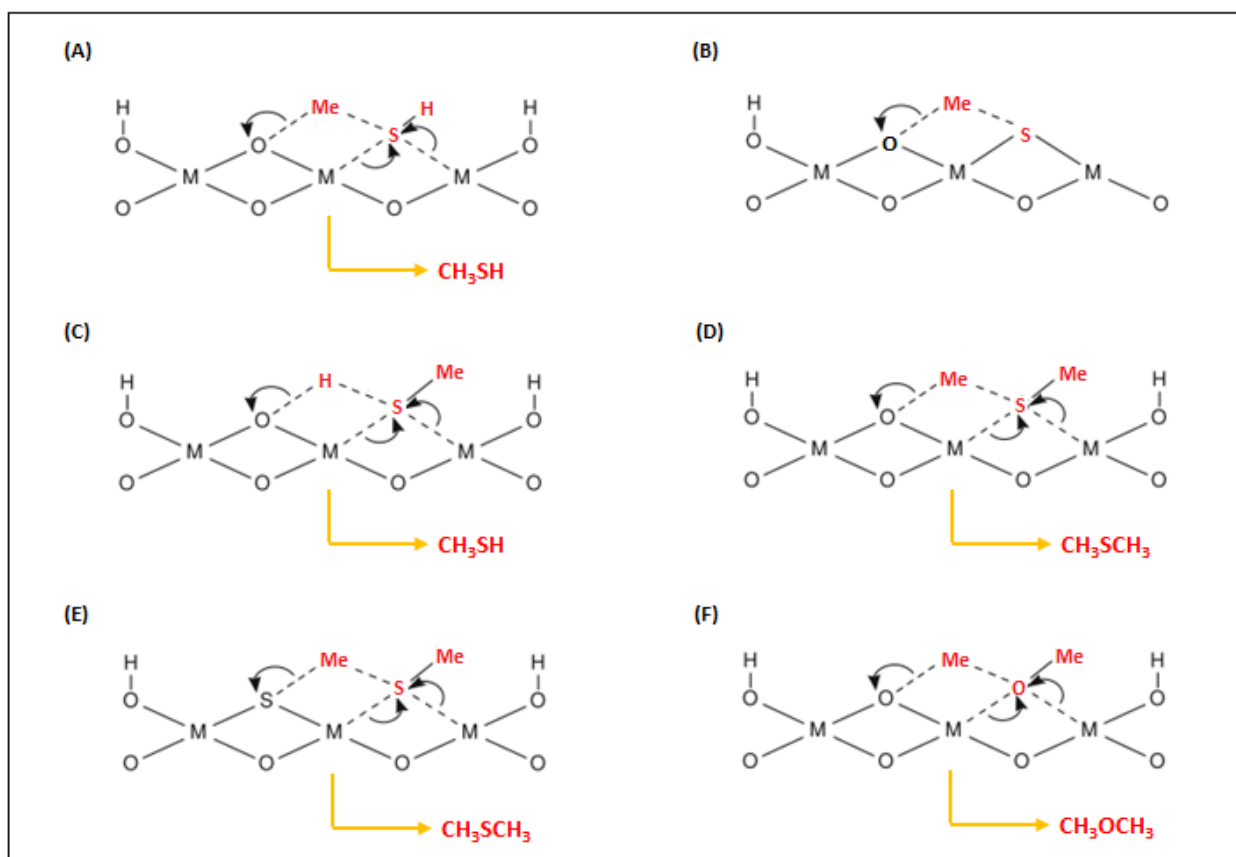


Figure 1.8. Reaction pathways in the thiolation of methanol

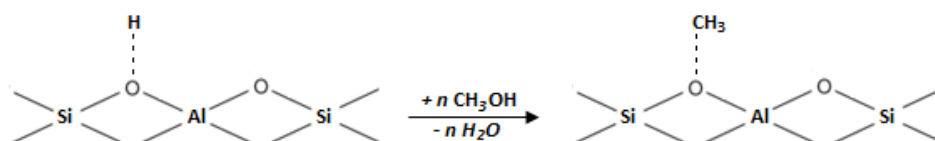
ii. Aluminosilicates, Zeolites and Hydroxyapatites

Silicon dioxide, which hardly exhibits any activity in the conversion of alcohols into thiols, acquires such an activity when some of the $(\text{SiO}_4)^{4-}$ ions are replaced by $(\text{AlO}_4)^{3-}$ ions with formation of aluminosilicates - amorphous (SiAl) and crystalline (zeolites). Thus, in the reaction of methanol with hydrogen sulfide on AlSi, the rate of conversion of methanol is seven times higher than on SiO_2 . At 360 °C, $M = 1.6$, $\tau = 6.3$ s, $x = 87\%$, the selectivity is 6% with respect to methanethiol and 62% with respect to dimethyl sulfide; dimethyl ether is also formed. The higher activity of AlSi compared with SiO_2 is due to the difference between

their acid-base properties. SiO_2 contains only very weak proton and basic centres, while AlSi contains strong proton and Lewis acid centres as well as moderately strong basic centres, which participate in the activation of the reactants [69].

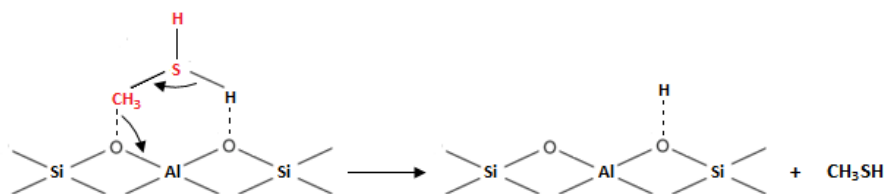
Zilek et al. [56] studied the reaction on H,Na-Y zeolites at 210-500°C. The reaction products were CH_3SH , $(\text{CH}_3)_2\text{S}$ and H_2O when an excess of hydrogen sulfide is used ($\text{CH}_3\text{OH}:\text{H}_2\text{S} = 1:4$) but for a ratio $\text{CH}_3\text{OH}:\text{H}_2\text{S}$ methanol = 1:1, methanol decomposition products were also noted. They observed that the increase of the reaction temperature causes the increase of the methanol conversion. The selectivity also changes with the variations on the reaction temperature. IR experiments allow to the authors concluded that the reaction on H,Na-Y zeolites occurs between CH_3OH chemisorbed and H_2S physically adsorbed. The followed reaction mechanism was proposed:

1. Methoxylation process:

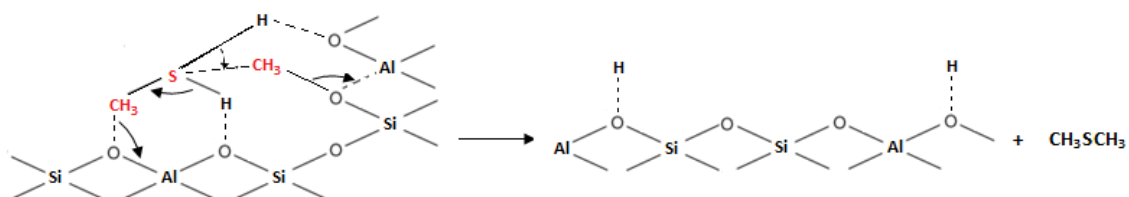


2. Reaction between methoxy groups and H_2S :

(2a) Methyl mercaptan desorption



(2b) Dimethyl sulfide desorption



Their results of catalytic conversion of isopropanol suggest that higher the Ca/P ratio, higher the conversion to acetone which implies the presence on higher concentration of basic sites. By contrast, the presence of HPO_4^{2-} ions increases the number of acid sites explaining the high conversion into propene of carbonated solids. The presence of Na slightly favors the propene formation but also increase the basicity of deficient, stoichiometric and Ca-rich solids, however, the most important effect on basicity enhancement was observed with the addition of carbonate ions into the structure of hydroxyapatite.

The best catalytic performance (high methanol conversion and high methyl mercaptan selectivity) was obtained using a slightly Ca-deficient solid modified by Na since the addition of both sodium and carbonated ions increased the number of basic sites without decreasing the acidic ones. The authors concluded that the ratio between acidic and basic sites could also influence the catalytic performance. In this case, catalytic performances of Hap-Na- CO_3 can be explained by both, the quantity of acidic and basic surface sites and by an optimal ratio acid sites/base sites for methanol catalytic reaction.

iii. Doped metal oxides

The doping effect of various alkali metals (Li, Na, K, Rb, Cs) on Al_2O_3 , SiO_2 and Nb_2O_5 (hydrated and dehydrated) were studied by Calvino-Casilda et al [68]. Their results of the reaction between methanol and hydrogen sulfide are in agreement with previous conclusions drawn for pure metal oxides. The introduction of alkali metal species into all the supports diminishes significantly methanol conversion, whereas methanethiol selectivity is enhanced by this modification. Alkali metal species decreases Lewis acidity of the catalysts and increases their basicity. In this way, Lewis acid–base pairs are formed and they play a crucial role in the mechanism of thiol formation.

The nature of the alkali metal elements affects both activity and the yield of methanethiol when the reaction is carried out on Al_2O_3 . They observed that the highest selectivity to methanethiol (MeSH) is achieved on $\text{K}/\text{Al}_2\text{O}_3$. The competitive reaction, ether formation, proceeds on all $\text{X}/\text{Al}_2\text{O}_3$ catalysts. The SiO_2 support impregnated with the alkali metal salts

shows a very low activity in this reaction. All alkali metal modified hydrated and dehydrated Nb_2O_5 exhibit above 90% selectivity to methanethiol and the highest methanol conversion was obtained on potassium and sodium forms of these catalysts. The influence of alkali metal nature on the catalyst activity was less pronounced in this series of catalysts than that on alumina support. Thus, the most promising catalysts for methyl mercaptan synthesis are based on niobia supports. Alkali metal species loaded on these matrices does not poison Lewis acidity too much and simultaneously creates basicity sufficient for a very high selectivity to methanethiol.

iv. Supported metal oxides

From the practical point of view, it is preferable to use catalysts obtained by depositing the active components on a support, since this involves a smaller consumption of the active substance, a high degree of its dispersion is attained, and thermal stability of the catalyst is ensured.

Mashkina et al. [92] evaluated the activity in methyl mercaptan synthesis over a series of potassium and tungstate supported catalysts on alumina, silica and silica-alumina. They related their results depending upon the acid-base properties of catalysts. Addition of WO_3 to $\gamma\text{-Al}_2\text{O}_3$ slightly exceeds the unmodified support in activity and selectivity towards MeSH. The presence of WO_3 increases the strength of Lewis sites with decreasing their concentration; the concentration of basic sites also decreases. The same behavior was observed with the addition of WO_3 to SiO_2 , however, a high rate of DMS formation was also observed. When using SiAl, addition of WO_3 enhances Lewis acidity and thus the activity and selectivity towards MeSH compared with SiAl non-promoted. DME was also detected on both WO_3/SiAl and SiAl.

Promotion with K_2WO_4 or K_2CO_3 decreases the catalytic activity but increases the selectivity towards MeSH. On SiO_2 and SiAl, base sites of moderate strength appear, compared to the non-supported oxides in which the presence of base sites were almost nonexistent. In $\gamma\text{-Al}_2\text{O}_3$, a decrease in concentration and strength of Lewis sites, disappearance of base sites

of moderate strength and appearance of base sites of strong strength were observed.

Their conclusions are similar to those discussed above for metal oxides: **i)** Interaction of SH⁻ with surface CH₃O groups for the production of MeSH. **ii)** Adsorption of MeSH on acid sites making its reaction with CH₃OH easy for the production of DMS. **iii)** Disproportionation of MeSH in the presence of strong Lewis sites leading to the formation of DMS. **iv)** Formation of DMS from DME and H₂S takes place on catalysts containing strong Brønsted sites and small amounts of L-sites (e. g. SiAl).

Mashkina et al. [93] also evaluated the performance of a series of alumina supported tungsten. In the presence of all catalysts tested, the main products were MeSH and DMS with traces of DME, carbon oxides methane and hydrogen in some cases. The rate of MeSH formation was between 5 and 60 times higher than the rate of DMS.

For the catalysts containing sodium tungstate, the authors established that with increasing the alkali metal to tungsten atomic ratio, the activity towards DMS tends to decrease.

The results achieved by Kudenkov et al. [94] using a series of Alumina based catalyst promoted by potassium hydroxide, carbonate and tungstate as well as sodium hydroxide suggest that the reaction under consideration occurs with the participation of strong basic sites, leading to an increase in activity and a slight decrease in MeSH selectivity.

The authors reported that the main reaction products were MeSH and DMS. Below 450 °C DME was also detected and over 400 °C, CO₂ and CH₄ appear also as sub-products of the reaction, resulting from the decomposition of CH₃OH, CH₃SH, DMS and DME. At the same time, a slight decrease in CH₃SH selectivity was observed with increasing the temperature.

As important conclusion, it had been found that the activity in DMS formation is around 3-4 times higher for K₂CO₃/Al₂O₃ and KOH/Al₂O₃ than that of K₂WO₄/Al₂O₃. In the same way, carbonate and hydroxide samples revealed a high activity towards decomposition products. Regarding the acid-base properties of catalysts, the tungstate sample presented a concentration in acid sites 2.5 times lower but slightly stronger of that of KOH and K₂CO₃.

Weaker base sites were detected in tungstate catalyst while stronger base sites were predominant in K_2CO_3/Al_2O_3 and KOH/Al_2O_3 .

The promoting effect of SiO_2 on K_2WO_4/Al_2O_3 catalysts for methanethiol synthesis from methanol and H_2S was studied by Zhang et al. [95]. They found that Si had a promoting effect on the K_2WO_4/Al_2O_3 catalyst for the synthesis of methanethiol. The appropriate amount of Si added to K_2WO_4/Al_2O_3 catalysts improves the specific surface area, restrains the aggregation of crystallites of the catalysts and greatly influences the acid–basic property of the catalysts.

The surface acidity properties of $K_2WO_4/SxAl$ were tested by in situ pyridine adsorption FTIR spectroscopy and NH_3 and CO_2 temperature program desorption. FTIR results suggest that more than one type of Lewis acid sites exists and Brønsted acid sites do not exist on the surface of the catalysts owing to the reaction of alkali metal salts and the supports. The intensities of the bands belonging to weak and moderate Lewis sites, rise at first then decline, suggesting that the quantity of Lewis acid sites increases at first then decreases, and reaches a maximum at $Si\%=5\%$. NH_3 -TPD results suggest that when the molar ratio of Si to Al is 5%, the strength and amounts of acid sites on the catalyst surface are the highest. Weak and moderate basic sites determined by CO_2 -TPD decrease with the addition of Si till 5% and then increase for the sample K_2WO_4/S_7Al . The authors suppose that the interaction of silica with support takes place by the bonding of silica to hydroxyl groups of alumina when the silica content was lower than 5% while silica may occupy some Al coordinatively unsaturated sites when the silica content increases to 7%, which leads to the decrease of Lewis acidity. The basicity of K_2WO_4/S_7Al increases because the amount of basic K_2WO_4 added was the same as that of S_5Al , but the consumption of base used to neutralize the acid was a little low. The catalyst with the molar ratio of Si to Al being 5% was found to exhibit the highest methanol conversion and catalytic activity.

The production of methyl mercaptan via methanol/hydrogen sulfide route is an efficient process in terms of methanol conversion and provides methyl mercaptan in high yield and purity. The principal disadvantage of this process is that a multiple-step pathway (figure 1.9.) for the synthesis of methanol is required, ($\text{CH}_4 + \text{H}_2\text{O} \longrightarrow \text{Syngas} \longrightarrow \text{Methanol}$) which results in costs of production.

This is the main reason why the development of new routes which may provide greater economies, by using a simple feedstock, avoiding the process of manufacture of methanol, is increasingly attractive in the industrial application.

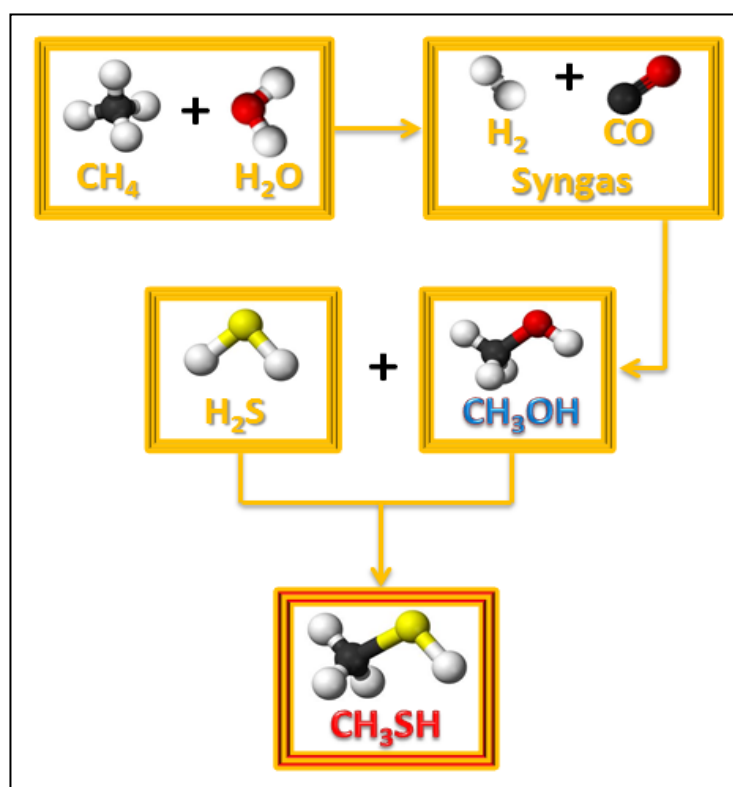


Figure 1.9. Pathway for methyl mercaptan synthesis from MeOH/H₂S mixture

1.3.2. Synthesis of Methyl mercaptan from Syngas

1.3.2.1. Reaction conditions

The synthesis of methyl mercaptan from carbon monoxide, hydrogen and hydrogen sulfide has been investigated since 1980s.

Mixtures of carbon monoxide and hydrogen in various stoichiometric ratios are known as synthesis gas (syngas) and are easily produced by various methods such as partial oxidation of hydrocarbons, steam reforming of natural gas, naphtha and high vacuum residues from crude oil distillation or coal gasification [96].

The pathway of reaction between syngas and hydrogen sulfide to produce methyl mercaptan is as displayed in figure 1.10.

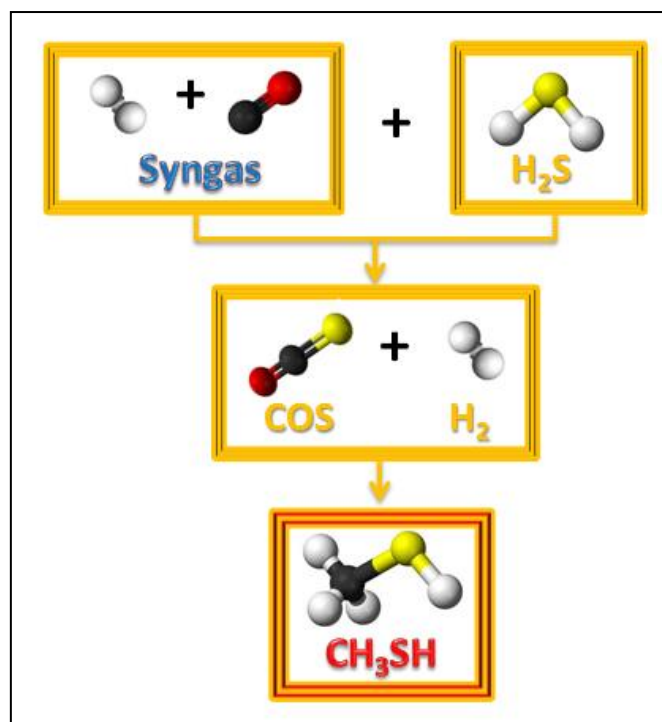
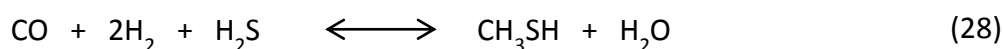
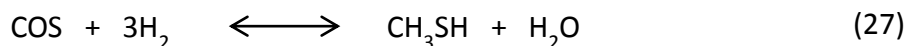
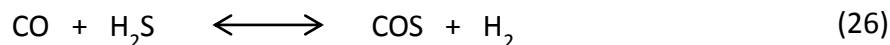


Figure 1.10. Pathway for methyl mercaptan synthesis from syngas/H₂S mixture

As can be seen, by blending directly syngas and hydrogen sulfide, methyl mercaptan is produced. This is the advantage of this process with regard to the MeOH/H₂S process in which syngas is used to obtain firstly methanol which reacts after with hydrogen sulfide

producing methyl mercaptan.

The reaction sequence by which carbon monoxide, hydrogen and hydrogen sulfide are converted to methanethiol is in accordance with reactions (26), (27) and (28) [96–101].



The reaction (28) is very exothermic ($\Delta_r H^\circ = -31,8$ kcal/mol) and has not thermodynamic limitation [102].

It is believed that the reaction proceeds via the hydrogenation of the intermediate carbonyl sulfide (COS), reaction (27), which is formed upon the reaction of carbon monoxide and hydrogen sulfide, reaction (26) [96], [100], [101], [103]. Experimental results of Barrault *et al.* [101] showed that reaction (26) is very fast compared to reaction (27) and that the latter is the rate-determining slow step for CH₃SH formation but has no significant role in the overall mechanism for syngas and H₂S conversion.

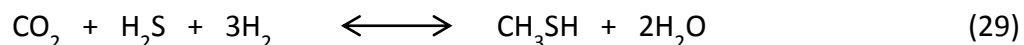
Ai Ping Chen *et al.* [103] conclude that according to Le Chatelier's principle, increasing the concentration of H₂ will suppress reaction (26) and lead to a decrease of the conversion of CO, while increasing the concentration of H₂S will increase the conversion of CO. Moreover, the decrease of the concentration of COS should coincide with the increase of that of CH₃SH.

The yield of the intermediate COS can be minimized by decreasing the total gas hourly space velocity GHSV and/or by increasing the reaction temperature, thus resulting in increased yields of MeSH [96]. The effect of the temperature in this case is interesting since usually the formation of by-products is supported by increasing the reaction temperature.

Carbon dioxide may be used to replace part or all of the carbon monoxide in the reaction

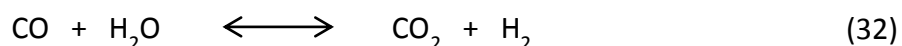
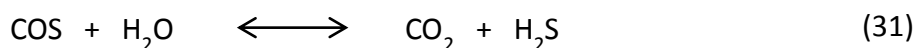
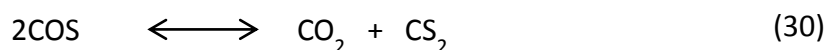
(26) but carbon monoxide is more reactive and provides higher conversions than carbon dioxide at high space velocities, in addition, the reaction employing carbon dioxide requires large amounts of hydrogen [98].

The process with carbon dioxide may be represented by the following equation [99], [104]:



Using carbon monoxide as carbon source, the principal potential reaction by-products are carbon dioxide, carbonyl sulfide, methane, carbon disulfide and dimethyl sulfide [96]. It has been found that at temperatures between 220 and 250 °C and pressures around 10 bars, the formation of methanol and dimethyl ether as reaction products of carbon oxide and hydrogen does not occur [96], [97]. The main factors responsible for the formation or absence of these products are temperature and pressure [96].

The possible reactions leading to the formation of CO₂ are listed below.



As shown, the CO₂ may be produced by the disproportionation or hydrolysis of COS (reaction 30 and 31 respectively) or by the water gas-shift reaction (32) [103]. These three reactions are favored over acid–base catalysts.

Experimental data of thermodynamic calculations made by Barrault *et al.* [101] and Guido *et al.* [105] show that water is not present in the product stream and CO₂ is produced instead by reaction of water with CO (WGS) or COS. In the same regard, other authors [103] reported that the decrease of COS leads to a simultaneous increase of CO₂, suggesting that CO₂ is also a product derivative of COS. Boulinguez *et al.* [98] also showed that in the

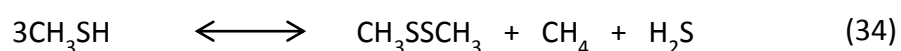
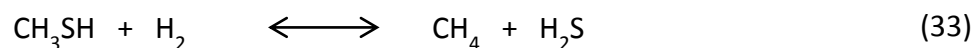
presence of oxidation-reduction catalysts such as those which demand the global reaction, the water is very rapidly eliminated from the medium by the water gas shift reaction (WGS).

A-P Chen *et al.* [103] performed a series of experiments in which they shown that the selectivity of CS₂ is only 0.3% over a KMoCo/SiO₂ catalyst. This observation suggests that most of the CO₂ cannot originate from reaction (30), otherwise the selectivity of CS₂ would be close to that of CO₂. However, it just indicates that CS₂ mainly comes from this reaction. The authors also reported that at high concentration of H₂S in the reaction system, the hydrolysis of COS is restrained, thus, it is impossible that most of the CO₂ originates from reaction (31). It is then reasonable to conclude that most of CO₂ should be from the water gas shift reaction, reaction (31).

Side-products as hydrocarbons and thioethers are considered to be produced from secondary reactions of CH₃SH but not from parallel reactions occurring at the same time that CH₃SH formation.

Obviously, as well as for the reaction of methanol and hydrogen sulfide, those undesired reactions may be suppressed or diminished by varying parameters such as temperature, and pressure abovementioned, contact time, molar ratios of reagents, etc. Regarding the contact time, it has been reported that the lower the space velocity the higher the selectivity for methyl mercaptan and the lower the formation of undesired by-products such as carbonyl sulfide and methane [96], [100].

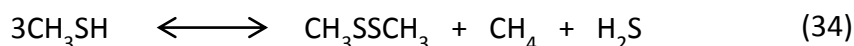
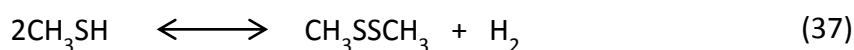
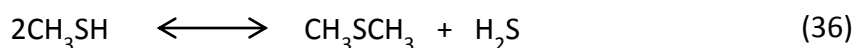
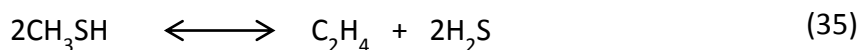
Methane formation is minimized by maintaining the reaction temperature below about 300 °C. Possible reactions for the methane formation are:



Methane is a dominant byproduct, which may be due to a large quantity of active H on the sulfide surface of catalysts and thus promoting the hydrogenation of CH₃SH. The results

obtained by Mul et al. [105] suggest that methane is formed principally by hydrogenation of methanethiol, reaction (33). This reaction becomes favored over hydrogenation of COS at temperatures above 350 °C.

Together with methane, carbon dioxide and carbonyl sulfide, amounts of carbon disulfide (reaction 30) and dimethyl sulfide as potential byproducts and small amounts of ethane (C₂H₆), ethene (C₂H₄), dimethyl disulfide (CH₃SSCH₃) and dimethyl trisulfide (CH₃SSSCH₃) may be also detected. The small amounts of such by-products may attribute to the kinetic limitations [96], [103]. These products can be obtaining by the followings reactions:



In summary, a system of the most important reactions described previously is shown in figure 1.11.

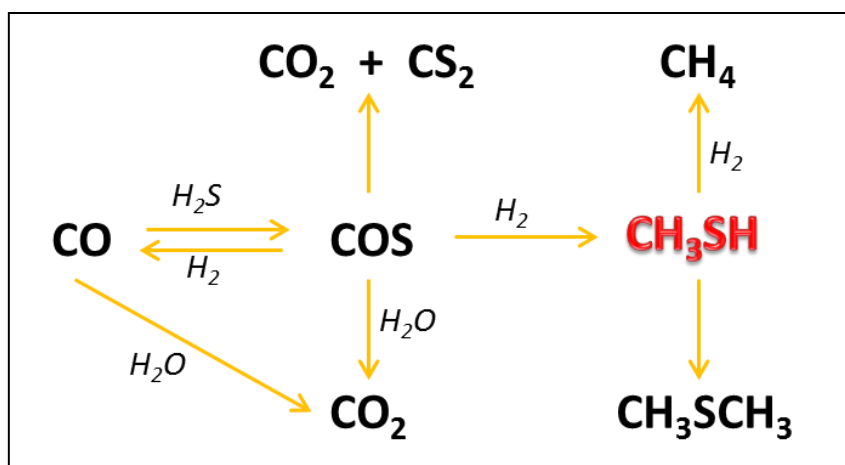


Figure 1.11. Reaction system involving syngas

As the reaction conditions employed in the synthesis of methyl mercaptan from syngas and hydrogen sulfide vary from a work to another, a compilation of those conditions are

summarized in table 1.6.

Table 1.6. Reaction conditions used by different authors for MeSH synthesis
from syngas/H₂S mixture

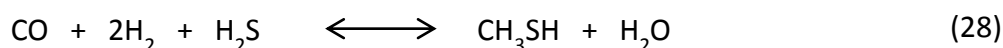
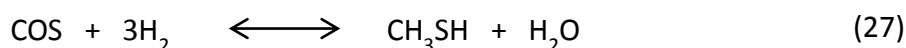
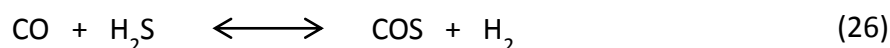
Author	Temperature °C	Pressure bar	Molar ratio CO/H₂/H₂S	GHSV h⁻¹
Yang et al. [96]	220 - 350	7 - 10	1-2 / 1-7 / 1-2	750 - 3000
Haines [97]	300 - 425	30 - 70	1 / 3-8 / 2-8	20 - 200
Bouliguez et al. [98]	250 - 450	30 - 50	1 / 4 / 2	500 - 1000
Barth et al. [100]	220 - 350	20 - 40	1 / 1-4 / 2-4	450 - 3000
Chen et al. [103]	300	2	1 / 1 / 2	3000
Zhang et al. [106]	340	20	4 / 5 / 1	200
Yi-Q Yang et al. [39]	295	10	2 / 2 / 0.1	3000
Dai et al. [40] and Yang et al. [107]	295	2	5 / 14 / 1	3000
Yang et al. [108]	295	2	2 / 7 / 1	3000
Hao et al. [109]	300	2	1 / 1 / 2	2000

1.3.2.2. Catalysts used in the reaction of syngas with hydrogen sulfide

As mentioned in the previous section (catalysts used in thiolation of methanol), the catalyst choice is of critical importance since both, conversions and selectivities toward one or another product is intimately related to the catalyst used in the process. Thus, by choosing carefully the catalytic system (active precursor, promoter, and support) the better performance could be achieved, trying to avoid the synthesis of undesirable products.

Fewer researches than by methanol route have been made regarding the synthesis of methyl mercaptan from syngas and hydrogen sulfide. In any case, the most important results are related to a supported catalysts promoted or not by some metal or metal oxide. Alumina or silica are the most common supports used and as active component, Mo (or W) and K containing compounds are usually selected.

In 1987, Barrault et al. [98], [101] worked with presulfided K-W-Al₂O₃ catalysts for the synthesis of MeSH from hydrogen, hydrogen sulfide and carbon oxides. The authors performed an interesting study about the optimum reaction conditions and the influence of the catalysts composition for this reaction. They determined that at temperatures between 240 and 335 °C a pressure equal to 12 and CO/H₂/H₂S ratio equal to 1/6/5, the conversion and selectivity of the catalyst used are in the order of 30 to 76% and 32 to 45% respectively but reaction temperature of about 300 °C and pressures around 30-45 bars, an important activity without significant increase of the byproducts (CH₄, CS₂ or DMS) was observed. Their study shows that the main steps of the reaction are the formation of carbonyl sulfide (reaction 26) and the hydrogenation of carbonyl sulfide to methyl mercaptan (reaction 27). The second step is generally the slow one, owing to the low hydrogenating properties of sulfide catalysts. Various equilibria between the initial CO, the COS intermediate and the main byproduct CO₂, are involved.



Concerning the catalysts used, their study showed that the tungsten/potassium ratio influenced catalytic properties and that a catalyst with a bulk composition corresponding to that of potassium tungstate (K_2WO_4 with $W/K = 0.5$) seemed more efficient. Potassium does not have a significant effect on overall activity and only a slight increase is observed. Selectivity, on the other hand varies to a far greater degree. When the potassium content is increased (W/K ratio < 0.5), a decrease in the hydrogenating properties is observed and with the highest K_2O content (4%), heavy products (CS_2 and DMS) appear and MeSH selectivity decreases.

The characterization of some catalytic systems before and after the catalytic reaction demonstrated that:

(i) The composition of the optimized catalyst, i.e., K_2WO_4 , is not preserved on the surface since is observed an enrichment in potassium.

(ii) In the presence of potassium, the tungsten does not appear to be affected by sulfidation, whereas, under the same conditions of pretreatment and in the absence of potassium, tungsten is partially sulfided into WS_2 .

(iii) The superficial composition of the catalyst evolves on contact with the CO , H_2S , H_2 mixture and partial sulfidation associated with a better tungsten dispersion after time on stream is observed.

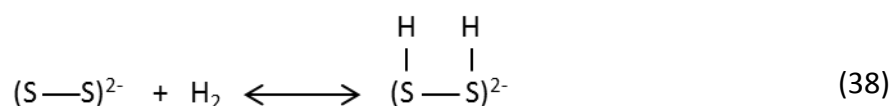
The synthesis of methanethiol from H_2S -rich syngas over sulfided Mo-based catalysts was investigated by Chen et al. [103], [110]. Mo catalyst was modified by the addition of K and/or Co. Li and Cs were also used replacing K with the aim to study the effect of alkali metals. It was observed that catalysts without alkali promoters (Mo/SiO_2 and $MoCo/SiO_2$) exhibited low CO conversion and low selectivity to CH_3SH , being the main product COS. Meanwhile, the potassium-promoted Mo-based catalysts revealed the high conversion of CO and the high selectivity to CH_3SH but also the selectivity towards CO_2 was important. The substitution of K by Li or Cs did not improve the catalytic activity and the selectivity towards MeSH was only slightly improved by using Li. The incorporation of cobalt into the K–Mo/ SiO_2 catalyst increased the conversion of CO and the selectivity to methane, but slightly decreased the selectivity to COS and CH_3SH . The authors suggest that these observations can

be attributed to the hydrogenating function of the cobalt promoter. With this catalyst, conversion and selectivity high as 42,7% and 48,5% respectively were achieved.

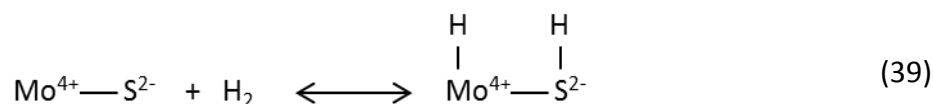
CO-TPD studies showed that the addition of potassium do not provides sites for CO adsorption but promotes the non-dissociative adsorption of CO on the KMo/SiO₂ and KMoCo/SiO₂ catalysts since this alkali metal is considered as a base which interacts with the transition metal components transferring electrons to the metallic phase (Mo), increasing the adsorption of such electron-acceptor molecules (CO) and weakening de C-O bonds, thus the deposit of potassium increases the coordinatively unsaturated molybdenum sites (presumably active sites) responsables of the formation of CH₃SH. XPS analysis indicates that the potassium increases the ratios of Mo⁵⁺/Mo⁴⁺ and low valent sulfur (S⁻ and S²⁻) /high valent sulfur (SO₄²⁻) favoring the synthesis of CH₃SH. Thus the reducibility of Mo species is diminished in the presence of potassium; as a result, the Mo⁵⁺ species are stabilized on the KMo/SiO₂ and KMoCo/SiO₂ catalysts after sulfidation, while the Mo⁴⁺ species are preferable on the Mo/SiO₂ and MoCo/SiO₂ catalysts. Concerning the influence of cobalt, the XPS results suggest that Co does not change the intrinsic activity of Mo, the promoting effect of Co on the synthesis of CH₃SH is possible related to the combination of Co with Mo-S species to form the so-called "Co-Mo-S" phase which favors the hydrogenation reactions or Co itself provides the active sites for CH₃SH synthesis.

Briefly, the presence of potassium favors the activation of CO and COS on the surface of the catalysts, which favors the subsequent hydrogenation to CH₃SH. These features explain the facts that CO conversion is low and COS selectivity is high over the potassium-free catalysts (Mo/SiO₂ and MoCo/SiO₂). So, potassium can be considered as one part of the active components on the sulfided K-Mo/SiO₂ and K-Mo-Co/SiO₂ for the synthesis of CH₃SH. The active phases may be thus the K-Mo-(Co)-S and/or K-Mo-(Co)-S-O species

Mechanism proposed: Regarding activated forms of H₂, two mechanisms for its activating have been suggested. One is homolytic cleavage over S₂²⁻:



The other is heterolytic cleavage over Mo–S bond:



Concerning the role of CO in the reaction, due to its electron-donor properties, electrons may be transferred from CO to sulfur ion belonging to the coordination sphere of Mo or Co:



Then, the formed carbonyl sulfide (COS_{ads}) and/or thioformate (HOCS_{ads}) species, can be hydrogenated to a methylthiolate intermediate ($\text{CH}_3\text{S}_{\text{ads}}$) by the spillover of active hydrogen atoms on the sulfided Mo or Co–Mo components ($\text{Mo}^{4+}\text{—S}^{2-}$, Co–Mo–S, or S_2^{2-} species), leading to the formation of CH_3SH (reaction 28).

The authors also suggest that water-gas shift reaction $\text{CO} + \text{H}_2\text{O} \rightleftharpoons \text{CO}_2 + 2\text{H}_2$ co-exists with the reaction of methanethiol synthesis, since K also promotes the water-gas shift reaction. This explained the high selectivity towards CO_2 between the products of the reaction. Thus, these two competing reactions, the reaction between H_2S and CO and the reaction between H_2O and CO, will determine the products distribution.

Yang et al. [39] in their work consisting in the use of $\text{K}_2\text{MoS}_4/\text{SiO}_2$ and $\text{MoS}_2/\text{K}_2\text{CO}_3/\text{SiO}_2$ catalysts in the one-step synthesis from high H_2S -content syngas found that $\text{K}_2\text{MoS}_4/\text{SiO}_2$ is the more effective catalyst. The results of XRD suggested the presence of a named “Mo–S–K” phase. The largest amount of this species on the surface of the catalyst $\text{K}_2\text{MoS}_4/\text{SiO}_2$ was responsible for the high activity and selectivity to methanethiol compared with $\text{MoS}_2/\text{K}_2\text{CO}_3/\text{SiO}_2$. XPS analysis showed that the absence of $(\text{S–S})^{2-}$ on the catalyst $\text{K}_2\text{MoS}_4/\text{SiO}_2$ resulted in a higher content of Mo–S–K active phase compared to the catalyst $\text{MoS}_2/\text{K}_2\text{CO}_3/\text{SiO}_2$, in consequence, the catalytic performance of the last-one was lower.

Later, Dai, Yang and co-workers [40], [107] studied the promoting effect of transition metal oxides (Mn, Fe, Co, Ni) and rare-earth oxides (La, Ce) on $\text{K}_2\text{MoS}_4/\text{SiO}_2$ catalysts. It was found that the addition of promoters, affect positively the catalytic performance of these catalyst.

The promoting effect of La_2O_3 to catalyst $\text{K}_2\text{MoS}_4/\text{SiO}_2$ was superior to that of CeO_2 ; the proper content of La_2O_3 may be 5% (wt.). When talking about transition metal oxides the promoting effect was in the following order: $\text{CoO} > \text{Fe}_2\text{O}_3 > \text{NiO} > \text{MnO}_2$. The best catalytic performance was obtained with the catalyst $\text{K}_2\text{MoS}_4/\text{CoO}/\text{SiO}_2$ reaching $0,37 \text{ Kg}_{\text{MeSH}} \cdot \text{h}^{-1} \cdot \text{Kg}_{\text{cat}}^{-1}$. A similar yield was obtained with the catalyst $\text{K}_2\text{MoS}_4/\text{La}_2\text{O}_3/\text{SiO}_2$. The results of XRD characterization show that two main phases are presents in the surface of promoted and non-promoted $\text{K}_2\text{MoS}_4/\text{SiO}_2$ catalysts: MoS_2 and Mo–S–K active phases, as was already reported [39]. It was observed that the addition of promoters increases the concentration of Mo-S-K active sites on the surface of the catalyst and thus the decomposition of K_2MoS_4 to MoS_2 is restrained. The XPS characterization displayed that the addition of promoters to the catalyst $\text{K}_2\text{MoS}_4/\text{SiO}_2$ can restrain the deep reduction of Mo species, thereby keeping the $\text{Mo}^{6+}/\text{Mo}^{4+}$ ratio on a higher level. Also the ratio $\text{S}^{2-}/(\text{S}-\text{S})^{2-}$ is strongly increased with the addition of transition metal oxides which has been reported to be in favor of the formation of CH_3SH . Briefly, addition of promoters not only can retard the decomposition of K_2MoS_4 to MoS_2 , thereby increasing the concentration of Mo^{6+} on the surface of the catalysts, but also increases the concentration of the S^{2-} species, which is beneficial for supplying activated hydrogen. Both Mo^{6+} and S^{2-} species on the surface of the catalysts are responsible for high yield and selectivity of methyl mercaptan.

The authors suggested a surface $\text{Mo}^{6+}-\text{S}_x-\text{K}^+$ as active sites for CH_3SH synthesis, while the MoS_2 phase was related to the formation of hydrocarbons. In figure 1.12 is presented the schemes proposed by the authors for the production of MeSH and hydrocarbons depending upon the active site considered, Mo-K-S or MoS_2 .

It is proposed that by increasing the concentration of surface S^{2-} species (in this case by the addition of promoters) is beneficial for supplying activated hydrogen. As a result, the increasing supplement of activated hydrogen may accelerate CO hydrogenation to produce CH_3 species owing to breakage of C–O bonds. Therefore, on the MoS_2 active phase (figure 1.12.a), it is easier to produce CH_4 through the addition of H (by the breakage of S–H) to the CH_3 species nearby than to produce CH_3SH through the addition of SH (by the breakage of Mo–SH) to the CH_3 species nearby. On the other hand, for the Mo–S–K active phase (figure 1.12.b), the SH^- group formed by the breakage of K–SH may readily move to CH_3 species to

form methyl mercaptan.

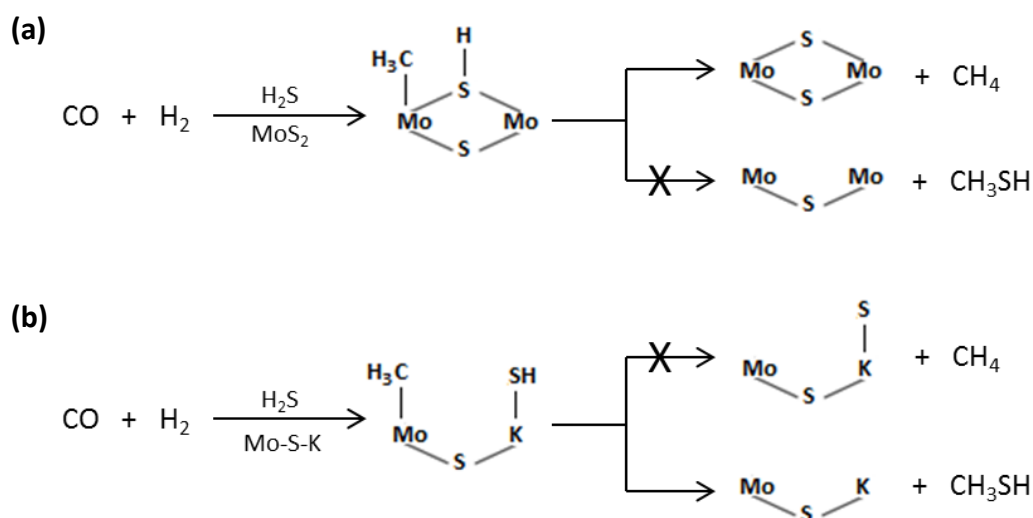


Figure 1.12. Schemes proposed for MeSH and CH₄ production in MoS₂ and Mo-S-K active phases

A similar investigation but this time using sulfided K₂MoO₄/SiO₂ catalysts [108]. The authors also studied the effect of the independent incorporation of Mo and K into the support. The activity assay shows that the incorporation of K₂CO₃ into MoO₃/SiO₂ leads to the formation of methyl mercaptan as a main product and the product distribution is found to be the same as that on the catalyst K₂MoO₄/SiO₂ prepared with K₂MoO₄. Under the reaction conditions of 0.2 MPa, 295 °C, GHSV = 3000 h⁻¹ and ratio CO:H₂:H₂S = 2:7:1, 0,58 Kg_{MeSH}·h⁻¹·Kg_{cat}⁻¹ were reached with this catalyst. The active site for these conversions appears to be the “Mo–S–K” phase. XPS results indicate Mo has mixed valence states of Mo⁶⁺, Mo⁵⁺, Mo⁴⁺, S²⁻ and [S–S]²⁻. The addition of K₂CO₃ to Mo-based catalysts is in favor of the formation of Mo⁵⁺, Mo⁴⁺, S²⁻ and [S–S]²⁻ species. The authors suggest that methanethiol synthesis is favored if the mole ratio of (Mo⁶⁺ + Mo⁵⁺)/Mo⁴⁺ ≤ 0.8 and S²⁻/[S–S]²⁻ is kept at a value of about 1.

Modification of SiO₂ support with small quantities of Ni was studied by Hao and co-workers [109], [111]. After addition of Ni to the support, the active component K₂MoO₄ was impregnated to obtain the catalyst K₂MoO₄/Ni-SiO₂. The obtained result suggested that the addition of Ni notably improves the catalytic performance of the catalyst compared to the non-modified catalyst. Modified catalyst exhibits higher conversion of carbon monoxide and

higher selectivity to methanethiol as well as a high selectivity to CO₂. BET results revealed K₂MoO₄ species dispersed better on the surface of Ni- SiO₂ than directly on SiO₂. Raman characterization of the sulfided catalyst K₂MoO₄/Ni-SiO₂ showed bands arising from MoS₂, reduced molybdenum and molybdenum oxysulfides, whereas in the solid without Ni, no signal originating from molybdenum oxysulfides was detected.

Another research on the influence of promoters addition was developed by Chen et al. [112], [113]. Tellurium was found to improve the activity of catalysts and the selectivity towards methyl mercaptan achieving 0,60 Kg_{MeSH}.h⁻¹.Kg_{cat}⁻¹. The effect of Te was related to the reduction of Mo⁶⁺ to Mo⁵⁺ or Mo⁴⁺, suggesting that Te may participate in the electron transform of redox processes of Mo species. It was also found that the concentration of low valences states of sulfur species increases with the addition of Te, consequently, higher concentrations of low valence states of Mo and S species in the sulfided catalysts lead to the higher yield of CH₃SH.

The same reaction using α-Al₂O₃ was investigated by Zhang et al. [42], [106]. Unmodified α-Al₂O₃ gave the best results for this in terms of methanethiol selectivity, arising 98% for 6% of conversion. A range of other catalysts were also investigated (e.g., γ- Al₂O₃, Cr₂O₃, WO₃, MoO₃, K/ α-Al₂O₃, Cr₂O₃/Al₂O₃, Cu/Cr₂O₃). All these solids gave inferior selectivities in CH₃SH when compared with α-Al₂O₃.

Detailed analysis of the products confirmed that the major by-product formed along with CH₃SH was water. Only slight trace amounts of CO₂ were observed at higher reaction temperatures and no COS was detected as a co-product. Based on thermodynamics, COS can be expected to be formed at the temperatures of test (340 °C) and the hydrolysis of COS
$$\text{COS} + \text{H}_2\text{O} \rightleftharpoons \text{CO}_2 + 2\text{H}_2\text{S}$$
is possible at temperatures below 100 °C. Since significant amounts of water are formed as a by-product, the absence of COS in this study is expected.

The authors found a relationship between CH₄, CH₃SH and (CH₃)₂S products since a decrease in CH₃SH selectivity leads to an increase in CH₄ and (CH₃)₂S. They attribute this effect to the

Lewis acidity of the catalysts since as it is known, the stronger Lewis acidity suppresses the formation of CH₃SH. It had been reported that the acidity of the oxides used for the reaction of CO+H₂+H₂S needs to be minimized if the maximum selectivity to methanethiol wants to be attained. With this purpose, a series of catalysts were evaluated and the results showed that K₂MoO₄/SiO₂ and MoO₃/α-Al₂O₃ presented higher CO conversion than α-Al₂O₃ and also high selectivity to CH₃SH. γ-Al₂O₃, which has surface Brønsted acid –OH groups in comparison with α-Al₂O₃, improved the selectivity to (CH₃)₂S formed from the acid-catalyzed reaction of CH₃SH, however, the surface acidity of γ-Al₂O₃ is insufficient to lead to further reaction of CH₃SH and (CH₃)₂S to form hydrocarbon products. Therefore, for the maximum selectivity to methanethiol, a relatively non-functionalized surface is required, which has minimal acidity. Pathways as that proposed by Chen and co-workers [103], [110] were similarly proposed by Zhang et al.

1.4. SUMMARY AND OBJECTIVES

Throughout this chapter was established that organosulfur compounds have been a continuing subject of interest due to the fact that they are very important and versatile materials in chemical research. Sulfur compounds are valued reagents widely used for synthesizing new compounds, thus, this synthesis is more and more important due to its increasing use in the manufacture of agrochemicals, petrochemicals, lubricants, cosmetics, pharmaceutical products and so on. One of the most important organosulfur compounds and which has been the subject under research in this work is methyl mercaptan. Currently, it is mainly used as intermediate in the synthesis of dimethyl disulfide (DMDS), methanesulfonic acid (MSA) and methionine, being the last one the more important so far. Actually, in spite of the fact that the exact numbers are unknown, it is believe that more than 1/3 of the production of methyl mercaptan is destined to the manufacture of methionine.

At industrial level, CH₃SH is produced by the reaction of methanol with hydrogen sulfide. Although the formation of CH₃SH from CH₃OH/H₂S route is a fast and selective reaction, this route require the synthesis of syngas from methane steam reforming and afterward

methanol is obtained from syngas, turning this process in some way as inefficient. Taking that into account, it is thought that the use of a simpler route of synthesis results in a process more attractive and in some way promising in industrial applications. Thus, the production of methyl mercaptan from syngas (H_2+CO) and hydrogen sulfide started to have an impact, not industrially so far but focused in this way.

Whatever the route used, the choice of the catalysts, becomes extremely important since the formation of byproducts can also take place, as dimethylsulfide (DMS) when using the methanol- H_2S route and carbon dioxide (CO_2) when using the H_2S -syngas route. Therefore, by regulating the catalysts composition, it is possible to direct the process towards the formation of the desired product. In this sense, it has been reported that the acid-base properties of catalysts is intimately related to the activity and selectivity in methyl mercaptan production. When the reaction of methanol with H_2S is carried out, catalysts exhibiting basic properties, mainly based on alkali metals supported on matrix having high surface area are preferred since when the basicity is increased, the selectivity towards MeSH is also increased, while the presence of acidic species into the catalyst increases the selectivity toward DMS. On the other hand, when using solids having both acidic and basic sites like hydroxyapatite, the methanol conversion and selectivity into MeSH are enhanced.

When talking about the syngas/ H_2S route, there are fewer researches than for the methanol/ H_2S route. In all published works, molybdenum, and in rarer cases tungsten, have been used as active component and silica and alumina are preferentially chosen as support. Unlike works dealing with the production of MeSH in the CH_3OH/H_2S route, only few works report on the use of supports with various acid-base properties. Concerning the active phase, the addition of potassium has been found to be favorable since a so-called "Mo-S-K phase" seems to be formed based on XRD measurements. It was proposed that this phase instead MoS_2 could be responsible of higher CO conversion and selectivity towards CH_3SH . Some authors [40] [107] reported that the presence of this phase increase the concentration of Mo^{6+} and S^- species at the surface of the catalyst through the formation of $Mo^{6+}-S_x-K^+$ phase; whereas, low valence state of Mo and S species were also claimed as active species by other authors [112]. The addition of promoters such as Fe, Ni and Co favor the formation of this Mo-S-K phase, increasing in this way the CO conversion and also the selectivity to

CH₃SH. Nevertheless, no concrete information has been reported regarding the exact nature of this Mo-S-K phase present in active catalysts.

Based on these statements, we will focus our investigation in the use of catalytic supported systems composed by different supports and active component (Mo or W and K) to obtain efficient catalysts. The three metallic elements will be introduced using tetraoxomolybdate and tetraoxotungstate of potassium (K₂MoO₄ and K₂WO₄) but also in the sulfided form by using the homemade tetrathiomolybdate and tetrathiotungstate of potassium (K₂MoS₄ and K₂WS₄). The supports chosen will be silica (a solid considered as non-acidic or weakly acidic), alumina (considered as an amphoteric solid) and hydroxyapatite (solid with acid sites and basic sites stronger than alumina) taking into account that different acid-base properties of supports could influence the catalytic performances in the synthesis of methyl mercaptan from syngas and hydrogen sulfide.

Study of the literature data highlights the lack of knowledge on the nature of the active phase for the thiolation from CO/H₂/H₂S. For better understanding the nature of the “Mo-S-K” phase proposed as active phase, we will focus this work on reference catalysts, supported on the same alumina support, with the same Mo and/or K low loading but varying the way of introduction of these metals on the carrier. Various characterization techniques (Raman, XPS, TEM...) will be performed in particular after activation procedure.

In order to increase catalytic performances, alumina, silica and hydroxyapatite supported catalysts will be also evaluated at high Mo(W) loadings. The role of the pre-treatment method, a parameter that has never been discussed in the academic literature, will be also studied.

1.5. REFERENCES

- [1] E. Block, *Reactions of Organosulfur Compounds*. Academic Press Inc, 1978, p. 317.
- [2] M. Qian, X. Fan, and K. Mahattanatawee, *Volatile Sulfur Compounds in Food*. American Chemical Society, 2011, p. 368.
- [3] M. J. Janssen, *Organosulfur Chemistry*. John Wiley & Sons, 1967, p. 351.
- [4] C. Forquy and E. Arretz, "Heterogeneous catalysis in mercaptan industrial synthesis," *Heterogeneous Catalysis and Fine Chemicals*, vol. 41, pp. 91-104, 1988.
- [5] T. L. Lemke, *Review of organic functional groups. Introduction to Medicinal Organic Chemistry*, 4th editio. Lippincott Williams & Wilkins, 2003, p. 157.
- [6] R. J. Cremlyn, *An Introduction to Organosulfur Chemistry*, 1st editio. Wiley, 1996, p. 262.
- [7] S. R. Ivanova, K. S. Minsker, and N. K. Lyapina, "Chemical transformations of organic sulfides during hydrogenolysis in the presence of metal chloride complexes," *Russian Chemical Bulletin*, vol. 44, no. 10, pp. 1917-1921, Oct. 1995.
- [8] M. Farahzadi, J. Towfighi, and a. Mohamadalizadeh, "Catalytic oxidation of isopropyl mercaptan over nano catalyst of tungsten oxide supported multiwall carbon nanotubes," *Fuel Processing Technology*, vol. 97, pp. 15-23, May 2012.
- [9] L. J. Ruano García, A. Parra, and J. Alemán, "Efficient synthesis of disulfides by air oxidation of thiols under sonication," *Green Chem.*, vol. 10, pp. 706-711, 2008.
- [10] H. E. Westlake, "The sulfurization of unsaturated compounds," no. 60, 1946, pp. 219-239.
- [11] K. Sato, M. Hyodo, M. Aoki, X.-qi Zheng, and R. Noyori, "Oxidation of sulfides to sulfoxides and sulfones with 30 % hydrogen peroxide under organic solvent- and halogen-free conditions," *Tetrahedron*, vol. 57, pp. 2469-2476, 2001.
- [12] A. V. Mashkina, "Catalytic Synthesis of Sulfoxides and Sulfones Via Oxidation of Sulfides by Molecular Oxygen," *Catalysis Reviews: Science and Engineering*, vol. 32, no. 1-2, pp. 105-161, Feb. 1990.
- [13] M. Finšgar and I. Milošev, "Corrosion behaviour of stainless steels in aqueous solutions of methanesulfonic acid," *Corrosion Science*, vol. 52, no. 7, pp. 2430-2438, Jul. 2010.
- [14] A. de Angelis, "Natural gas removal of hydrogen sulphide and mercaptans," *Applied Catalysis B:*

Environmental, vol. 113–114, pp. 37-42, Feb. 2012.

- [15] B. Aellach, "Préparation, caractérisation et évaluation des propriétés catalytiques des catalyseurs à base d'apatite dans la thiolation et dans l'oxydation du méthanol," Université Hassan II Ain Chock Casablanca, 2010.
- [16] L. Von Szeszich, "Process for the production of mercaptans," U.S. Patent N° 20707611937.
- [17] J. P. Lyon Jr., "Process for the production of mercaptans," U.S. Patent N° 24355451948.
- [18] E. Cadot, M. Lacroix, M. Breysse, and E. Arretz, "Catalytic Synthesis of Methylmercaptan by Selective Reduction of Dimethyldisulfide," *Journal of Catalysis*, vol. 164, no. 2, pp. 490-492, 1996.
- [19] R. T. Bell, "Process for the preparation of methyl and methylene sulfur compounds," U.S. Patent N° 25651951951.
- [20] H. O. Folkins, "Production of organic thiols," U.S. Patent N° 27860791957.
- [21] J. J. Cinque, H. D. Grove Jr., W. F. Hoot, and J. A. Jarooe III, "Methyl mercaptan production process," U.S. Patent N° 28224001958.
- [22] T. F. Doumani, "Preparation of mercaptans and sulfides," U.S. Patent N° 28291711958.
- [23] T. E. Deger, B. Buchholz, and R. Goshorn, "Novel catalytic process for preparation of mercaptans by reaction of H₂S with alcohols or ethers," U.S. Patent N° 30350971962.
- [24] D. O. Hanson, "Apparatus and process for producing methyl mercaptan," U.S. Patent N° 37920941974.
- [25] C. A. Audeh, "Methanol conversion process," U.S. Patent N° 44827441984.
- [26] R. T. Clark and J. A. Elkins Jr., "Selective synthesis of mercaptans and catalyst therefor," U.S. Patent N° 52833691994.
- [27] H. Ponceblanc and F. Tamburro, "Process for the preparation of methyl mercaptan," U.S. Patent N° 58472231998.
- [28] J. Sauer et al., "Catalyst, process for its preparation and use for synthesis of methyl mercaptan," U.S. Patent N° 58522191998.
- [29] C. M. Cook, D. E. Albright, and M. C. Savidakis, "Synthesis of mercaptans from alcohols," U.S. Patent N° 58746301999.

- [30] D. E. Stinn, H. J. Swindell, D. H. Kubicek, and M. M. Johnson, "Compositions comprising inorganic oxide and process for producing mercaptans," U.S. Patent N° 58980121999.
- [31] D. M. Hasenberg and M. D. Refvik, "Process and catalyst for synthesis of mercaptans and sulfides from alcohols," U.S. Patent N° 2007/01356582007.
- [32] H. Redlingshöfer, C. Weckbecker, and K. Huthmacher, "Catalysts containing tungstate for the synthesis of alkyl mercaptan and method for the production thereof," U.S. Patent N° 2010/0248952 A12010.
- [33] "http://www.arkema.com/sites/group/en/products/product_viewer.page?p_filepath=/templatedata/Content/Product_Datasheet/data/en/thiochemicals/060331_mercaptans.xml."
- [34] "<http://www.icis.com/Articles/1999/05/10/84243/phillipss-methyl-mercaptan-entry-makes-market-more.html>," 1999. .
- [35] "<http://www.chemeurope.com/en/news/24068/degussa-s-methylmercaptan-production-goes-online.html>."
- [36] "http://www.arkema.com/sites/group/en/press/pr_detail.page?p_filepath=/templatedata/Content/Press_Release/data/en/2011/110411_cj_cheiljedang_and_arkema_announce_a_project_to_build_the_world_s_first_bio_methionine_pla.xml," 2011. .
- [37] "http://www.arkema.com/pdf/EN/press_release/2012/cp_demarrage_construction_thiochimie_malaisie_va.pdf," 2012. .
- [38] H. Folkins and E. Miller, "Synthesis of mercaptans," *Industrial & Engineering Chemistry. Process, design and development*, vol. 1, no. 4, pp. 271-276, 1962.
- [39] Y.-Q. Yang, Y.-Z. Yuan, S.-J. Dai, B. Wang, and H.-B. Zhang, "The catalytic properties of supported K₂MoS₄/SiO₂ catalyst for methanethiol synthesis from high H₂S-content syngas," *Catalysis letters*, vol. 54, pp. 65-68, 1998.
- [40] S. Dai, Y.-Q. Yang, Y. Yuan, D. Tang, R. Lin, and H. Zhang, "On methanethiol synthesis from H₂S-containing syngas over K₂MoS₄/SiO₂ catalysts promoted with transition metal oxides," *Catalysis letters*, vol. 61, no. 3-4, pp. 157-160, 1999.
- [41] T. J. Paskach, G. L. Schrader, and R. E. McCarley, "Synthesis of Methanethiol from Methanol over Reduced Molybdenum Sulfide Catalysts Based on the Mo₆S₈ Cluster," *Journal of Catalysis*, vol. 211, no. 2, pp. 285-295, Oct. 2002.
- [42] B. Zhang, S. H. Taylor, and G. J. Hutchings, "Synthesis of methyl mercaptan and thiophene from

- CO/H₂/H₂S using α -Al₂O₃," *Catalysis letters*, vol. 91, no. 3–4, pp. 181-183, 2003.
- [43] W. Leuchtenberger, K. Huthmacher, and K. Drauz, "Biotechnological production of amino acids and derivatives: current status and prospects," *Applied microbiology and biotechnology*, vol. 69, no. 1, pp. 1-8, Nov. 2005.
- [44] J. Gomes and D. Kumar, "Production of L-methionine by submerged fermentation: A review," *Enzyme and Microbial Technology*, vol. 37, no. 1, pp. 3-18, Jun. 2005.
- [45] D. Kumar and J. Gomes, "Methionine production by fermentation," *Biotechnology advances*, vol. 23, no. 1, pp. 41-61, Jan. 2005.
- [46] J.-F. Devaux and J.-L. Dubois, "Method for Manufacturing Methylmercaptopropionaldehyde and Methionine Using Renewable Raw Materials," U.S. Patent N° 2011/0229626 A12011.
- [47] "<http://www.allaboutfeed.net/Processing/General/2011/10/The-complex-process-of-manufacturing-methionine-AAF012677W/>," 2011. .
- [48] "<http://corporate.evonik.com/en/media/search/pages/news-details.aspx?newsid=24201>." .
- [49] L. Gillete, "Preparation of dimethyl disulfide," U.S. Patent N° 32991461967.
- [50] E. Arretz, "Process for the manufacture of dimethyl disulphide," U.S. Patent N° 53129931994.
- [51] P. Sabatier, "-", *Comptes Rendus*, vol. 150, pp. 1217-1221, 1910.
- [52] R. L. Kramer and E. E. Reid, "The catalytic preparation of mercaptans," *Journal of the American Chemical Society*, vol. 43, no. 4, pp. 880-890, 1921.
- [53] T. F. Doumani, "Preparation of mercaptans," U.S. Patent N° 30069661961.
- [54] A. Mashkina, "Heterogeneous catalytic synthesis of alkanethiols and dialkyl sulfides from alcohols and hydrogen sulfide," *Russian Chemical Reviews*, vol. 64, no. 12, pp. 1131-1147, 1995.
- [55] D. M. Hasenberg and M. D. Refvik, "Graded catalyst bed for methyl mercaptan synthesis," U.S. Patent N° 7645906 B22010.
- [56] M. Ziolk and I. Bresinska, "Reactions of alcohols with hydrogen sulphide over zeolites. I. Activity of H, Na-Y zeolites in CH₃OH+H₂S reaction," *Zeolites*, vol. 5, pp. 245-250, 1985.
- [57] V. Mashkin, V. Kudenkov, and A. Mashkina, "Kinetics of the Catalytic Reaction between Methanol and Hydrogen Sulfide," *Ind. Eng. Chem. Res.*, vol. 34, pp. 2964-2970, 1995.

- [58] M. Ziolk, J. Czyniewska, J. Kujawa, a. Travert, F. Mauge, and J. C. Lavalley, "Reactions of alcohols with hydrogen sulphide on zeolites. Part 7: the effect of Brønsted acidity of faujasite type zeolites on methanol hydrosulphurisation," *Microporous and Mesoporous Materials*, vol. 23, no. 1–2, pp. 45-54, Jul. 1998.
- [59] M. Ziolk, J. Kujawa, O. Saur, and J. C. Lavalley, "Metal oxides as catalysts for the reaction between methanol and hydrogen sulfide," *The Journal of Physical Chemistry*, vol. 97, no. 38, pp. 9761-9766, Sep. 1993.
- [60] M. Ziolk et al., "Effect on the reaction between methanol and hydrogen sulphide of Na or Mo doping on zirconia and alumina," *Applied Catalysis A: General*, vol. 171, no. 1, pp. 109-115, Jun. 1998.
- [61] C. P. Plaisance and K. M. Dooley, "Zeolite and Metal Oxide Catalysts for the Production of Dimethyl Sulfide and Methanethiol," *Catalysis Letters*, vol. 128, no. 3–4, pp. 449-458, Nov. 2009.
- [62] A. V. Mashkina, "Synthesis of methylmercaptan from methanol and hydrogen sulfide at elevated pressure on an industrial catalyst," *Petroleum Chemistry*, vol. 46, no. 1, pp. 28-33, Jan. 2006.
- [63] M. F. Pankratova and Y. M. Pinegina, "Catalyst selection for dimethyl sulfide synthesis," *Kinetica I Kataliz*, vol. 12, no. 2, pp. 390-395, 1971.
- [64] V. Y. Mashkin, V. R. Grunvald, B. P. Yakovleva, B. P. Borodin, and V. I. Nasteka, "Kinetic regularities in reaction of methanethiol with methanol," *React. Kinet. Catal. Lett.*, vol. 45, no. 1, pp. 93-99, 1991.
- [65] A. V. Yermakova and A. V. Mashkina, "Kinetic Model of the Reaction of Methanol with Hydrogen Sulfide," *Kinetics and Catalysis*, vol. 45, no. 4, pp. 522-529, Jul. 2004.
- [66] H. O. Folkins, E. L. Miller, and A. Kempf, "Preparation of organic thiols," U.S. Patent N° 28200611958.
- [67] H. O. Folkins, E. L. Miller, and K. Adolph, "Preparation of organic thiols," U.S. Patent N° 28200621958.
- [68] V. Calvino-Casilda, R. Martin-Aranda, I. Sobczak, and M. Ziolk, "Modification of acid–base properties of alkali metals containing catalysts by the application of various supports," *Applied Catalysis A: General*, vol. 303, no. 1, pp. 121-130, Apr. 2006.
- [69] A. V. Mashkina, E. A. Paukshtis, and V. N. Yakovleva, ".,," *Kinet. Katal.*, vol. 29, p. 1174, 1988.
- [70] M. Miki, T. Ito, K. Nomura, and N. Mitsui, ".,," *J. Soc. Org. Synth.*, vol. 24, p. 482, 1966.
- [71] A. V. Mashkina, E. A. Paukshtis, V. N. Yakovleva, and G. V. Timofieeva, ".,," *Kinet. Katal.*, vol. 30, p. 1239, 1989.

- [72] M. Waqif, A. M. Saad, M. Bensitel, J. Bachelier, O. Saur, and J.-C. Lavalley, "Comparative study of SO₂ adsorption on metal oxides," *Journal of the Chemical Society, Faraday Transactions*, vol. 88, no. 19, pp. 2931-2936, 1992.
- [73] A. Gervasini and A. Auroux, "Acidity and basicity of metal oxides surfaces," *Journal of Catalysis*, vol. 131, pp. 190 - 198, 1991.
- [74] J.-C. Lavalley, "Use of probe molecules for the characterization of the surface basicity of divided metal oxides," *Trends Phys. Chem.*, vol. 2, p. 305, 1991.
- [75] P. F. Rossi, G. Busca, V. Lorenzelli, M. Lion, and J. C. Lavalley, "Characterization of the surface basicity of oxides by means of microcalorimetry and fourier transform infrared spectroscopy of adsorbed hexafluoroisopropanol," *Journal of Catalysis*, vol. 109, no. 4, p. 1988, 1988.
- [76] P. F. Rossi, G. Busca, V. Lorenzelli, M. Waqif, O. Saur, and J. C. Lavalley, "Surface basicity of mixed oxides: magnesium and zinc aluminates," *Langmuir*, vol. 7, no. 11, pp. 2677-2681, Nov. 1991.
- [77] M. I. Zaki and H. Knözinger, "Carbon monoxide - A low temperature infrared probe for the characterization of hydroxyl group properties on metal oxide surfaces," *Materials Chemistry and Physics*, vol. 17, no. 1-2, pp. 201-215, Apr. 1987.
- [78] J. C. Lavalley, "Infrared spectrometric studies of the surface basicity of metal oxides and zeolites using adsorbed probe molecules," *Catalysis Today*, vol. 27, pp. 377-401, 1996.
- [79] C. Pighini, T. Belin, J. Mijoin, P. Magnoux, G. Costentin, and H. Lauron-pernot, "Microcalorimetric and thermodynamic studies of CO₂ and methanol adsorption on magnesium oxide," *Applied Surface Science*, vol. 257, pp. 6952-6962, 2011.
- [80] O. Saur, T. Chevreau, J. Lamotte, J. Travertand, and J.-C. Lavalley, "Comparative Adsorption of H₂S, CH₃SH and (CH₃)₂S on Alumina," *J. Chem. Soc., Faraday Trans. 1*, vol. 77, no. 2, pp. 427-437, 1981.
- [81] Y. Okamoto, M. Oh-Hara, A. Maezawa, T. Imanaka, and T. S., "Hydrogen sulfide adsorption on alumina, modified alumina, and molybdenum trioxide/alumina," *J. Phys. Chem.*, vol. 90, no. 11, pp. 2396 - 2407, 1986.
- [82] A. Datta and R. Cavell, "An FTIR study of the adsorption of hydrogen sulfide on the alumina catalyst," *J. Phys. Chem.*, vol. 89, no. 3, pp. 450 - 454, 1985.
- [83] M. Ziolk, J. Kujawa, and J. C. Lavalley, "Influence of hydrogen sulfide adsorption on the catalytic properties of metal oxides," *Journal of Molecular Catalysis A: Chemical*, vol. 97, pp. 49 - 55, 1995.

- [84] D. Beck and J. White, "Catalytic reduction of CO with hydrogen sulfide. 2. Adsorption of water and hydrogen sulfide on anatase and rutile," *American Chemical Society*, vol. 90, no. 3, pp. 3123-3131, 1986.
- [85] A. V. Nosov, V. M. Mastikhin, and A. V. Mashkina, "¹H and ¹³C NMR study of catalytic reaction between CH₃OH and H₂S," *Journal of Molecular Catalysis*, vol. 66, no. 1, pp. 73-83, 1991.
- [86] A. M. Deane, D. L. Griffiths, Y. A. Lewis, J. A. Winter, and A. J. Tench, "Infra-red Study of the Interaction of Hydrogen Sulphide and Water with a Magnesium Oxide Surface," *J. Chem. Soc., Faraday Trans. 1*, vol. 71, pp. 1005-1012, 1975.
- [87] V. M. Mastikhin, I. L. Mudrakovsky, A. V. Nosov, and A. V. Mashkina, "High-resolution ¹H Nuclear Magnetic Resonance Study of Hydrogen Sulphide Adsorption on Heterogeneous Catalysts," *J. Chem. Soc., Faraday Trans. 1*, vol. 85, no. 9, pp. 2819-2825, 1989.
- [88] D. D. Beck and J. M. White, "Catalytic reduction of carbon monoxide with hydrogen sulfide. 2. Adsorption of water and hydrogen sulfide on anatase and rutile," *J. Phys. Chem.*, vol. 90, no. 14, pp. 3123 - 3131, 1986.
- [89] A. Travert, O. V. Manoilova, A. A. Tsyganenko, F. Mauge, and J. C. Lavalley, "Effect of Hydrogen Sulfide and Methanethiol Adsorption on Acidic Properties of Metal Oxides: An Infrared Study," *J. Phys. Chem. B*, vol. 106, pp. 1350-1362, 2002.
- [90] A. V. Mashkina, V. N. Yakovleva, and L. N. Khairulina, "Synthesis of dimethyl sulfide in the presence of zeolites," *React. Kinet. Catal. Lett.*, vol. 43, pp. 405 - 411, 1991.
- [91] C. Lamonier, J.-F. Lamonier, B. Aellach, A. Ezzamarty, and J. Leglise, "Specific tuning of acid/base sites in apatite materials to enhance their methanol thiolation catalytic performances," *Catalysis Today*, vol. 164, no. 1, pp. 124-130, Apr. 2011.
- [92] A. V. Mashkina, E. A. Paukshtis, and E. N. Yurchenko, "Effect of acid-base properties of catalysts on their activity in methylmercaptane synthesis," *React. Kinet. Catal. Lett.*, vol. 34, no. 2, pp. 407 - 412, 1987.
- [93] A. V. Mashkina, M. R. I., V. N. Yakovleva, and E. P. Starodubtseva, "Activity of tungstate catalysis in the synthesis of methyl mercaptane from methanol and hydrogen sulfide.pdf," *React. Kinet. Catal. Lett.*, vol. 36, no. 1, pp. 159 - 164, 1988.
- [94] V. M. Kudenkov, E. A. Paukshtis, and A. V. Mashkina, "Synthesis of methyl mercaptane in the presence of base catalysts," *React. Kinet. Catal. Lett.*, vol. 38, no. 1, pp. 199 - 203, 1989.
- [95] Y. Zhang, S. Chen, M. Wu, W. Fang, and Y.-Q. Yang, "Promoting effect of SiO₂ on the K₂WO₄/Al₂O₃

- catalysts for methanethiol synthesis from methanol and H₂S," *Catalysis Communications*, vol. 22, pp. 48-51, May 2012.
- [96] Y.-Q. Yang et al., "Process for the manufacture of methylmercaptan," U.S. Patent N° WO 2005/040082 A22005.
- [97] P. G. Haines, "Preparation of methyl mercaptan from carbon oxides," U.S. Patent N° 44490061984.
- [98] M. Boulinguez, C. Forquy, and J. Barrault, "Process for the production of methyl mercaptan from oxides of carbon," U.S. Patent N° 46652421987.
- [99] J. F. Olin, B. Buchholz, and R. H. Goshorn, "Process for preparation of methyl mercaptan," U.S. Patent N° 30706321962.
- [100] J.-olaf Barth, H. Redlingshöfer, C. Weckbecker, K. Huthmacher, H.-werner Zanthoff, and R. Mayer, "Catalyst for the preparation of methyl mercaptan," U.S. Patent N° 1982764 A12008.
- [101] J. Barrault, M. Boulinguez, C. Forquy, and R. Maurel, "Synthesis of methyl mercaptan from carbon oxides and H₂S whit tungsten-alumina catalysts," *Applied Catalysis*, vol. 33, pp. 309-330, 1987.
- [102] F. Faraji, I. Safarik, O. P. Strausz, M. E. Torres, and E. Yildirim, "CO-Catalyzed Conversion of H₂S to H₂ + S . 1 . Reaction between CO and H₂S," *Ind. Eng. Chem. Res.*, vol. 35, pp. 3854-3860, 1996.
- [103] A. P. Chen, Q. Wang, Y. J. Hao, W. P. Fang, and Y.-Q. Yang, "Catalytic Synthesis of Methanethiol from H₂S-rich Syngas Over Sulfided SiO₂-supported Mo-based Catalysts," *Catalysis Letters*, vol. 121, no. 3-4, pp. 260-265, Nov. 2008.
- [104] B. Buchholz, "Process for the manufacture of methyl mercaptan from carbon oxides," U.S. Patent N° 44107311983.
- [105] G. Mul, I. E. Wachs, and A. S. Hirschon, "Catalytic synthesis of methanethiol from hydrogen sulfide and carbon monoxide over vanadium-based catalysts," *Catalysis Today*, vol. 78, no. 1-4, pp. 327-337, Feb. 2003.
- [106] B. Zhang, S. H. Taylor, and G. J. Hutchings, "Catalytic synthesis of methanethiol from CO/H₂/H₂S mixtures using α -Al₂O₃," *New Journal of Chemistry*, vol. 28, no. 4, pp. 471-476, 2004.
- [107] Y.-Q. Yang, S. Dai, Y. Yuan, R. Lin, D. Tang, and H. Zhang, "The promoting effects of La₂O₃ and CeO₂ on K₂MoS₄/SiO₂ catalyst for methanthiol synthesis from syngas blending with H₂S," *Applied Catalysis A: General*, vol. 192, no. 2, pp. 175-180, 2000.

- [108] Y.-Q. Yang et al., "Study of the supported K₂MoO₄ catalyst for methanethiol synthesis by one step from high H₂S-containing syngas," *Catalysis Letters*, vol. 74, no. 3–4, pp. 221-225, 2001.
- [109] Y. Hao, Y. Zhang, A. Chen, W. Fang, and Y.-Q. Yang, "Study on Methanethiol Synthesis from H₂S-Rich Syngas Over K₂MoO₄ Catalyst Supported on Electrolessly Ni-Plated SiO₂," *Catalysis Letters*, vol. 129, no. 3–4, pp. 486-492, Jan. 2009.
- [110] A. Chen, Q. Wang, Q. Li, Y. Hao, W. Fang, and Y.-Q. Yang, "Direct synthesis of methanethiol from H₂S-rich syngas over sulfided Mo-based catalysts," *Journal of Molecular Catalysis A: Chemical*, vol. 283, no. 1–2, pp. 69-76, Mar. 2008.
- [111] Y.-Q. Yang et al., "Supported Mo-O-K-Mexoy catalyst for the synthesis of methanethiol from high H₂S-containing syngas," U.S. Patent N° 2010/0286448 A12010.
- [112] A. Chen, Q. Wang, Y. Hao, W. Fang, and Y.-Q. Yang, "The Promoting Effect of Tellurium on K₂MoO₄/SiO₂ Catalyst for Methanethiol Synthesis from High H₂S-Containing Syngas," *Catalysis Letters*, vol. 118, no. 3–4, pp. 295-299, Jul. 2007.
- [113] Y.-Q. Yang, A. Chen, Q. Wang, J.-olaf Barth, C. Weckbecker, and K. Huthmacher, "Mo containing catalyst, a preparation method and a method for preparing methyl mercaptan," U.S. Patent N° 2010/0094059 A12010.

CHAPTER 2

Materials and Methods

Materials and Methods: Summary

2.1. CATALYSTS PREPARATION	73
2.1.1. Precursors preparation	73
2.1.2. Support preparation	76
2.1.3. Catalysts preparation	77
2.1.4. Reference catalysts	80
2.1.4.1. Monometallic catalysts	80
2.1.4.2. Bimetallic catalyst	81
2.1.4.3. Na based catalyst	81
2.2. EX SITU SULFIDATION OF CATALYSTS FOR CHARACTERIZATION	81
2.3. CHARACTERIZATION TECHNIQUES	83
2.3.1. Elemental Analysis	83
2.3.2. Specific Surface Area	84
2.3.3. X-Ray diffraction (XRD)	85
2.3.4. Laser Raman spectroscopy (LRS)	87
2.3.5. UV-Visible spectroscopy	88
2.3.6. Scanning electron microscopy (SEM)	89
2.3.7. Transmission electron microscopy (TEM)	90
2.3.8. X-Ray photoelectron spectroscopy (XPS)	91
2.3.9. Electron probe microanalysis (EPMA)	96
2.3.10. Characterization techniques of acid-base properties of solids	97
2.3.10.1. Temperature programmed desorption (TPD)	97
2.3.10.2. Isopropanol test reaction	98
2.4. EXPERIMENTAL SET-UP	100
2.4.1. Catalytic test procedure	100
2.4.2. Gas chromatograph GC	104
2.4.2.1. Experimental setup GRL	104
2.4.2.2. Experimental setup UCCS	105
2.4.3. Pretreatment of catalysts	110
2.4.4. Reaction conditions	112
2.4.5. Experimental procedure	112
2.4.6. Data analysis	113
2.5. VALIDATION OF UCCS CATALYTIC TEST	114
2.6. REFERENCES	115

This chapter describes the preparation procedures of catalysts and the experimental techniques employed for their physico-chemical characterization. In addition, the experimental set-ups used for the evaluation of the catalytic performance of samples are described.

2.1. CATALYSTS PREPARATION

A total of 4 series of catalysts were used in this work. Two series of Mo-based solids (oxides and presulfided) and two series of W-based solids (oxides and presulfided). For their preparation, the following steps were carried out:

2.1.1. Precursors preparation

Two types of precursors were used in this study, oxides precursors and presulfided precursors. The oxides precursors were based on commercial compounds K_2MoO_4 and K_2WO_4 . Presulfided precursor, K_2MoS_4 and K_2WS_4 were synthesized in the laboratory. A two-step procedure was used for the preparation of the potassium salts:

2.1.1.1. FIRST STEP: Preparation of ammonium tetrathiomolydate (ATTM) and ammonium tetrathiotungstate (ATW)

In figure 2.1 is showed the experimental set-up used for obtaining ATTM and ATW. This one is constituted by a three-neck round bottom flask placed on a heating magnetic agitator. Two gas inlets are used alternately and one outlet. In case of obstruction of one inlet, a three-way valve allows to overturn toward the second inlet. In the balloon's outlet, are placed an empty trap followed by a second trap containing a sodium hydroxide concentrated solution to trap the not-reacted outgoing hydrogen sulfide. Nitrogen is used as purge gas to eliminate the residual hydrogen sulfide after stop the experience.

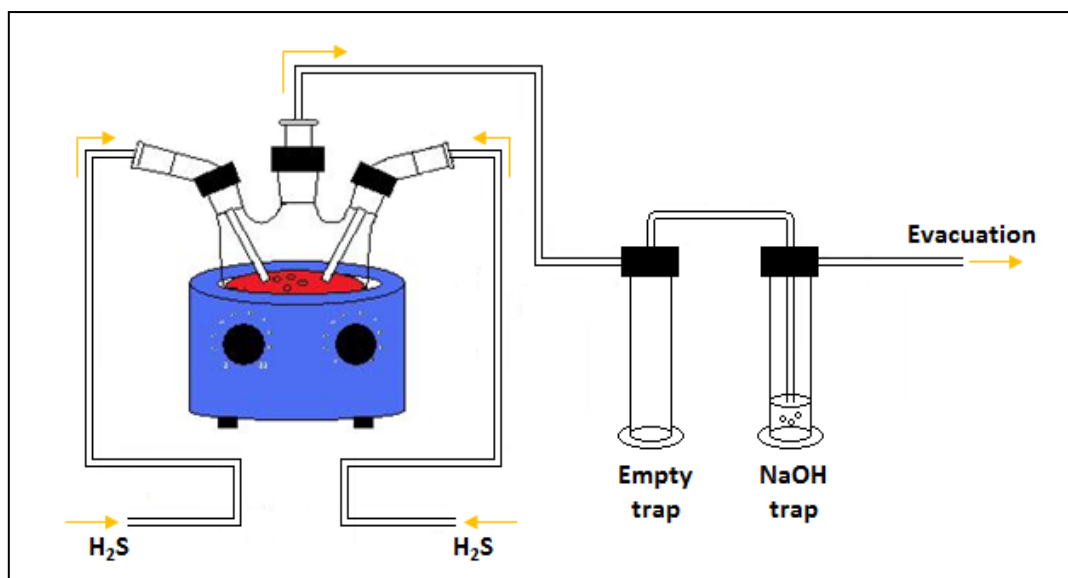


Figure 2.1. Experimental set-up for the synthesis of ATTm and ATW

ATTm $(\text{NH}_4)_2\text{MoS}_4$ were synthesized according to methods of Harmer and Sykes [1]. Thus for its preparation, high purity H_2S was bubbled through a solution of ammonium heptamolybdate, $(\text{NH}_4)_6\text{Mo}_7\text{O}_{24}\cdot 4\text{H}_2\text{O}$ (50 g) and ammonium hydroxide at 25 % (650 mL) for about 60 minutes. Since the reaction is exothermic, the synthesis is considered completed when the temperature begins to decrease. During this time, the solution became yellow and then dark red. Brown-red crystals formed were filtered off, washed with ethanol and then dried in *vacuo*. The yield of the reaction was close to 97%.

ATW $(\text{NH}_4)_2\text{WS}_4$ was prepared through a similar procedure [2]. A vigorous stream of H_2S was bubbled through a solution of ammonium metatungstate, $(\text{NH}_4)_6\text{H}_2\text{W}_{12}\text{O}_{40}\cdot 4\text{H}_2\text{O}$ (185 g) and ammonium hydroxide at 25 % (500 mL) for about 3 hours 30 minutes. $(\text{NH}_4)_2\text{WS}_4$ crystallized as orange translucent crystals which were filtered off, washed with ethanol and then dried in *vacuo*. The yield of the reaction was around 65%.

2.1.1.2. SECOND STEP: Preparation of potassium tetrathiomolybdate (K_2MoS_4) and potassium tetrathiotungstate (K_2WS_4)

The methodology used for the preparation of K_2MoS_4 and K_2WS_4 is as showed in figure 2.1. In a typical preparation, 10 g of ATTM or ATW were dissolved in 100 mL of an aqueous solution of potassium hydroxide 2M. The ammonia formed in this point was evacuated by vacuum pumping. After complete removal of NH_3 , a solution containing the ions K^+ and MS_4^{2-} was obtained. This solution was divided in several containers to which were added equal volumes of ethanol. The resultant solution contained a precipitate of K_2MS_4 ($M = Mo$ or W) and K^+ and MS_4^{2-} ions in solution. The latter was filtered and washed with ethanol. The procedure was repeated up to not observing any precipitate. Following this procedure, a maximum yield near to 98 % was achieved.

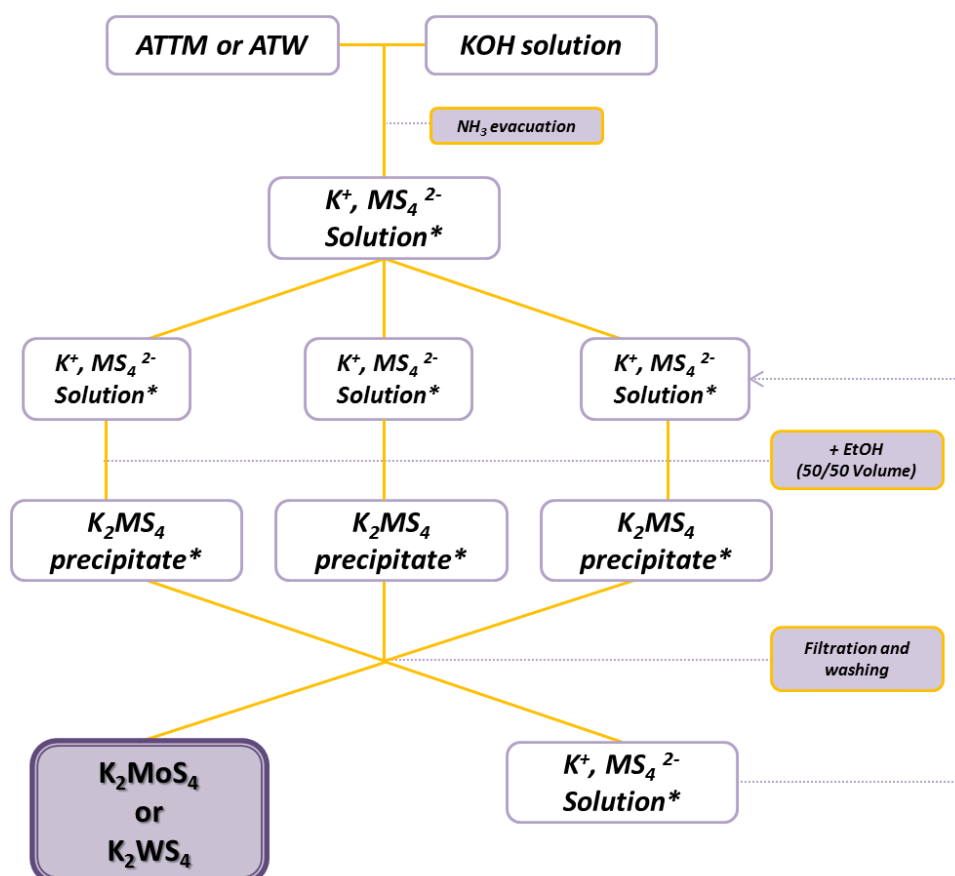


Figure 2.2. Experimental methodology for the preparation of K_2MoS_4 and K_2WS_4

(*M = Mo or W)

All the presulfided salts were stored under vacuum.

2.1.2. Support preparation

Seven supports were used for the preparation of catalysts. Three commercial alumina, two commercial silica and two homemade hydroxyapatites $\text{Ca}_{10}(\text{PO}_4)_6(\text{OH})_2$.

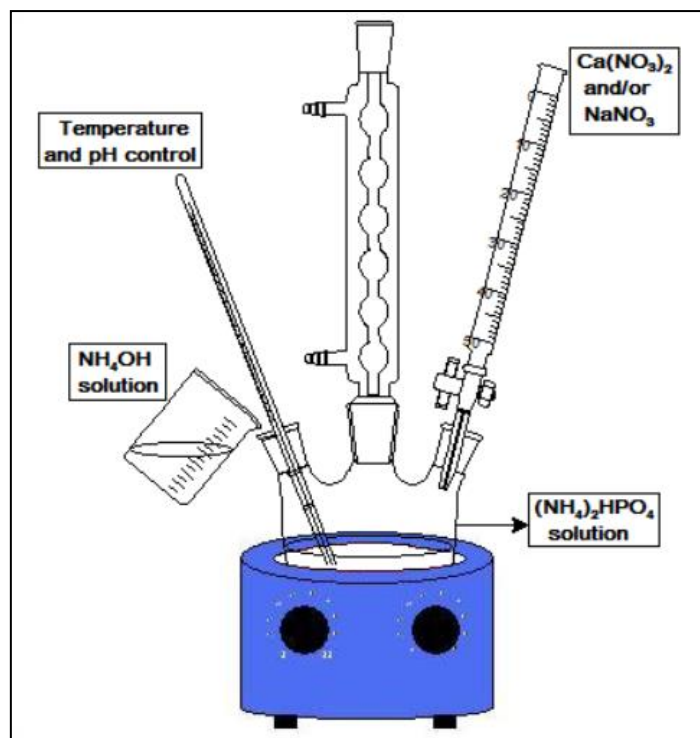


Figure 2.3. Experimental montage for hydroxyapatite synthesis

A stoichiometric hydroxyapatite (Hap) and a sodium-doped stoichiometric hydroxyapatite (HapNa) were synthesized by the co-precipitation method described in literature [3]. As showed in figure 2.3, an aqueous solution containing 0.0835 mol of calcium nitrate $\text{Ca}(\text{NO}_3)_2 \cdot 4\text{H}_2\text{O}$ was added drop wise to a solution containing 0.05 mol of ammonium dihydrogen phosphate $(\text{NH}_4)_2\text{H}_2\text{PO}_4$ while stirring. Throughout the synthesis, the temperature was maintained at around 80 °C and the pH was maintained at 10 by addition of ammonia solution 25% NH_4OH . The resulting precipitate was filtered, washed with hot water, dried overnight at 80 °C and calcined at 400°C with oxygen for 2 hours. Stoichiometric hydroxyapatite $\text{Ca}_{10}(\text{PO}_4)_6(\text{OH})_2$ was obtained with a Ca/P molar ratio in solution equal to 1,67. Sodium ions were introduced by dissolving sodium nitrate precursor NaNO_3 in the calcium nitrate solution. In this case, the Ca(+Na)/P molar ratio in solution was fixed to 2.2. Carbonated groups CO_3^{2-} were provided from the atmospheric CO_2 . Thus, carbonated groups

replace phosphate groups in the initial hydroxyapatite to give a solid with the formula $\text{Ca}_{(10-0.5x)}(\text{PO}_4)_{6-x}(\text{CO}_3)_x(\text{OH})_2$.

2.1.3. Catalysts preparation

In our study, incipient wetness impregnation method was used to synthesize oxide supported catalysts and presulfided supported catalysts. Thus, the required amounts of precursor solution were introduced in a volume corresponding to the pore volume of the support. Therefore, in order to prepare the catalysts, measures of pore volume of supports (volume of water uptake by the supports) and solubility of precursor salts were made and they are shown in tables 2.1 and 2.2 respectively.

Table 2.1. Pore volume of supports used

Supports	Volume of water uptake / $\text{cm}^3 \cdot \text{g}^{-1}$	Physical form of solid
Al_2O_3 -1	0,70	Pellets
Al_2O_3 -2	1,08	Pellets
Al_2O_3 -3	1,11	Pellets
SiO_2 -1	1,12	Granules
SiO_2 -2	1,94	Granules
Hap	1,43	Powder
HapNa	1,69	Powder

Table 2.2. Solubility of precursors salts in water at room temperature

Precursor	Solubility / g.cm ⁻³
K ₂ MoO ₄	0,900
K ₂ MoS ₄	0,352
K ₂ WO ₄	0,453
K ₂ WS ₄	0,409

The procedure follows for the synthesis of catalysts is as showed in figure 2.4.

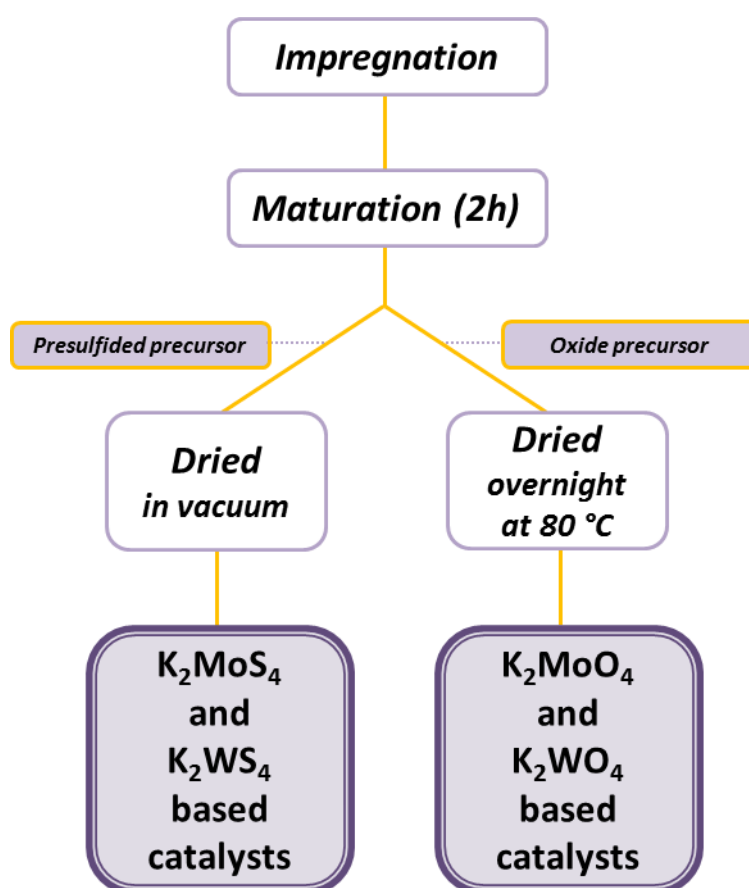


Figure 2.4. Procedure used for catalysts preparation

In a specific synthesis, for a give metallic loading of the catalyst, a calculated amount of

precursor salt was dissolved in a volume of water corresponding to the values of solubility reported in table 2.2. The resulting solutions were added drop wise to the different supports in a volume corresponding to the pore volume of each support followed by maturation in a steamy atmosphere by 2 hours. After that, the obtained solids were submitted to a drying step depending on the kind of precursor (oxide or presulfided). Presulfided catalysts were always stored under vacuum.

The nomenclature used for the four series of catalysts prepared is showed in figure 2.5. Catalysts were prepared with a Mo loading between 5,8 and 23,5 wt.% and W loading between 13,7 and 19,7 wt.% according to the solubility of precursors and the pore volume of supports.

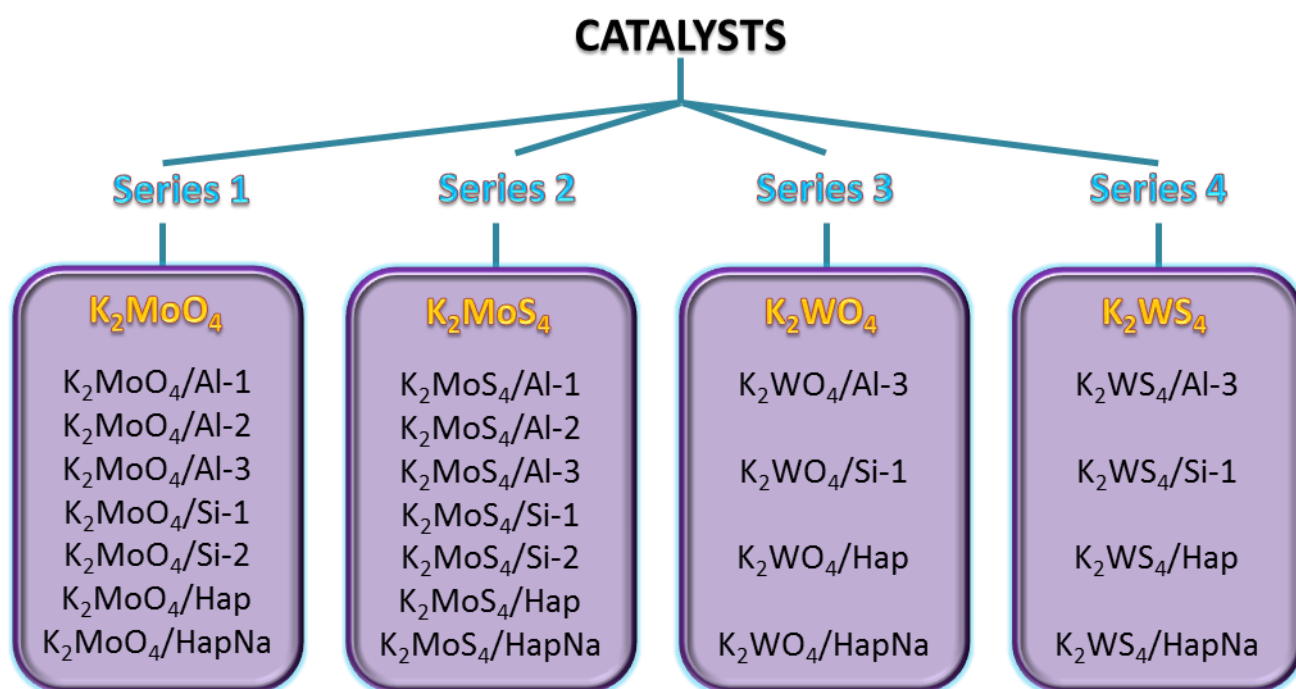


Figure 2.5. Nomenclature used for the series of catalysts prepared

The composition of the prepared catalysts is presented the table 2.3.

Table 2.3. Metal loading of catalysts

Catalyst	Mo wt.%	K wt.%	W wt.%
K ₂ MoO ₄ /Al-1	13,5	11,0	---
K ₂ MoO ₄ /Al-2	17,6	14,4	---
K ₂ MoO ₄ /Al-3	17,9	14,6	---
K ₂ MoO ₄ /Si-1	18,0	14,7	---
K ₂ MoO ₄ /Si-2	23,5	19,1	---
K ₂ MoO ₄ /Hap	20,4	16,7	---
K ₂ MoO ₄ / HapNa	22,1	18,0	---
K ₂ MoS ₄ /Al-1	5,8	4,7	---
K ₂ MoS ₄ /Al-2	8,1	6,6	---
K ₂ MoS ₄ /Al-3	8,1	6,6	---
K ₂ MoS ₄ /Si-1	8,4	6,8	---
K ₂ MoS ₄ /Si-2	12,1	9,9	---
K ₂ MoS ₄ /Hap	9,9	8,1	---
K ₂ MoS ₄ / HapNa	11,1	9,1	---
K ₂ WO ₄ /Al-3	---	7,5	17,6
K ₂ WO ₄ /Si-1	---	7,6	17,7
K ₂ WO ₄ /Hap	---	7,6	17,8
K ₂ WO ₄ / HapNa	---	8,6	19,9
K ₂ WS ₄ /Al-3	---	5,8	13,7
K ₂ WS ₄ /Si-1	---	5,9	13,8
K ₂ WS ₄ /Hap	---	6,9	16,3
K ₂ WS ₄ / HapNa	---	7,7	18,1

2.1.4. Reference catalysts

In order to better understand the behavior of catalysts during the reaction studied, reference solids were prepared using alumina (Al-3) as support and a fixed Mo and K content equal to 8,1 wt.% and 6,6 wt.% respectively.

2.1.4.1. Monometallic catalysts

Monometallic catalysts were prepared using alumina (Al-3) as support and a fixed Mo and K content equal to 8,1 wt.% and 6,6 wt.% respectively. These solids were synthesized following the same procedure explained above. After dried, the catalysts were calcined at 490 °C for

2h ($50\text{ }^{\circ}\text{C h}^{-1}$). The nomenclature used for this solids was 8,1%Mo/Al-3 and 6,6%K/Al-3.

2.1.4.2. Bimetallic catalyst

Bimetallic reference was prepared using alumina (Al-3) as support. Mo and K were impregnated over the support with a content equal to 8,1 wt.% and 6,6 wt.% respectively. With this loading, the K/Mo ratio corresponds to the molar ratio of K_2MoO_4 supported catalysts (K/Mo=2). After dried, the catalysts were calcined at $490\text{ }^{\circ}\text{C}$ for 2h ($50\text{ }^{\circ}\text{C.h}^{-1}$). The nomenclature used for this solids was 8,1%Mo+K/Al-3.

2.1.4.3. Na based catalyst

Catalyst containing Na was prepared in the same way that K_2MoO_4 catalysts, using as precursor salt Na_2MoO_4 and maintaining the Mo loading at 8,1 wt.%

Table 2.4. Reference catalysts

Reference catalysts
6,6% K/ Al-3
8,1% Mo/ Al-3
8,1% Mo+K/ Al-3
8,1 % Na_2MoO_4 / Al-3

2.2. EX SITU SULFIDATION OF CATALYSTS FOR CHARACTERIZATION

The characterization by Scanning Electron Microscopy SEM, Transmission Electron Microscopy TEM, Electron Probe MicroAnalysis EPMA and X-ray Photoelectron Spectroscopy XPS was performed over fresh samples but also over sulfided catalysts with the aim of determine the nature of the active phase of the catalyst studied.

The experimental setup used for the sulfidation of catalysts is schematized in figure 2.6.

Sulfidation runs were performed at atmospheric pressure by using a sealed glass reactor placed in a temperature-controlled oven. The reactants (N_2 , H_2S and H_2) were supplied by gas tubes to the reactor and their flows were fixed by mass flow controllers. The non-reacted hydrogen sulfide was trapped at the exit of the reactor by using sodium hydroxide placed in a glass vial.

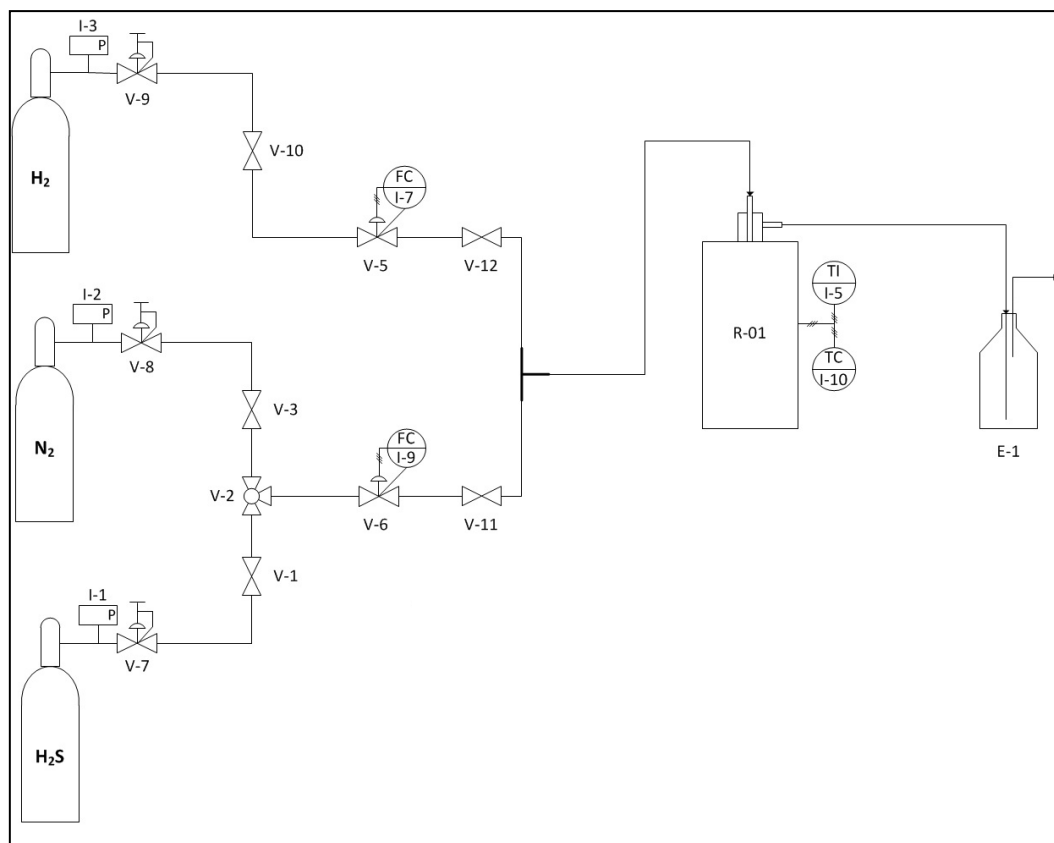


Figure 2.6. Setup used for the sulfidation of catalysts

In a typical sulfidation test, about 150 mg of catalysts are used with a sulfidation test protocol as schematized in figure 2.7. At the end of the sulfidation, the reactor is sealed in H_2S/H_2 atmosphere avoiding the air inlet towards the reactor.

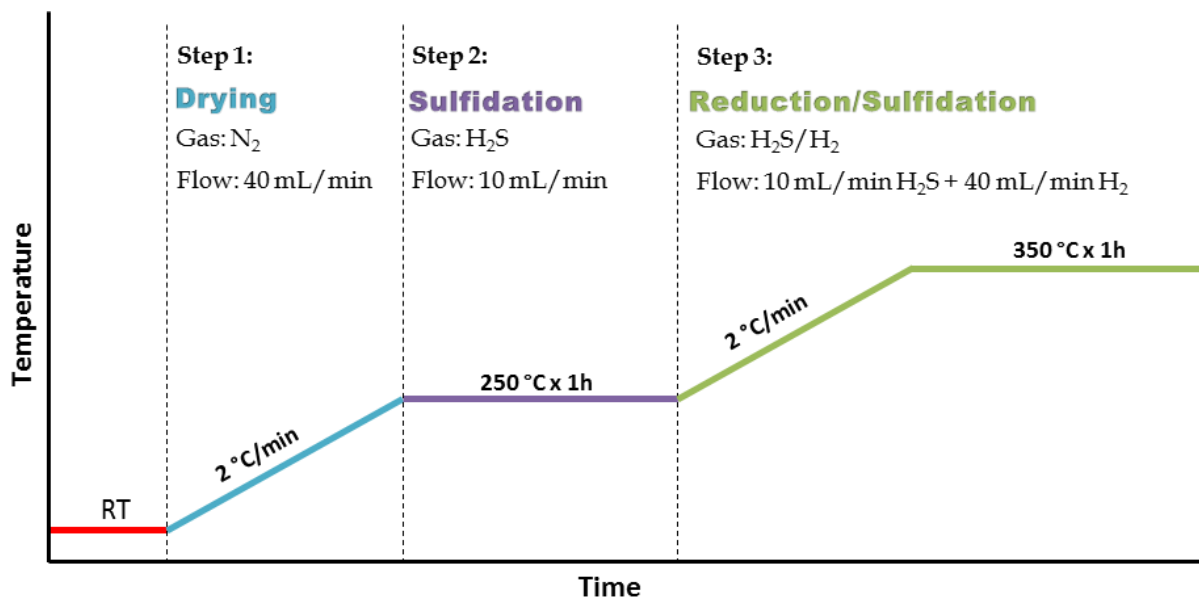


Figure 2.7. Ex-situ sulfidation test protocol

2.3. CHARACTERIZATION TECHNIQUES

Characterization techniques have been employed to obtain information on the physical-chemical properties of catalysts in order to understand their catalytic properties.

2.3.1. Elemental Analysis

The elemental analysis allows determining the weight composition of every species present in the solid. The elemental compositions of catalyst have been obtained by Inductively Coupled Plasma atomic emission spectroscopy (ICP-AES) technique. These analyses were made at *Service Central d'Analyse du Centre National de la Recherche Scientifique (CNRS) – Vernaison*. The samples were digested by microwave, and then the elements were measured by ICP-AES.

2.3.2. Specific Surface Area

Most heterogeneous catalysts are porous solids; in any case, the size and volume of pores depend on preparation method. The porosity arises from the preparation methods of the solids. The pores are classified in different classes depending on their sizes [4]:

1. Micropores ($\Phi < 2$ nm)
2. Mesopores ($2 < \Phi < 50$ nm)
3. Macropores ($\Phi > 50$ nm)

The porous structure enables the solid to have a total surface much higher than that corresponding to the external one. Most common catalysts have a specific surface area between 1 and 1000 $\text{m}^2 \cdot \text{g}^{-1}$, while their external specific surface area is in the range 0.01 - 10 $\text{m}^2 \cdot \text{g}^{-1}$. In the particular case of supported metal catalysts several techniques may be used to estimate the surface area.

Surface area determination by gas adsorption involves determination of the volume of an inert gas (typically nitrogen) adsorbed on a solid surface at low temperatures as a function of increasing pressure. The most common method of measuring the surface area of powder is that developed by Brunauer, Emmett and Teller using the so called BET method [5]. In essence, the BET isotherm is an extension of the Langmuir isotherm that also considers multilayer adsorption. By the Brunauer, Emmet and Teller (BET) theory, the amount of a define gas, physically adsorbed on the whole surface at very low temperature (-196 °C), is measured, and the total surface area can be estimated according to:

$$S = V_m \cdot N \cdot A_m \cdot 10^{-20} \quad (1)$$

Where V_m is the monolayer capacity (moles per gram of solid), N is Avogadro's constant ($6.023 \cdot 10^{23}$ molecules per mole) and A_m is the molecular cross-sectional area of the adsorbate, i.e. the area which an adsorbate molecule occupies on the surface of the solid in a complete monolayer (\AA^2). For nitrogen at -196 °C the value of A_m is 16.2 \AA^2 [6].

The monolayer capacity was determined by applying the BET equation to the experimental data. The BET equation is given by:

$$\frac{P}{V(P_0 - P)} = \frac{1}{V_m C} + \frac{(C - 1)P}{V_m C P_0} \quad (2)$$

where P is the equilibrium pressure, P_0 is the saturation vapour pressure of the adsorbate (N_2 in the present case), V is the amount of gas adsorbed at the pressure P , C is a constant and V_m is the amount of the gas adsorbed at saturation (monolayer capacity). According to this equation, when $\frac{P}{V \cdot (P_0 - P)}$ is plotted against $\frac{P}{P_0}$ a straight line results with slope

$$\frac{C - 1}{V_m \cdot C} \text{ and intercept } i = \frac{1}{V_m \cdot C} \text{ Finally, the monolayer capacity } V_m \text{ can be determined}$$

and by applying equation 18, the total surface area of the catalyst is found. It has to be mentioned that the BET theory is valid in the pressure range $0.05 < P/P_0 < 0.3$.

Equipment and conditions for surface area determination

N_2 adsorption-desorption isotherms were recorded at -196 °C using a TRISTAR II 3020 instrument from MICROMERITICS. Prior to the experiments, a known mass of sample (around 200 mg) was outgassed at 150 °C under vacuum for 4 h to remove the moisture and other adsorbed gases from the catalyst surface. Specific surface areas were calculated from the linear part of the Brunauer-Emmett-Teller line.

2.3.3. X-Ray diffraction (XRD)

X-ray diffraction XRD is a standard tool for the characterization and identification of bulk crystalline phases and to estimate particle sizes. The working principle of X-ray diffraction is shown in figure 2.8.

The diffraction method is based on Bragg's law which is the condition for the constructive interference of scattering from a set of planes with a d-spacing (d_{hkl}) at an angle (2θ), with a wavelength (λ) according to the Bragg equation:

$$n \lambda = 2 d_{hkl} \sin\theta \quad (3)$$

where λ is the wavelength of the incident beam, θ is the incidence angle and d is the distance between two successive planes characterized by Miller indices (h,k,l).

The X-ray powder diffraction of a compound provides a convenient and characteristic fingerprint which can be used in qualitative analysis. Values of d_{hkl} spacing line intensities can be compared with those listed in the Powder Diffraction File, which contains entries for more than 500,000 inorganic compounds over 400,000 organic compounds, up to year 2010 [7].

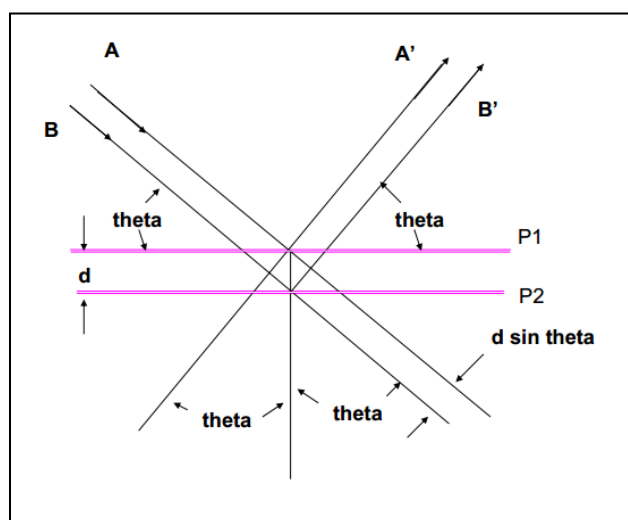


Figure 2.8. Principle of X-ray diffraction

X-Ray diffraction equipment and conditions

Powder X-ray diffraction (XRD) patterns were recorded on a Bruker D8 X-ray diffractometer at room temperature with CuK α radiation ($\lambda = 1.5406 \text{ \AA}$). For the preparation of the sample, the solid to be analyzed was finely crushed and then deposited in a thin uniform layer on a glass plate which was then loaded in the analysis chamber. The diffractograms were recorded for 2θ values comprised between 10 and 90° using a step size of 0.02° and a time per step equal to 4 s. The treatment of results was made with the software EVA and the diffraction patterns have been indexed by comparison with the Joint Committee on Powder Diffraction Standards (JCPDS) files.

2.3.4. Laser Raman spectroscopy (LRS)

Nowadays Raman spectroscopy is a vibration spectroscopy widely used to analyze materials well beyond the capabilities of other methods, with the ability to obtain a detailed account of the physical and chemical makeup of a material at the molecular level.

The fundamental process of the Raman Effect is the transfer of energy between light and matter. Raman spectroscopy employs this effect by measuring the scattering of light from molecules in different vibrational states of a material and the consequent energy exchange between the incoming light and the molecules [8]. When a beam of monochromatic electromagnetic radiation impinges on a material, it can be either scattered or absorbed (Figure 2.9). If light is scattered from an atom or molecule within the material, most photons are elastically scattered. This is known as Rayleigh scattering, in which the scattered photons have the same energy E as the incident photons given by:

$$E = h \nu_0 \quad (4)$$

where h is Planck constant and ν_0 is the frequency of the incident light. However, a small fraction of scattered light (approximately 1 in every billion photons) undergoes what is known as inelastic or Raman scattering. In this case light is scattered from molecules with frequencies of oscillation that vary from the frequency of the incident photons. It is this difference in frequency, or energy between the incoming and outgoing light that is the measurable quantity used as the basis of Raman spectroscopy.

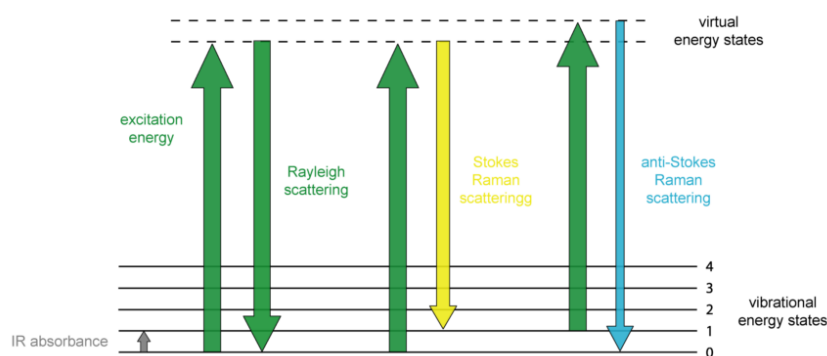


Figure 2.9. The absorbance and scattering of light from matter

Laser Raman spectroscopy equipment and conditions

The Raman spectra of the samples, were recorded at room temperature using a Raman microprobe LabRam infinity (Jobin Yvon), equipped with a photodiode array detector in the spectral zone 100-1500 cm^{-1} . The exciting light source was the 532 nm line of an Nd-YAG laser and the wavenumber accuracy was $\pm 4 \text{ cm}^{-1}$. The Raman spectrometer was calibrated using the silicon line at 521 cm^{-1} .

2.3.5. UV-Visible spectroscopy

Ultraviolet and visible (UV-Vis) absorption spectroscopy (UV = 200 – 400 nm, Visible = 400 – 800 nm) is the measurement of light when it is passed through a sample. The principle of UV-Vis spectroscopy is based on the ability of molecule to absorb ultraviolet and visible light. The absorption of light corresponds to the excitation of outer electrons in the molecule. When a molecule absorbs energy, the outer electrons in the molecule are excited from the Highest Occupied Molecular Orbital (HOMO) to Lowest Unoccupied Molecule Orbital (LUMO). The occupied molecular orbitals with lowest energy are known the σ orbitals, at slightly higher energy are called π orbitals and at still higher energy are known non – bonding orbitals (unshared pair electrons). The π^* and σ^* are called the highest energy state. The figure 2.10 shows the electronic energy levels and transitions [9].

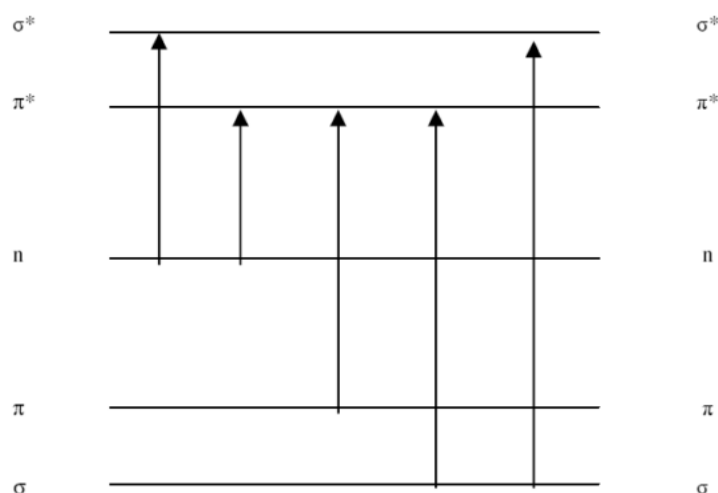


Figure 2.10. Electronic energy level and transition state

The absorption can be measured at a single wavelength or on spectral extended range. Ultraviolet and visible spectroscopy are enough energetic to excite outer electrons to high energy level and it is very useful for quantity measurement. The Beer – Lambert Law is the relationship between absorbance and concentration and is expressed as:

$$I = I_0 \cdot e^{-\varepsilon \cdot c \cdot l} \quad (5)$$

Where I and I_0 are the intensity of the transmitted light and the incident light respectively, ε is the molar absorptivity expressed in units $\text{L} \cdot \text{mol}^{-1} \cdot \text{cm}^{-1}$, c is the concentration of the sample expressed as $\text{mol} \cdot \text{L}^{-1}$ and l is length of cell expressed in cm. This equation is used to determine the concentration of chemical species by measuring the absorbance at various wavelengths. The absorbance is defined as:

$$A = -\log\left(\frac{I}{I_0}\right) \quad (6)$$

This implies that the absorbance becomes linear with the concentration and can be rewritten as:

$$A = \varepsilon \cdot c \cdot l \quad (7)$$

UV-Vis spectroscopy equipment and conditions

Absorption spectra of the samples were recorded by using UV-Vis spectrophotometer Perkin Elmer Lambda 650. The spectrometer consists in a double beam and a monochromator. The sources used are type tungsten-halogen and deuterium. Spectra of solid samples were recorded between 200 and 900 nm with a step of 0.2 nm and liquid samples were recorded with a step of 1 nm. The molar absorptivity was calculated by using the Beer – Lambert law (Equation 7).

2.3.6. Scanning electron microscopy (SEM)

In a typical SEM, an electron beam is emitted from an electron gun fitted with a tungsten filament cathode, which typically has an energy ranging from 0.2 keV to 40 keV. In scanning electron microscopy visual inspection of the surface of a material utilizes signals of two

types, secondary and backscattered electrons. Secondary electrons are a result of the inelastic collision and scattering of incident electrons with specimen electrons. They are generally characterized by possessing energies less than 50 eV. They are used to reveal the surface structure of a material with a resolution of ~ 10 nm or better [7]. Backscattered electrons are a result of an elastic collision and scattering event between incident electrons and specimen nuclei or electrons. Backscattered electrons can be generated further from the surface of the material and help to resolve topographical contrast and atomic number contrast with a resolution >1 micron. While there are several types of signals that are generated from a specimen under an electron beam, the X-ray signal is typically the only other signal that is used for scanning electron microscopy. The X-ray signal is a result of recombination interactions between free electrons and positive electron holes that are generated within the material. The X-ray signal can originate from further down into the surface of the specimen surface and allows for determination of elemental composition through EDS (energy dispersive X-ray spectroscopy). EDS analyzes the x-rays that are emitted from charged particles.

Scanning electron microscopy equipment

The Scanning Electron Microscope (SEM) images were taken on a HITACHI 4100 S equipped with micro-analysis (Energy-Dispersive X-ray Spectroscopy, EDS) and a field emission gun allowing a qualitative analysis of the composition of the sample until $1\ \mu\text{m}$ of thickness.

2.3.7. Transmission electron microscopy (TEM)

In TEM, a thin specimen is irradiated with an electron beam of uniform current density as shown in the figure 2.11 [10]. Electrons are emitted from the electron gun and illuminate the specimen through a two or three stage condenser lens system. The objective lens forms a diffraction pattern of the specimen. The electron intensity distribution behind the specimen is magnified with a three or four stage lens system and viewed on a fluorescent screen. The image can be recorded by direct exposure of an image plate by a CCD camera. Since the wavelength of electrons is much smaller than that of light, the optimal resolution attainable for TEM images is many orders of magnitude higher than that from a light microscope. Thus, TEM images can reveal the finest details of internal structure, in some cases as small as

individual atoms [11].

Transmission electron microscopy equipment

The TEM images were taken on a TECNAI electron microscope operating at an accelerating voltage of 200 kV. For the preparation of the sample grid, the sample was grounded into fine powder and dispersed in ethanol. A very small drop of ethanol with suspended particles was dropped onto a holey-carbon copper grid. The grid was loaded into the sample chamber. The analysis was conducted under high vacuum.

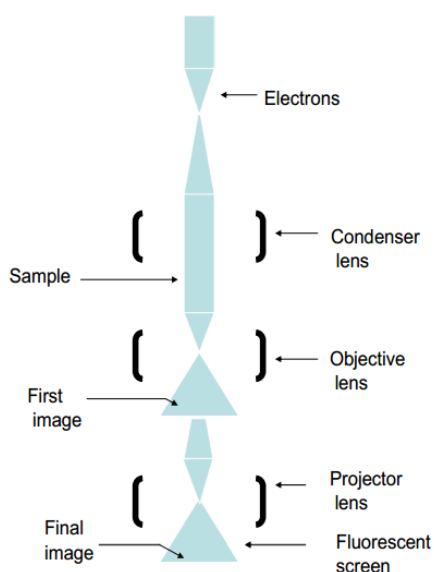


Figure 2.11. Working principle of transmission electron microscopy

2.3.8. X-Ray photoelectron spectroscopy (XPS)

X-ray photoelectron spectroscopy (XPS) is a quantitative spectroscopic technique that measures the elemental composition, empirical formula, chemical state and electronic state of the elements that exist within a material. XPS spectra are obtained by irradiating a material with a beam of X-rays while simultaneously measuring the kinetic energy and number of electrons that escape from the top 1–10 nm of the material being analyzed.

X-ray photoelectron spectroscopy (XPS) is a technique based on the photoelectric effect, as enunciated by Einstein in 1905. Whereby an atom absorbs a photon of energy, $h\nu$, after

which a core or valence electron with binding energy E_b is ejected with kinetic energy expressed by the equation 8.

$$E_k = h\nu - E_b - \phi \quad (8)$$

Where E_k is the kinetic energy of the photoelectron, h is the Planck's constant, ν is the frequency of the of the exciting radiation, E_b is the binding energy of the photoelectron with respect to the Fermi level and ϕ is the work function of the spectrometer [5].

The basic elements of an XPS instrument are a light source, an electron energy analyzer and an electron detector as it is drawn on Figure 2.12.

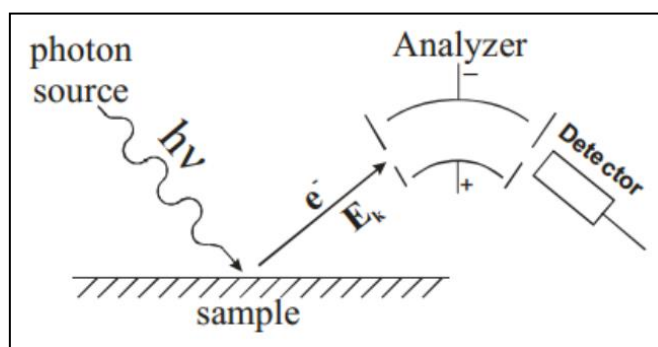


Figure 2.12. Basic elements of XPS experiment

X-Ray photoelectron spectroscopy equipment and conditions

The composition and chemical state of the elements were studied using X-ray Photoelectron Spectroscopy (XPS) on a KRATOS Axis Ultra spectrometer equipped with a monochromatic Al K α (1486.6 eV) x-ray radiation (powered at 100 watts). The analysis chamber was operated under ultrahigh vacuum with a pressure close 10^{-10} torr. The binding energy values were referred to the Al $_{2p}$, Si $_{2p}$ and P $_{2p}$ at 74.6 eV, 103.7 eV and 133.5 eV respectively on depending in the support used (Al $_2$ O $_3$, SiO $_2$ or Hap). Simulation of the experimental photopeaks was carried out using a mixed Gaussian/Lorentzian peak fit procedure according to the software supplied by *Casa XPS*. Shirley background subtraction was used for atomic concentrations calculation. The surface atomic concentrations were calculated by correcting the intensities with theoretical sensitivity factors based on Wagner cross section.

The stoichiometry of the sample surface can be estimated from the area ratio of XPS peaks.

The general formula for the XPS peak area is:

$$I = nF\sigma\lambda AT \sin \theta \quad (9)$$

where I is the intensity of the XPS peak, n is the atomic concentration of the element, F is the X-ray flux, σ is the photoelectronic cross-section for the atomic orbital of interest, λ is the mean free path of the photoelectrons in the sample, A is the area of the sample from which photoelectrons are detected, T is the detection efficiency for electrons emitted from the sample and θ is the angular efficiency factor for the instrumental arrangement.

The atomic composition, N_A/N_B , between A and B atoms are derived from the equation 10:

$$\frac{N_A}{N_B} = \frac{I_A}{I_B} \times \left(\frac{E_{CA}}{E_{CB}} \right)^{-0.23} \times \frac{\sigma_A}{\sigma_B} \quad (10)$$

where σ is the cross section, E_C kinetic energy and I is the intensity of the peak. The -0.23 value is dependent of the device used.

Spectra decomposition for Mo_{3d} and S_{2p}

In promoted molybdenum oxide catalysts in the sulfided form, the Mo and S coexist. The spectral envelope of Mo3d covers the energy range of 227–238 eV as the chemical states of Mo vary from 0 to +6, while that of S2s covers from 224 to 235 eV, suppose that the chemical states of S vary from +2 to +6. It is obvious that the BE regions of Mo3d and S2s overlap with each other. Therefore, the influence of S2s must be initially ruled out to obtain the true contribution of Mo3d level. The BEs, full width at half maximum (FWHM) and peak area of S2s can be derived from that of S2p. At this respect, the following constraint should be respected:

- $A(S2p_{1/2}) = A(S2p_{3/2}) * 0.5$; where A represents the area of peaks
- $BE(S2p_{1/2}) = BE(S2p_{3/2}) + 1.1$
- $FWHM(S2p_{1/2}) = FWHM(S2p_{3/2}) * 1.1$

The constraints used for the decomposition of S2p level are resumed in table 2.5. These parameters were used for the decomposition of fresh K₂MoS₄-based catalysts and sulfided reference, K₂MoS₄ and K₂MoO₄ based catalysts.

Table 2.5. XPS parameters used to obtain S2p contributions

Phase	Contribution	Constraint Area	Constraint FWHM	Constraint BE (eV)
S ²⁻ (MoS ₂)	S2p _{3/2}	A	D = FWHM _{Al 2p} * 0.82 D = FWHM _{P 2p} * 0.84 D = FWHM _{Si 2p} * 0.86	G = 162,1 ; 161,1
	S2p _{1/2}	A * 0,5	D * 1,1	G + 1,1
S ²⁻ (K _x MoS ₂)	S2p _{3/2}	B	D * 1,3	H = 163,4 ; 162,4
	S2p _{1/2}	B * 0,5	E * 1,1	H + 1,1
S ⁶⁺ (SO ₄ ²⁻)	S2p _{3/2}	C	F	I = 168,0 ; 167,0
	S2p _{1/2}	C * 0,5	F * 1,1	I + 1,1

Therefore, the preclusion of the influence of S2s from Mo3d is necessary and important for the accurate peak-fitting of Mo3d. Mo3d XP spectrum is a guide line to speculate the sulfidation extent of Mo and to estimate the distribution of Mo on the carrier. The constraints used for the decomposition of sulfided catalysts are displayed in table 2.6. These parameters were used for the decomposition of sulfided reference, K₂MoS₄ and K₂MoO₄ based catalysts.

Table 2.6. XPS parameters used for the decomposition of Mo3d level of Mo-sulfided catalysts

Phase	Contribution	Constraint Area	Constraint FWHM	Constraint BE (eV)
S ²⁻	S2s ²⁻	(A+A')/1,7 ; (A+A')/1,4	D * 1,5	(G+65) ; (G+64)
S ²⁻	S2s ²⁻	(B+B')/1,7 ; (B+B')/1,4	E * 1,5	(H+65) ; (H+64)
S ⁶⁺	S2s ⁶⁺	(C+C')/1,7 ; (C+C')/1,4	F * 1,5	(I+65) ; (I+64)
MoS ₂	Mo 3d _{5/2} ⁴⁺	J	M = FWHM _{Al 2p} * S	228,4 ; 227,8 (P)
	Mo 3d _{3/2} ⁴⁺	J * 0,67	M * 1,05	P + 3,15
K _x MoS ₂	Mo 3d _{5/2} ⁴⁺	K	N = FWHM _{Al 2p} * T	229,4 ; 228,8 (Q)
	Mo 3d _{3/2} ⁴⁺	K * 0,67	N * 1,05	Q + 3,15
K ₂ MoS ₄	Mo 3d _{5/2} ⁶⁺	L	O = FWHM _{Al 2p} * U	230,4 ; 229,8 (R)
	Mo 3d _{3/2} ⁶⁺	L * 0,67	O * 1,05	R + 3,15

The constants S, T and U are dependent of the precursor (K₂MoO₄ or K₂MoS₄) used and also of the support (alumina, silica or hydroxyapatite). Thus the values used are listed in table 2.7.

Table 2.7. FWHM as a function of the precursor and the support

Constant	K ₂ MoO ₄ -based catalysts			K ₂ MoS ₄ -based catalysts		
	Al	Si	Hap	Al	Si	Hap
S	0,39	0,43	0,49	0,56	0,56	0,70
T	0,43	0,54	0,53	0,61	0,66	0,76
U	0,47	0,63	0,58	0,79	0,75	0,79

Spectra decomposition for W_{4f}

The chemical state and content of W are usually characterized via the BE and peak area of

W4f XP spectrum, respectively. The spectra of W4f were decomposed in 5 contributions, 4 corresponding to W and 1 corresponding to K (K3s). The exclusion of the influence of K3s from W4f is necessary and important for the accurate peak-fitting of W4f and the posterior quantification of W species. The constraints used for the decomposition of sulfided W-catalysts are displayed in table 2.8.

Table 2.8. XPS parameters used for the decomposition of W4f level of W-sulfided catalysts

Phase	Contribution	Constraint Area	Constraint FWHM	Constraint BE (eV)
K3s	K3s	A(K2p _{3/2})/30	FWHM(K2p _{3/2})/1,2	BE(K2p _{3/2})-260
WS ₂	W4f _{7/2} ⁴⁺	B	F	31,7 ; 31,1 (J)
	W4f _{5/2} ⁴⁺	B * 0,75	F * 1	J + 2,15
K _x WS ₂	W4f _{7/2} ⁴⁺	C	G	32,1 ; 31,5 (K)
	W4f _{5/2} ⁴⁺	C * 0,75	G * 1	K + 3,15
K ₂ WS ₄	W4f _{7/2} ⁶⁺	D	H	34,1 ; 33,3 (L)
	W4f _{5/2} ⁶⁺	D * 0,75	H * 1,05	L + 2,15
K ₂ WO ₄	W4f _{7/2} ⁶⁺	E	I	36,0 ; 35,4 (M)
	W4f _{5/2} ⁶⁺	E * 0,75	I * 1	M + 2,15

2.3.9. Electron probe microanalysis (EPMA)

Electron Probe Microanalysis (EPMA) is an elemental analysis technique developed by R. Castaing in Paris as his 1950 Ph.D. thesis. EPMA uses a focused beam of high energy electrons (5 - 30 KeV) to non-destructively ionize a solid specimen surface (including thin films and particles) for inducing emission of characteristic x-rays (0.1 - 15 KeV). The electron microprobe is designed specifically for detecting and measuring characteristic X-rays. The high-energy focused beam of electrons generates X-rays characteristic of the elements within a sample from volumes as small as a micrometer (10⁻⁶m) across. The resulting X-rays are diffracted by analyzing crystals and counted using gas-flow and sealed proportional detectors.

EPMA equipment and conditions

An electron probe microanalyser Cameca SX100 has been used for the detection and quantification of elements in the sample surface. Profiles and x-ray mapping of sample surfaces has been made at 15 kV, 40 nA. The samples analyzed (extrudates) have been polished prior to the analysis so that surface imperfections do not interfere with electron-sample interactions.

2.3.10. Characterization techniques of acid-base properties of solids***2.3.10.1. Temperature programmed desorption (TPD)***

Temperature programmed desorption is commonly used to study the bonding energy of adsorbates on catalytic surfaces. The temperature of the desorption peak maximum is indicative of the strength with which the adsorbate is bound to the surface. The higher the temperature of the desorption peak the stronger the bond between the adsorbate and the surface. Temperature programmed desorption uses probe molecules to examine the interactions between the surface with gases or liquid-phase molecules [10]. The probe molecules are chosen with respect to the nature of the adsorbed species believed to be important for the catalytic reaction under study or chosen to provide information about the specific type of surface sites. Analysis of temperature programmed desorption profiles can provide adsorption-desorption mechanisms and their associated kinetics. Kinetic parameters such as heat of adsorption, activation energy of the adsorption and desorption process, order of desorption can also be determined. In a typical TPD experiment, the catalyst is pretreated and then saturated with an adsorbing gas under well-defined conditions. The excess gas is purged out of the reactor with an inert gas and then the sample is subjected to a linear temperature ramp. The effluent gas composition is continuously monitored by a detector placed at the exit of the reactor. The experiment permits the total determination of gas that was adsorbed. Surface concentrations of acidic and basic centres were determined by temperature-programmed desorption of ammonia (NH₃-TPD) and carbon dioxide (CO₂-TPD), respectively.

NH₃-TPD and CO₂-TPD equipment and conditions

The measurements were performed on a Micromeritics Autochem II (2920) instrument. Before the measurement, a sample (100 mg) was outgassed in a flow of pure helium (30 ml.min⁻¹), at 400 °C for 1 hour. Subsequently, the sample was cooled down to room temperature and then saturated in a flow of 10 vol.% NH₃/He or alternatively 5 vol.% CO₂/He at 30 ml.min⁻¹ for about 1 hour. Then, the catalyst was purged in a helium flow until a constant baseline level was attained. After purging, the NH₃ and CO₂ desorption was carried out in the temperature range of 100–1200 °C with a linear heating rate of 10 °C.min⁻¹ in a flow of He equal to 30 ml.min⁻¹. The temperature in the catalyst bed was measured by a K-type thermocouple located in a quartz capillary immersed in the catalyst bed. The molecules desorbing from the samples were monitored on-line by a mass spectrometer Omnistar Balzers connected to the reactor outlet. The NH₃-TPD spectra were obtained from the m/z = 17 mass-to-charge signal ratio, taking into account the contribution of the amount of water formed by the analysis of the peak m/z = 18. The CO₂-TPD spectra were obtained from the m/z = 44 mass-to-charge signal ratio.

The number and of acid/basic sites is proportional to the amount of gas desorbed (NH₃ or CO₂). Assuming that each gas molecule is adsorbed on an acid/basic site it is possible to trace the amount of acid sites per gram of sample.

2.3.10.2. Isopropanol test reaction

The reaction of decomposition of 2-propanol or isopropanol (IPA) is a widely used test reaction for characterizing both acidic and basic properties of solids. On contact with an acidic or basic solid, isopropanol undergoes two types of competitive reactions namely: (a) Dehydrogenation to acetone and hydrogen which is characteristic of basic sites. (b) Intramolecular dehydration, which yields to propene being characteristic of acidic catalyst, then, the dehydration of propene leads to di-isopropyl ether [11], [12]. The explanation about the formation of di-isopropyl ether is still subject to controversy: acid-basic sites or very closer acid sites could be necessary for the formation of this product (Figure 2.15).

Isopropanol test reaction equipment and conditions

The tests were carried out under helium atmosphere in a range of temperature of 175 at 400°C in fixed bed reactor. The mixture isopropanol/helium was made in a saturator at room temperature and the concentration of isopropanol in the gas flow was controlled by a condenser connected to the saturator. The test sample (100 mg) was diluted in silicon carbide (100 mg). The flow of the reaction mixture was fixed at 25 mL·min⁻¹ and the decomposition products were analyzed by gas chromatography using a FID detector. The main products observed were acetone, propene and in some cases di-isopropyl ether.

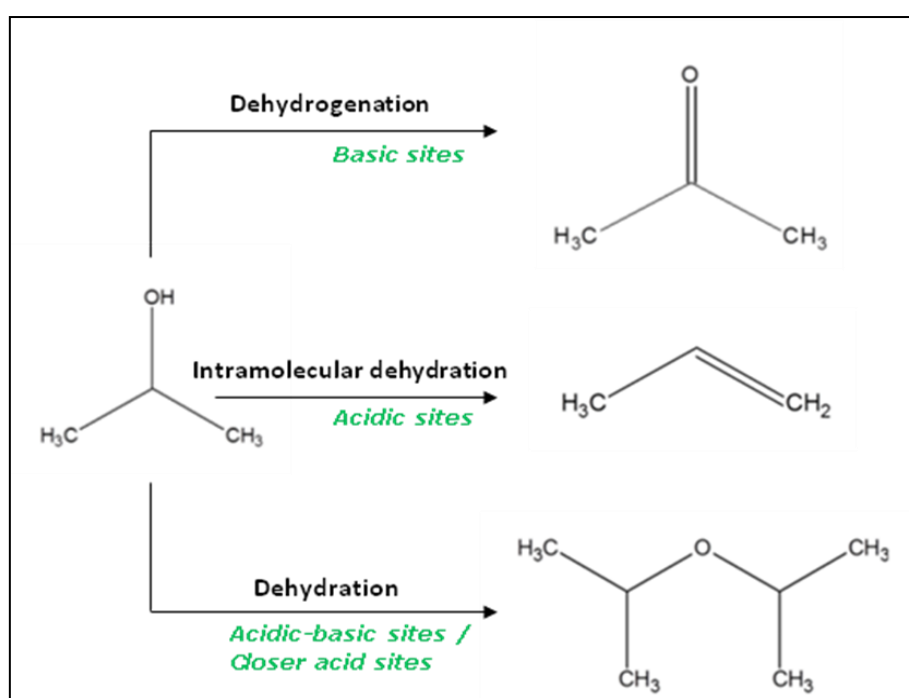


Figure 2.15. Reaction pathway for the decomposition of isopropanol

Conversion and selectivities are calculated according to equations 11 and 12 respectively.

$$X(\%) = \frac{C_i - C_f}{C_i} \quad (11)$$

Where X = % Conversion, C_i = initial concentration of isopropanol and C_f = final concentration of isopropanol.

$$S(\%) = \frac{C_x}{C_{IP_{transf}}} \quad (12)$$

Where S = % Selectivity, C_x = Concentration of desired product and $C_{IP_{transf}}$ = concentration of isopropanol transformed.

2.4. EXPERIMENTAL SET-UP

In this section, two lab-scale catalytic units for the synthesis of methyl mercaptan will be described.

A. Experimental setup used for the catalytic test of all the solids prepared. This unit bellows to the *Groupement de Recherches de Lacq GRL – Arkema – Pau (64000)*. We will name this unit **experimental setup GRL**.

B. Experimental setup designed, purchased, calibrated, configured and put into operation at the *Unité de Catalyse et de Chimie du Solide UCCS – Université Lille 1 – Lille (59655)*. We will name this unit **experimental setup UCCS**.

2.4.1. Catalytic test procedure

The experimental setup GRL is presented in Figure 2.16. In our study, MeSH synthesis was carried out using a fixed bed reactor (stainless steel tube with 320 mm of length, inner diameter 15.75 mm and 3.17 mm wall thickness). The reactor was placed in a temperature-controlled oven. The temperature was monitored and controlled at 4 points: feed line, product line, catalyst and oven using K-type thermocouples. External electric heaters with heating-bands were used to keep the feed line and product line at about 120 °C. All the heated parts were well insulated to minimize energy losses and temperature gradients in the system. The feed gases (CO, H₂, H₂S and N₂) were supplied from cylinders and the flow rate of each gas is controlled individually by a mass flow controller. The operating conditions of the activity tests (flow, temperature and pressure) were computer monitored. The outlet gas concentration was analyzed by a gas chromatograph GC (Agilent 6890N) equipped with a column hp-plot Q and a thermal conductivity detector TCD.

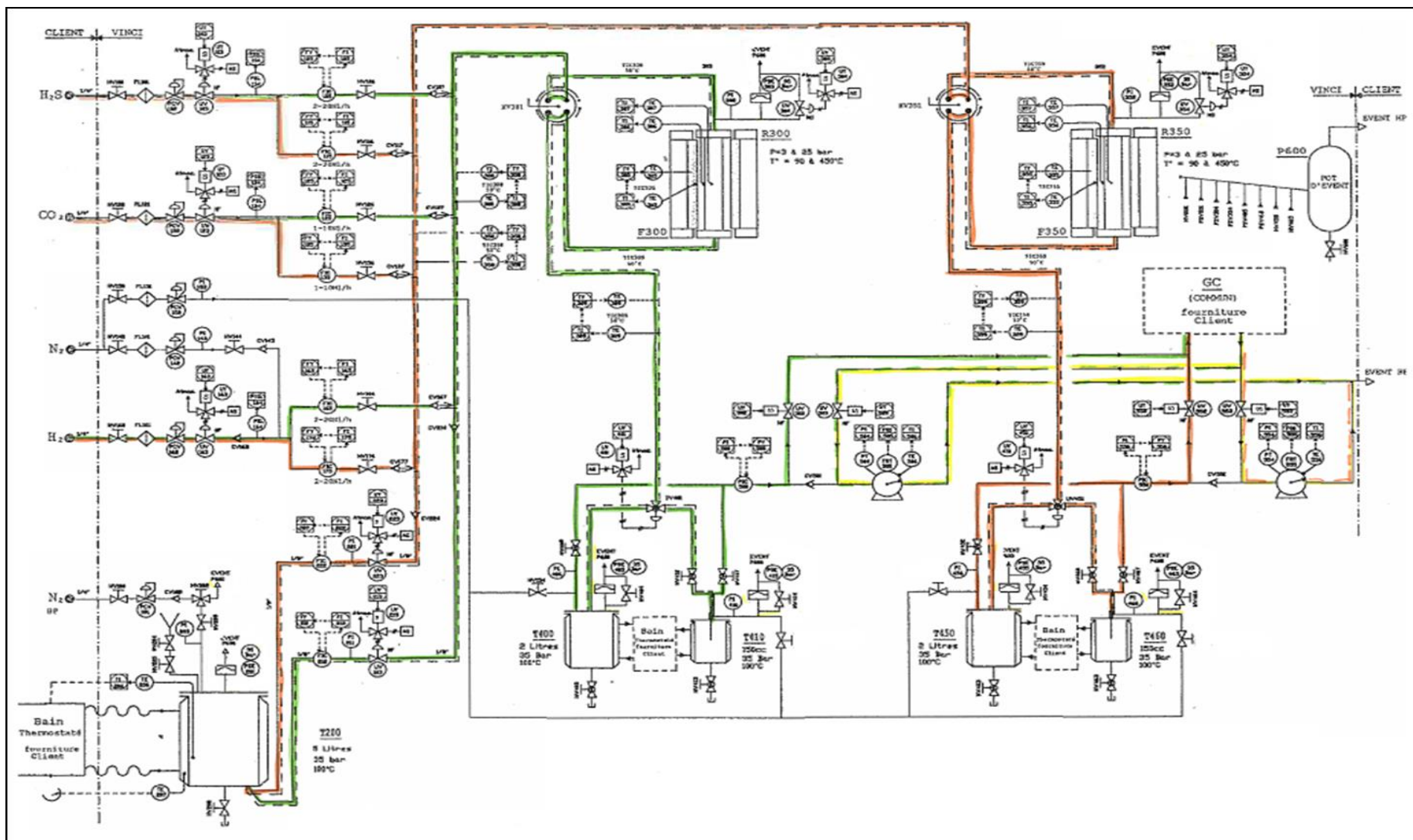


Figure 2.16. Schematic drawing of the experimental setup GRL

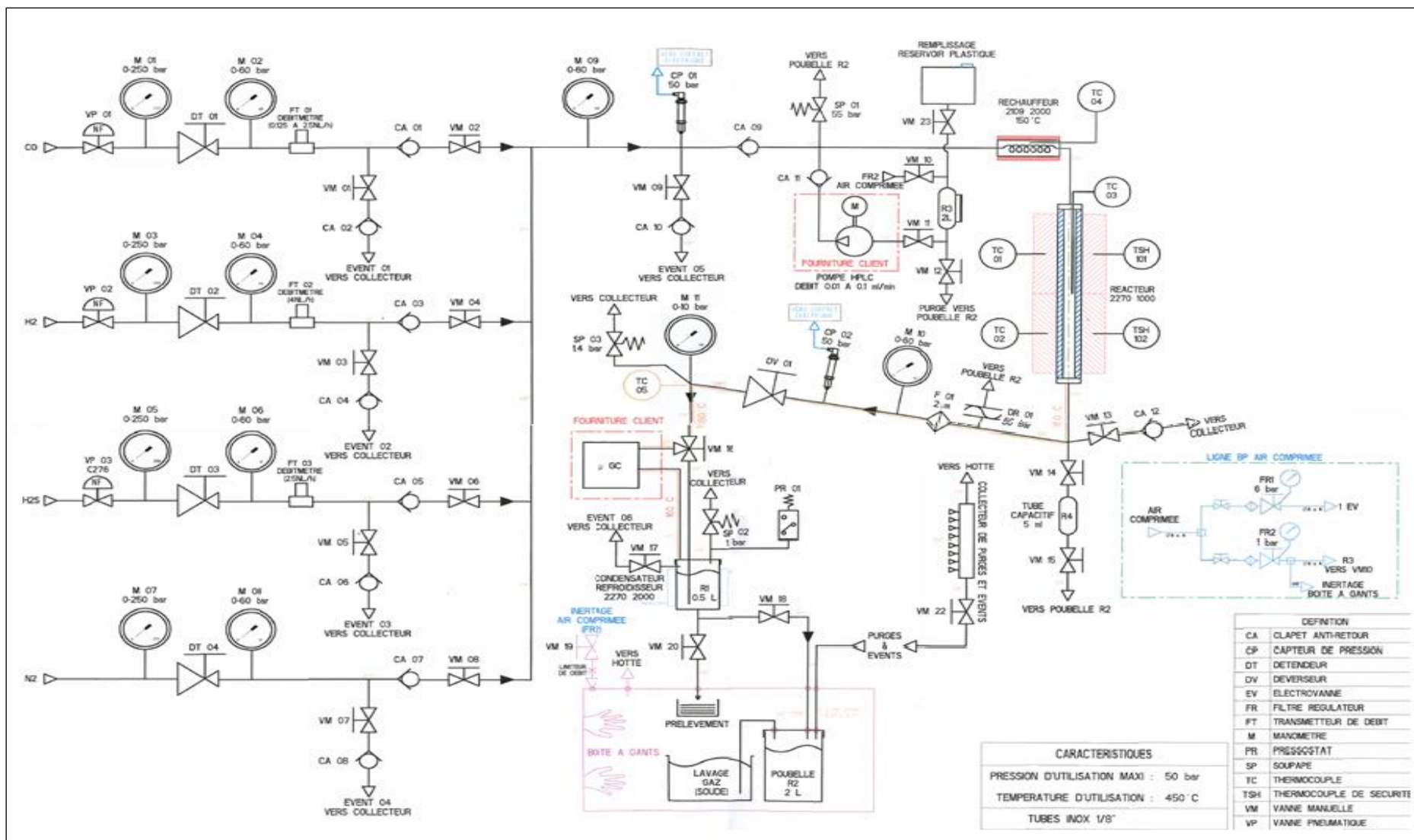


Figure 2.17. Schematic drawing of the experimental setup UCCS

The experimental setup UCCS is illustrated in Figure 2.17. The fixed-bed reactor used to measure the catalytic activity is a stainless steel tube 570 mm long with 5 mm of inner diameter. The reactor was placed in a temperature- controlled oven. The temperature was monitored and controlled at 3 points: product line, catalyst and oven (two zones of control) using K-type thermocouple. The flow lines (tubing) at the outlet of reactor were wrapped, first, with conventional heating tape, then with insulating tape to prevent heat dissipation and better maintain line temperature. Hydrogen, carbon monoxide and hydrogen sulfide were fed to the reactor at desired flow rates using mass flow controllers. Calibration curves for the mass flow controllers of the **experimental setup UCCS** were made and are shown in figure 2.18.

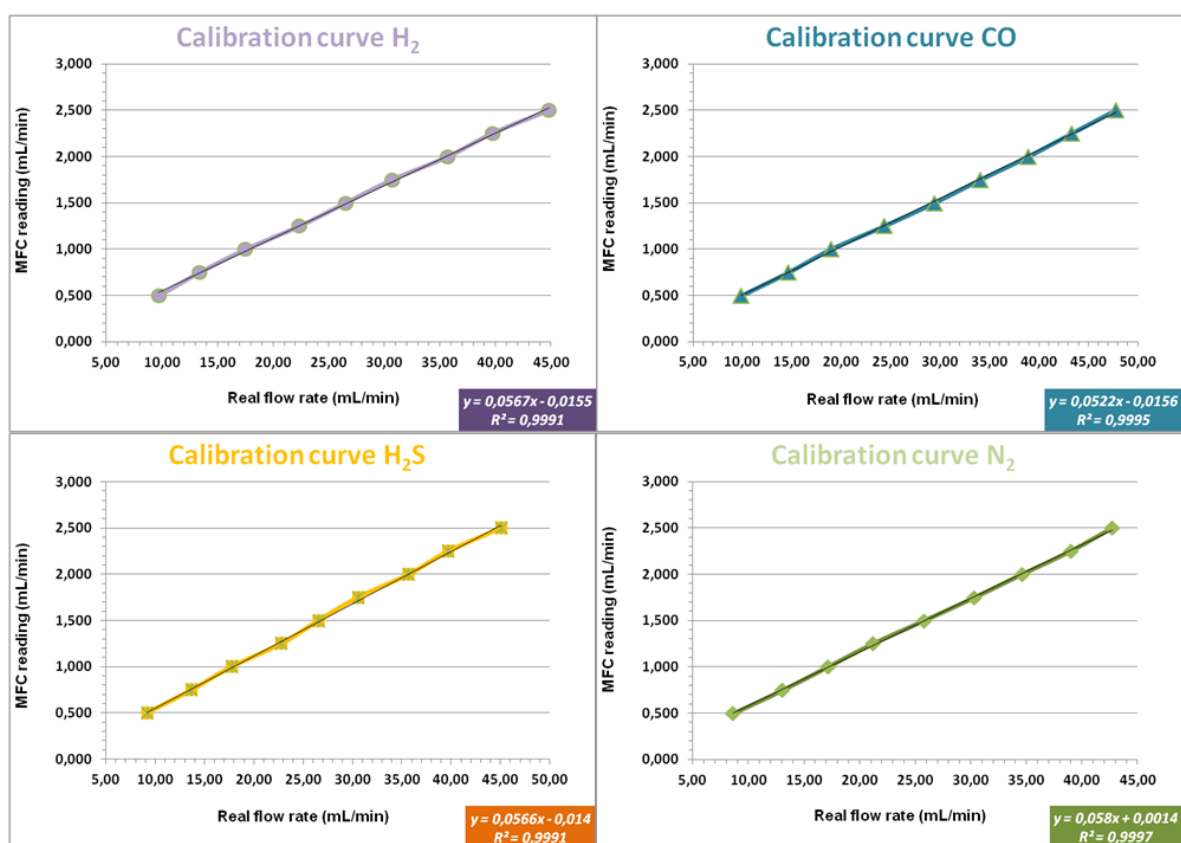


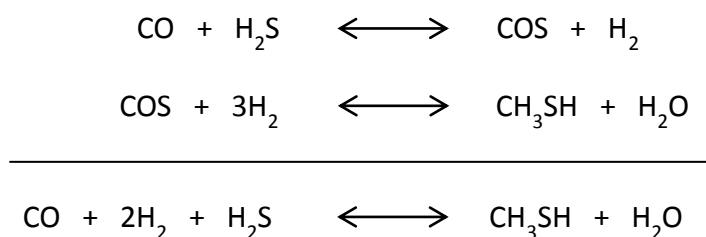
Figure 2.18. Calibration curves of mass flow controller (MFC)

The operating conditions of the activity tests (flow and temperature) were computer monitored; moreover, the pressure of the system was controlled by a back-pressure regulator. The gas phase products were analyzed using an online gas chromatograph (Shimadzu 2014) equipped with three columns, a thermal conductivity detector TCD and a

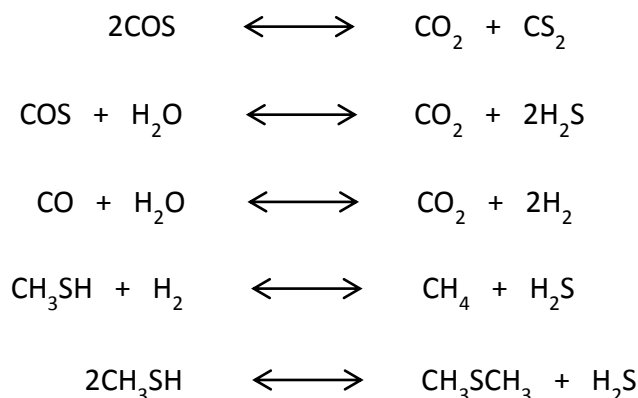
flame ionization detector FID. The concentration of products was measured and presented as area peaks by the data acquisition system.

2.4.2. Gas chromatograph GC

As discussed in chapter 1, the main reactions leading to the formation of methyl mercaptan from syngas and hydrogen sulfide are as follow:



Nevertheless, other reactions leading to the formation of undesirable products can also take place. These products are mainly CO_2 , CH_4 , CS_2 , DMS and DMDS obtained by the following reactions:



Thus, the analysis by gas chromatography was made for all reactants, intermediaries, desired and undesired products.

2.4.2.1. Experimental setup GRL

The GC parameters used for the GC analysis of gas products of the experimental setup GRL are shown in table 2.9.

Table 2.9. Gas chromatographic conditions GC-GRL

GC	Agilent 6890N
Carrier	Helium, constant flow mode
Sample loop size	0.25 mL
Column	Hp-plot Q (30m x 530 μ m x 40 μ m)
Oven program	40 °C (4 min) to 200 °C (21 min) at 10 °C/min
TCD Temperature	200 °C
TCD make-up flow	10 mL/min
Injection	Split mode

A single Hp plot Q column was used for the separation of all the products. A typical chromatograph of the products analyzed is shown in figure 2.19.

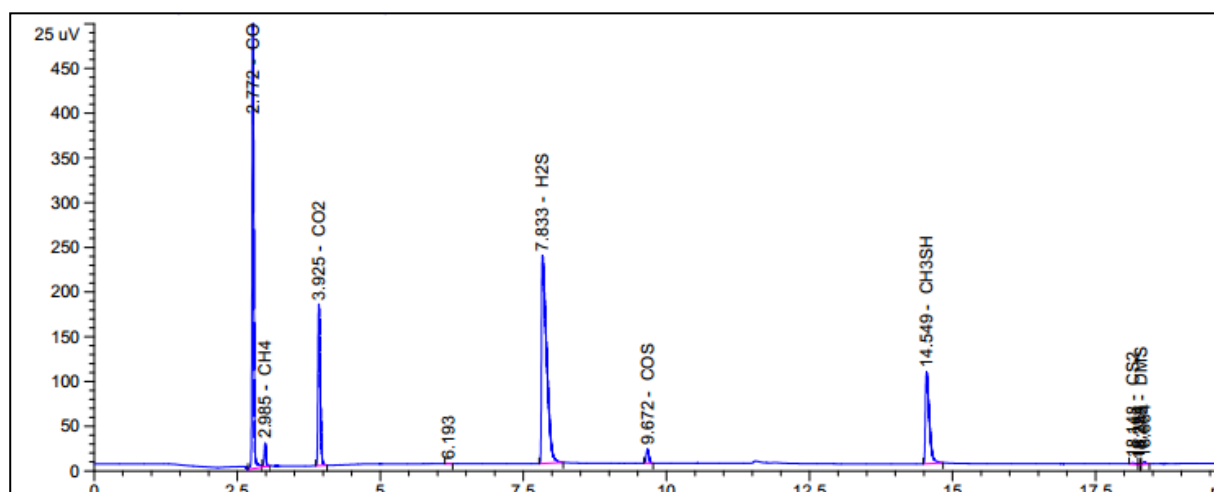


Figure 2.19. Typical chromatograph of products analyzed by using the GC-GRL

2.4.2.2. Experimental setup UCCS

Conditions

GC conditions and gas and valve time events for the experimental setup UCCS are presented in table 2.10 and 2.11 respectively.

Table 2.10. Gas chromatographic conditions GC-UCCS

GC	Shimadzu 2014
<i>Carrier</i>	Helium, constant flow mode
<i>Carrier flow program</i>	30 mL/min (9 min) to 35 mL/min (70 min) at 1,5 mL/min
<i>Sample loop size</i>	1 mL
<i>Oven program</i>	40 °C (9 min) to 120 °C (1 min) at 15 °C/min, then to 200 °C (11,5 min) at 25 °C/min
Line 1 - FID	
<i>Temperature</i>	200 °C
<i>Column</i>	Porapak Q 100/120 Mesh (10m x 2mm ID) Porapak Q 100/120 Mesh (20m x 2mm ID)
Line 2 - TCD	
<i>Temperature</i>	200 °C
<i>Column</i>	Porapak Q 100/120 Mesh (10m x 2mm ID) Molecular Sieve 5A 100/120 Mesh (10m x 2mm ID)

Table 2.11. Time events GC-UCCS

Event	Time
<i>Valve 1 ON</i>	0.01 min
<i>Valve 2 ON</i>	0.01 min
<i>TCD Negative polarity ON</i>	0.5 min
<i>Valve 1 OFF</i>	0.5 min
<i>Valve 2 OFF</i>	2.65 min
<i>TCD Negative polarity OFF</i>	2.65 min
<i>TCD Negative polarity ON</i>	6.5 min
<i>TCD Negative polarity OFF</i>	10 min
<i>TCD Negative polarity ON</i>	14.5 min
<i>TCD Negative polarity OFF</i>	75 min

The scheme of valves configuration is presented in figure 2.20. The system used is composed by two six-way valves working with compressed air. The path crossed by the sample

collected in the sample loop is divided in three steps:

1. Initially, the valves 1 and 2, corresponding respectively to the sampling valve and the column selection valve, are in position OFF (T_0). It means that the gas flows in the sample loop and therefore it is not injected into the column porapak Q-1.
2. The launch of an acquisition at time T_1 allows the switching of valves 1 and 2 from the position OFF to the position ON. At this moment the sample enters the first column porapak Q-1 which works as a pre-column allowing the pre-separation of permanent gases in two groups, G1 (H_2 , N_2 , CH_4 and CO) and G2 (CO_2). When the first group entered in the molecular sieve column, G1 is separated in four peaks, H_2 , N_2 , CH_4 and CO .
3. At the time $T_0 + 2.65$ min, the valve 2 switches to the position OFF. Thus the CO_2 (G2) is conducted and separated to the second porapak Q-2 column as well as the sulfide gases (H_2S , COS , CH_3SH and CS_2). At this time, valve 1 and valve 2 are in the initial position T_0 . The gas stream leaving the molecular sieve and porapak Q-2 are combined to form a single gaseous stream containing all the compounds. These are detected by the TCD and FID.

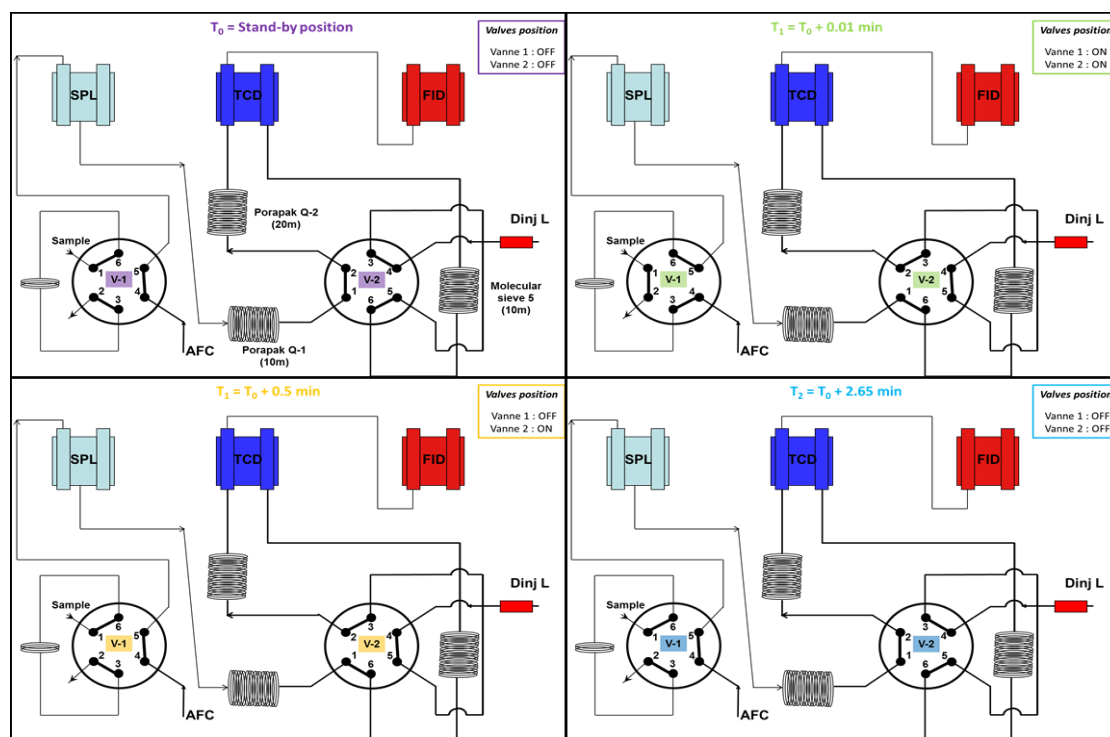


Figure 2.20. Scheme of valves configuration GC-UCCS

Calibration

In chromatography, the calculation of the absolute amount of a component involves measuring the area of the peak and the determination of the response factor for this compound. The amount is calculated by the equation:

$$Q = A \times f \quad (13)$$

where A and f are respectively the peak area and the response factor.

When using standard gas bottles, the curves: $Q_n = A_n \times f_n$ are plotted and the response factors obtained, f_n , correspond to the slope.

To perform the calibration, two standard gas bottles were used and their concentrations are shown in table 2.12.

Table 2.12. Composition of standard gas bottles

<i>Element</i>	<i>Etalon 1 / %</i>	<i>Etalon 2 / %</i>
H ₂	10,030	-
N ₂	9,996	73,979
CH ₄	9,999	-
CO ₂	9,995	-
CO	9,993	-
COS	-	5,064
CH ₃ SH	-	19,960
CS ₂	-	0,991

Additionally, mixtures of H₂, N₂, CO and H₂S were made by using the mass flow controllers, the concentrations obtained are showed in table 2.13.

Table 2.13. Composition of mixture H_2 , N_2 , CO and H_2S

Concentration %	H_2	N_2	CO	H_2S
1	33,33	1,66	31,67	33,33
2	50,00	1,25	23,75	25,00
3	22,22	2,77	52,78	22,22
4	45,45	0,45	8,64	45,45
5	66,67	0,83	15,83	16,67
6	45,45	2,27	43,18	9,09

The calibration plots obtained for each gas are presented in figure 2.21.

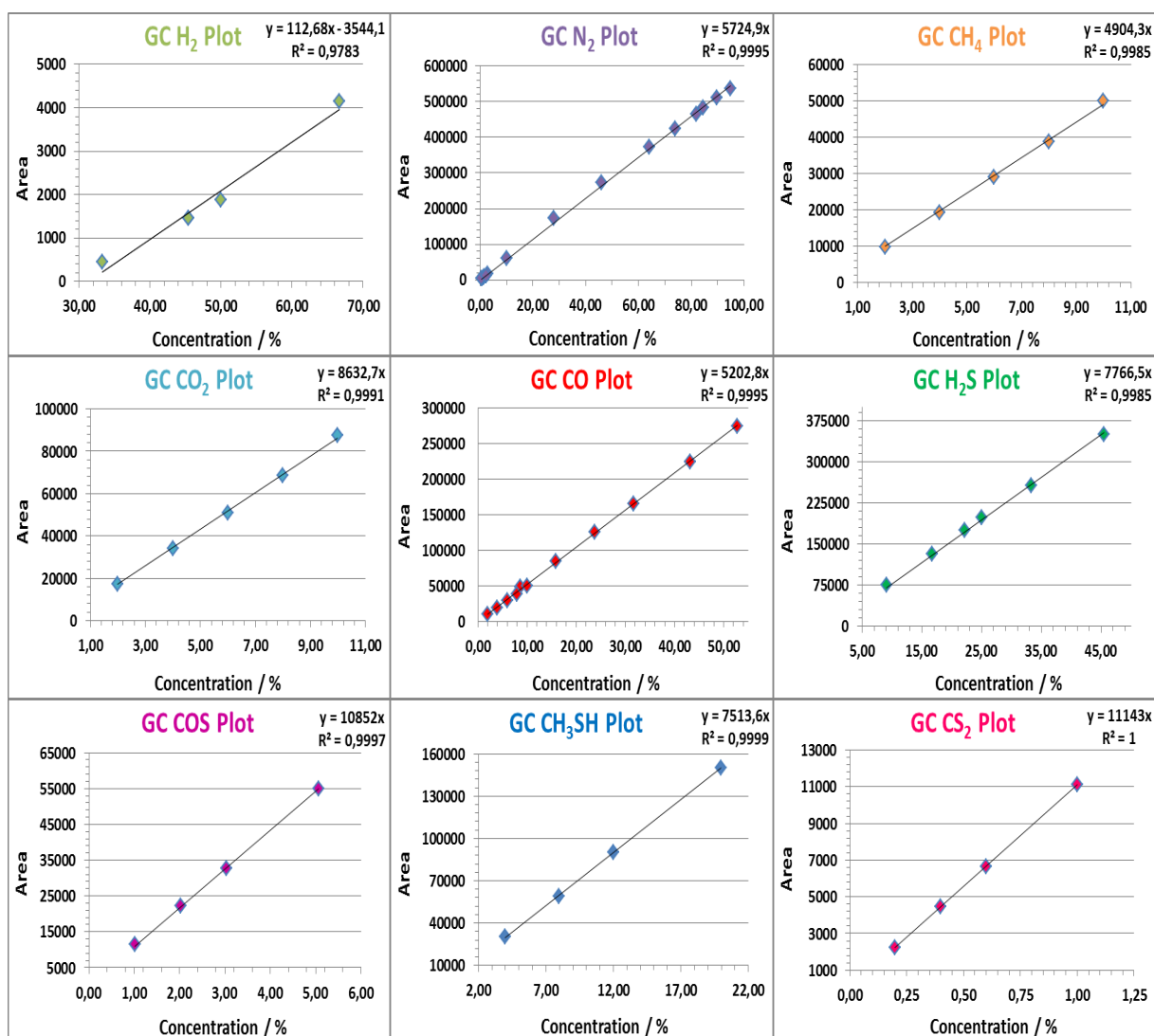


Figure 2.21. Calibration plots GC-UCCS

A typical chromatograph of the products analyzed by the GC-UCCS is displayed in figure 2.22. Retention time (min) and position of each compound are showed.

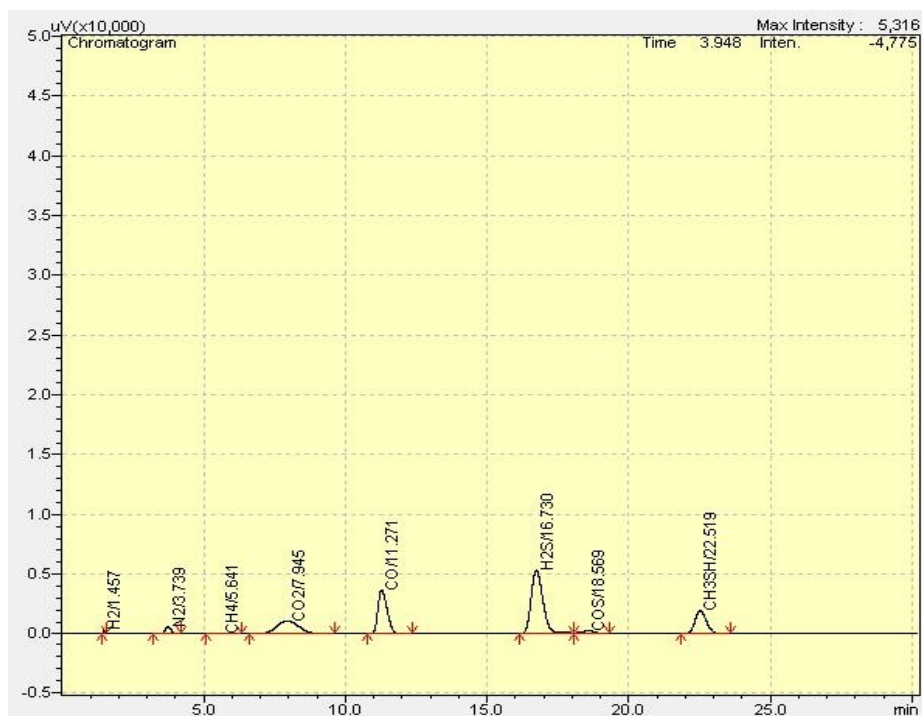


Figure 2.22. Typical chromatograph of products analyzed by using the GC-UCCS

2.4.3. Pretreatment of catalysts

Before the activity tests, the catalyst was pretreated in situ by following four different methods displayed in figure 2.23. Different methods were tested with the aim of found the optimal pretreatment conditions to be used.

A drying step was used independently of the method used with the purpose to remove adsorbed water and surface impurities eventually present on the catalyst. Method S/RS involves a pre-sulfidation step with pure H₂S followed by simultaneous reduction/ sulfidation with a mixture H₂:H₂S (80:20). Method R/RS consists in a reduction step using pure H₂ followed by a reduction/sulfidation step as in method S/RS. Method RS involves a conventional sulfidation using a mixture H₂/H₂S (90:10). Method RS+CO consists in pretreatment with the reaction mixture H₂S:H₂:CO (1:2:1).

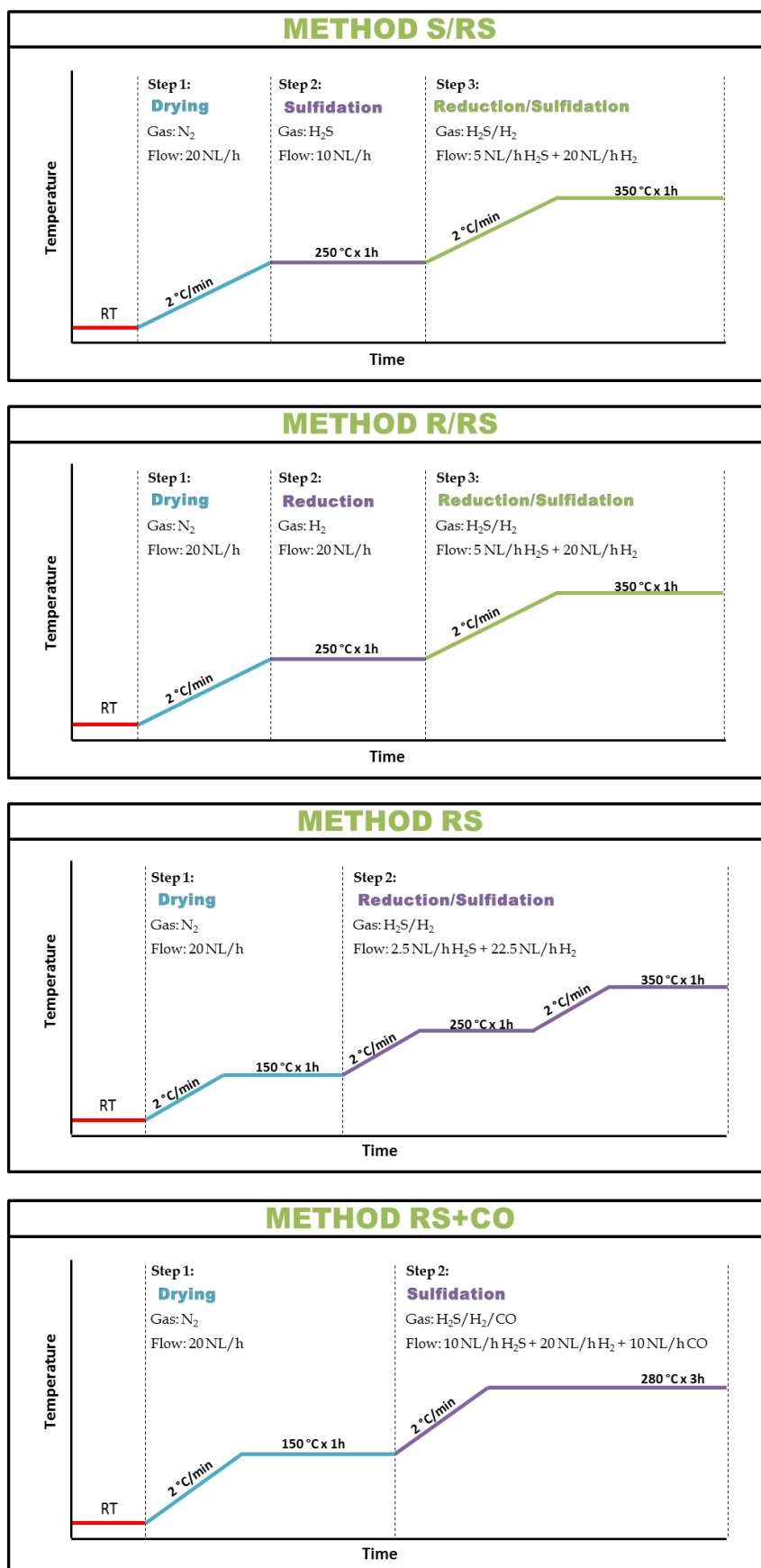


Figure 2.23. Pretreatment methods used after catalytic test

2.4.4. Reaction conditions

Table 2.14. Reaction conditions

<i>Conditions</i>	<i>Experimental setup GRL</i>	<i>Experimental setup UCCS</i>
<i>Temperature</i>	280 – 300 – 320 °C	280 – 300 – 320 °C
<i>Pressure</i>	10 Bar	10 Bar
<i>Flow rate</i>	40 NL/h	0,847 NL/h
<i>GHSV</i>	1333,33 h ⁻¹	1333,33 h ⁻¹
<i>H₂S:H₂:CO ratio</i>	1:2:1	1:2:1
<i>Volume of catalyst</i>	30 cc	0,635 cc

2.4.5. Experimental procedure

After the completion of the pretreatment stage, the temperature was decreased until 280 °C, start temperature of catalytic test. The reactants were introduced at the required H₂S/H₂/CO ratio and the pressure was increased at 10 bars. After about 15 hours of stabilization (one night) the first products were analyzed by GC. The temperature was then increased at 300 °C. After about 1 hour of stabilization, products were analyzed. Same procedure was follows at 320 °C. The hot line after the reactor was kept at a temperature above 100 °C to prevent condensation of the water vapor and condensable sulfide products.

In experimental setup GRL, a half of the reactor was filled with 30 cc of catalysts while the other half was filled with 30 cc of silicon carbide SiC. On the other hand, in experimental setup UCCS, the catalytic bed of the reactor had 11 cm height and was constituted for 0,635 cc of catalyst (0.5 mm > ϕ > 0.3mm) mixed with 0.635 cc of SiC (ϕ =0.25 mm).

2.4.6. Data analysis

The conversion ($X\%$) of a reactant A at the temperature T, $X_{A(T)}$ is defined as the amount of the reactant A ($\text{mol}\cdot\text{ml}^{-1}$) transformed at the temperature T divided by the total amount of A in the gas feed ($\text{mol}\cdot\text{ml}^{-1}$). The corresponding equation is defined as follows:

$$X_{CO}(\%) = \frac{n_{CO,i} - n_{CO,f}}{n_{CO,i}} \times 100 \quad (14)$$

where $n_{CO,i}$ represents the initial moles of CO and $n_{CO,f}$ represents the final moles of CO.

The selectivity ($S\%$) of products was calculated according to the following formula:

$$S_x(\%) = \frac{n_x}{n_{CO,i} - n_{CO,f}} \times 100 \quad (15)$$

Where n_x are the formed moles of the product "x" and $n_{CO_{transf}}$ are the moles of CO transformed. $n_{CO_{transf}} = n_{CO,i} - n_{CO,f}$.

The productivity expressed in $\text{g}\cdot\text{h}^{-1}\cdot\text{L}_{\text{cat}}^{-1}$ is determined as:

$$P = \frac{n_{CO,i} \cdot X_{CO}(\%) \cdot S_x(\%) \cdot M_x}{M_{CO} \cdot V_{\text{cat}}} \quad (16)$$

Where $n_{CO,i}$ is the initial concentration of CO ($\text{g}\cdot\text{h}^{-1}$), $\%X_{CO}$ is the conversion of CO, $\%S_x$ is the selectivity of the product "x", M_{CO} is the molecular weight of CO ($\text{g}\cdot\text{mol}^{-1}$), M_x is the molecular weight of the product "x" ($\text{g}\cdot\text{mol}^{-1}$) and V_{cat} is the volume of catalyst (L).

Finally, the product yield ($Y\%$) is calculated as follow

$$Y(\%) = \frac{n_x \cdot N_{C,x}}{n_{CO,i}} \times 100 \quad (17)$$

Where n_x are the formed moles of the product "x", $N_{C,x}$ is the number of carbon atoms in product "x" and $n_{CO,i}$ represents the initial moles of CO.

2.5. VALIDATION OF UCCS CATALYTIC TEST

In order to validate the complete setup, calibration and put into operation of the **experimental setup UCCS**, a catalytic test was carried out and compared with the catalytic results obtained using the experimental setup GRL with the same catalysts. The results are showed in table

Table 2.15. Comparison of catalytic results made in experimental setup UCCS and GRL

TEST	X_{CO} (%)	Selectivity (%)			CH_3SH Productivity ($g \cdot h^{-1} \cdot L^{-1}$)	COS Productivity ($g \cdot h^{-1} \cdot L^{-1}$)	CO_2 Productivity ($g \cdot h^{-1} \cdot L^{-1}$)	CH_3SH Yield (%)	Carbon balance (%)
		CH_3SH	COS	CO_2					
UCCS	47	47	3	50	164	13	158	23	96
GRL	38	47	3	49	129	12	123	18	93

REACTION CONDITIONS: 320 °C, CO:H₂:H₂S = 1:2:1, 1333,33 h⁻¹, 10 bar

Similar results are obtained by means of the two catalytic tests. A higher CO conversion is attained when working on the experimental setup UCCS; nevertheless, the same trend in selectivities is observed. These results confirm the correct configuration of all the worked parameters.

2.6. REFERENCES

- [1] M. A. Harmer and G. Sykes, "Kinetics of the Interconversion of Sulfido- and Oxomolybdate(VI) Species MoOxS4-x2- in Aqueous Solutions," *Inorganic Chemistry*, vol. 19, pp. 2881–2885, 1980.
- [2] R. W. Mooney and C. W. W. Hoffman, "X-Ray diffraction data for ammonium tetrathiotungstate," *Canadian Journal of Chemistry*, vol. 41, pp. 2237–2239, 1963.
- [3] C. Lamonier, J.-F. Lamonier, B. Aellach, A. Ezzamarty, and J. Leglise, "Specific tuning of acid/base sites in apatite materials to enhance their methanol thiolation catalytic performances," *Catalysis Today*, vol. 164, no. 1, pp. 124–130, Apr. 2011.
- [4] G. Leofanti, G. Tozzola, M. Padovan, G. Petrini, S. Bordiga, and A. Zecchina, "Catalyst characterization : characterization techniques," *Catalysis Today*, vol. 34, pp. 307–327, 1997.
- [5] S. Brunauer, P. H. Emmett, and E. Teller, "Adsorption of gases in multimolecular layers," *Journal of the American Chemical Society*, vol. 60, pp. 309–319, 1938.
- [6] S. J. Gregg and K. S. W. Sing, *Adsorption, Surface Area and Porosity*. London: Academic Press Inc., 1967, p. 67.
- [7] R. Asahi, Y. Taga, W. Mannstadt, and A. J. Freeman, ".,," *Physical Review B*, vol. 61, p. 7459, 2000.
- [8] J. R. Ferraro and K. Nakamoto, *Introductory Raman Spectroscopy*. Academic Press Ltd, 1994.
- [9] S. Shehzad, "Optical Spectroscopic and theoretical investigations of a series of fluoroquinolones," Roskilde University, Denmark, 2010.
- [10] M. Boudart, *Principles of Heterogeneous Catalysis. Handbook of Heterogeneous Catalysis*, vol. 1. Wiley-VCH, 1997.
- [11] M. Alsawalha, "Characterization of acidic and basic properties of heterogeneous catalysts by test reactions," Carl Von Ossietzky Universität, Oldenburg, 2004.
- [12] B. Aellach, "Préparation, caractérisation et évaluation des propriétés catalytiques des catalyseurs à base d'apatite dans la thiolation et dans l'oxydation du méthanol," Université Hassan II Ain Chock Casablanca, 2010.

CHAPTER 3

Precursors, supports and fresh catalysts characterization

Precursors, supports and fresh catalysts characterization: Summary

3.1. CHARACTERIZATION OF PRECURSORS	119
3.1.1. UV-Vis spectroscopy	119
3.1.2. Laser Raman spectroscopy	121
3.1.3. Wide angle powder XRD	122
3.2. CHARACTERIZATION OF SUPPORTS	124
3.2.1. Specific surface areas of supports	124
3.2.2. Wide angle powder XRD	124
3.2.3. Laser Raman spectroscopy	126
3.2.4. Scanning electron microscopy (SEM).....	126
3.2.5. Acid-base properties of solids.....	128
3.2.5.1. <i>Temperature programmed desorption of ammonia and carbon dioxide</i>	128
3.2.5.2. <i>Acid-base behavior determined by catalytic decomposition of isopropanol</i>	132
3.3. CONCLUSIONS OF SECTION 3.1 AND 3.2	135
3.4. CHARACTERIZATION OF Mo-BASED FRESH CATALYSTS	136
3.4.1. Characterization of oxidic reference catalysts.....	136
3.4.1.1. <i>Laser Raman spectroscopy</i>	136
3.4.1.2. <i>X-Ray Photoelectron Spectroscopy (XPS)</i>	138
3.4.2. Characterization of K ₂ MoO ₄ -based catalysts.....	140
3.4.2.1. <i>Bulk composition and specific surface area</i>	140
3.4.2.2. <i>Laser Raman Spectroscopy</i>	142
3.4.2.3. <i>Wide angle powder XRD</i>	143
3.4.2.4. <i>X-ray photoelectron spectroscopy (XPS)</i>	145
3.4.2.5. <i>Scanning Electron Microscopy (SEM)</i>	147
3.4.2.6. <i>Electron probe microanalysis (EPMA)</i>	148
3.4.3. Characterization of K ₂ MoS ₄ -based catalysts.....	150
3.4.3.1. <i>Bulk composition and specific surface area</i>	150
3.4.3.2. <i>Laser Raman Spectroscopy</i>	151
3.4.3.3. <i>Wide angle powder XRD</i>	152
3.4.3.4. <i>X-ray photoelectron spectroscopy (XPS)</i>	154
3.4.3.5. <i>Scanning Electron Microscopy (SEM)</i>	157
3.5. CONCLUSION OF SECTION 3.4	158
3.6. REFERENCES	159

The prepared (K_2MoS_4 and K_2WS_4) and commercial (K_2MoO_4 and K_2WO_4) precursors salts as well as the home-made hydroxyapatites and commercial alumina and silica supports and the catalysts prepared from them have been characterized by means of various characterization techniques: UV-Vis, Raman, XRD, XPS, BET, SEM, NH_3 -TPD, CO_2 -TPD and isopropanol test reaction.

This chapter presents a comprehensive study of the physico-chemical properties of precursors and supports used forward for the preparation of catalysts as well as the characterization of the fresh catalysts. Section 3.1 presents results concerning the characterization of precursors, section 3.2 deals with characterization results obtained for supports and finally in section 3.3 are exposed the results of chemical characterization of fresh catalysts.

3.1. CHARACTERIZATION OF PRECURSORS

3.1.1. UV-Vis spectroscopy

The UV-Visible spectroscopy can be used to determine the purity of thiomolybdate and thiotungstate salts. Several solutions of K_2MoS_4 and K_2MoW_4 at various concentrations were prepared in deionized water (previously bubbled with N_2) and analyzed by UV-Vis spectroscopy. Absorbance values at wavelengths between 200 and 600 nm were plotted against the concentrations and are showed in figure 3.1.

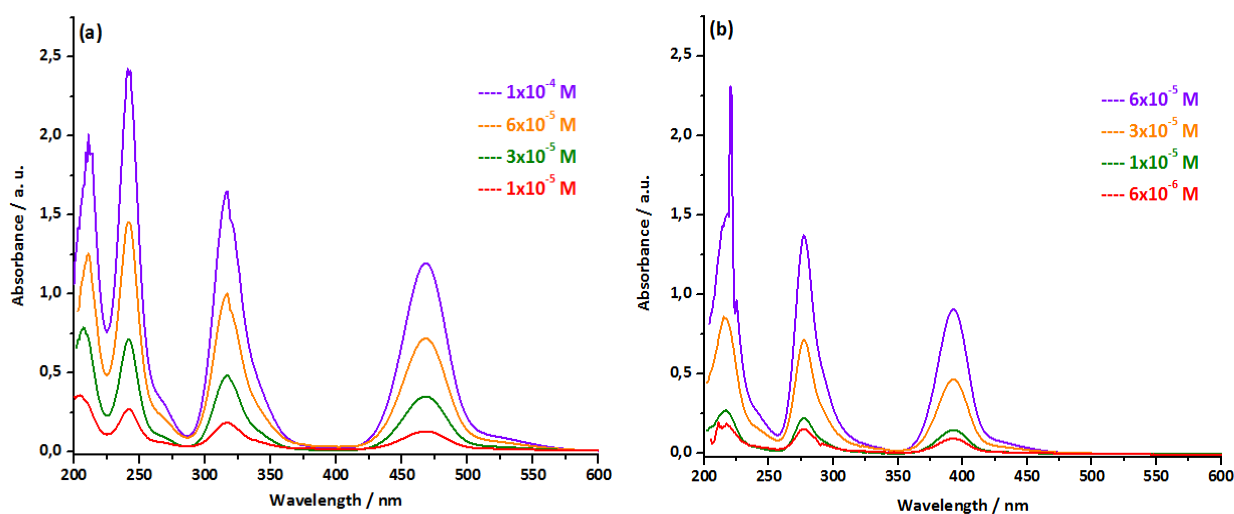


Figure 3.1. UV-Vis spectra of (a) K_2MoS_4 and (b) K_2WS_4 in H_2O

K_2MoS_4 exhibits absorption bands in the UV-Vis spectral region at about 468, 316 and 241 nm which are attributed to tetrahedral groups $(MoS_4)^{2-}$ in accordance with the formation of this thio salt [1–5]. K_2WS_4 exposes three bands at above 393, 277 and 216 nm assigned to tetrahedral groups $(WS_4)^{2-}$ of this species [2], [6], [7]. These results are in good agreement with the data found in literature establishing that no contamination by neighboring oxythio ions takes place.

The extinction coefficient $\varepsilon / L.mol^{-1}.cm^{-1}$ for K_2MoS_4 and K_2WS_4 were determined and are showed in figure 3.2.

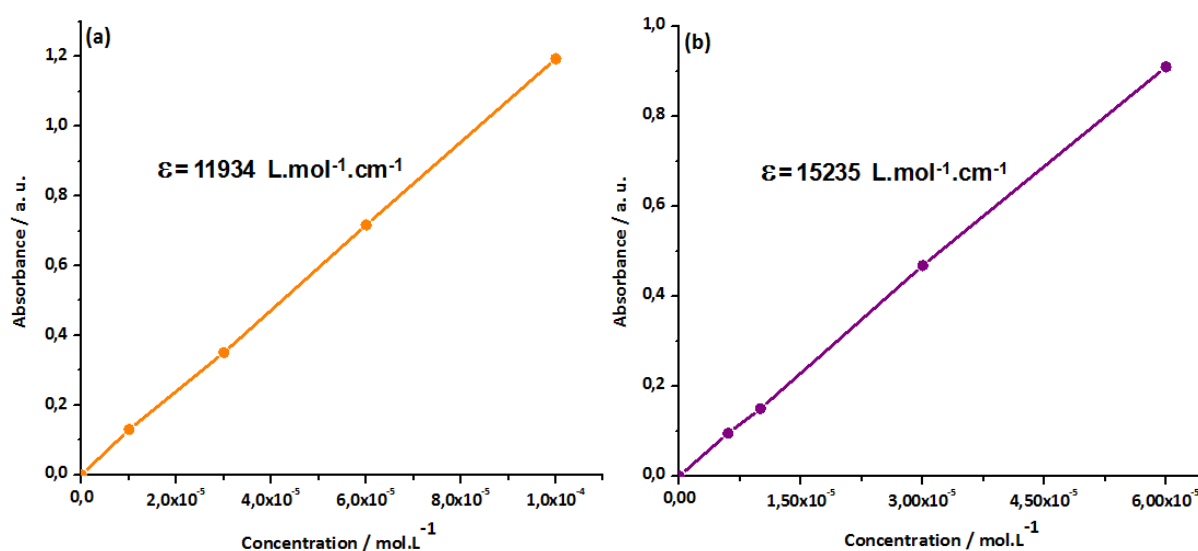


Figure 3.2. Extinction coefficient $\varepsilon (L.mol^{-1}.cm^{-1})$ for (a) K_2MoS_4 ($\lambda_{max}=468 nm$) and (b) K_2WS_4 ($\lambda_{max}=393 nm$)

Linear regression, obtained by plotting the absorbance as a function of the concentration, was used to determine the slope, which allows to obtain the molar extinction coefficient ε . $\varepsilon = 11934 L.mol^{-1}.cm^{-1}$ and $15235 L.mol^{-1}.cm^{-1}$ were attained for K_2MoS_4 and K_2WS_4 respectively. The obtaining line intercepting at the origin as well as the values of ε , are consistent with other literature values and confirm the stability of these species in solution [4], [7], [8].

3.1.2. Laser Raman spectroscopy

As described in chapter 2, potassium tetrathiomolybdate and potassium tetrathiotungstate were obtained by the exchange between ammonium and potassium during the dissolution of the corresponding ammonium salt in the potassium hydroxide solution. The characterization by Raman spectroscopy allows ensuring if the exchange between the NH_4^+ and K^+ was completely achieved by the identification of the lines corresponding to one or the other compound. The figure 3.3 displays the Raman spectra of the two sulfide precursors K_2MoS_4 and K_2WS_4 and their corresponding ammonium precursor $(\text{NH}_4)_2\text{MoS}_4$ and $(\text{NH}_4)_2\text{WS}_4$. No lines in the region $700\text{-}1200\text{ cm}^{-1}$ were observed, reason by which the spectra are showed in the wavenumber region $150\text{-}700\text{ cm}^{-1}$.

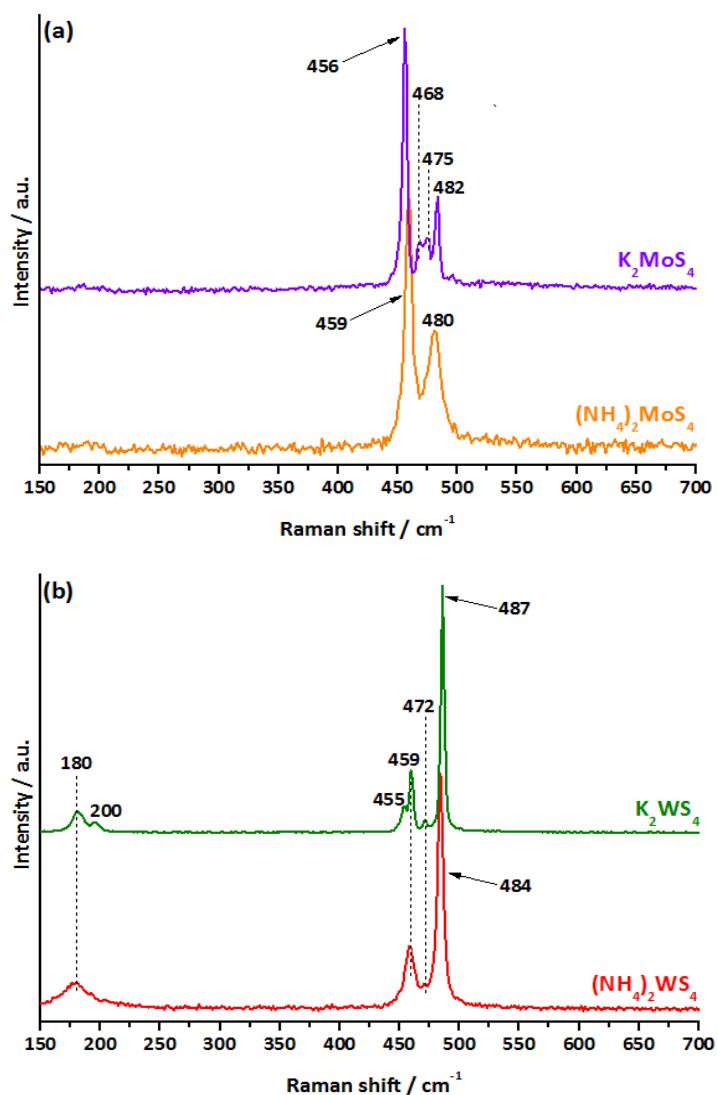


Figure 3.3. Raman spectra of (a) K_2MoS_4 and $(\text{NH}_4)_2\text{MoS}_4$ and (b) K_2WS_4 and $(\text{NH}_4)_2\text{WS}_4$

The spectrum of $(\text{NH}_4)_2\text{MoS}_4$ (figure 3.1(a) orange) contains two sharp lines at 459 and 480 cm^{-1} corresponding to the symmetric (ν_1) and antisymmetric (ν_3) $\nu(\text{Mo-S})$ vibrations of the MoS_4^{2-} anion, respectively. Meanwhile, the spectrum of K_2MoS_4 (figure 3.1(a) violet) comprises four lines at 456, 468, 475 and 482 cm^{-1} also assigned to the to the $\nu(\text{Mo-S})$ vibration of the MoS_4^{2-} anion. Our results were found to be congruent and comparable with the data collected by other authors [9–11]. Initially, the presence of lines characteristics from MoS_4^{2-} ions, coupled to the lack of lines in the region 700-1200 cm^{-1} , confirms the results obtained by UV-Vis spectroscopy about the absent of contamination coming from oxomolybdate ions. In a second approach, the comparison between the spectrum of $(\text{NH}_4)_2\text{MoS}_4$ and K_2MoS_4 allowed us to confirm that the exchange of NH_4^+ ions by K^+ ions is at least partially achieved since two new lines at 469 and 475 cm^{-1} related with K_2MoS_4 appear.

As observed in figure 3.3.(b), lines at 459, 472 and 484 cm^{-1} were observed for $(\text{NH}_4)_2\text{WS}_4$, whereas K_2WS_4 exhibits four lines at 455, 459, 472 and 487 cm^{-1} . As reported in the literature [10], [11], the line at about 485 cm^{-1} is assigned to the symmetric (ν_1) vibration of the WS_4^{2-} anion and the lines at lower frequencies are attributed to antisymmetric (ν_3) vibrations of the WS_4^{2-} . The line at 455 cm^{-1} detected in K_2WS_4 represents a clearly evidence of the conversion of ammonium tetrathiomolybdate into potassium tetrathiomolybdate. Additionally, as well as for thiomolybdates compounds, the nonexistence of lines at wavenumbers at about 860 cm^{-1} corresponding at vibrations W-O is an excellent indication of the purity of the synthesized compounds.

3.1.3. Wide angle powder XRD

The wide angle powder XRD patterns of sulfide solids are displayed in figure 3.4. The XRD patterns of the four samples analyzed essentially revealed a bulk structure with sharp and strong peaks corresponding to a very high crystalline structure. The X-ray diffraction patterns of ammonium tetrathiomolybdate (JCPDS 00-038-0075) and potassium tetrathiomolybdate (JCPDS 00-019-1001) are in good agreement with the JCPDS files, showing that the prepared crystalline potassium tetrathiomolybdate is obtained quantitatively by ion exchange. The pattern of ammonium tetrathiotungstate (JCPDS 00-048-1663) is also consistent with the

JCPDS file; in contrast, no JCPDS file has been reported for potassium tetrathiotungstate, nevertheless, the evident difference between the patterns of both tungsten-based compounds suggest that the ion exchange among ammonium and potassium was accomplished. Moreover, the obtained patterns are in agreement with the data earlier reported by Clarke and Mooney [12], [13].

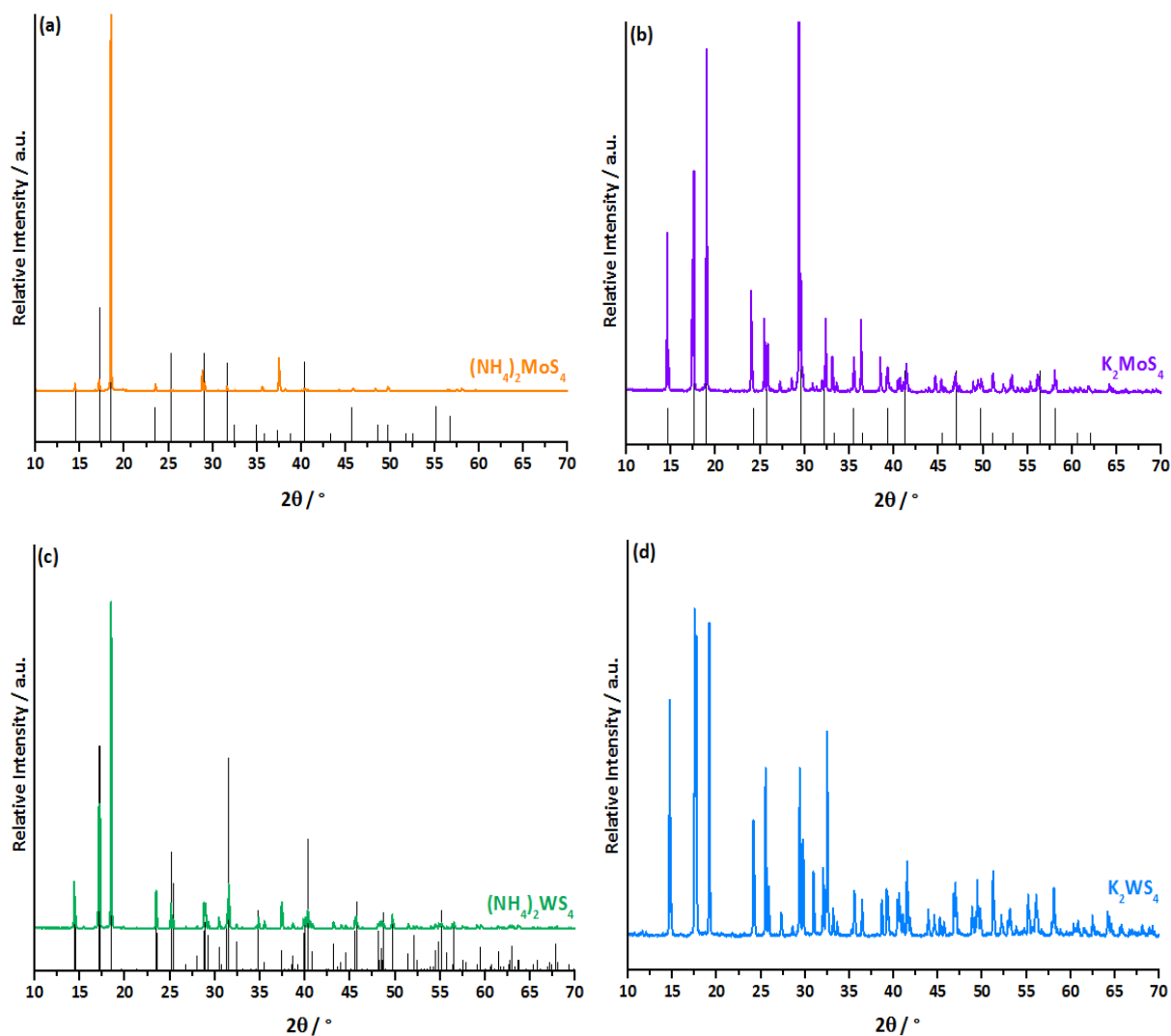


Figure 3.4. XRD patterns of (a) $(\text{NH}_4)_2\text{MoS}_4$ (b) K_2MoS_4 (c) $(\text{NH}_4)_2\text{WS}_4$ and (d) K_2WS_4 . The black lines in each diffractogram correspond to the JCPDS pattern.

3.2. CHARACTERIZATION OF SUPPORTS**3.2.1. Specific surface areas of supports**

Specific surface areas of all the solids chosen as supports are detailed in table 3.1.

Table 3.1. *Specific surface area of solid supports*

Solid	BET surface area m².g⁻¹
Al ₂ O ₃ -1	244
Al ₂ O ₃ -2	181
Al ₂ O ₃ -3	280
SiO ₂ -1	205
SiO ₂ -2	142
Hap	103
HapNa	111

All the solids under study show areas between 100 and 300 m².g⁻¹. The supports with higher surface areas are the aluminas, followed by the silicas at around 150 and 200 m².g⁻¹, ending with hydroxyapatite with surface areas nearby to 100 m².g⁻¹. The SSA found for the homemade carbonated hydroxyapatites Hap and HapNa are in agreement with those reported by Lamonier et al. [14].

3.2.2. Wide angle powder XRD

Diffraction patterns of commercial aluminas and silicas and the as-prepared hydroxyapatites are showed in figure 3.5. Four mainly peaks at $2\theta = 37.2, 39.5, 46.0$ and 66.8° are detected for alumina type-solids as found in literature according with JCPDS files JCPDS 00-050-0741.

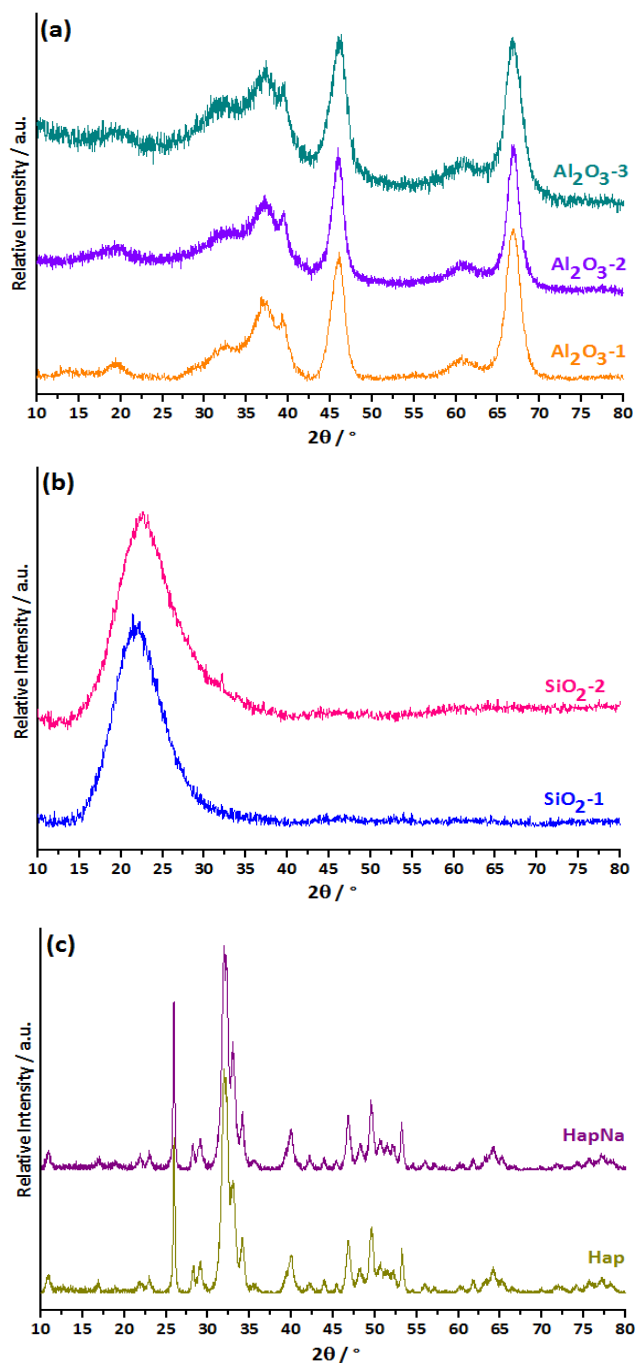


Figure 3.5. Diffraction patterns of (a) Aluminas, (b) Silicas and (c) Hydroxyapatites

Silica displayed a broad peak nearby to 22° characteristic to silica phase, as reported in JCPDS files (JCPDS 00-001-0438). Concerning hydroxyapatite supports, diffraction patterns of stoichiometric and sodium-doped stoichiometric hydroxyapatite reveals only the presence of the crystalline hydroxyapatite $\text{Ca}_{10}(\text{PO}_4)_6(\text{OH})_2$ phase (JCPDS 01-086-074) and no other crystalline phases could be detected in the samples.

3.2.3. Laser Raman spectroscopy

Raman scattering spectra of as-prepared hydroxyapatite Hap and HapNa in the range from 200 cm^{-1} to 1200 cm^{-1} are represented in figure 3.6. The spectra obtained reveal the characteristics bands of hexagonal hydroxyapatite, being in perfect agreement with results reported previously by some authors [15–17].

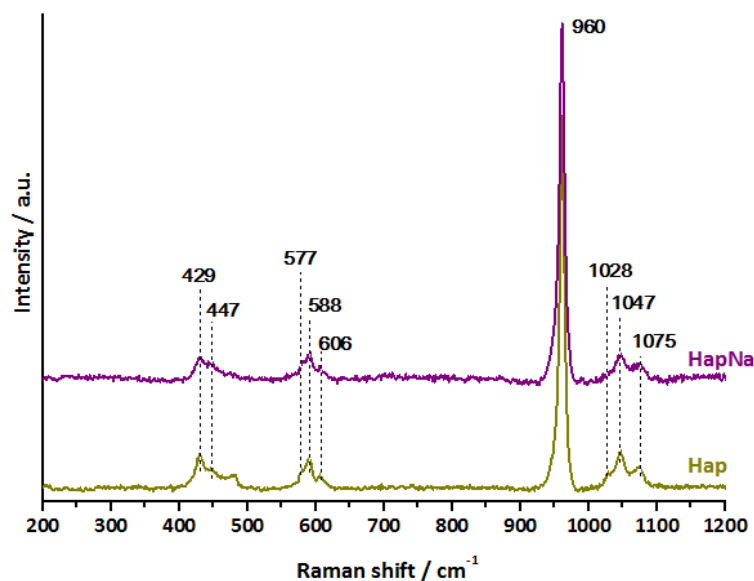


Figure 3.6. Raman spectra of the synthesized hydroxyapatites

All the peaks are caused by the phosphate (P–O) vibration (stretching and bending) modes. The 1076 cm^{-1} , 1047 cm^{-1} and 1028 cm^{-1} bands arise from $\nu_3\text{ PO}_4$, the very strong 960 cm^{-1} band arises from $\nu_1\text{ PO}_4$, the 606 cm^{-1} , 588 cm^{-1} , and 577 cm^{-1} bands arise from $\nu_4\text{ PO}_4$, and the 447 cm^{-1} and 421 cm^{-1} bands arise from $\nu_2\text{ PO}_4$. No difference between Hap and HapNa are observed by Raman spectroscopy.

3.2.4. Scanning electron microscopy (SEM)

In order to investigate the morphology of the three different types of supports used, SEM photographs were taken for the samples $\text{Al}_2\text{O}_3\text{-3}$, Hap and $\text{SiO}_2\text{-1}$ and the obtained images are showed in figure 3.7. Agglomerates with irregular shape were observed for alumina $\text{Al}_2\text{O}_3\text{-3}$, while flat needle shaped or rodlike clusters were observed for hydroxyapatite Hap. On the other hand, for silica solid $\text{SiO}_2\text{-1}$, spherically shaped grains were observed.

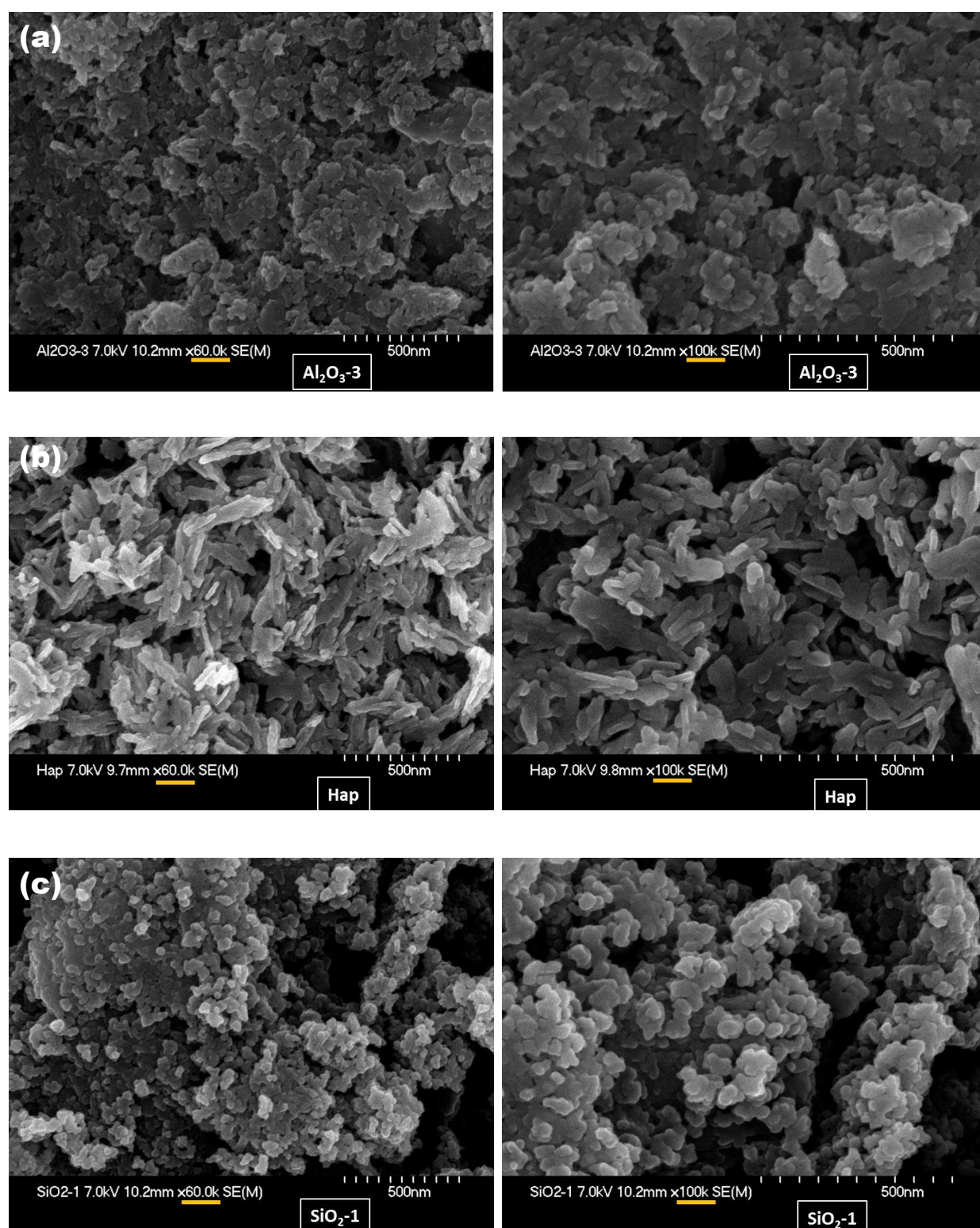


Figure 3.7. SEM photographs of (a) $\text{Al}_2\text{O}_3\text{-3}$, (b) Hap and (c) $\text{SiO}_2\text{-1}$.

3.2.5. Acid-base properties of solids

The role of the acidic-basic properties in the catalytic performance of supported catalysts has been mentioned in chapter 1, literature review. Therefore, acid-base properties of solids were determined by means of two different techniques:

- Temperature programmed desorption of ammonia (NH_3 -TPD) and carbon dioxide (CO_2 -TPD) for the determination of the number of acid and basic sites respectively.
- Catalytic decomposition of isopropanol for the acid-base behavior of solids.

3.2.5.1. Temperature programmed desorption of ammonia and carbon dioxide

NH_3 -TPD

NH_3 -TPD curves of the commercial aluminas and silicas as well as those for the synthesized hydroxyapatite solids are displayed in figure 3.8. This technique allows to estimate the total quantity of acid sites and also the relative strength of these sites since the strength of the acid sites is directly related to the desorption temperature of ammonia.

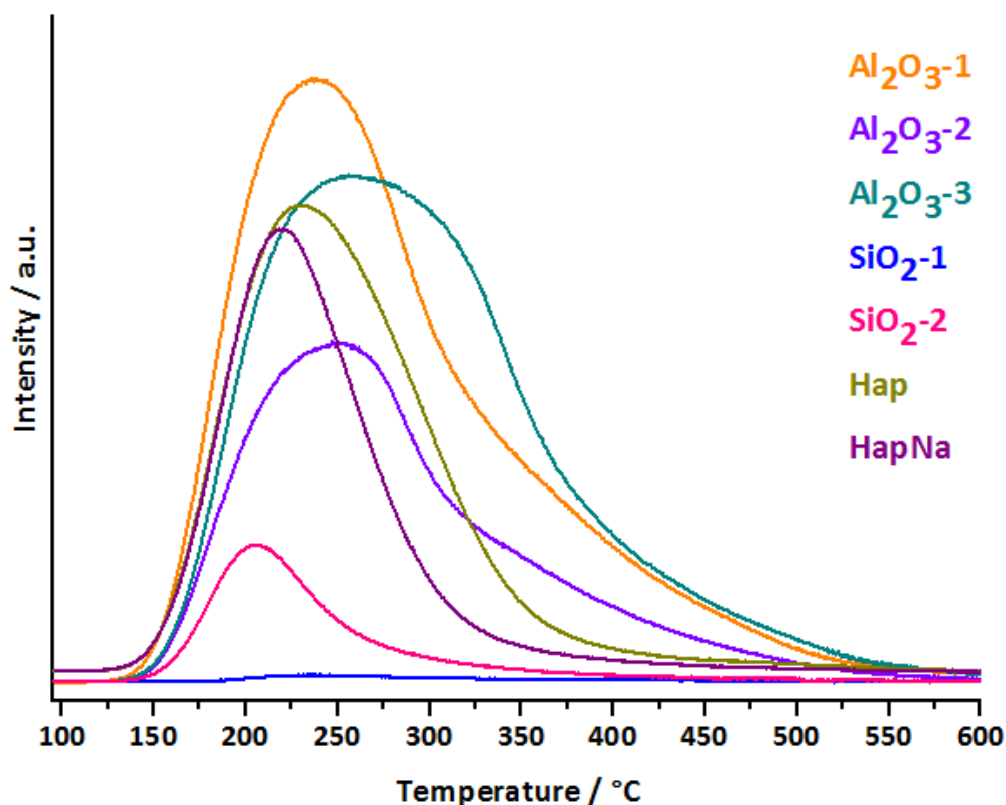


Figure 3.8. NH_3 -TPD curves of the supports

Starting with alumina, the peaks corresponding to these solids are broader, having a larger full width at half maximum (FWHM), than those of the other supports. In fact, for alumina supports, the desorption of ammonia is extended to 500 °C approximately, putting in evidence the presence of stronger acid sites, corresponding to higher desorption temperatures, compared to the other samples. Among the three aluminas, Al₂O₃-3 exhibited the maximal temperature of ammonia desorption (see table 3.2) followed by Al₂O₃-2 and finally Al₂O₃-1. The two hydroxyapatites Hap and HapNa displayed sharper peaks than alumina with maximum desorption at 231,4 and 219,5 °C respectively. The desorption temperature over these two samples are extended up to 400 °C for Hap and 300 °C for HapNa which means that acid sites of high strength are also presented in hydroxyapatite solids. Nevertheless, the presence of sodium in HapNa decreases the quantity of acid sites, particularly those with a higher strength. A different behavior is observed for silica samples which displayed peaks considerably less intense but also less wide than alumina and hydroxyapatite, being in agreement with the literature data since silica is well known for having very low density of acid sites [18], [19].

The number of acid sites was calculated by integrating the NH₃-TPD profiles and the values of the amount of ammonia desorbed expressed in μmol.g⁻¹ and μmol.m⁻² are grouped in Table 3.2.

Table 3.2. Amount of acid sites determined by NH₃-TPD

Solid	Maximal temperature of NH ₃ desorption / °C	Acid sites / μmol.g ⁻¹	Specific acidity / μmol.m ⁻²
Al ₂ O ₃ -1	237,5	343,9	1,41
Al ₂ O ₃ -2	249,3	203,9	1,13
Al ₂ O ₃ -3	257,9	352,0	1,26
SiO ₂ -1	229,5	22,4	0,11
SiO ₂ -2	204,9	75,4	0,53
Hap	231,4	248,6	2,42
HapNa	219,5	190,8	1,72

Among the studied materials the highest ammonia desorption expressed as $\mu\text{mol.g}^{-1}$ was measured for the three aluminas, somewhat lower quantity of NH_3 desorbed was obtained for hydroxyapatites Hap and HapNa and silicas SiO_2 -1 and SiO_2 -2. Significant differences in the concentrations of desorbed NH_3 related to the surface area of the samples ($\mu\text{mol.m}^{-2}$) were observed. In this regard, hydroxyapatites revealed the highest specific acidity followed by aluminas which showed also a considerable specific acidity while for silica samples acidity was significantly lower.

CO₂-TPD

The CO_2 -TPD profiles of aluminas, silicas and hydroxyapatites are comparatively shown in figure 3.9.

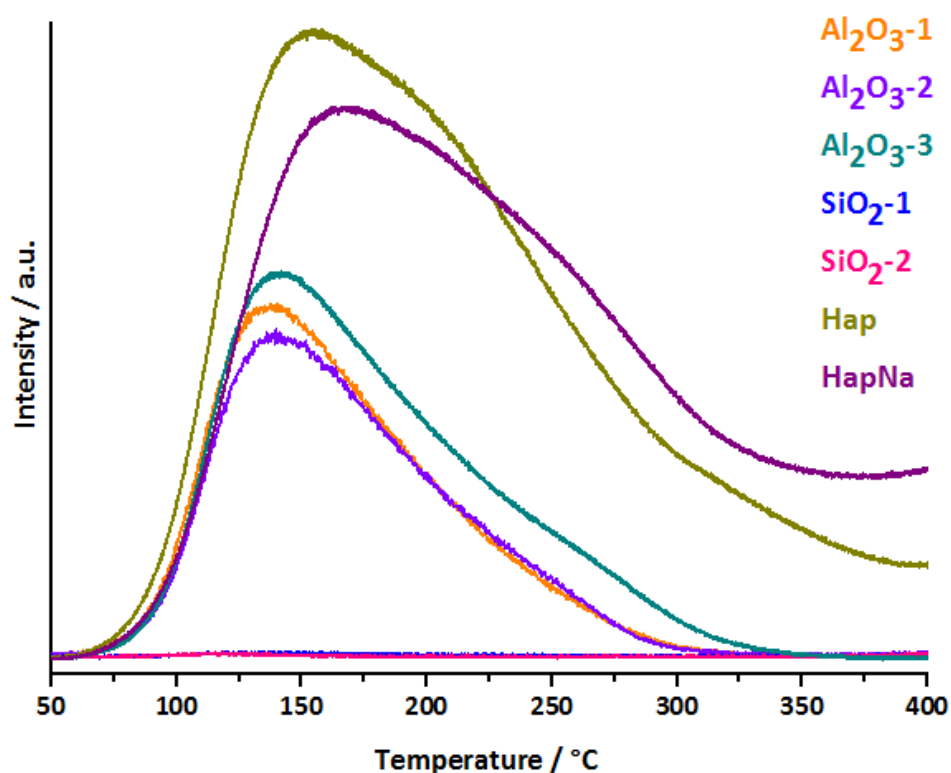


Figure 3.9. CO_2 -TPD curves of the supports

Three completely different behaviors were observed depending of the nature of the solid analyzed. Silica samples exhibited an almost nonexistent basicity. As discussed in NH_3 -TPD section, this behavior is not unexpected since silica samples are well-known for having a

weak acid-base character. Alumina solids exposed some basic character with a large desorption peak suggesting the presence of basic sites with different strengths. A first peak is clearly attained at about 140 °C (See table 3.3) which seems to be related to the presence of weak basic sites. Basic sites with more strength are also suggested by the presence of a shoulder nearby to 250-275 °C. Hydroxyapatite solids revealed basic sites with a higher strength than alumina; the main desorption peak appears at a temperature at least 10 °C higher than alumina and this wider peak is extended to about 400 °C, suggesting the presence of basic sites with at least three different strength. The main contribution in both Hap and HapNa which maximum is observed near to 160 °C could be attributed to the presence of basic sites with a weak strength. A second contribution at 240 ± 10 °C related the existence of basic sites with medium strength is also observed. A last peak due to the presence of strong basic sites is detected at around 325 °C.

The amount of basic sites was determined and the values obtained are displayed in table 3.3. The number of basic sites increased from silica which exposed no basicity, to alumina with an amount of basic sites between 5 to $10 \mu\text{mol.g}^{-1}$ and finally hydroxyapatites for which the amount of basic sites arises $21 \mu\text{mol.g}^{-1}$. Same trend was observed when talking about specific basicity; specific basicity of $0,026 \mu\text{mol.m}^{-2}$ was observed for the more basic alumina (Al_2O_3 -3) and both hydroxyapatites showed at least seven times this quantity of basic sites per m^2 .

Table 3.3. Amount of basic sites determined by CO_2 -TPD

Solid	Maximal temperature of CO_2 desorption / °C	Basic sites / $\mu\text{mol.g}^{-1}$	Specific basicity / $\mu\text{mol.m}^{-2}$
Al_2O_3 -1	138	5,0	0,021
Al_2O_3 -2	138	4,8	0,026
Al_2O_3 -3	142	6,1	0,022
SiO_2 -1	---	0,1	0,000
SiO_2 -2	---	0,0	0,000
Hap	154	22,7	0,221
HapNa	165	21,4	0,193

3.2.5.2. Acid-base behavior determined by catalytic decomposition of isopropanol

The isopropanol decomposition is a test reaction for the characterization of acidic (Brønsted or Lewis) and/or basic properties of the solids. The conversion of isopropanol is much higher in the presence of acidic centres on the solid surface than that noted on basic samples [20]. Dehydration of alcohol to propene requires acidic centres (Lewis or Brønsted) while dehydration of di-isopropyl ether (DPE) requires both acidic centres (Lewis or Brønsted) and basic centers [21]. Meanwhile, the dehydrogenation to acetone occurs on basic sites. Nevertheless, some authors have stated that acetone formation takes place on redox centres [22].

Figure 3.10 exhibits the reaction temperature and product distribution of the reaction of 2-propanol at a conversion of 12 ± 2 % for the solids $\text{Al}_2\text{O}_3\text{-3}$, $\text{SiO}_2\text{-1}$ and Hap.

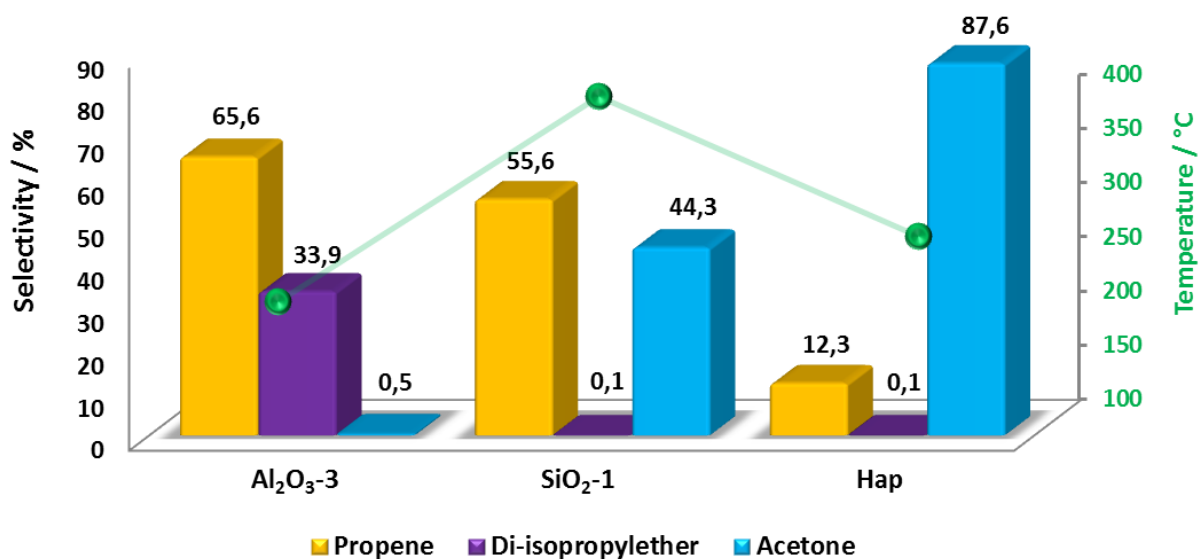


Figure 3.10. Product distribution of isopropanol decomposition at iso-conversion

For a conversion of 12 ± 2 %, the reaction temperature is 190 °C, 380 °C and 250 °C for $\text{Al}_2\text{O}_3\text{-3}$, $\text{SiO}_2\text{-1}$ and Hap respectively. Alumina, silica and hydroxyapatite are active for the conversion of isopropanol into propene and acetone and only alumina converted also isopropanol into di-isopropyl ether. Silica showed around 50/50 % of selectivity in propene

and acetone; however, this is a solid that cannot really be considered as acid or basic since when compared with alumina or hydroxyapatite at a same reaction temperature, this sample exposed a very low conversion. Alumina sample exhibits the formation of dehydration products propene and di-isopropyl ether, while only 0,5% of acetone is observed. As has been stated, alumina is a solid with amphoteric properties having acid/base sites of balanced strength, thus the presence of acetone in a greater degree was expected since the existence of basic sites in alumina should lead to the formation of this product. This result suggests two possibilities: (i) The basic sites present in the surface of alumina take part in the formation of di-isopropyl ether bearing in mind the mechanism exposed by Gervasini et al. [21] shows in figure 3.11. Accordingly, the conversion of isopropanol to di-isopropyl ether requires the presence in the solid surface of Brønsted acid sites and Lewis acid sites and basic sites (pairs Lewis acid-base) of strong and/or medium strength as the amphoteric alumina. (ii) The basic sites present in the alumina are not strong enough to produce acetone. Nevertheless, the trend of selectivities observed suggests that the acid character of alumina leads to propene as major product.

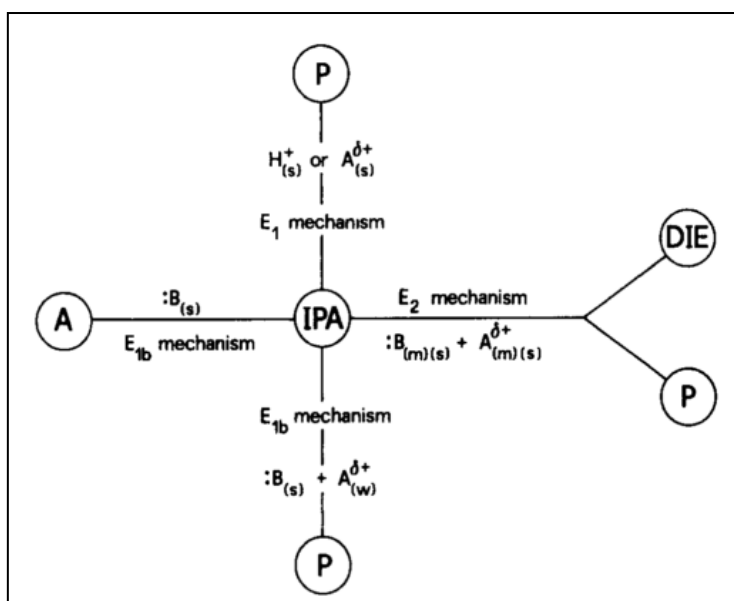


Figure 3.11. Reaction mechanisms of isopropanol decomposition on acid and basic solids leading to dehydration products: di-isopropyl ether (DIE), and propene (P), and to dehydrogenation product: acetone (A). (H^+ : Brønsted acid site; $A^{\delta+}$: Lewis acid site; B: basic site; m, s, w indicate medium, strong, and weak sites)[21]

Hydroxyapatite shows a different product distribution conformed by 88% of acetone and the

remaining 12% was attributed to propene, putting in evidence the acid-base properties of this solid. It is though that Lewis and Brønsted acidity of hydroxyapatite is related to the presence of HPO_4^{2-} ions [14] while the strong basicity characterizing these compounds is given by the presence of Ca^{2+} ions and OH groups in the structure of Hap [23].

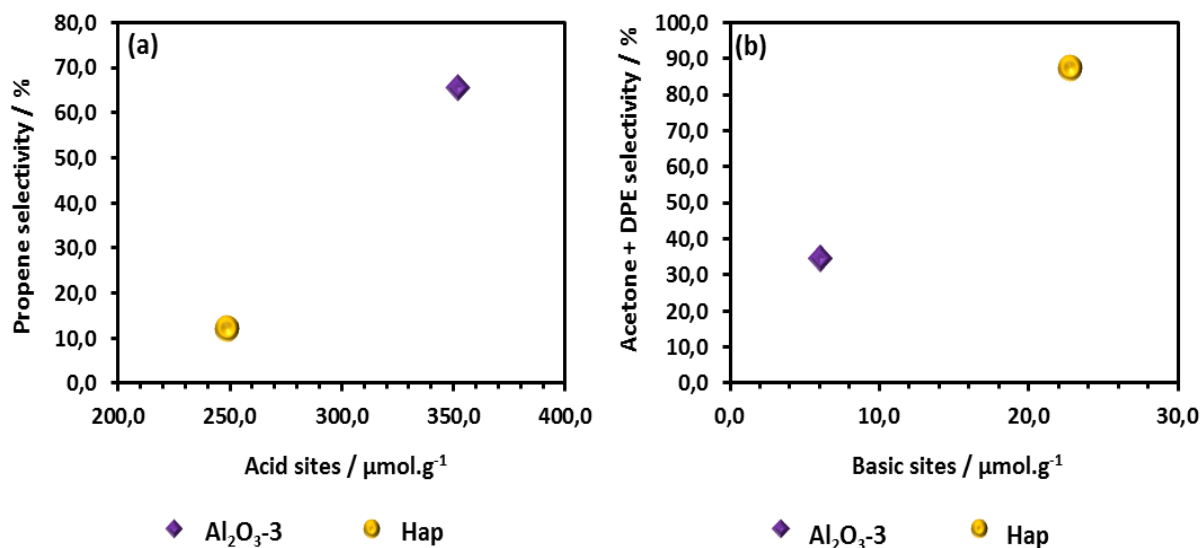


Figure 3.12. Correlation between acid-base character of solids determined by temperature programmed desorption and isopropanol test. (a) Selectivity of propene as a function of acid sites ($\mu\text{mol.g}^{-1}$) and (b) Selectivity of acetone+DPE as a function of basic sites ($\mu\text{mol.g}^{-1}$)

In order to compare the acid-base properties of solids, plots of (a) propene selectivity (determined by isopropanol test) as a function of acid sites (determined by NH_3 -TPD) and (b) acetone+DPE selectivity (determined by isopropanol test) as a function of basic sites (determined by CO_2 -TPD) are shown in figure 3.12. Only alumina and hydroxyapatite which exhibited both acid and basic sites by both techniques of characterization were taken into account for this comparison. The plots suggest that the two solids follow the same tendency regarding their acid-base properties either by TPD characterization or by isopropanol test. Acid properties are more important in alumina solid but some basic character was also observed meanwhile hydroxyapatite exposed the opposite behavior, a strong basic character and a weak acidic character.

3.3. CONCLUSIONS OF SECTION 3.1 AND 3.2

Ammonium tetrathiomolybdate (ATTM) and ammonium tetrathiotungstate (ATW) were prepared without contamination of neighboring oxothio ions as demonstrated by UV-Vis spectroscopy, Raman spectroscopy and X-Ray Diffraction. The subsequent transformation of ammonium tetrathiomolybdate and ammonium tetrathiotungstate into potassium tetrathiomolybdate (K_2MoS_4) and potassium tetrathiotungstate (K_2WS_4) respectively by ion exchange of ammonium ions by potassium ions was achieved and verified by Raman spectroscopy. Raman lines corresponding to Mo-O or W-O vibrations were not observed, in contrast, signals attributed to K_2MoS_4 and K_2WS_4 were detected.

Specific surface areas and morphologies of the three kinds of solids were determined. Acid-base properties were further determined by means of temperature programmed desorption of acid and basic molecules and by isopropanol test reaction. A good correlation was found between both techniques. Silica was found to be a solid with a very low density of acidic and basic sites. Alumina exhibited its amphoteric properties by the presence of acid and basic sites determined by NH_3 -TPD and CO_2 -TPD, while isopropanol was converted into propene and di-isopropyl ether, both of them produced over Brønsted acid sites and pairs of Lewis acid-basic sites. Hydroxyapatite was found to be a more basic solid but exposing also some acidic character.

3.4. CHARACTERIZATION OF Mo-BASED FRESH CATALYSTS

3.4.1. Characterization of oxidic reference catalysts

Reference catalysts 8.1% Mo/Al-3, 6.6% K/Al-3, 8.1% Mo+K/Al-3, 8.1% K_2MoO_4 /Al-3 and 8.1% Na_2MoO_4 /Al-3 where characterized by means of Laser Raman Spectroscopy and X-Ray Photoelectron Spectroscopy. The results are shown below.

3.4.1.1. Laser Raman spectroscopy

Raman spectra of reference samples are displayed in figure 3.13. Figure 3.14(a) displays the Raman spectra of 8.1% Mo/Al-3, 6.6% K/Al-3 and 8.1% Mo+K/Al-3 catalysts and figure 3.14(b) displays the Raman spectra of 8.1% K_2MoO_4 /Al-3 and 8.1% Na_2MoO_4 /Al-3 catalysts.

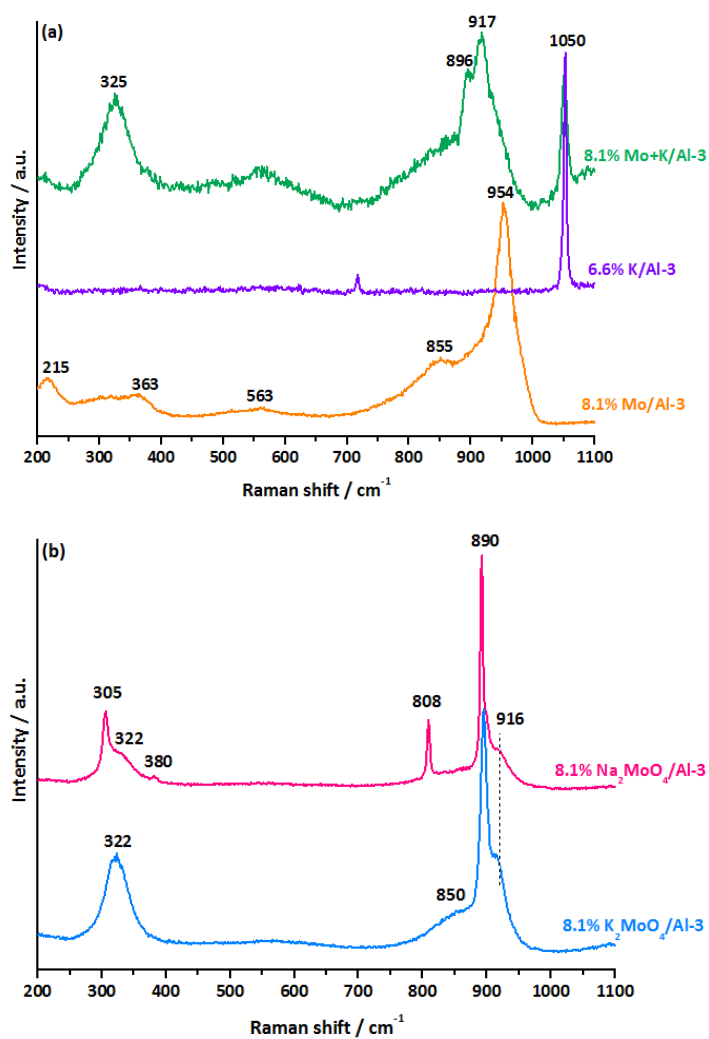


Figure 3.13. Raman spectra of reference catalysts

Figure 3.14(a) compares the Raman spectrum of and 8.1% Mo+K/Al-3 catalysts. In the Raman spectrum of 8.1% Mo/Al-3, five different broad lines are observed and these lines correspond to the presence of well dispersed $\text{AlMo}_6\text{O}_{24}\text{H}_6^{-3}$ species formed from the alumina support dissolution [24–26]. The very intense line at 954 cm^{-1} can be attributed to the symmetric stretching mode $\nu_s(\text{Mo}=\text{O}_t)$; a shoulder appearing around 855 cm^{-1} is attributed to the antisymmetric stretching mode $\nu_s(\text{Mo}=\text{O}_t)$; the line at 563 cm^{-1} can be attributed to symmetric Mo-O-Mo stretches as reported by Carrier et al. [24] or to the stretching mode $\nu(\text{Al-O})$ as reported by Le Bihan et al. [25]; the line at 363 cm^{-1} is due to the bending modes $\delta(\text{Mo}=\text{O}_t)$ and the line at 215 cm^{-1} is assigned to the deformation mode $\delta[\text{O}(\text{Mo})_2]$. The addition of potassium to the Mo based catalyst results in a complete evolution of the Raman spectrum as observed for the catalyst 8.1% Mo+K/Al-3. For this solid, four main lines are observed. The line at 1050 cm^{-1} belongs to the symmetric ν_1 mode of NO_3^- due to nitrate residues from KNO_3 precursor [27], as observed for the solid 6.6% K/Al-3. Lines at 917, 896 and 325 cm^{-1} suggest the presence of the monomolybdate species MoO_4^{2-} and correspond to MoO_4^{2-} with distorted tetrahedral symmetry and to the vibration mode of $\nu_s(\text{Mo}-\text{O})$ and $\delta(\text{Mo}-\text{O})$, respectively [28], [29].

Figure 3.13(b) shows the Raman spectrum of 8.1% $\text{K}_2\text{MoO}_4/\text{Al-3}$ and 8.1% $\text{Na}_2\text{MoO}_4/\text{Al-3}$ samples. 8.1% $\text{K}_2\text{MoO}_4/\text{Al-3}$ exhibits a sharp line at 890 cm^{-1} with shoulders at both sides placed at 850 and 916 cm^{-1} and a line at 322 cm^{-1} , all lines being characteristics of MoO_4^{2-} entities [28], [30–32]. 322 and 890 cm^{-1} lines are attributed to the vibration model of $\delta(\text{Mo}-\text{O})$ and $\nu_s(\text{Mo}-\text{O})$, respectively, the shoulder positioned at around 850 cm^{-1} can be representative to the not resolved lines at 822 and 852 cm^{-1} also characteristic of K_2MoO_4 . Finally, the shoulder at 916 cm^{-1} can be attributed to the Mo=O stretching mode of MoO_4^{2-} with distorted tetrahedral symmetry. 8.1% $\text{Na}_2\text{MoO}_4/\text{Al-3}$ catalysts exhibits lines at 890, 808, 380, 322 and 305 cm^{-1} attributed to the stretching modes of the M=O bond of the tetrahedral molybdate species due to the formation of Na_2MoO_4 [29], [33], [34]. Finally, a line at 916 cm^{-1} also presented on the sample 8.1% $\text{K}_2\text{MoO}_4/\text{Al-3}$ is identified. This line is attributed to the Mo=O stretching mode of MoO_4^{2-} with distorted tetrahedral symmetry.

Evident differences are observed between the catalyst in which Mo and K are coming from

different precursors and those in which Mo and K(Na) are part of the same precursor. In the first sample (8.1% Mo+K/Al-3), the line at 917 cm^{-1} is most intense, while for 8.1% $\text{K}(\text{Na})_2\text{MoO}_4/\text{Al-3}$ samples this line is less intense; besides, in these samples, the lines are narrow when compared with those observed in 8.1% Mo+K/Al-3 which exhibits wider lines, suggesting that Mo species are better dispersed in this catalyst and by contrast, over $\text{K}(\text{Na})_2\text{MoO}_4$ -based solids, this species seems to be in the form of big crystallites.

3.4.1.2. X-Ray Photoelectron Spectroscopy (XPS)

XPS analyses were carried out in order to obtain information about the distribution, oxidation state and dispersion of the different elements in the surface of catalysts. Figure 3.14 shows the spectra of the Mo 3d level of the reference catalysts.

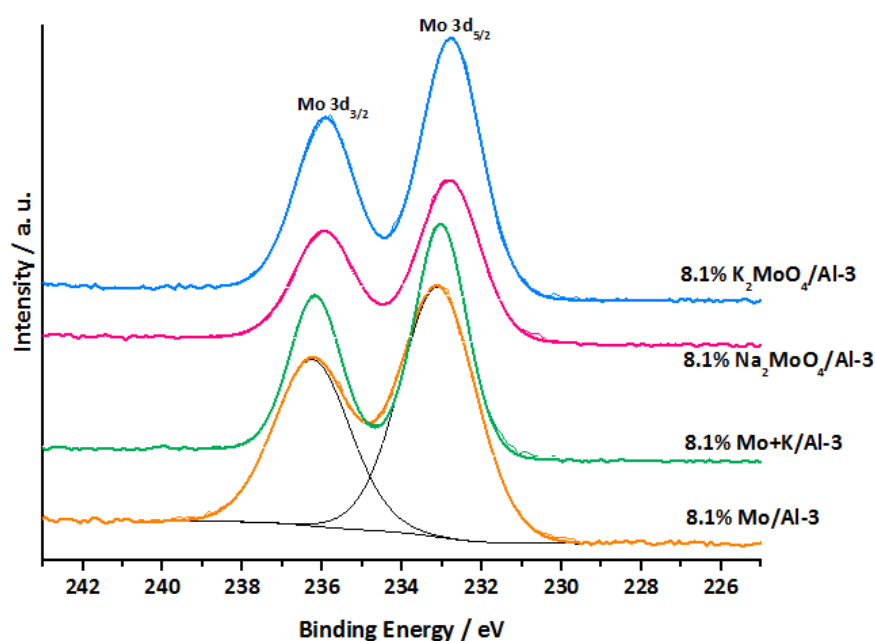


Figure 3.14. XPS spectra of Mo 3d level of reference catalysts

The spectrum of all the samples in the Mo 3d region shows the presence of two well resolved spectral lines at 232.9 ± 0.2 and 236.0 ± 0.2 eV assigned to the Mo $3d_{5/2}$ and Mo $3d_{3/2}$ spin-orbit components, respectively. These positions are characteristics of Mo^{6+} in oxidic environment [35], [36] which is totally expected due to the presence of $\text{AlMo}_6\text{O}_{24}\text{H}_6^{-3}$ species in Mo-containing catalysts and MoO_4^{2-} species in the K(Na) and Mo-containing catalysts.

Table 3.4. Comparison of bulk At.% and XPS At.%

CATALYSTS	%At. Mo	
	XPS	Bulk
8.1% Mo/Al-3	2,1	1,8
8.1% Mo+K/Al-3	1,7	1,9
8.1% Na ₂ MoO ₄ /Al-3	1,1	1,8
8.1% K ₂ MoO ₄ /Al-3	1,3	1,9

XPS analyses also allow to estimate the atomic percentage (At.%) of element. The At.% determined by XPS for Mo as well as the bulk (theoretical) atomic percentage are exposed in table 3.4. XPS surface analysis is in good agreement with the bulk analysis for samples 8.1% Mo/Al-3 and 8.1% Mo+K/Al-3. For 8.1% K₂MoO₄/Al-3 and 8.1% Na₂MoO₄/Al-3 catalysts, bulk at.% Mo is higher than the at.% Mo obtained from XPS. This result should indicate that Mo species are not sufficiently exposed at the surface to be detected which can be due to a bad dispersion of the Mo precursor over the support and to the presence of big particles of Mo.

Thus, in order to investigate the dispersion degree of molybdenum on the surface of alumina, we studied the variation of $(I_{\text{Mo}}/I_{\text{Al}})_{\text{XPS}}$ intensity ratio as a function of the bulk Mo/Al atomic ratio $(n_{\text{Mo}}/n_{\text{Al}})_{\text{Bulk}}$. These results were compared to theoretical values calculated according to the monolayer model of Kerkhof and Moulijn as shown in figure 3.15. [37].

For 8.1% Mo/Al-3, the experimental intensity ratio $I_{\text{Mo}}/I_{\text{Al}}$ measured is slightly higher than that predicted by the KM model and for the sample 8.1% Mo+K/Al-3 no variation was found with respect to those calculated by the KM model thus confirming that both samples adopt a monolayer dispersion and are homogeneously distributed throughout the surface of the support. For 8.1% K₂MoO₄/Al-3 and 8.1% Na₂MoO₄/Al-3 catalysts a deviation from the Kerkhof–Moulijn model was observed, a result that could be indicative of a multilayer deposition, suggesting the agglomeration of the impregnated species in the surface of support. Thus, it is possible to assume that when Mo and K are impregnated over alumina separately, a good dispersion is achieved; by contrast, when Mo and K(Na) come from the same precursor, even when the Mo loading is the same, the agglomeration of supported species is observed. These observations are in agreement with Raman characterization

where 8.1% Mo/Al-3 and 8.1% Mo+K/Al-3 catalysts exposed wide lines, characteristic of well dispersed Mo species, whereas for 8.1% K₂MoO₄/Al-3 and 8.1% Na₂MoO₄/Al-3 catalysts, narrower lines were observed.

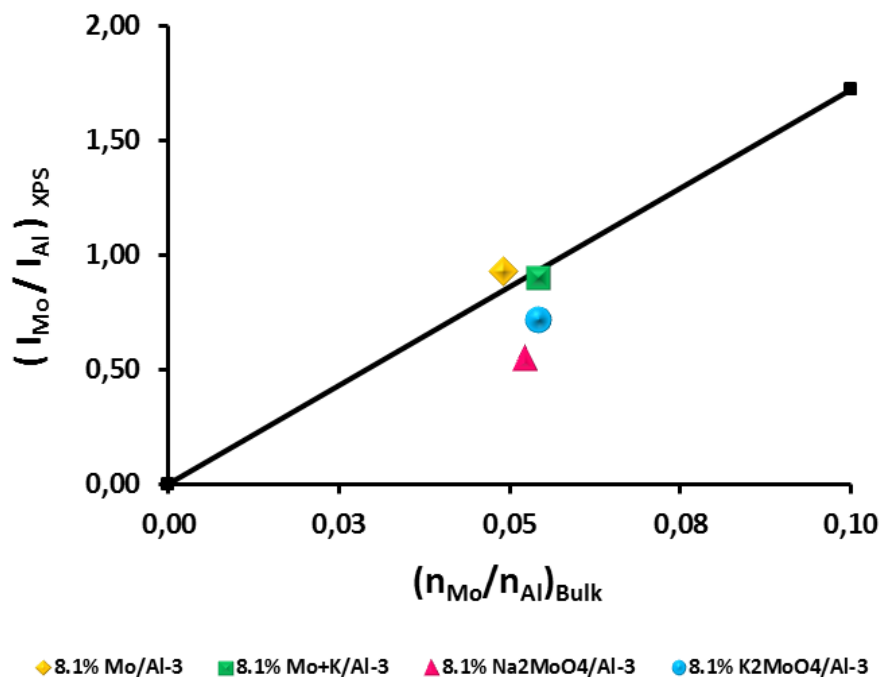


Figure 3.15. $(I_{\text{Mo}}/I_{\text{Al}})_{\text{XPS}}$ intensity ratio as a function of Mo/Al bulk atomic ratio for reference catalysts. The solid line corresponds to theoretical values calculated according to the Kerkhof–Moulijn model.

3.4.2. Characterization of K₂MoO₄-based catalysts

In this section are exposed the characterization results of seven catalysts prepared by incorporation of K₂MoO₄ over the carriers alumina (Al-1, Al-2 and Al-3), silica (Si-1 and Si-2) and hydroxyapatite (Hap and HapNa) with Mo loading varying from 13.5% and 23.5% depending on the pore volume of the support.

3.4.2.1. Bulk composition and specific surface area

Mo and K bulk compositions of solids determined by ICP (see table 3.5) are closer to the nominal composition. No more than 10% of difference was observed between the real and

the nominal values. Only the sample 18.0% K₂MoO₄/Si-1 exhibited an ICP composition of Mo higher than the nominal value. When determined the K/Mo atomic ratio by ICP, all the samples showed a K/Mo atomic ratio equal to 2, which correspond to the ratio K/Mo of the precursor K₂MoO₄, with the only exception of the 18.0% K₂MoO₄/Si-1 catalyst indicating that possibly, an error in the analysis of Mo composition could be made.

Table 3.5. Bulk composition and specific surface area of K₂MoO₄-based solids

CATALYSTS	Theoretical wt.%		ICP wt.%		K/Mo atomic ratio	Specific surface area (m ² .g ⁻¹)	Loss in specific surface area (%)
	Mo	K	Mo	K			
13.5% K ₂ MoO ₄ /Al-1	13,5	11,0	12,9	10,5	2,0	93	62
17.6% K ₂ MoO ₄ /Al-2	17,6	14,4	17,4	14,0	2,0	47	74
17.9% K ₂ MoO ₄ /Al-3	17,9	14,6	16,3	13,3	2,0	80	71
18.0% K ₂ MoO ₄ /Si-1	18,0	14,7	20,2	14,0	1,7	20	90
23.5% K ₂ MoO ₄ /Si-2	23,5	19,1	22,8	18,3	2,0	11	92
20.4% K ₂ MoO ₄ /Hap	20,4	16,7	18,9	15,2	2,0	29	71
22.1% K ₂ MoO ₄ /HapNa	22,1	18,0	20,3	16,1	1,9	28	75

Specific surface area of solid are also grouped in table 3.5. A large decrease in the initial area of support is observed. The loss in specific surface area (%) estimated was plotted against the wt.% Mo and displayed in figure 3.16. It is clearly evidenced that higher the wt.% Mo, higher the loss in specific surface area which can be due to the bad dispersion and formation of agglomerates over the surface of supports as the concentration of the impregnation solution is greater, leading to the blockage of support pores.

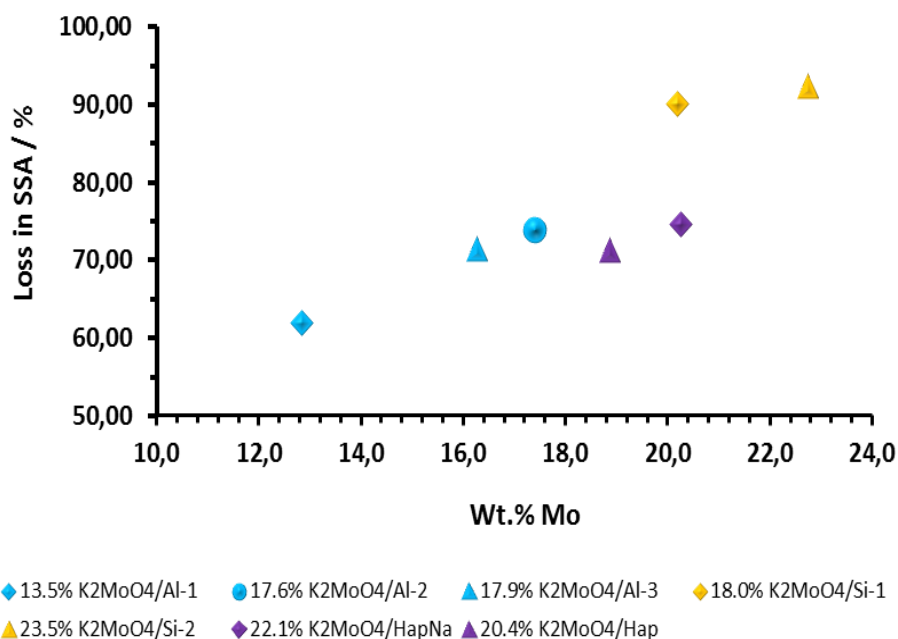


Figure 3.16. Loss in specific surface area as a function of the wt.%Mo.

3.4.2.2. Laser Raman Spectroscopy

Figure 3.17 shows the Raman scattering spectrum of K₂MoO₄-containing catalysts. Spectrum of all the samples exhibited lines at 893, 851, 821 and 317 cm⁻¹ characteristic of K₂MoO₄ [28], [31]. The line at 893 cm⁻¹ is attributed to symmetric vibration of terminal Mo=O bonds, the lines at 851 and 821 cm⁻¹ are assigned to asymmetric and symmetric stretches of the bridging Mo–O–Mo bond and finally the line at 317 cm⁻¹ is associated with the vibration model of $\delta(\text{Mo–O})$. Additionally, over the catalysts 20.4% K₂MoO₄/Hap and 22.1% K₂MoO₄/HapNa a line at 961 cm⁻¹ was observed. This line is characteristic of hydroxyapatite and corresponds to the vibrational mode $\nu_1(\text{PO}_4)$. Raman lines are very well defined for solids supported on hydroxyapatites as shown by the doublet at 821 cm⁻¹ and 851 cm⁻¹ which appears as a broad line in alumina and silica-supported solids. It can be supposed that bigger crystallites are formed on Hap in agreement with the Mo loading on these samples and to the lower specific surface area of hydroxyapatites compared with aluminas and silicas.

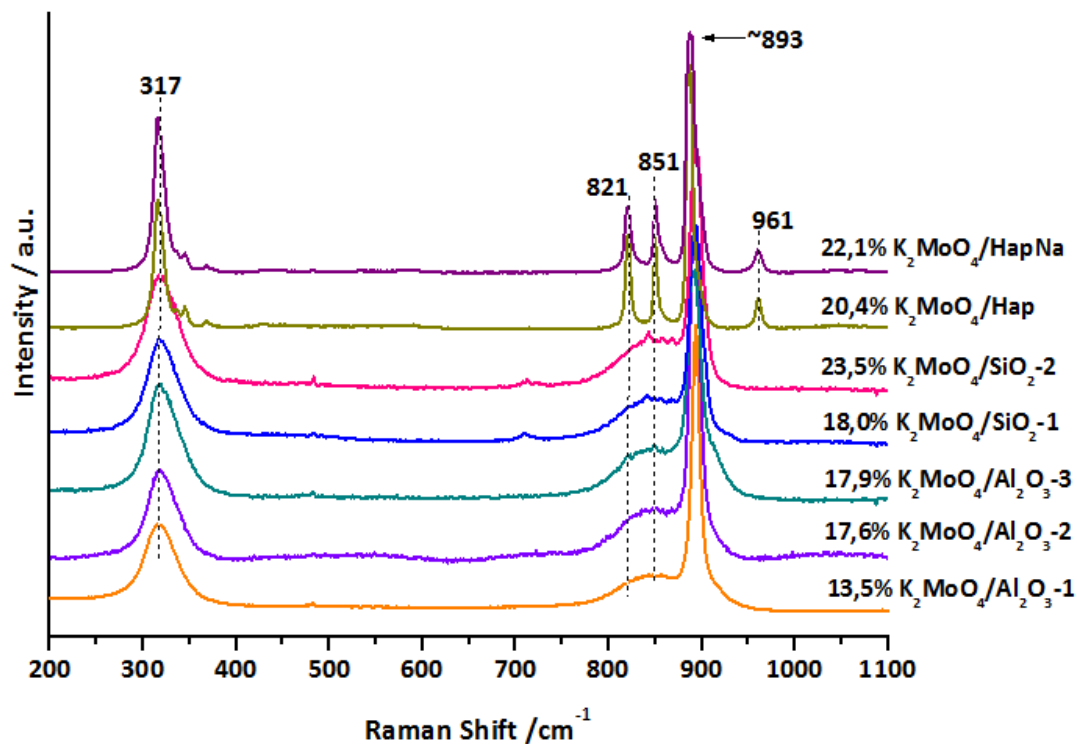


Figure 3.17. Raman spectra of K_2MoO_4 based catalysts

3.4.2.3. Wide angle powder XRD

The X-ray diffraction patterns for the K_2MoO_4 -based catalysts in fresh state are showed in figure 3.18. The patter for Al_2O_3 (a), SiO_2 (b) and Hap(c) supports are also included for comparison. In addition to supports diffraction peaks, diffraction peaks at $2\theta = 13.1, 15.6, 16.7, 18.9, 22.7, 24.0, 26.3, 28.2, 29.4, 30.7, 39.9, 44.2, 48.1, 48.9, 50.8$ and 54.1° are observed and are characteristic of K_2MoO_4 phase (JCPDS 00-029-1021). K_2MoO_4 diffraction lines are sharp, indicating the good crystallinity of this phase and a high crystallite size. For Hap-based solids and for the high-loaded alumina and silica solids, no other crystalline phase is observed, in agreement with Raman results. For the low-loaded alumina and silica samples (13.5% K_2MoO_4/Al -1 and 18.0% K_2MoO_4/Si -1) the presence of diffraction peaks corresponding to K_2MoO_4 , is less evident, almost imperceptible, which can be related to a better dispersion of this entity on the support surface.

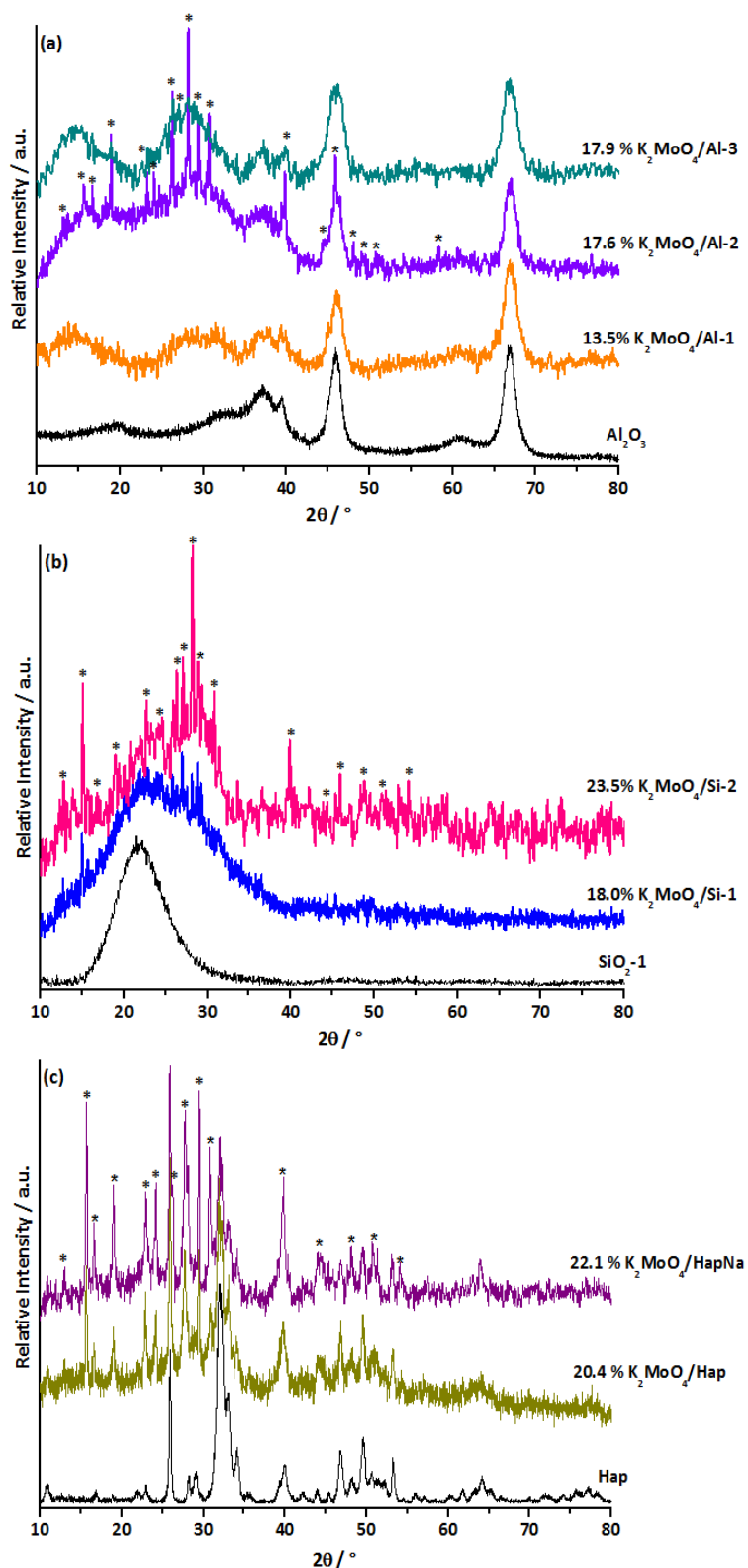


Figure 3.18. XRD patterns of (a) alumina supported K_2MoO_4 based catalysts, (b) silica supported K_2MoO_4 based catalysts and (c) hydroxyapatite supported K_2MoO_4 based catalysts. K_2MoO_4 phase is represented by *.

Table 3.6 shows the average crystallite size of the high-loaded samples estimated from the Scherrer equation. For catalysts 13,5% K_2MoO_4/Al -1, 17,9% K_2MoO_4/Al -3 and 18,0% K_2MoO_4/Si -2, the estimation was impossible since no diffraction peaks were observed. Among the analyzed samples, all of them exhibit crystallite size in the order of 40-50 nm and generally, it can be observed an increase in the crystallite size as a function of the Mo load.

Table 3.6. Estimation of crystallite size of K_2MoO_4 -based solids

CATALYST	AVERAGE CRYSTALLITE SIZE (nm)
17,6% K_2MoO_4/Al -2	44,7
23,5% K_2MoO_4/Si -2	46,2
20,4% K_2MoO_4/Hap	40,9
22,1% $K_2MoO_4/HapNa$	45,6

3.4.2.4. X-ray photoelectron spectroscopy (XPS)

The Mo 3d spectra for the K_2MoO_4 -based catalysts are presented in figure 3.19. The shape and positions (see table 3.7) of the Mo 3d photopeaks, correspond exclusively to Mo^{6+} in an oxidic surrounding, meaning that this is the only Mo species presented in the fresh catalysts.

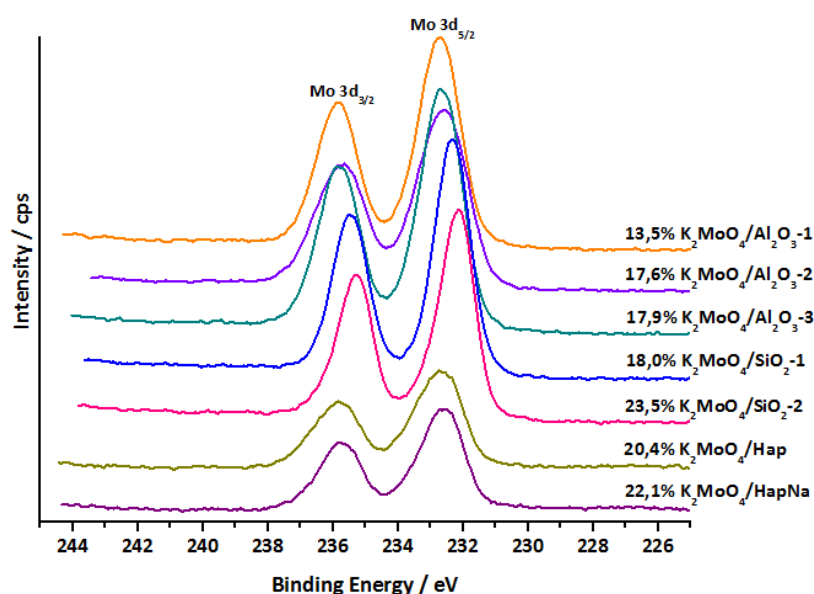


Figure 3.19. XPS spectra of Mo 3d level of K_2MoO_4 -based catalysts

Table 3.7. Binding energy of Mo 3d level and At.% Mo of K₂MoO₄-based solids

CATALYSTS	Binding Energy (eV)		At.% Mo		%Mo detected by XPS
	Mo 3d _{5/2}	Mo 3d _{3/2}	XPS	Bulk	
13.5% K ₂ MoO ₄ /Al-1	232,7	235,9	1,9	3,0	64
17.6% K ₂ MoO ₄ /Al-2	232,6	235,7	1,9	4,4	43
17.9% K ₂ MoO ₄ /Al-3	232,6	235,8	2,0	4,0	49
18.0% K ₂ MoO ₄ /Si-1	232,3	235,4	2,4	5,1	48
23.5% K ₂ MoO ₄ /Si-2	232,2	235,3	1,4	6,0	23
20.4% K ₂ MoO ₄ /Hap	232,7	235,9	0,9	5,3	18
22.1% K ₂ MoO ₄ /HapNa	232,6	235,8	0,8	5,7	14

Table 3.7 lists the atomic percentage (At.%) of Mo obtained by means of surface analysis (XPS) and ICP analysis. It is noticeable that the At.% of Mo obtained by surface analysis are considerable lower than the obtained by ICP analysis. With the aim to determine the dispersion of the Mo species impregnated on the surface of supports, we calculated the % Mo detected by XPS (see table 3.7). The % Mo detected by XPS is a good indicator of the dispersion of Mo since it is considered that for a catalysts in which the Mo species are well dispersed, the At.% Mo determined by XPS and ICP analyses are really close, so the % Mo detected by XPS should be near to 100%. Thus, the % Mo detected by XPS is calculated as follow:

$$\%Mo_{\text{detected XPS}} = \left(\frac{\text{At. \%}Mo_{\text{XPS}}}{\text{At. \%}Mo_{\text{ICP}}} \right) \times 100$$

Hence, it is noticeable that the higher the Mo loading, the lower the % Mo detected by XPS. The samples 13.5% K₂MoO₄/Al-1, 17.9% K₂MoO₄/Al-3 and 18.0% K₂MoO₄/Si-1 exhibit the higher % Mo detected by XPS; these are also the samples in which only a low quantity of crystallized K₂MoO₄ phase is detected by XRD. Thus, the high crystallinity of K₂MoO₄ leading to a big K₂MoO₄ crystallites size is related to the low % Mo detected by XPS. These results put in evidence the intimate relation between Mo loading and crystallinity and dispersion of Mo entities. At the same time, the results obtained by XPS regarding the dispersion of Mo species are in well agreement with those discussed for XRD, Raman and SSA determination.

3.4.2.5. Scanning Electron Microscopy (SEM)

The SEM images of 17.9% K_2MoO_4 -/Al-3, 18.0% K_2MoO_4 -/Si-1 and 20.4% K_2MoO_4 -/Hap catalysts are displayed in figure 3.20. For comparison, the micrographs of supports before the impregnation of precursor are showed.

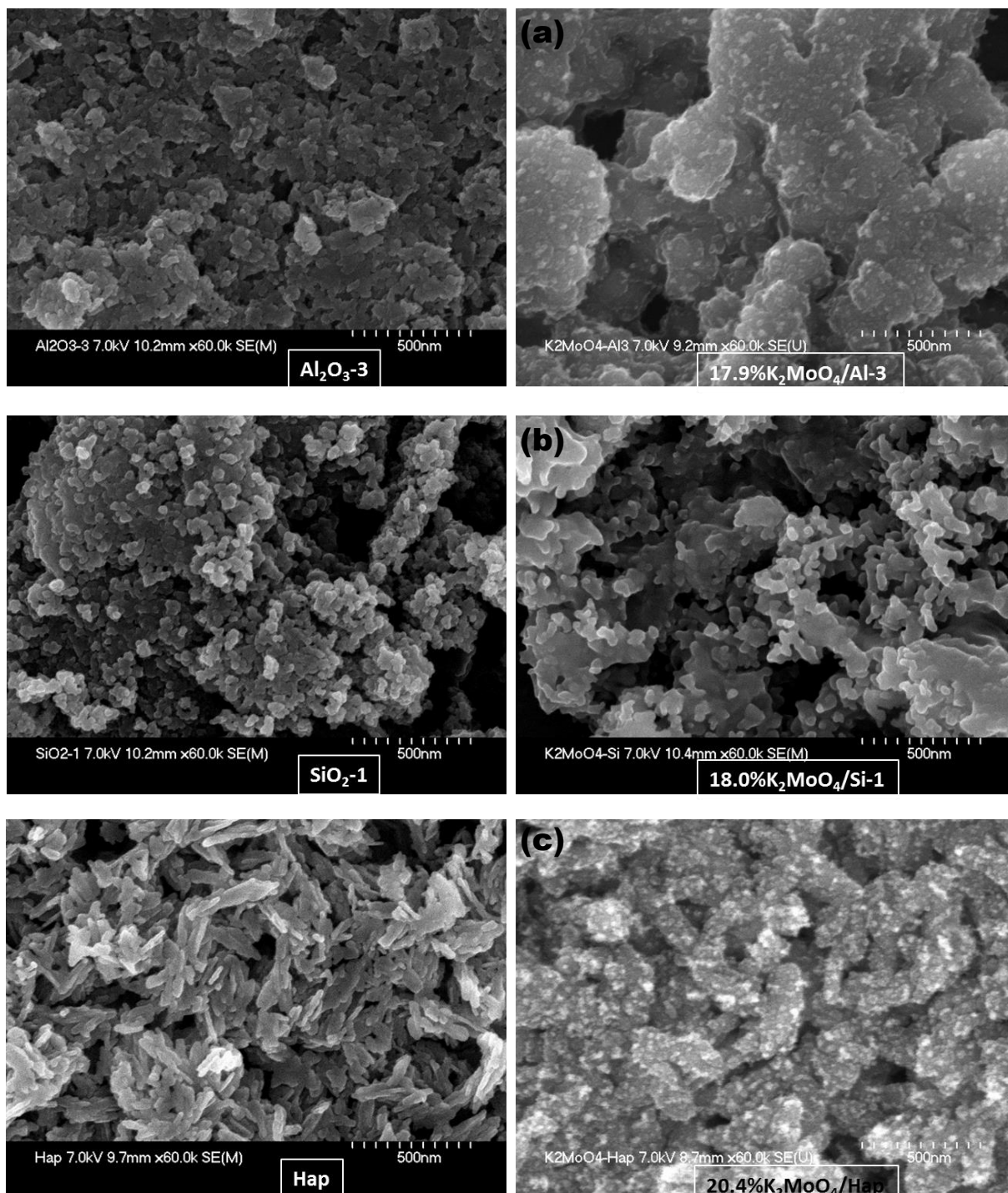


Figure 3.20. SEM images of (a) 17.9% K_2MoO_4 /Al-3, (b) 18.0% K_2MoO_4 /Si-1 and (c) 20.4% K_2MoO_4 /Hap catalysts. Figures on the left correspond to the supports before impregnation

The morphological differences among the support before and after impregnation of the precursors were evident. For the alumina-supported catalyst, the same shape of alumina support is conserved; however, after the impregnation of K_2MoO_4 , the presence of small white particles is detected. For the silica-supported catalyst, a different morphology is detected after deposition of the active component; the spherical particles observed on silica support disappeared and particles with a heterogeneous shape appeared. For Hap-supported-catalyst, the same behavior than for alumina catalyst is observed; the shape of the support is preserved with the difference that white particles are detected after impregnation of K_2MoO_4 . An estimation of the size of these white particles observed over the Al_2O_3 and Hap-supported catalysts was made. The average size of particles for the sample 17.9% $K_2MoO_4/Al-3$ is 28 nm, a lower value compared to the obtained in general for the higher loaded catalysts by XRD. This result explains very well the reason why weak diffraction peaks are observed for this solid. 20.4% K_2MoO_4/Hap catalyst exposes bigger particles in the order of 37 nm which matches very well with that detected by XRD (41 nm).

3.4.2.6. Electron probe microanalysis (EPMA)

Electron Probe Micro Analysis was used in order to evaluate the distribution of the elements Mo, K and Al(Si) in the catalysts in form of pellet (Al_2O_3-3) and granulates (SiO_2-1). The obtained micrographs are exposed in figure 3.21. The analysis was made over a sample supported on Al_2O_3 (17.9% $K_2MoO_4/Al-3$) and a sample supported on SiO_2 (18.0% $K_2MoO_4/Si-1$). It can be seen that metals (Mo and K) are uniformly distributed inside the alumina extrudates and silica spheres. The corresponding EDX profiles for both samples were also measured and are shown in figure 3.22. Same behavior is observed; metals are better distributed over alumina surface than on silica surface.

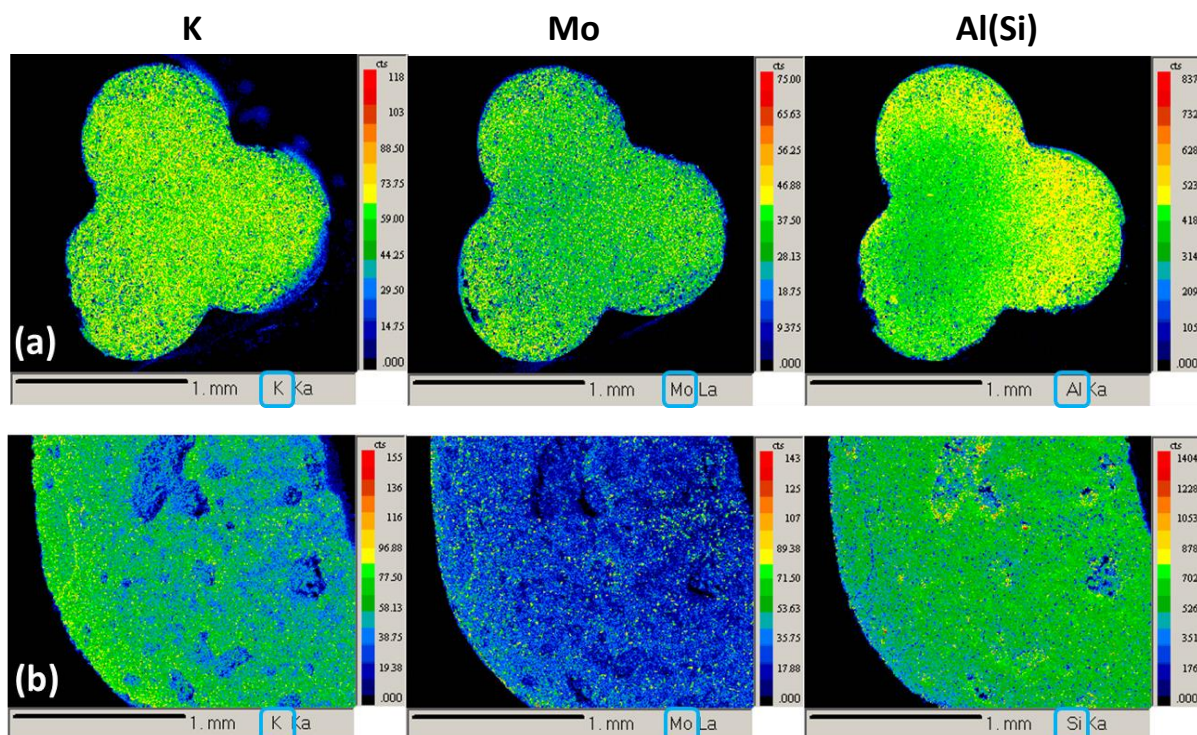


Figure 3.21. Cross section micrograph of (a) 17.9% $K_2MoO_4/Al-3$ and (b) 18.0% $K_2MoO_4/Si-1$ analyzed by EPMA

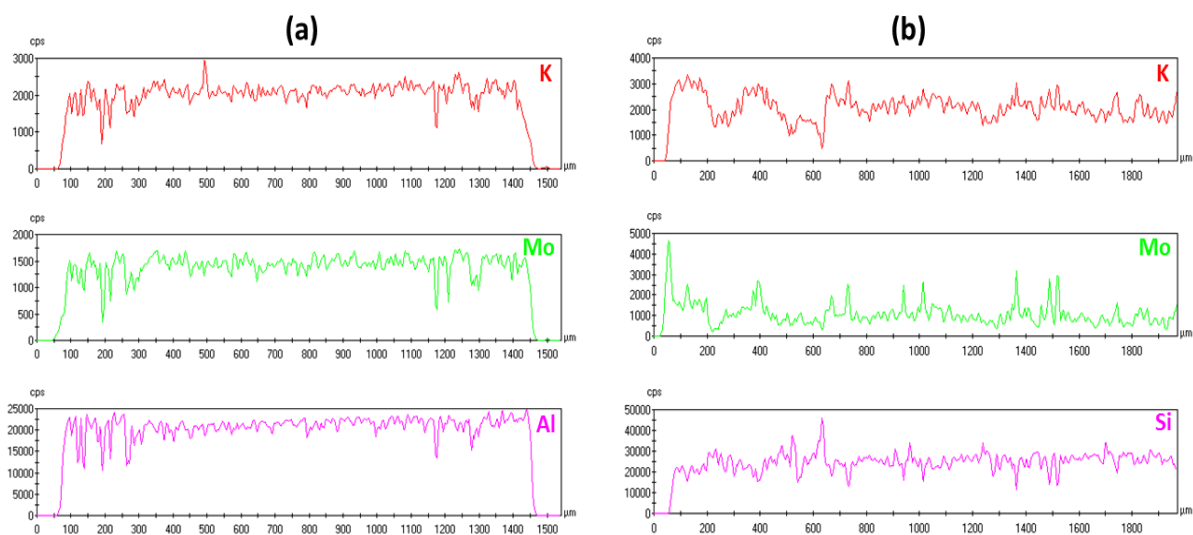


Figure 3.22. Metal-concentration profiles, derived from EDX measurements for (a) 17.9% $K_2MoO_4/Al-3$ and (b) 18.0% $K_2MoO_4/Si-1$

3.4.3. Characterization of K₂MoS₄-based catalysts

In this section, seven catalysts prepared by impregnation of K₂MoS₄ on Al₂O₃, SiO₂ and Hap are characterized. As a function of K₂MoS₄ solubility and pore volume of supports, the Mo loading in these catalysts varies between 5.8% and 12.1%.

3.4.3.1. Bulk composition and specific surface area

The Mo and K bulk compositions of K₂MoS₄-based solids determined by ICP are displayed in table 3.8. Differences among the nominal (exposed in the first column of the table) and real metal loading are between 10 and 20%. When determined the K/Mo atomic ratio by ICP, all the samples show a K/Mo atomic ratio equal or close to 2, which correspond to the ratio K/Mo of the precursor K₂MoS₄.

Table 3.8. Bulk composition and specific surface area of K₂MoS₄-based solids

CATALYSTS	Theoretical wt.%		ICP wt.%		K/Mo atomic ratio	Specific surface area (m ² .g ⁻¹)	Loss in specific surface area (%)
	Mo	K	Mo	K			
5.8% K ₂ MoS ₄ /Al-1	5,8	4,7	4,9	3,9	2,0	137	44
8.1% K ₂ MoS ₄ /Al-2	8,1	6,6	8,1	5,9	1,8	83	54
8.3% K ₂ MoS ₄ /Al-3	8,3	6,8	6,2	5,0	2,0	144	49
8.4% K ₂ MoS ₄ /Si-1	8,4	6,8	7,3	5,9	2,0	111	46
12.1% K ₂ MoS ₄ /Si-2	12,1	9,9	9,9	7,6	1,9	64	55
9.9% K ₂ MoS ₄ /Hap	9,9	8,1	8,2	6,7	2,0	55	46
11.1% K ₂ MoS ₄ /HapNa	11,1	9,1	7,5	6,0	2,0	50	55

Specific surface of solid and loss in specific surface area (%) are also grouped in table 3.8. A significant decrease in the initial area of support is observed; area loss is in the order of 50% for all the samples analyzed. The loss in specific surface area (%) is higher as the wt.% Mo increases. This trend may be related to the fact that the formation of agglomerates increases as the metal content is greater as observed for K₂MoO₄ based solids.

3.4.3.2. Laser Raman Spectroscopy

Figure 3.23 displays the Raman scattering spectrum of K_2MoS_4 -based catalysts. Spectrum of all the samples exhibited lines 482, 468 and 456 cm^{-1} characteristics of potassium tetrathiomolybdate [9–11]. Thus, these three lines are assigned to the vibration mode $\nu(Mo-S)$ of the MoS_4^{2-} anion and are representative of the preservation of K_2MoS_4 species after impregnation. Another line appearing at 908 cm^{-1} was attributed to symmetric vibration of terminal $Mo=O$ bonds. This latter line is broader in alumina and silica supported solids and extended until higher wavenumbers values indicating the presence of an oxidized species that we named as $Mo_xO_y^{n-}$. In contrast, for hydroxyapatite supported catalysts this line is sharper and it is not displaced to higher wavenumbers values, possibly due to the presence of oxo-thio compounds designed as $K_2MoO_xS_y$. Additionally, multiple small and wide Raman lines in the low-wavenumber region between 250 and 400 cm^{-1} and others between 500 and 560 cm^{-1} were also observed; Again, the lines observed in these regions are more evident in alumina and silica supported samples than in hydroxyapatite samples. These lines were attributed to Mo-S or Mo-O bonds, indicating that, in some way, the replacement of atoms of sulfur by oxygen takes place.

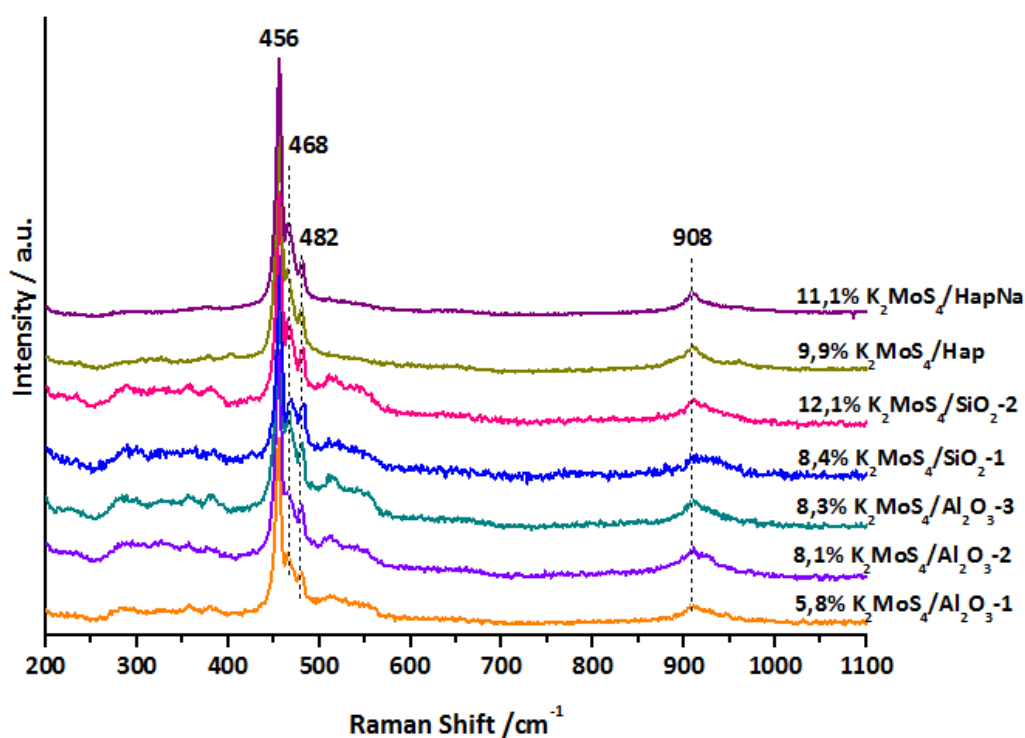


Figure 3.23. Raman spectra of K_2MoS_4 based catalysts

3.4.3.3. Wide angle powder XRD

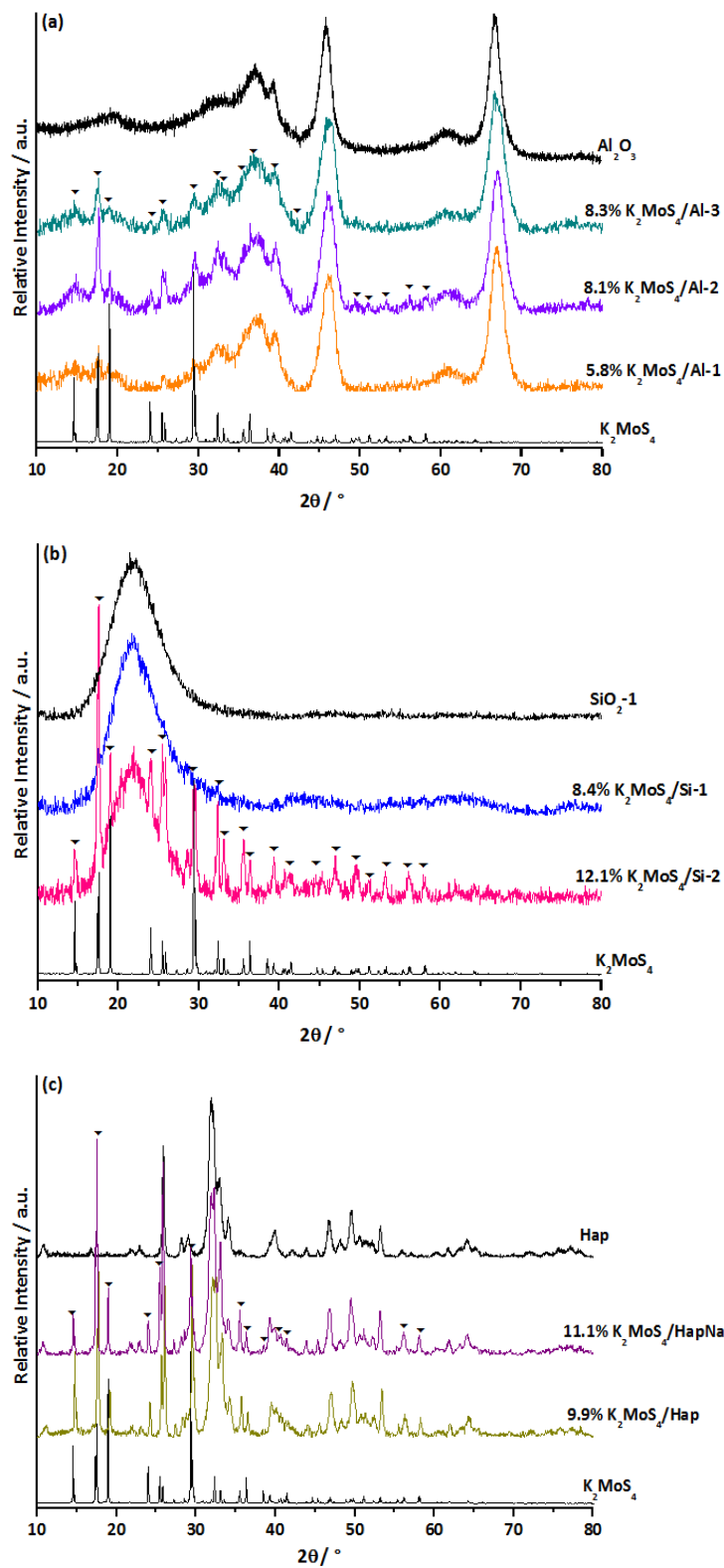


Figure 3.24. XRD patterns of (a) alumina supported K_2MoS_4 based catalysts, (b) silica supported K_2MoS_4 based catalysts and (c) hydroxyapatite supported K_2MoS_4 based catalysts. K_2MoS_4 phase is represented by ▼.

The XRD patterns of the K_2MoS_4 -based catalysts are displayed in figure 3.24. The XRD patterns of the supports and of the precursor salt impregnated K_2MoS_4 are also included. Additionally to the peaks assigned to alumina, silica and hydroxyapatite, peaks at $2\theta = 14.6, 17.5, 19.0, 23.8, 25.8, 29.3, 32.2, 33.1, 35.4, 36.3, 38.4, 39.2, 41.3, 44.6, 47.0, 49.9, 51.1, 53.2, 56.1$ and 58.1° are detected, characterizing potassium tetrathiomolybdate species (JCPDS 00-019-1001). This observation suggests that when the supports are impregnated with K_2MoS_4 , this latter salt is preserved, in accordance with the results obtained by Raman spectroscopy. Additionally, no other crystallized species are visible on the support. It seems evident that the intensity and width of diffraction peaks is directly proportional to the Mo loading of solids, suggesting that for the high-loaded catalysts, this species is forming bigger crystallites and less dispersed particles on the surface of support. In contrast, for the low-loaded samples (those supported on Al-1, Al-2 and Si-1), the peaks corresponding to the impregnated species K_2MoS_4 are almost imperceptibles, putting in evidence a better dispersion in these samples. Table 3.9 displays the average crystallite size of the high-loaded samples 8,1% K_2MoS_4 /Al-2, 12,1% K_2MoS_4 /Si-2, 9,9% K_2MoS_4 /Hap and 11,1% K_2MoS_4 /HapNa, estimated from the Scherrer equation. Average crystallite size in the order of 50 nm are detected for alumina and hydroxyapatite solids, in agreement with the loss in SSA observed for these solids as well as with the high crystallinity observed in XRD pattern; unexpectedly, silica-supported solid exhibits a lower particle size which did not correspond to the high decrease in SSA observed for this sample. In general, it can be suggested that it exists a direct correlation between the crystallite size and Mo loading of this catalysts.

Table 3.9. Estimation of crystallite size of K_2MoS_4 -based solids

CATALYST	AVERAGE CRYSTALLITE SIZE (nm)
8,1% K_2MoS_4 /Al-2	52,0
12,1% K_2MoS_4 /Si-2	36,6
9,9% K_2MoS_4 /Hap	51,2
11,1% K_2MoS_4 /HapNa	52,5

3.4.3.4. X-ray photoelectron spectroscopy (XPS)

XPS analysis was used in order to estimate the phase composition and the distribution of Mo species presents in the samples. Figure 3.25 displays the Mo3d-S2s region of the XPS spectra for the catalyst $K_2MoS_4/Al-3$ as example. The Mo 3d core level of alumina and silica supported catalysts is decomposed in four components, two components concerning sulfur species and two components concerning molybdenum species as shown in the figure below.

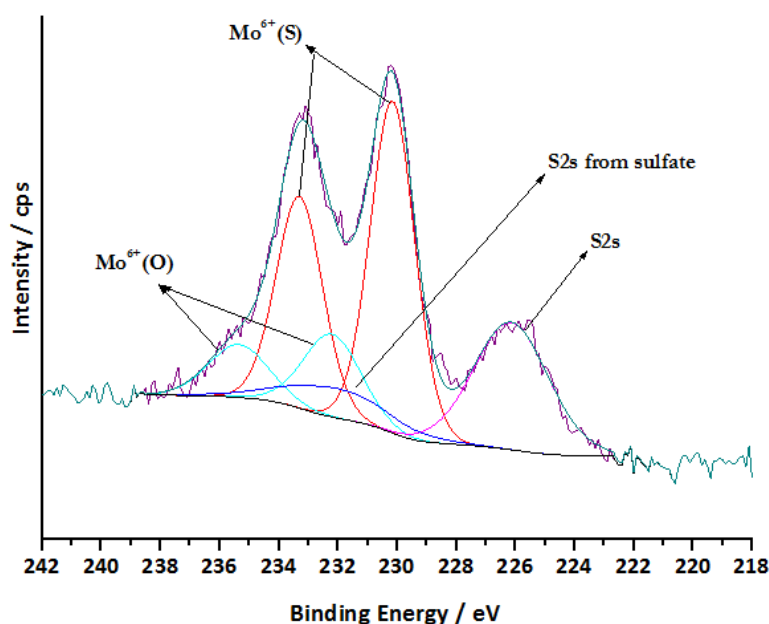


Figure 3.25. XPS spectra of Mo3d-S2s core level of 8.3%K₂MoS₄/Al-3 catalyst

The binding energies and At.% of Mo3d contributions of K₂MoS₄-based alumina and silica-supported catalysts are reported in table 3.10. As mentioned above, two kinds of Mo are found in the fresh K₂MoS₄-based catalysts. The positions of the Mo3d_{5/2} component of the two identified species were around 230.1±0.2 eV and 232.2±0.2 eV for alumina and silica-supported samples. The component located at lower binding energy was assigned to Mo⁶⁺ species bonded to sulfur atoms; the position of this component corresponds perfectly with that observed in the unsupported K₂MoS₄ (annex 1), thus this species is assigned to Mo in K₂MoS₄ compound. The component positioned at higher binding energy was assigned to Mo⁶⁺ species in an oxidic environment [35], [36], [38]. We assign this component to a completely re-oxidized compound with Mo atoms bounded exclusively to oxygen atoms.

Table 3.10. Binding energy of Mo 3d level and at.% of Mo of K₂MoS₄/Al and K₂MoS₄/Si solids

CATALYST	Binding Energy (eV)				At.%	
	Mo ⁶⁺ (S)		Mo ⁶⁺ (O)		Mo ⁶⁺ (S)	Mo ⁶⁺ (O)
	Mo 3d _{5/2}	Mo 3d _{3/2}	Mo 3d _{5/2}	Mo 3d _{3/2}		
5.8% K ₂ MoS ₄ /Al-1	230,2	233,4	232,4	235,6	71,9	28,1
8.1% K ₂ MoS ₄ /Al-2	230,2	233,4	232,2	235,4	69,2	30,8
8.3% K ₂ MoS ₄ /Al-3	230,2	233,3	232,2	235,4	75,8	24,2
8.4% K ₂ MoS ₄ /Si-1	229,9	233,0	232,2	235,3	87,2	12,8
12.1% K ₂ MoS ₄ /Si-2	229,9	233,1	232,3	235,4	84,1	15,9

Anyhow, the predominant species (greater than 69%) in all the samples is Mo⁶⁺ (S), indicating that K₂MoS₄ is conserved as observed by XRD and Raman, nevertheless, the replacement of sulfur by oxygen takes place, as also observed by Raman spectroscopy, leading to the presence of oxidized species, possibly due to the exposure to air of the catalysts.

Hydroxyapatite-based catalysts exhibited a different behavior. Figure 3.26 displays the Mo3d-S2s region of the XPS spectra for supported-hydroxyapatite catalyst (9.9%K₂MoS₄/Hap as example).

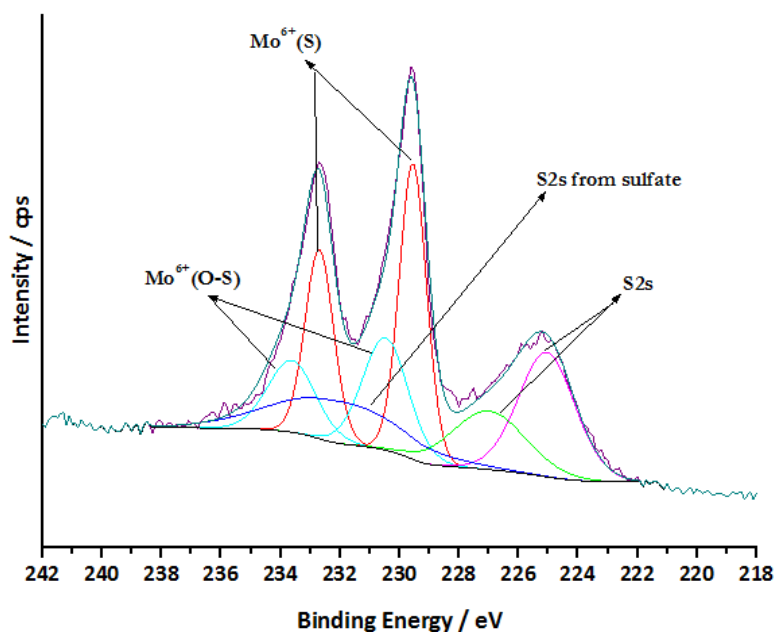
**Figure 3.26.** XPS spectra of Mo3d-S2s core level of 9.9%K₂MoS₄/Hap catalyst

Table 3.11. Binding energy of Mo 3d level and at.% of Mo of K₂MoS₄/Hap and K₂MoS₄/HapNa solids

CATALYST	Binding Energy (eV)				At.%	
	Mo ⁶⁺ (S)		Mo ⁶⁺ (O)			
	Mo 3d _{5/2}	Mo 3d _{3/2}	Mo 3d _{5/2}	Mo 3d _{3/2}	Mo ⁶⁺ (S)	Mo ⁶⁺ (O)
9.9% K ₂ MoS ₄ /Hap	229,6	232,7	230,5	233,6	60,66	39,34
11.1% K ₂ MoS ₄ /HapNa	230,0	233,2	231,0	234,2	80,43	19,57

The Mo 3d core level of hydroxyapatite samples is decomposed in five components, three components related to sulfur species and two components related to molybdenum species. So, also two Mo species were observed but at different binding energies than alumina and silica-supported solids (see table 3.11). The Mo components (Mo3d_{5/2}) positioned at lower binding energy (229.8±0.2) eV is attributed to Mo⁶⁺ surrounded by sulfur atoms as for K₂MoS₄-based alumina and silica supported catalysts. This component is thus assigned to K₂MoS₄. The second component is situated at higher binding energy (230.8±0.2). This component is thus placed between the completely sulfided species K₂MoS₄ and the completely re-oxidized species observed for K₂MoS₄-based alumina and silica supported catalysts at 232.2±0.2 eV. It seems logic to assign this position to the presence of an oxysulfide (--S--Mo⁶⁺--O--) species in an oxidic-sulfidic surrounding as K₂MoO₂S₂ or K₂MoOS₃. These attributions are in perfect agreement with those concluded by Raman spectroscopy.

In order to estimate the dispersion of the K₂MoS₄-species impregnated on the surface of supports, we determined the % Mo detected by XPS as for K₂MoO₄-based catalysts and the results are showed in table 3.12. It can be seen that a considerably small amount of Mo is detected by XPS meaning that big K₂MoS₄ crystallites are present on the surface of support. These results seem to be in good agreement with those discussed for XRD, Raman and SSA determination, as the preservation of the impregnated compound K₂MoS₄ observed by Raman and XRD as well as the crystallite size and the substantial decrease in SSA suggests the presence of big particles of K₂MoS₄, otherwise, no signals of this compound would be observed.

Table 3.12. at.% Mo and % of Mo detected by XPS for K₂MoS₄-based catalysts

CATALYST	%At. Mo		%Mo detected by XPS
	XPS	Bulk	
5.8% K ₂ MoS ₄ /Al-1	0,3	1,1	30
8.1% K ₂ MoS ₄ /Al-2	0,4	1,8	21
8.3% K ₂ MoS ₄ /Al-3	0,3	1,3	25
8.4% K ₂ MoS ₄ /Si-1	0,4	1,7	24
12.1% K ₂ MoS ₄ /Si-2	0,4	2,2	20
9.9% K ₂ MoS ₄ /Hap	0,6	2,1	29
11.1% K ₂ MoS ₄ /HapNa	0,5	1,8	26

3.4.3.5. Scanning Electron Microscopy (SEM)

SEM micrographs of K₂MoS₄-Al-3 and K₂MoS₄-Hap catalysts showed in figure 3.27 suggest that support structure is preserved after K₂MoS₄ deposition. Nevertheless, after impregnation, white particles appear over the support in both cases. We attributed these particles at the impregnated compound K₂MoS₄. The observed particles seem to be fairly homogeneously distributed over the support (grey regions). In addition, it is also visible in the figure that some of the particles do not exhibit a round shape, but rather an irregular one. The average size of particles for the samples 8.3% K₂MoS₄/Al-3 and 9.9% K₂MoS₄/Hap are 34 nm and 38 nm respectively. The low value of the alumina-supported solid compared to those obtained for the higher loaded catalysts by XRD is expected since very weak diffraction peaks are observed in this solid. Regarding the Hap-supported solid, a perceptible difference is observed between the measures performed by XRD and SEM. Anyhow, the presence of particles considerably large are in perfect accordance with the results obtained by means of the other characterization techniques.

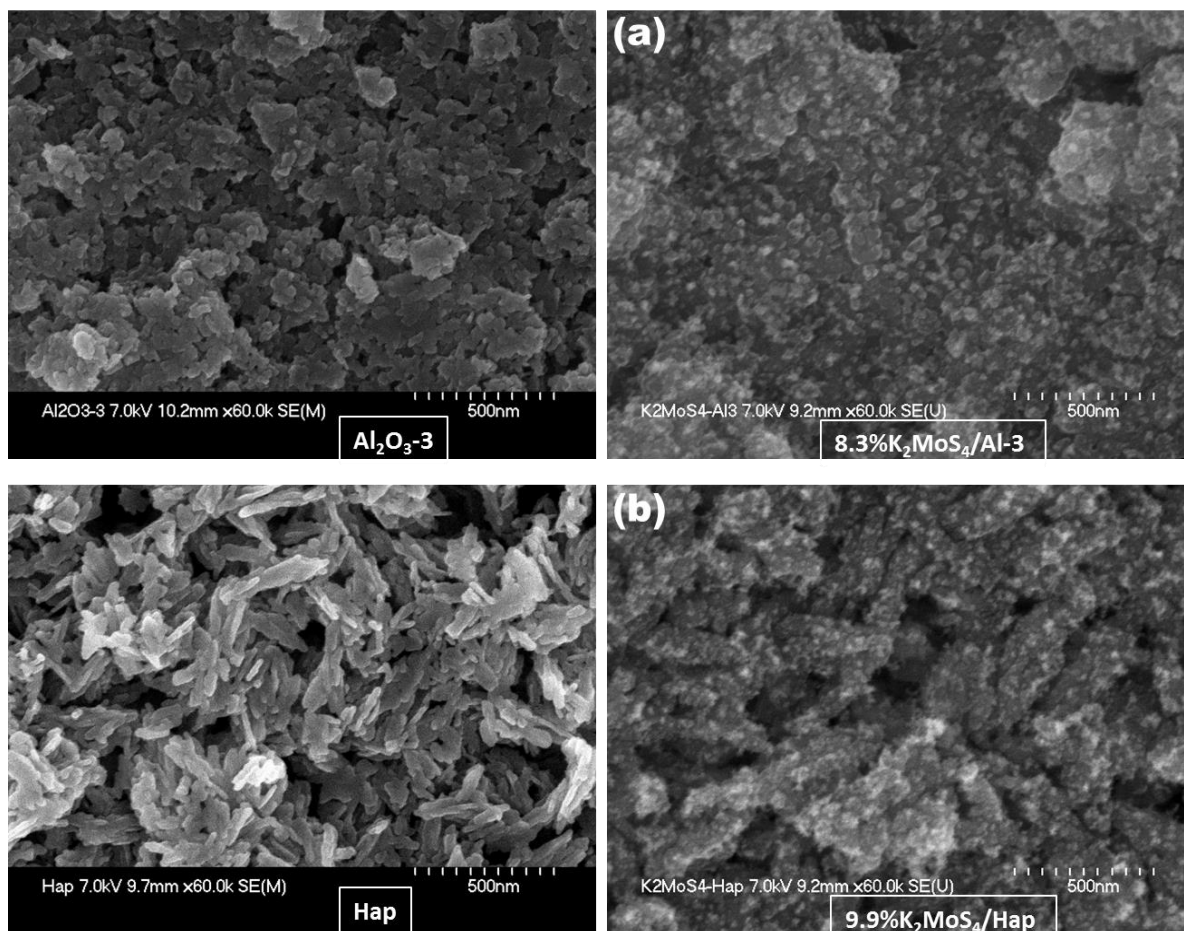


Figure 3.27. SEM images of (a) $8.3\% \text{K}_2\text{MoS}_4/\text{Al-3}$ and (b) $9.9\% \text{K}_2\text{MoS}_4/\text{Si-1}$ catalysts. The figures on the left correspond to the supports before impregnation

3.5. CONCLUSION OF SECTION 3.4

In section 3.4, the characterization results of catalysts in fresh state were discussed. Three series of catalysts were characterized by means of different techniques including BET, XRD, Raman and XPS. Concerning reference catalysts, we observed that the incorporation of Mo and K(Na) coming from the same precursor, leads to a high crystallized species, characterized by narrow Raman lines and significant difference between Mo bulk composition and Mo surface composition (XPS).

In K_2MoO_4 and K_2MoS_4 -based catalysts, the preservation of the impregnated species was

observed. The first evidence of that fact was the presence of Raman lines and XRD peaks characteristic of these precursors. In addition, the high loss in SSA, was indicative of the presence of big crystallites but dispersed on the supports. The determination of particle size by both, XRD and SEM techniques was made; crystallite size in the order of 25 to 55 nm was obtained. Another evidence of the presence of big particles was the fact that an important quantity of Mo was not detected by XPS, which is normal if bad dispersed particles exist on the support. In general, we correlate these results to the amount of Mo in the samples and we found that the higher the Mo loading, the higher the loss in SSA and the lower the Mo detected by XPS and also that The higher the Mo content, the higher the XRD peak intensity and the greater the particle size (determined by XRD and SEM).

3.6. REFERENCES

- [1] E. K. Quagraine, I. Georgakaki, and D. Coucouvanis, "Reactivity and kinetic studies of $(\text{NH}_4)_2(\text{MoS}_4)$ in acidic aqueous solution: Possible relevance to the angiostatic function of the $\text{MoS}_4(2-)$ ligand.," *Journal of inorganic biochemistry*, vol. 103, no. 1, pp. 143-55, Jan. 2009.
- [2] G. Alonso, G. Berhault, and R. R. Chianelli, "Synthesis and characterization of tetraalkylammonium thiomolybdates and thiotungstates in aqueous solution," *Inorganica Chimica Acta*, vol. 316, no. 1-2, pp. 105-109, May 2001.
- [3] E. K. Quagraine and R. S. Reid, "UV/visible spectrophotometric studies of the interactions of thiomolybdates, copper(II) and other ligands," *Journal of inorganic biochemistry*, vol. 85, no. 1, pp. 53-60, May 2001.
- [4] B. E. Erickson and G. R. Helz, "Molybdenum (VI) speciation in sulfidic waters : Stability and lability of thiomolybdates," *Geochimica and Cosmochimica acta*, vol. 64, no. 7, pp. 1149-1158, 2000.
- [5] S. H. Laurie, "Thiomolybdates — Simple but Very Versatile Reagents," *European Journal of Inorganic Chemistry*, vol. 2000, no. 12, pp. 2443-2450, Dec. 2000.
- [6] G. Alonso, J. Yang, M. H. Siadati, and R. R. Chianelli, "Synthesis of tetraalkylammonium thiomolybdates in aqueous solution," *Inorganica Chimica Acta*, vol. 325, no. 1-2, pp. 193-197, Dec. 2001.
- [7] J. W. McDonald, G. D. Friesen, L. D. Rosenhein, and W. E. Newton, "Syntheses and characterization of ammonium and tetraalkylammonium thiomolybdates and thiotungstates," *Inorganica Chimica Acta*, vol. 72, pp. 205-210, Jan. 1983.
- [8] N. J. Clarke and S. H. Laurie, "The copper-molybdenum antagonism in ruminants. I. The formation of thiomolybdates in animal rumen.," *Journal of inorganic biochemistry*, vol. 12, no. 1, pp. 37-43, Jan. 1980.

-
-
- [9] T. Weber, J. C. Muijsers, and N. J. W., "Structure of Amorphous MoS₃," *J. Phys. Chem.*, vol. 99, pp. 9194-9200, 1995.
- [10] A. Müller, N. Weinstock, and H. Schulze, "Laser-Raman-Spektren der Ionen MoS₄(2-), WS₄(2-), MoOS₃(2-) und WOS₃(2-) in wässriger Lösung sowie der entsprechenden kristallinen Alkalisalze," *Spectrochimica Acta*, vol. 28A, pp. 1075-1082, 1972.
- [11] A. Müller, E. J. Baran, and R. O. Carter, "Vibrational Spectra of Oxo-, Thio-, and Selenometallates of Transition Elements in the Solid State," *Vibrational spectra of transition element compounds*, vol. 3, pp. 81-139, 1975.
- [12] G. M. Clarke and W. P. Doyle, "Properties of some solids tetrathiomolybdates," *J. Inorg. Nucl. Chem.*, vol. 28, pp. 381-385, 1966.
- [13] R. W. Mooney and C. W. W. Hoffman, "X-Ray diffraction data for ammonium tetrathiotungstate," *Canadian Journal of Chemistry*, vol. 41, pp. 2237-2239, 1963.
- [14] C. Lamonier, J.-F. Lamonier, B. Aellach, A. Ezzamarty, and J. Leglise, "Specific tuning of acid/base sites in apatite materials to enhance their methanol thiolation catalytic performances," *Catalysis Today*, vol. 164, no. 1, pp. 124-130, Apr. 2011.
- [15] A. Krajewski et al., "Synthesis of carbonated hydroxyapatites: efficiency of the substitution and critical evaluation of analytical methods," *Journal of Molecular Structure*, vol. 744-747, pp. 221-228, Jun. 2005.
- [16] M. Markovic and B. Fowler,, "Preparation and Comprehensive Characterization of a Calcium Hydroxyapatite Reference Material," *J. Res. Natl. Inst. Stand. Technol.*, vol. 109, no. 6, pp. 553-568, 2004.
- [17] B. Wopenka and J. D. Pasteris, "A mineralogical perspective on the apatite in bone," *Materials Science and Engineering: C*, vol. 25, no. 2, pp. 131-143, Apr. 2005.
- [18] A. Auroux, R. Monaci, E. Rombi, V. Solinas, A. Sorrentino, and E. Santacesaria, "Acid sites investigation of simple and mixed oxides by TPD and microcalorimetric techniques," *Thermochimica Acta*, vol. 379, no. 1-2, pp. 227-231, Nov. 2001.
- [19] Z. Zhao, Y. Yamada, A. Ueda, H. Sakurai, and T. Kobayashi, "The roles of redox and acid-base properties of silica-supported vanadia catalysts in the selective oxidation of ethane," *Catalysis Today*, vol. 93-95, pp. 163-171, Sep. 2004.
- [20] V. Calvino-Casilda, R. Martin-Aranda, I. Sobczak, and M. Ziolek, "Modification of acid-base properties of alkali metals containing catalysts by the application of various supports," *Applied Catalysis A: General*, vol. 303, no. 1, pp. 121-130, Apr. 2006.
- [21] A. Gervasini, J. Fenyvesi, and A. Auroux, "Study of the acidic character of modified metal oxide surfaces using the test of isopropanol decomposition," *Catalysis Letters*, vol. 43, pp. 219-228, 1997.
- [22] C. Lahousse, J. Bachelier, J.-C. Lavalley, H. Lauron-Pernot, and A.-M. Le Govic, "Validity of using isopropanol decomposition as a test- reaction for the characterization of metal oxides basicity; comparison with results obtained from methylbutynol decomposition," *Journal of Molecular Catalysis*, vol. 87, no. 2-3, pp. 329-332, 1994.
- [23] T. Tsuchida, J. Kubo, T. Yoshioka, S. Sakuma, T. Takeguchi, and W. Ueda, "Reaction of ethanol over hydroxyapatite affected by Ca/P ratio of catalyst," *Journal of Catalysis*, vol. 259, no. 2, pp. 183-189, Oct. 2008.

-
-
- [24] X. Carrier, J. F. Lambert, and M. Che, "Ligand-Promoted Alumina Dissolution in the Preparation of MoOX/ γ -Al₂O₃ Catalysts. Evidence for the Formation and Deposition of an Anderson-type Alumino Heteropolymolybdate," *Journal of the American Chemical Society*, vol. 119, pp. 10137-10146, 1997.
- [25] L. Le Bihan, P. Blanchard, M. Fournier, J. Grimblot, and E. Payen, "Raman spectroscopic evidence for the existence of 6-molybdoaluminate entities on an Mo/Al₂O₃ oxidic precursor," *J. Chem. Soc., Faraday Trans.*, vol. 94, no. 7, pp. 937-940, 1998.
- [26] P. Blanchard, C. Lamonier, a. Griboval, and E. Payen, "New insight in the preparation of alumina supported hydrotreatment oxidic precursors: A molecular approach," *Applied Catalysis A: General*, vol. 322, pp. 33-45, Apr. 2007.
- [27] R. Murugan, P. J. Huang, A. Ghule, and H. Chang, "Studies on thermal hysteresis of KNO₃ by thermo-Raman spectroscopy," *Thermochimica Acta*, vol. 346, pp. 83-90, 2000.
- [28] Y. Hao, Y. Zhang, A. Chen, W. Fang, and Y.-Q. Yang, "Study on Methanethiol Synthesis from H₂S-Rich Syngas Over K₂MoO₄ Catalyst Supported on Electrolessly Ni-Plated SiO₂," *Catalysis Letters*, vol. 129, no. 3-4, pp. 486-492, Jan. 2009.
- [29] D. J. Pérez-Martínez, P. Eloy, E. M. Gaigneaux, S. A. Giraldo, and A. Centeno, "Study of the selectivity in FCC naphtha hydrotreating by modifying the acid-base balance of CoMo/ γ -Al₂O₃ catalysts," *Applied Catalysis A: General*, vol. 390, no. 1-2, pp. 59-70, Dec. 2010.
- [30] V. La Parola, G. Deganello, C. R. Tewell, and A. M. Venezia, "Structural characterisation of silica supported CoMo catalysts by UV Raman spectroscopy, XPS and X-ray diffraction techniques," *Applied Catalysis A: General*, vol. 235, no. 1-2, pp. 171-180, Aug. 2002.
- [31] O. Y. Gutiérrez, C. Kaufmann, A. Hrabar, Y. Zhu, and J. a. Lercher, "Synthesis of methyl mercaptan from carbonyl sulfide over sulfide K₂MoO₄/SiO₂," *Journal of Catalysis*, vol. 280, no. 2, pp. 264-273, Jun. 2011.
- [32] A. Erdöhelyi, K. Fodor, and F. Solymosi, "Partial Oxidation of Methane on Supported Potassium Molybdate," *Journal of Catalysis*, vol. 166, pp. 244-253, 1997.
- [33] J. E. Herrera and D. E. Resasco, "Loss of single-walled carbon nanotubes selectivity by disruption of the Co-Mo interaction in the catalyst," *Journal of Catalysis*, vol. 221, no. 2, pp. 354-364, Jan. 2004.
- [34] V. P. Mahadevan Pillai, T. Pradeep, M. J. Bushiri, R. S. Jayasree, and V. U. Nayar, "Vibrational spectroscopic studies of FeClMoO₄, Na₂MoO₄ and Na₂MoO₄.2H₂O/D₂O," *Spectrochimica Acta Part A*, vol. 53, pp. 867-876, 1997.
- [35] L. Qiu and G. Xu, "Peak overlaps and corresponding solutions in the X-ray photoelectron spectroscopic study of hydrodesulfurization catalysts," *Applied Surface Science*, vol. 256, no. 11, pp. 3413-3417, Mar. 2010.
- [36] C. Roukoss, D. Laurenti, E. Devers, K. Marchand, L. Massin, and M. Vrinat, "Hydrodesulfurization catalysts: Promoters, promoting methods and support effect on catalytic activities," *Comptes Rendus Chimie*, vol. 12, no. 6-7, pp. 683-691, Jun. 2009.
- [37] F. P. J. M. Kerkhof and J. A. Moulijn, "Quantitative analysis of XPS intensities for supported catalysts," *The Journal of Physical Chemistry*, vol. 83, no. 12, pp. 1612-1619, Jun. 1979.
- [38] H. W. Wang, P. Skelton, and G. E. Thompon, "XPS studies of MoS₂ formation from ammonium tetrathiomolybdate solutions," *Surface and Coatings Technology*, vol. 91, pp. 200-207, 1997.

CHAPTER 4

Mo-based catalysts for the synthesis of MeSH from syngas/H₂S mixture

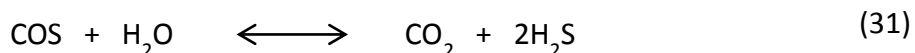
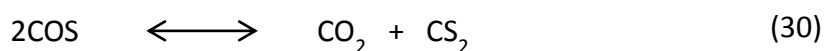
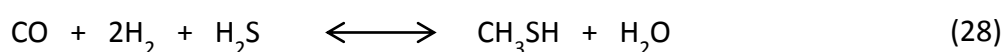
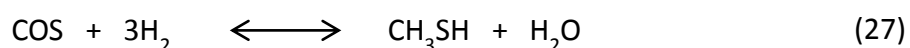
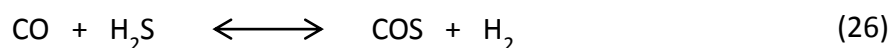
Mo-based catalysts for the synthesis of MeSH from syngas/H₂S mixture: Summary

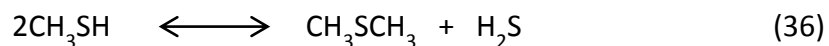
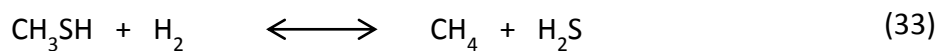
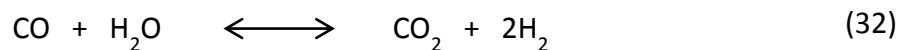
4.1. SULFIDED REFERENCE CATALYSTS	166
4.1.1. Catalytic test of sulfided reference results	166
4.1.1.1. <i>Effect of the incorporation of potassium</i>	168
4.1.1.2. <i>Effect of the way of incorporation of molybdenum and potassium</i>	171
4.1.1.3. <i>Effect of the alkali promoter (K or Na) and the state of the precursor incorporated (oxidic or pre-sulfided)</i>	172
4.1.2. Characterization of sulfided reference catalysts. Comprehension and approach to the active phase	174
4.1.2.1. <i>X-ray photoelectron spectroscopy (XPS)</i>	174
4.1.2.2. <i>High resolution transmission electron microscopy (HRTEM)</i>	185
4.2. K₂MoO₄-BASED CATALYSTS	190
4.2.1. Catalytic test of sulfided K ₂ MoO ₄ -based.....	190
4.2.2. Characterization of sulfided K ₂ MoO ₄ -based catalysts	191
4.2.2.1. <i>Raman spectroscopy</i>	192
4.2.2.2. <i>High resolution transmission electron microscopy (HRTEM)</i>	194
4.2.2.3. <i>X-ray photoelectron spectroscopy (XPS)</i>	198
4.2.2.4. <i>Correlation between catalytic performance and active K_xMoS₂ phase</i>	199
4.3. K₂MoS₄-BASED CATALYSTS.....	200
4.3.1. Catalytic test of sulfided K ₂ MoS ₄ -based catalysts.....	201
4.3.2. Characterization of sulfided K ₂ MoS ₄ -based catalysts.....	203
4.3.2.1. <i>Raman spectroscopy</i>	203
4.3.2.2. <i>High resolution transmission electron microscopy (HRTEM)</i>	204
4.3.2.3. <i>X-ray photoelectron spectroscopy (XPS)</i>	205
4.3.2.4. <i>Correlation between catalytic performance and active K_xMoS₂ phase</i>	206
4.4. EFFECT OF Mo LOADING OVER A SERIES OF ALUMINA-SUPPORTED CATALYSTS	207
4.5. EFFECT OF CATALYST PRETREATMENT OVER THE CATALYTIC ACTIVITY	209
4.5.1. Catalytic test	209
4.6. CONCLUSIONS	211
4.7. REFERENCES	213

In this chapter, we discussed the catalytic performances of Mo-based catalysts aimed to the direct conversion of the mixture CO+H₂+H₂S in CH₃SH. Following the catalytic results section, we also focus the chapter on the characterization of catalysts after sulfidation, correlating these measures with the catalytic behavior, trying to determine the active phase responsible of the catalytic performances. Laser Raman spectroscopy (LRS), powder X-ray diffraction (XRD), scanning electron microscopy (SEM), transmission electron microscopy (TEM) and X-ray photoelectron spectroscopy (XPS) were used with this purpose.

In the first section we study a series of reference catalysts all prepared with the same Mo loading (8.1wt.% Mo) and over the same support (Al₂O₃-3). Catalytic performances of those catalysts and the correlations with the sulfided phase analyzed by XPS are discussed in this part. Second and third sections are destined to evaluate K₂MoO₄ and K₂MoS₄-based catalysts supported in different carriers (alumina, silica and hydroxyapatite) and high-loaded at different wt.% Mo. Characterization techniques have been performed and discussed trying to correlate the catalytic properties of the samples. Fourth section consists in the study of the effect of catalyst pretreatment on the reaction of syngas with H₂S using the catalyst 17.9% K₂MoO₄/Al-3, looking forward the improvement of CH₃SH production.

For clarity reasons, the reactions leading to the formation of main products CH₃SH, CO₂, COS, CH₄, CH₃SCH₃ and CS₂ discussed in chapter 1, are presented in this chapter here below:





4.1. SULFIDED REFERENCE CATALYSTS

The aim of this section is to compare and evaluate catalysts containing or not potassium, catalysts in which Mo and K are incorporated in different ways but maintaining the molar ratio K/Mo=2, catalysts with different alkali promoter (K or Na) and catalysts in which the precursor is incorporated in oxidic or pre-sulfided form (K₂MoO₄ and K₂MoS₄). The wt.% Mo loading of the aforementioned catalysts was fixed to 8,1% (8,3% for K₂MOS₄/Al-3) and by consequence the wt.% K was equal to 6,6% in order to maintain the K/Mo ratio equal to 2.

4.1.1. Catalytic test of sulfided reference results

Six reference catalysts have been evaluated and exposed in this section. Catalytic results of referenced samples are gathered in table 4.1. The analysis of catalytic results of these catalysts leads to divide the catalysts in three groups as follow.

Table 4.1. *Catalytic performance of sulfided reference catalysts in the reaction of syngas and H₂S*

CATALYST	CO Conversion (%)			Selectivity (%)												Productivity (g.h ⁻¹ .L ⁻¹)								
				CH ₃ SH			COS			CO ₂			CH ₄			CH ₃ SH			COS			CO ₂		
	280 °C	300 °C	320 °C	280 °C	300 °C	320 °C	280 °C	300 °C	320 °C	280 °C	300 °C	320 °C	280 °C	300 °C	320 °C	280 °C	300 °C	320 °C	280 °C	300 °C	320 °C	280 °C	300 °C	320 °C
8.1% K/Al-3	4	6	8	23	25	27	37	32	33	40	42	38	0	2	2	7	11	15	14	17	23	11	16	20
8.1% Mo/Al-3	12	14	18	22	17	9	25	20	16	51	60	74	3	2	2	19	18	11	26	25	24	40	57	85
8.1% Mo+K/Al-3	26	32	40	43	43	42	7	5	4	48	49	49	2	3	5	80	100	121	16	15	13	81	103	130
8.1% K ₂ MoO ₄ /Al-3	28	36	43	43	43	40	6	4	3	48	49	49	2	3	7	87	112	126	16	14	12	89	115	139
8.1%Na ₂ MoO ₄ /Al-3	27	35	43	43	42	35	6	4	3	50	53	60	0	1	1	82	106	108	15	13	13	88	123	167
8.3% K ₂ MoS ₄ /Al-3	28	38	48	45	44	41	7	5	3	47	48	48	1	2	6	90	122	141	18	16	14	86	121	151

4.1.1.1. Effect of the incorporation of potassium

The CO conversion and selectivities towards CH₃SH, COS and CO₂ of the catalysts 6.6% K/Al-3, 8.1% Mo/Al-3 and 8.1% Mo+K/Al-3 as a function of reaction temperature are exposed in figure 4.1.

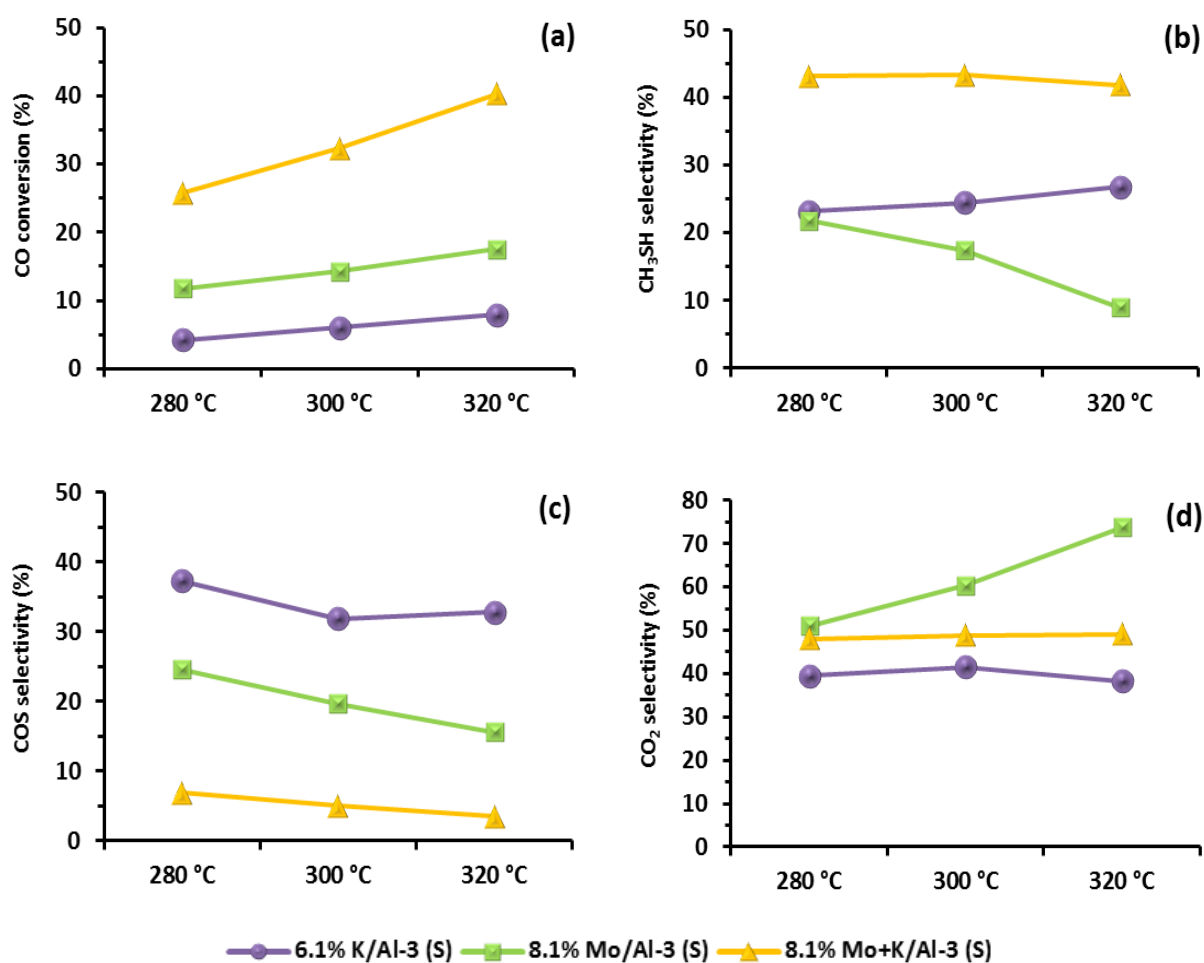


Figure 4.1. Evolution of the CO conversion (a) and selectivity in CH₃SH (b), COS (c) and CO₂ (d) of 6.6% K/Al-3, 8.1% Mo/Al-3 and 8.1% Mo+K/Al-3 catalysts.

For this series of catalysts, with increasing temperature, the conversion of CO increases linearly. The major products of reaction are methyl mercaptan (CH₃SH), carbonyl sulfide (COS) and carbon dioxide (CO₂). However, for each catalyst, a small quantity of other products is observed, these are CS₂ (about 2%) for 6.6% K/Al-3, CH₃SCH₃ (about 2%) for 8.1% Mo/Al-3 and CH₄ (about 5%) for 8.1% Mo+K/Al-3. The three catalysts exhibit the same trend

regarding COS selectivity, decreasing with increasing the temperature, an expected behavior according to Yang *et al.* [1]. CH₃SH and CO₂ selectivities have shown a different behavior; for 6.6% K/Al-3 and for 8.1% Mo+K/Al-3 catalysts the selectivity towards these two products is almost constant in the range of temperatures evaluated. By the contrary, for 8.1% Mo/Al-3, the selectivity in CH₃SH and CO₂ decreases and increases respectively with the increase of temperature.

The less active catalyst is 6.6% K/Al-3 exhibiting a CO conversion between 4% and 8% in the range of temperatures 280-320 °C. CO conversion of 8.1% Mo/Al-3 is almost twice than the former solid and 8.1% Mo+K/Al-3 is five times more active than the solid without Mo and at least two times more active than the solid without K. This observation is a first evidence of the interest of having both elements (K and Mo) in the catalytic system, revealing the synergetic effect between K and Mo since the Mo+K-based catalyst shows a higher CO conversion as compared to the sum of the CO conversion of K and Mo-based catalysts. Regarding the selectivities towards the main products, the solid 6.6% K /Al-3 exposes an equal distribution of COS and CO₂ (around 40%) and the remaining belongs to CH₃SH; these values remain almost stable in the whole range of temperature. The catalyst 8.1% Mo/Al-3 is more selective toward CO₂, from 50% at 280 °C to 74% at 320 °C. In contrast, COS and CH₃SH selectivities decrease from around 22% to 16% (COS) and 9% (CH₃SH). Finally, the most active catalyst of this group, 8.1% Mo+K/Al-3, exposes constant selectivities in CO₂ (48-49%) and CH₃SH (42-43%) while the selectivity toward COS decreases from 7% to 3.5% and at the same time CH₄ selectivity increases. The productivity of CH₃SH over 6.6% K/Al-3, 8.1% Mo/Al-3 and 8.1% Mo+K/Al-3 catalysts has been calculated as 15.0, 11.3 and 120.5 g.h⁻¹.L⁻¹ respectively, showing the beneficial effect of having both elements (Mo and K) in the catalytic system.

From catalysts 6.6% K/Al-3 and 8.1% Mo+K/Al-3, it can be seen that the addition of Mo favors the decrease in the COS selectivity and that coincides with the increase of the selectivity of CH₃SH. This observation allows us to conclude that without Mo, the reaction (26) takes place but the hydrogenation of COS to produce CH₃SH (reaction 27) is only achieved in some extend. In contrast, when Mo is present (8.1% Mo+K/Al-3 solid), the hydrogenation of COS to produce CH₃SH is achieved in a greater extend since the selectivity

in CH₃SH increases and the selectivity toward COS decreases considerably. By the other hand, it can also be presumed that the presence of Mo favors the production of CO₂ since the 8.1% Mo/Al-3 sample is highly selective to this product, especially at high temperatures, at which CO₂ selectivity reaches 70%, at expense of the decrease towards CH₃SH selectivity. By contrast, the presence of K promotes the decrease in CO₂ production since the selectivity towards this product is lower for 8.1% Mo+K/Al-3 sample than 8.1% Mo/Al-3 and at the same time, the selectivity towards CH₃SH is increased. In this regard, CO₂, which reaches always at least 40% of selectivity, may be produced by the disproportionation or hydrolysis of COS or by the water-gas shift reaction (reactions 30, 31 and 32 respectively). Taking into account our results and the observations of Chen *et al.* [2], most of the CO₂ cannot originate from reaction (30), otherwise the selectivity of CS₂ would be close to that of CO₂. Concerning the hydrolysis of COS (reaction 31), it is considered that this reaction is restrained at high concentrations of H₂S in the reaction system, which is not our case as we work at stoichiometric molar concentration (CO/H₂/H₂S=1/2/1), but if this reaction takes place, there would be a competition between the hydrogenation (reaction 27) and hydrolysis (reaction 31) of COS which is observed among our results. The other possible reaction (32), is quite probably and also accepted by others authors [2–4], thus in any case, CO₂ must be produced by hydrogenolysis of CO or COS which is reasonable enough since the water produced in reaction (27) would be consumed by means of one of these reactions. The latter observations also put in evidence that whatever the reaction path, COS acts as a reaction intermediate, either for the production of CH₃SH or CO₂.

The presence of some byproducts also takes place as mentioned earlier. 6.6% K/Al-3 solid is slightly selective towards CS₂ which is produced by reaction (30) accompanied by CO₂, suggesting a possible competition between COS disproportionation (reaction 30) and hydrolysis (reaction 27) to form CO₂, a product formed with 40% of selectivity on this catalyst. CH₄ is formed when using the catalyst 8.1% Mo+K/Al-3; this compound is formed by the hydrogenation of CH₃SH (reaction 33), putting in evidence the hydrogenating properties of this catalyst since two hydrogenation reaction (reaction 27 and 33) take place.

In summary of this subsection, we conclude that the simultaneous presence of Mo and K in the catalytic system allows achieving higher CO conversion and CH₃SH selectivity and a

decrease in CO₂ selectivity, highlighting the favorable influence of the coexistence of both metals in the catalytic system.

4.1.1.2. Effect of the way of incorporation of molybdenum and potassium

In this subsection, we analyze the effect of the way Mo and K are incorporated over the carrier with a molar ratio K/Mo equal to 2. Two solids are evaluated, the first is 8.1% Mo+K/Al-3 in which the Mo precursor is impregnated, dried and calcined and after that the K precursor is impregnated over this solid, dried and calcined. The second solid is 8.1% K₂MoO₄/Al-3 in which Mo and K belong to the same precursor K₂MoO₄. The CO conversion and selectivities to CH₃SH, COS and CO₂ of both catalysts as a function of reaction temperature are showed in figure 4.2.

No significant differences between these two solids concerning the selectivities towards the main products CH₃SH, COS and CO₂ are observed. At 320 °C, CH₃SH selectivity is slightly higher over the catalyst 8.1% Mo+K/Al-3 than over 8.1% K₂MoO₄/Al-3 at expense of an increase in the selectivity to CH₄ of this latter solid, which means that in some way the hydrogenation of CH₃SH into CH₄ (reaction 33) is more favored over the 8.1% K₂MoO₄/Al-3 catalyst.

Regarding CO conversion, 8.1% K₂MoO₄/Al-3 catalyst is somewhat more active than 8.1% Mo+K/Al-3 which exhibits a conversion 3% lower in the complete range of temperature evaluated. In terms of CH₃SH productivity, this results in an increase in 4% in the productivity of this target product, which reaches 125.5 g.h⁻¹.L⁻¹. These results suggest that the incorporation of K and Mo coming from a unique precursor is beneficial when talking about catalytic performance but also must be advantageous when talking about time and costs of preparation of catalysts, which are reduced when synthesized 8.1% K₂MoO₄/Al-3.

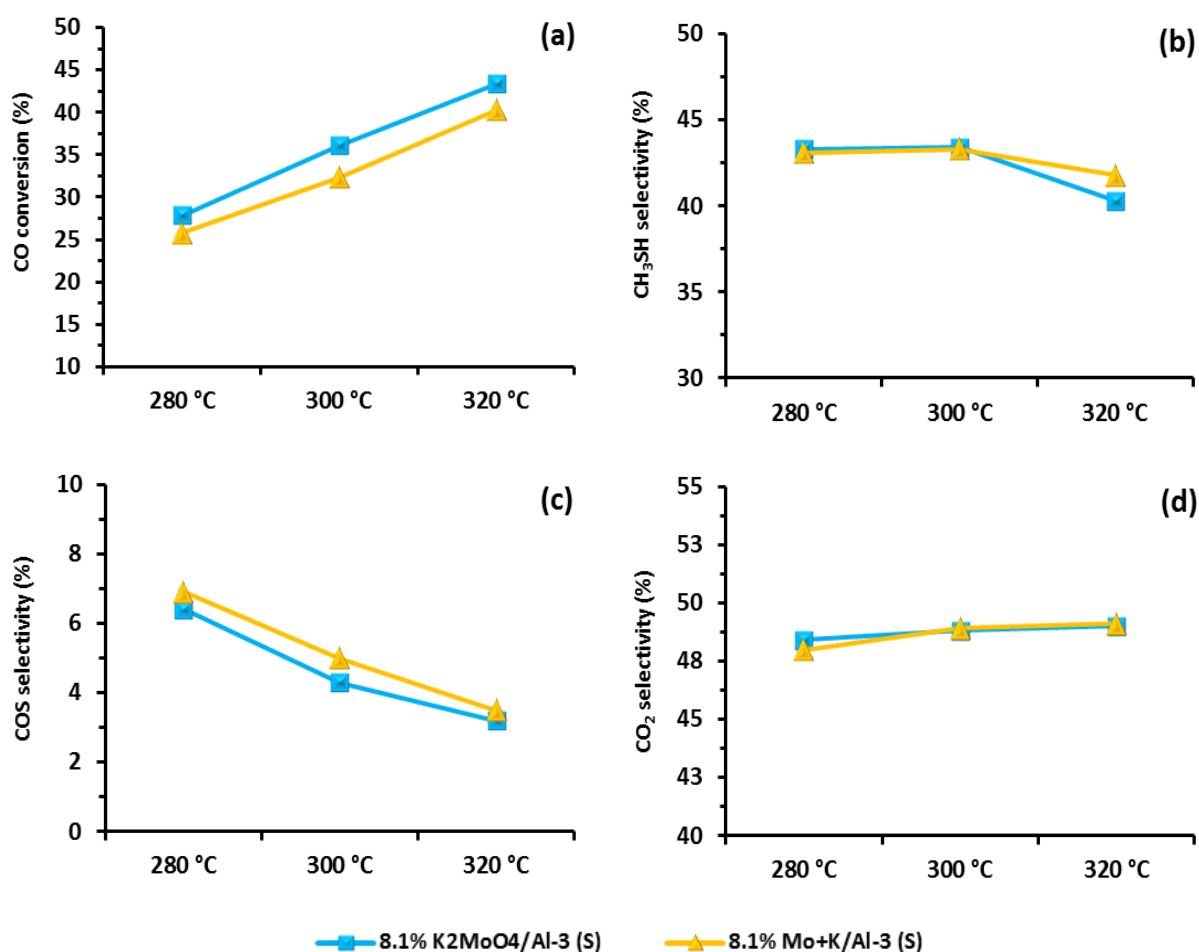


Figure 4.2. Evolution of the CO conversion (a) and selectivity in CH₃SH (b), COS (c) and CO₂ (d) of 8.1% Mo+K/Al-3 and 8.1% K₂MoO₄/Al-3 catalysts.

4.1.1.3. Effect of the alkali promoter (K or Na) and the state of the precursor incorporated (oxidic or pre-sulfided)

8.1% K₂MoO₄/Al-3, 8.1% Na₂MoO₄/Al-3 and 8.3% K₂MoS₄/Al-3 catalysts are examined in this section. 8.1% K₂MoO₄/Al-3 and 8.1% Na₂MoO₄/Al-3 are compared in order to analyze the effect of a different alkali promoter. Then, 8.1% K₂MoO₄/Al-3 and 8.3% K₂MoS₄/Al-3 are compared with the aim to investigate the influence of the initial state of the precursor impregnated, either oxidic state (K₂MoO₄) or presulfided state (K₂MoS₄). The catalytic performance of the three catalysts is displayed in figure 4.3.

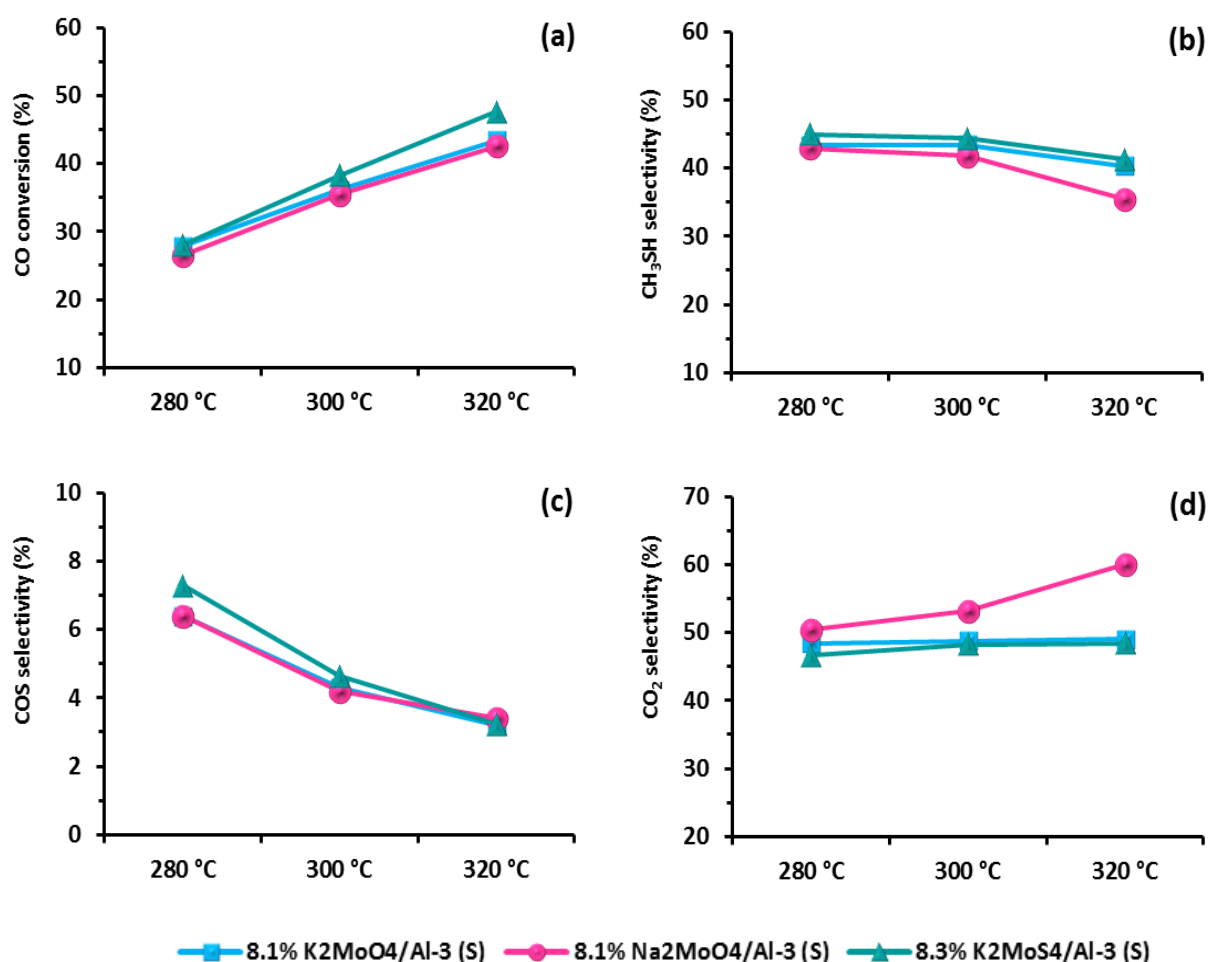


Figure 4.3. Evolution of the CO conversion (a) and selectivity in CH₃SH (b), COS (c) and CO₂ (d) of 8.1% K₂MoO₄/Al-3, 8.1% Na₂MoO₄/Al-3 and 8.3% K₂MoS₄/Al-3 catalysts.

When comparing 8.1% K₂MoO₄/Al-3 and 8.1% Na₂MoO₄/Al-3 catalysts, no difference in CO conversion and COS selectivity is observed, nevertheless a different trend in CH₃SH and CO₂ selectivities is showed. A decrease in CH₃SH selectivity (5%) and an increase in CO₂ selectivity (11%) is obtained with the catalyst promoted with Na, particularly at high temperature (320 °C). Additionally, no CH₄ production is observed with this solid but small amounts of CS₂ and CH₃SCH₃ (0.2% and 1.0% respectively at 320 °C). These results mean that when replacing K by Na, the reactions of production of CO₂, either by hydrolysis of COS (reaction 31) or CO (WGS) (reaction 32) are favored over the hydrogenation of COS to CH₃SH. CH₄ absence and the decrease in CH₃SH selectivity are evidence of the lower hydrogenating effect of Na compared to K based catalysts. Besides, the reactions of disproportionation of COS (reaction 30) and CH₃SH (reaction 36) also takes place since CS₂ and CH₃SCH₃ are observed among the

byproducts of reaction with the Na based catalyst.

The other comparison is made between the samples 8.1% K₂MoO₄/Al-3 and 8.3% K₂MoS₄/Al-3. Only slight differences are observed in terms of selectivities for these two solids. 8.3% K₂MoS₄/Al-3 is slightly more selective towards CH₃SH and less selective to CO₂ while the selectivity toward COS remains similar. The most noticeable difference is observed in terms of CO conversion, especially at 320 °C where the catalysts 8.3% K₂MoS₄/Al-3 is about 4% more active than 8.1% K₂MoO₄/Al-3. This difference is more evident regarding the productivity in CH₃SH which was increased in 4% at 280 °C, 8% at 300 °C and 11% at 320 °C when using the catalysts 8.3% K₂MoS₄/Al-3 (CH₃SH productivity = 140.7 g.h⁻¹.L⁻¹). In conclusion of this part, it is remarkable that the use of potassium as promoter is more advantageous than using sodium since a higher CH₃SH selectivity and a lower CO₂ selectivity are achieved. By the other hand, when comparing 8.1% K₂MoO₄/Al-3 with its presulfided counterpart 8.3% K₂MoS₄/Al-3, the latter is a slightly more active solid towards the production of CH₃SH.

4.1.2. Characterization of sulfided reference catalysts. Comprehension and approach to the active phase

As stated before, a part of the present work aims at investigating the nature of the active phase playing an important role in the catalytic performance. With this purpose, in this subsection, correlations of the sulfided reference solids catalytic behavior with characterization results of these solids at the active state are proposed from the use of X-ray photoelectron spectroscopy and transmission electron microscopy techniques. The catalysts are characterized after a pretreatment *ex situ* (method S/RS as described in chapter 2), similar to that used before each catalytic test.

4.1.2.1. X-ray photoelectron spectroscopy (XPS)

This technique was used in order to estimate the surface composition and oxidation state of activated solids. Mo3d-S2s spectra of sulfided reference catalysts are shown in figure 4.4. As

can be seen, different distributions of Mo species are identified for sulfided reference catalysts as a function of the presence or absence of K and the way in which K and Mo are incorporated on the support. The Mo3d core level of sulfided reference K-Mo catalysts is decomposed in six components, three components regarding sulfur species - instead of two for 8.1% Mo/Al-3 - and also three components concerning Mo species.

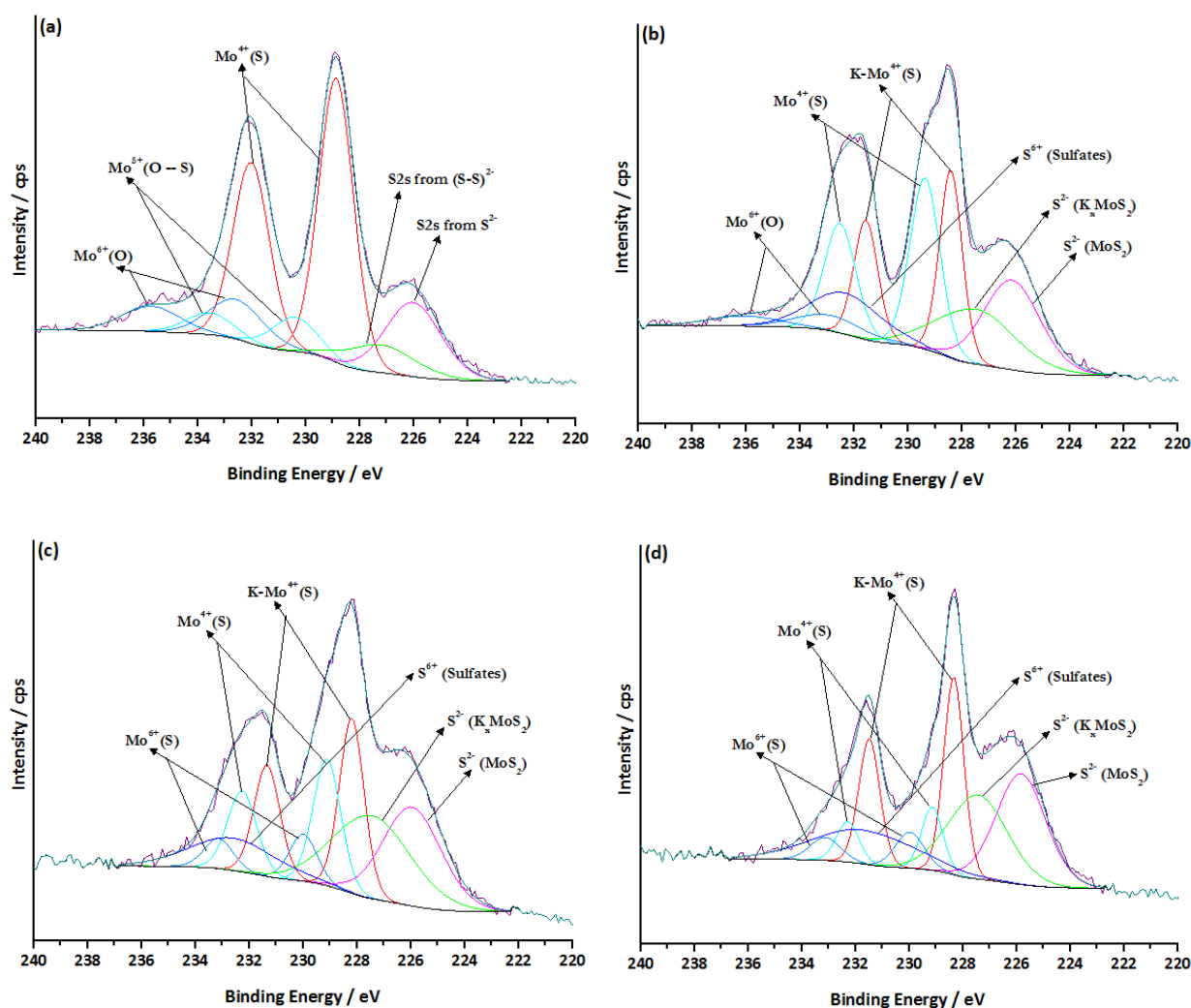


Figure 4.4. XPS spectra of Mo3d-S2s core level of sulfided reference catalysts. (a) 8.1% Mo/Al-3, (b) 8.1% Mo+K/Al-3, (c) 8.1% K₂MoO₄/Al-3 and (d) 8.3% K₂MoS₄/Al-3

The exact position and distribution of these species are listed in table 4.2. Starting with 8.1% Mo/Al-3 catalyst, as usually reported for classical CoMo hydrotreatment catalysts [5], this sample exhibits three well known Mo doublets whose Mo3d_{5/2} components are placed at 228.9 eV, 230.4 eV (S) and 232.6 eV and these three doublets represent three oxidation states of Mo. According to several authors these species correspond to Mo⁴⁺, Mo⁵⁺ and Mo⁶⁺

[5–10]; the first contribution is attributed to MoS₂ phase, the second contribution is attributed to Mo⁵⁺ surrounded by oxygen and sulfur atoms (intermediate phase) and the contribution at higher binding energy is assigned to oxidized species. For 8.1%Mo/Al-3 the contributions of S2s at about 227.4 eV and 226 eV are assigned to bridging disulfide (S-S)²⁻ ligands and sulfide S²⁻ ligands respectively. The latter component is consistent with the S²⁻ type ligands present in MoS₂, whereas (S-S)²⁻ entities are present in oxysulfide compounds containing Mo⁵⁺ species.

Table 4.2. Binding energies and relative at.% of Mo species of sulfided reference catalysts

CATALYST	Mo 3d _{5/2} binding energy (eV) of			Relative at.% of Mo species		
	Mo ⁴⁺ (S)	Mo ⁵⁺ (O-S)	Mo ⁶⁺ (O)	Mo ⁴⁺ (S)	Mo ⁵⁺ (O-S)	Mo ⁶⁺ (O)
8.1% Mo/Al-3	228,9	230,4	232,6	72,1	11,6	16,3
	<i>K-Mo⁴⁺(S)</i>	<i>Mo⁴⁺(S)</i>	<i>Mo⁶⁺(O)</i>	<i>K-Mo⁴⁺(S)</i>	<i>Mo⁴⁺(S)</i>	<i>Mo⁶⁺(O)</i>
8.1% Mo+K/Al-3	228,4	229,4	232,9	40,8	49,3	9,9
	<i>K(Na)-Mo⁴⁺(S)</i>	<i>Mo⁴⁺(S)</i>	<i>Mo⁶⁺(S)</i>	<i>K(Na)-Mo⁴⁺(S)</i>	<i>Mo⁴⁺(S)</i>	<i>Mo⁶⁺(S)</i>
8.1% Na ₂ MoO ₄ /Al-3	228,4	229,2	230,2	48,3	43,1	8,6
8.1% K ₂ MoO ₄ /Al-3	228,2	229,1	230,0	48,0	38,0	14,0
8.3% K ₂ MoS ₄ /Al-3	228,3	229,1	230,0	60,9	21,7	17,4

These two components of the S2s core level are in agreement with the two components obtained from the decomposition of XPS S2p core level as shown in figure 4.5.

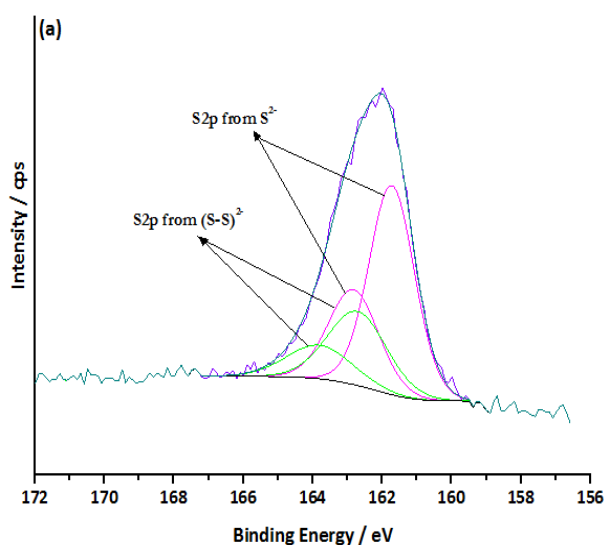


Figure 4.5. XPS spectra of S2p core level of the sulfided 8.1% Mo/Al-3

For catalysts containing K(Na) regarding molybdenum species, the decomposition reveals also the presence of three components.

- 8.1% Mo+K/Al-3 solid exhibits three Mo doublets in which the Mo3d_{5/2} components are situated at 228.4 eV, 229.2 eV and 232.9 eV. The latter component is attributed to Mo⁶⁺ in oxidic environment as for the 8.1% Mo/Al-3 catalyst. The position of the second component matches very well with this assigned to Mo⁴⁺ species in the form of MoS₂, found it as well in the catalyst without K. The component at lower binding energy was not identified in the sample that does not contain K.

- 8.1% K₂MoO₄/Al-3, 8.3% K₂MoS₄/Al-3 and 8.1% Na₂MoO₄/Al-3 catalysts exhibit also three Mo components. The component situated at 229.1±0.1 eV is attributed to “classical” MoS₂ phase well known for hydrotreating catalysts and identified in the non-promoted catalyst. The component positioned at lower binding energy (228.3±0.1) was also presented in 8.1% Mo+K/Al-3 solid and not in 8.1% Mo/Al-3. It can be reasonable to relate this component to a species interacting with potassium (sodium) since it is present in all solids containing K(Na) and absent in the solid in which K is also absent. Moreover, it can be noticed that this binding energy value at 228.3±0.1, obtained for Mo3d_{5/2}, shifted towards lower value compared to classical MoS₂ phase indicates metallic properties. These metallic properties could explain the by-product CH₄ observed in low quantity for K based catalysts since MoC with metallic properties is known to produce CH₄ during Fisher-Tropsh synthesis [11].

The third component, different to that found in 8.1% Mo/Al-3 and 8.1% Mo+K/Al-3 samples, is placed at 230.2±0.2 eV and is ascribed to Mo⁶⁺ in a sulfidic surrounding. This attribution is made based in the XPS results of fresh K₂MoS₄-based catalysts presented in chapter 3. For this series of catalysts, the component positioned at 230.2 eV was assigned to Mo⁶⁺ species bonded to sulfur atoms, namely K₂MoS₄. Thus, for the sulfided reference catalysts it seems reasonable to assigned the component at 230.2±0.2 eV at K(Na)₂MoS₄ phase, corresponding to the initial K₂MoS₄ phase in 8.3% K₂MoS₄/Al-3 or appearing as an intermediate during the sulfidation in 8.1% K₂MoO₄/Al-3 and 8.1% Na₂MoO₄/Al-3 catalysts.

Nature of the K-MoS₂ phase

In K(Na)Mo based sulfide catalysts, decomposition of Mo3d XPS level brings out a particular MoS₂ phase (K-MoS₂), in interaction with potassium, for which Mo binding energy is shifted towards lower values by 0.8 eV with respect to the Mo 3d level attributed to MoS₂.

Gutiérrez *et al.* [12] when working with a sulfided K₂MoO₄/SiO₂ catalyst for the reaction of disproportionation of COS, suspected the presence of an interaction between potassium and MoS₂ phase. They assume that a fraction of K⁺ adsorbs on MoS₂ resulting of K⁺-decorated MoS₂ phase formation where K cations would be distributed randomly on the MoS₂ surface, without modifying the crystalline structure of the MoS₂ cluster, doing impossible to differentiate the pure MoS₂ phase and that decorated by K⁺ by means of XRD. According to Gutiérrez *et al.* [12], K⁺-decorated MoS₂ phase formation was supported by work of Chen *et al.* [13] dealing with the study of sulfided (K)(Li)(Co)Mo SiO₂ supported catalysts (obtained after reaction for the direct synthesis of methanethiol) characterized by XPS. Nevertheless no relevant information can be noticed on the K-MoS₂ phase. The main conclusions concerned the influence of potassium on the Mo^V/Mo^{VI} and (S⁻+S²⁻)/SO₄²⁻ ratios increasing with the deposit of potassium.

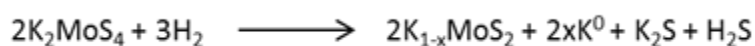
On the other hand, it is very well known that molybdenum disulfide (MoS₂) features a layered structure, in which the atoms are covalently bonded to form two dimensional layers that are stacked together through weak van der Waals interactions. The weak interlayer interaction allows foreign ions or molecules to be introduced between the layers through intercalation. In this regard, numerous works have been reported concerning the intercalation of ions or molecules into the structure of MoS₂ layers and among those, the intercalation of lithium has been widely discussed, mainly due to its application as electrode materials for batteries with high energy storage [14–19].

The intercalation of an alkali metal like lithium into MoS₂ layers (Li_xMoS₂) may be described as an ion-electron transfer reaction. The electrons from the lithium (guest) are transferred to the unoccupied energy levels of the MoS₂ (host) which are principally transition metal *d*

bands [16]. However, the intercalation actually may also induce important structural changes in the host at high doses of alkali metal. Upon intercalation, the local coordination geometry of the Mo centers of the host lattice changes from trigonal prismatic (2H-MoS₂) to distorted octahedral (1T-MoS₂) and to the clustering of Mo atoms due to displacements from their ideal positions in the layer. This 2H to 1T phase transition is accompanied by considerable changes in the band structure and an increased electron density on the sulfur atoms of the MoS₂ lattice [20], [21]. Thus, the induced electronics and structural changes of MoS₂ by the incorporation of Li have been studied by Raman spectroscopy and X-ray photoelectron spectroscopy. After intercalation with Li, the Raman spectra show drastic changes by the presence of new Raman lines and the decrease in intensity of some existing lines [15], [16]. XPS results obtained by Papageorgopoulos *et al.* [17] performed on a Li-intercalated MoS₂ single crystal showed the shift of binding energies of Mo 3d core levels by about 1.1 eV because of the increasing coverage of lithium which can be explained by the 2H → 1T phase transition [16], [17]. According to [17], increase in Li deposition caused also a broadening of the S2p peak which may be fitted by two independent components separated by 0.8 eV.

The replacement of Li by K cation has been studied in a similar approach to obtain K_xMoS₂ phase [21], [22]. From studies on a single crystal (hydrated) K_xMoS₂, the authors suggest that in contrast to 2H-MoS₂, every Mo center in this compound is octahedrally surrounded by six sulfur ligands, whereas the hydrated K⁺ cations are located in the van der Waals gap between the layers. The octahedral structure [MoS₆] of this species depends largely on the amount of potassium located between the layers. Thus, if the number of K⁺ cations in the van der Waals gap decreases, the stabilization of the octahedral Mo coordination becomes less effective and an increased tendency for a reorientation to the trigonal prismatic coordination mode can be observed.

The way for preparing the intercalated compound K_xMoS₂ consists in the initial sulfidation of K₂MoO₄ with H₂S to obtain K₂MoS₄, followed by reduction of this latter species to produce K_xMoS₂ by the following reaction (where x<1):



Based on literature data on the formation of $K_x\text{MoS}_2$ intercalated phase and taking into account the results obtained by XPS by Papageorgopoulos [17] on Li intercalated MoS_2 compound, we propose that for $K(\text{Na})\text{Mo}$ sulfided catalysts, the $\text{Mo}3d_{5/2}$ component positioned at 228.4 eV is an evidence of the $K(\text{Na})_x\text{MoS}_2$ intercalated phase corresponding to the MoS_2 phase with $K(\text{Na})$ cations intercalated between the MoS_2 layers (named $K(\text{Na})\text{-Mo}^{4+}$ in table 4.1). From our knowledge, it is the first time that such a phase is put in evidence by XPS on sulfided $K(\text{Na})\text{Mo}$ supported catalysts.

The formation of $K_x\text{MoS}_2$ intercalated phase could be also supported by the decomposition of $\text{S}2p$ photopeak. The decomposition of the $\text{S}2s$ core level of the K-promoted catalysts 8.1% $\text{K}_2\text{MoO}_4/\text{Al-3}$ is shown in figure 4.6 as example. Additionally, the positions and distribution of the sulfur species detected for the sulfided reference catalysts are listed in table 4.3.

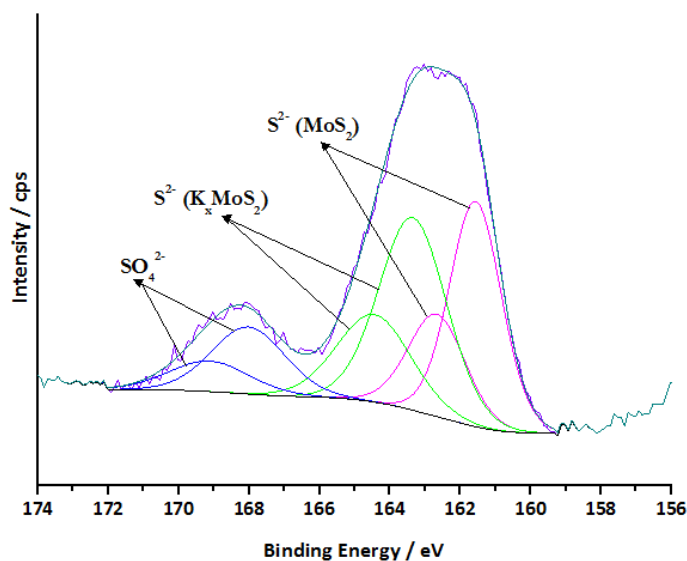


Figure 4.6. XPS spectra of $\text{S}2p$ core level of the sulfided 8.1% $\text{K}_2\text{MoO}_4/\text{Al-3}$

The three different species of the $\text{S}2p$ core level are in agreement with the three components proposed for the decomposition of XPS $\text{S}2s$ core level in the $\text{Mo}3d\text{-S}2s$ spectra shown in figure 4.4. Compared to the non-promoted solid, a new component at higher binding energy (167.9 ± 0.2 eV) is detected for promoted catalysts. This component is attributed to the presence of sulfate species (SO_4^{2-}), in agreement with literature data [10].

The component at lower binding energies (161.7 ± 0.2 eV) is identified for both, non-promoted and K-promoted solids. This component is thus assigned to S^{2-} species present in MoS_2 . A second component at 163.4 ± 0.2 eV appears on the K-promoted catalysts. This component obviously cannot be related to $(S-S)^{2-}$ species as in 8.1%Mo/Al-3. Indeed, for K containing catalysts, Mo3d decomposition does not reveal the presence of oxysulfide species (Mo^{5+}) correlated to $(S-S)^{2-}$ species. Papageorgopoulos [17] reported that Li deposition between MoS_2 layers caused a shift of the S2p photoemission peak to higher BE by 0.35 eV and that further increase of Li deposition cause a broadening of the S2p peak which may be fitted by two independent components. We observed the widening of S2p peak after introduction of potassium and also a shift towards higher binding energies. We propose that this component with unusual binding energy is also linked to the presence of $K(Na)_xMoS_2$ intercalated species.

Table 4.3. Binding energies and relative at.% of S species of sulfided reference catalysts

CATALYST	Binding energy (eV) of S 2p _{3/2}			Relative at.% S		
	S ²⁻	(S-S) ²⁻	SO ₄ ²⁻	S ²⁻	(S-S) ²⁻	SO ₄ ²⁻
8,1% Mo/Al-3 (S)	161,7	162,7	--	68,6	31,4	--
	S ²⁻ (MoS ₂)	S ²⁻ (K _x MoS ₂)	SO ₄ ²⁻	S ²⁻ (MoS ₂)	S ²⁻ (K _x MoS ₂)	SO ₄ ²⁻
8,1% Mo+K/Al-3 (S)	161,8	163,4	168,1	40,7	37,6	21,7
8,1% Na ₂ MoO ₄ /Al-3 (S)	161,7	163,4	167,8	51,1	38,4	10,5
8,1% K ₂ MoO ₄ /Al-3 (S)	161,6	163,3	168,0	39,7	43,5	16,7
8.3% K ₂ MoS ₄ /Al-3 (S)	161,6	163,3	167,7	43,6	33,5	22,9

Moreover the K2p photopeak does not show any change regarding its binding energy value before or after sulfidation, as shown in Annex 2, indicating the potassium preserves as K⁺ species in the intercalated K_xMoS₂ phase.

Correlation between catalytic performance and active K_xMoS₂ phase

Regarding the Mo distribution (see table 4.2), for the non-promoted catalyst, the predominant phase (over 70%) is MoS₂ and Mo oxysulfide and oxidized are the minority phases. In the more active K(Na) promoted solid, different relative amount of K_xMoS₂ phase have been found : 8.1% Mo+K/Al-3, 40% of the Mo corresponds to K_xMoS₂ phase whereas in K(Na)₂MoO₄ and K₂MoS₄-based catalysts, the major phase is K_xMoS₂. The relative distribution of Mo species obtained by XPS Mo3d decomposition could then indicate that the quantity of the intercalated K_xMoS₂ phase could be linked to the CO conversion.

Nevertheless, two important parameters have to be taken into account in order to correlate the relative quantity of K_xMoS₂ with the catalytic performance of sulfided reference solids:

- **The amount of Mo phase introduced into the reactor charged with 30 ml of catalyst**, related to the density of the solid. This data is labeled as n_{Mo} in table 4.4.
- **The % of Molybdenum species detected by XPS**. Indeed, as showed in chapter 3 the Mo % detected by XPS has been calculated. At the fresh state, characterizations have highlighted the formation of big crystallites leading to lower quantity of Mo detected at the surface. For sulfide catalysts, the same trend is observed with still much less of Mo % detected by XPS (table 4.4). From these observations, we consider that the active phase originates from the Mo species detected by XPS. The big particles not detected by XPS are then considered to be inactive.

From these calculations, the quantity of Mo (n_{Mo}) present in the reactor, detected by XPS is then obtained.

The CO conversion per number of Mo atoms charged in the reactor and detected by XPS ($\%X_{CO}/n_{Mo}$) was plotted against the relative percent of K_xMoS₂ and MoS₂. The obtained plots are displayed in figure 4.7 and 4.8. Figure 4.7 shows the CO conversion ($\%X_{CO}/n_{Mo}$) as a function of the relative % of MoS₂ phase. It exists an inverse linear correlation between $\%X_{CO}/n_{Mo}$ of K(Na)-promoted catalysts and the relative % of MoS₂ phase. In fact, higher the

relative % of this phase, lower the CO conversion, highlighting the fact that this phase is not responsible of the good catalytic performance of K-promoted catalysts. The opposed behavior is observed when %X_{CO}/n_{Mo} is plotted against the relative % of K(Na)_xMoS₂ phase (figure 4.7). Indeed, higher the relative % of K(Na)_xMoS₂ phase, higher the CO conversion. These results suggest that CO conversion is governed by the amount of K(Na) intercalated MoS₂ phase in catalysts loaded at 8.1 wt.% of Mo.

Table 4.4. Values of amount of Mo charged in the reactor, detected by XPS (n_{Mo})

CATALYST	Catalyst density (g.mL ⁻¹)	m _{Mo} charged in reactor (g)	n _{Mo} charged in reactor	Mo % detected by XPS	n _{Mo} detected by XPS
8.1% Mo/Al-3 (S)	0,48	1,152	7,2E+21	71,4	5,2E+21
8.1% Mo+K/Al-3 (S)	0,53	1,264	7,9E+21	38,2	3,0E+21
8.1% Na ₂ MoO ₄ /Al-3 (S)	0,49	1,184	7,4E+21	31,9	2,4E+21
8.1% K ₂ MoO ₄ /Al-3 (S)	0,52	1,256	7,9E+21	29,2	2,3E+21
8.3% K ₂ MoS ₄ /Al-3 (S)	0,63	1,512	9,5E+21	16,5	1,6E+21

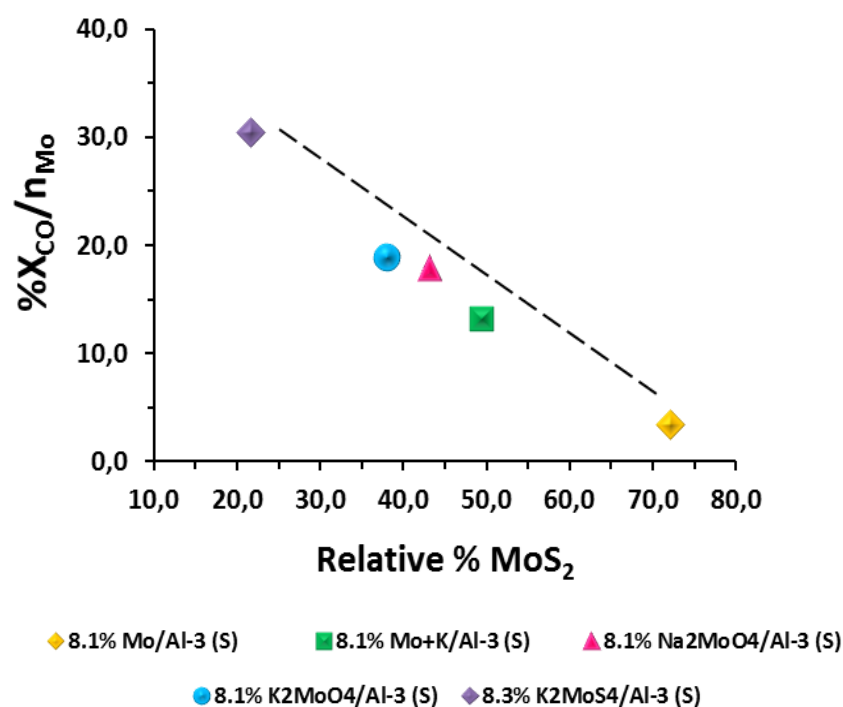


Figure 4.7. Correlation between CO conversion and relative% of MoS₂ phase in sulfided reference catalysts. %X_{CO} at 320 °C

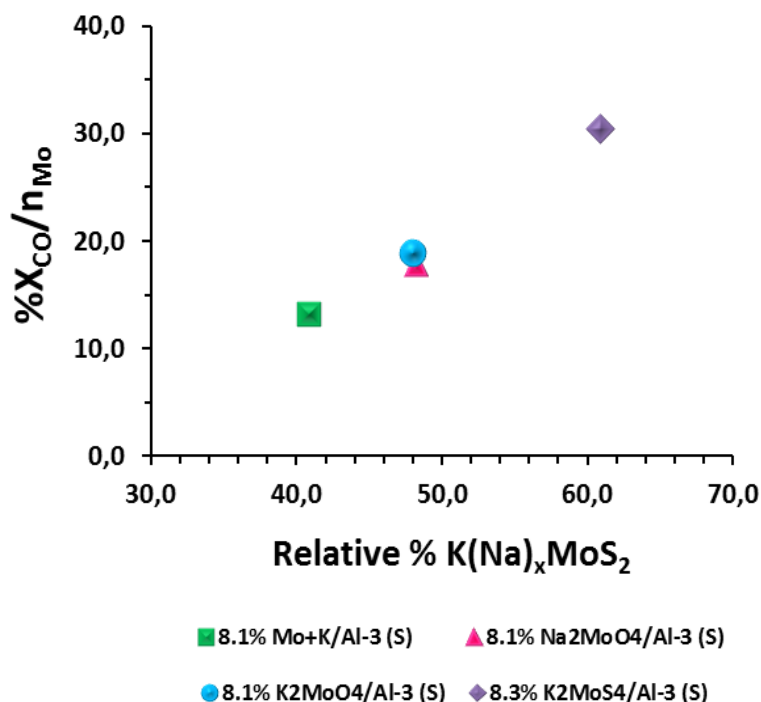


Figure 4.8. Correlation between CO conversion and relative% of $K_x MoS_2$ phase in sulfided reference catalysts. % X_{CO} at 320 °C

A good correlation is also observed when plotting the CH₃SH productivity against the relative% of $K(Na)_x MoS_2$ phase (see figure 4.9). In fact, CH₃SH productivity increases with the amount of $K_x MoS_2$ for K-promoted catalysts. The beneficial effect of promoter type (K or Na) is also revealed by this plot. If we compare 8.1% K₂MoO₄/Al-3 and 8.1% Na₂MoO₄/Al-3 catalysts, for the same amount of K(Na)-MoS₂, the productivity of the K-promoted solid is considerably higher than that of Na-promoted solid, meaning that among those two promoters, K is more efficient. Briefly, the presence of $K_x MoS_2$ species is required to reach a higher CO conversions and also higher CH₃SH selectivity.

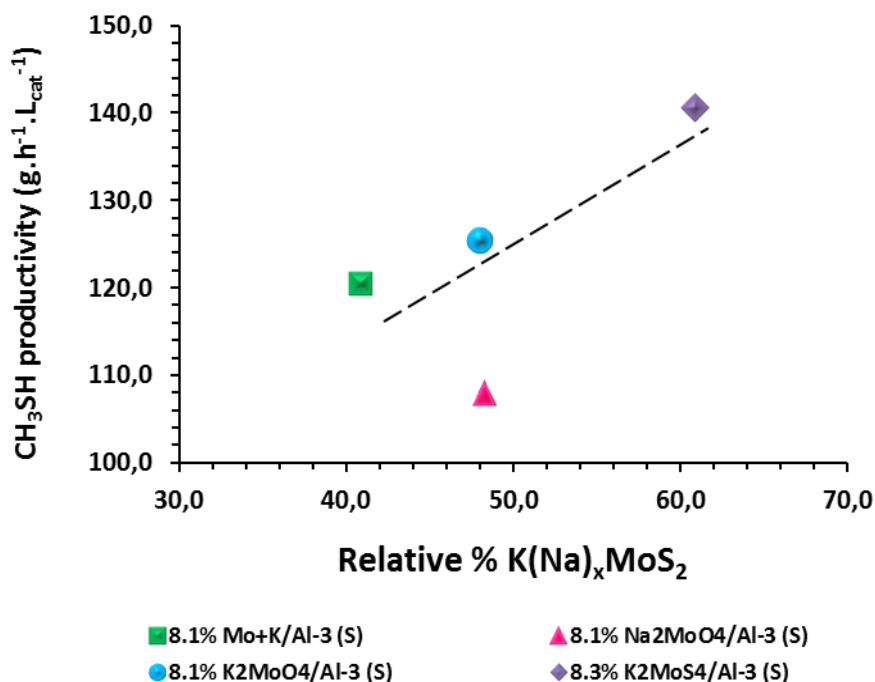


Figure 4.9. Correlation between CH₃SH productivity and Mo phases distribution in sulfided reference catalysts. %X_{CO} at 320 °C

4.1.2.2. High resolution transmission electron microscopy (HRTEM)

With the aim to determine the morphology of the active phase, sulfided reference catalysts were analyzed using high resolution transmission electron microscopy HRTEM. As example, typical HRTEM images of three reference catalysts are shown in figure 4.10. The micrographs display the presence of MoS₂ layers in the three analyzed samples. Images of 8.1%Mo/Al-3 (a) and 8.3% K₂MoS₄/Al-3 (b) samples seem very similar with bent MoS₂ slabs poorly stacked. In contrast, 8.1% K₂MoO₄/Al-3 (c) sample shows also bent MoS₂ slabs but apparently longer, with greater stacking and with a better distribution along the surface than the former solids. Moreover, on K-Mo catalysts, TEM image (d) evidence also the presence of big particles discussed in the XPS section and considered as inactive.

The statistical analysis of these three samples was carried out in order to determine the average slabs length and the average stacking degree. The obtained histograms are exposed in figure 4.11 and 4.12. For the three catalysts evaluated, the slab length distribution is

centered between 2 and 5 nm and with an average stacking degree between 1,5 and 2,5. When comparing the non-promoted and promoted-K samples, the former sample exhibits the lower slab distribution (2,9 nm) while for 8.3% K₂MoS₄/Al-3 and 8.1% K₂MoO₄/Al-3 samples, this values are higher (3,9 and 4,9 nm respectively). This observation suggests a possible effect of potassium over the slab length but also over the stacking degree since when potassium is incorporated, the stacking degree (in 8.1% K₂MoO₄/Al-3 samples) is increased. This effect of intercalation was noticed by Afanasiev [14] who indicated an expected change of the stacking mode and length of MoS₂ layers in intercalated potassium MoS₂ phase. These increases appear as a drawback considering the preparation of highly active HDS catalysts whose catalytic activity is mostly due to the edges of the MoS₂ slabs. By contrast, for CH₃SH synthesis by reaction of syngas and hydrogen sulfide, at this stage of the study, the location of the active sites is still unknown. The catalytic performance has been shown to be correlated to the intercalated phase leading however to average slab morphology with higher stacking and/or length. Observation of TEM images does not allow differentiating between MoS₂ and the active K_xMoS₂ phase. In this case the “hypothetic” number of active sites supposed to be located on the edges of the K_xMoS₂ slabs could not be estimated from basic TEM analysis. Work is under progress to go further trying to correlate (or not) the number of edge sites to catalytic activities.

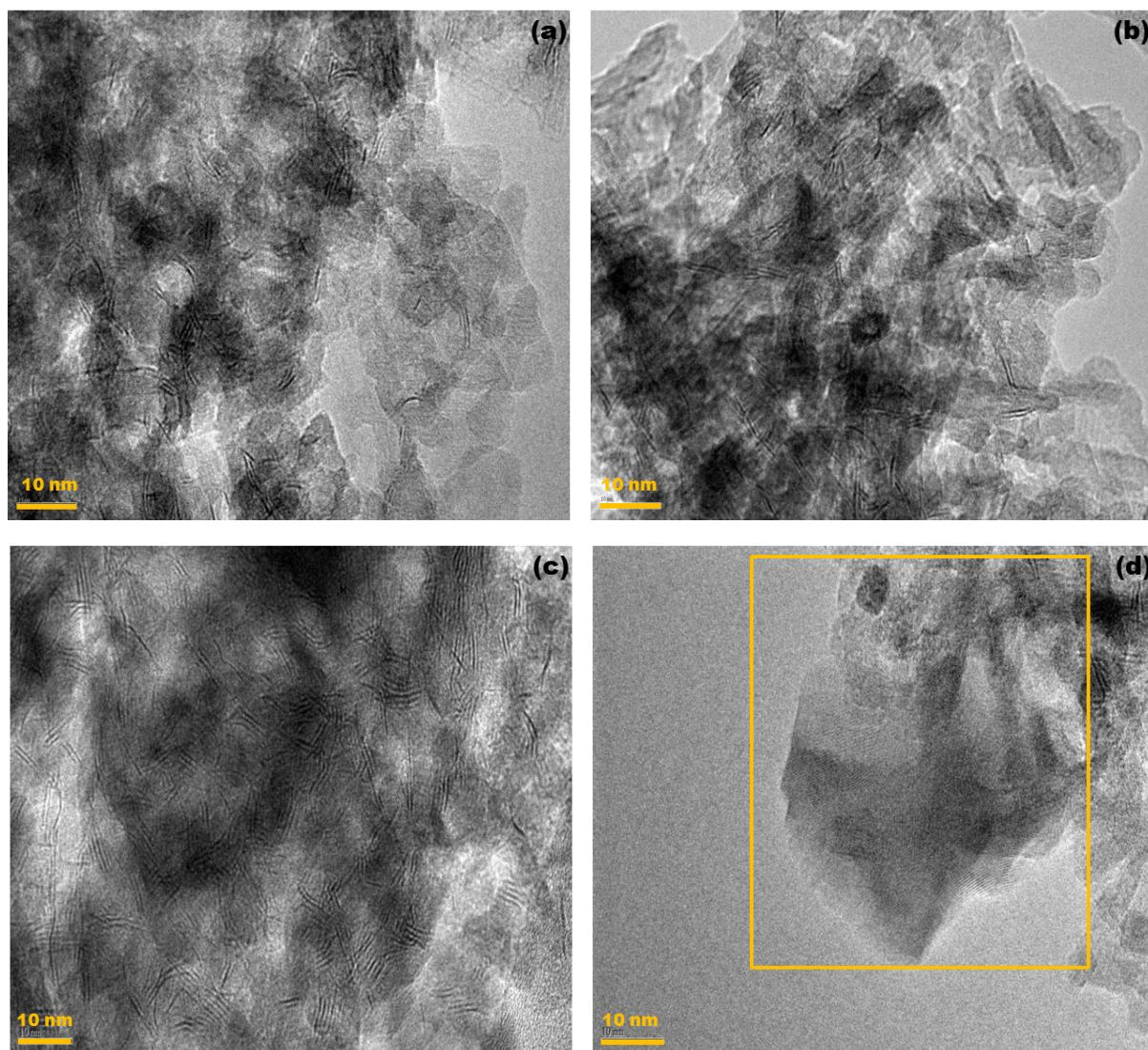


Figure 4.10. High resolution TEM images of sulfided catalysts, (a) 8.1% Mo/Al-3(S), (b) 8.3% K₂MoS₄/Al-3(S), (c) 8.1% K₂MoO₄/Al-3(S) (MoS₂ slabs) and (d) 8.1% K₂MoO₄/Al-3(S) (big particles)

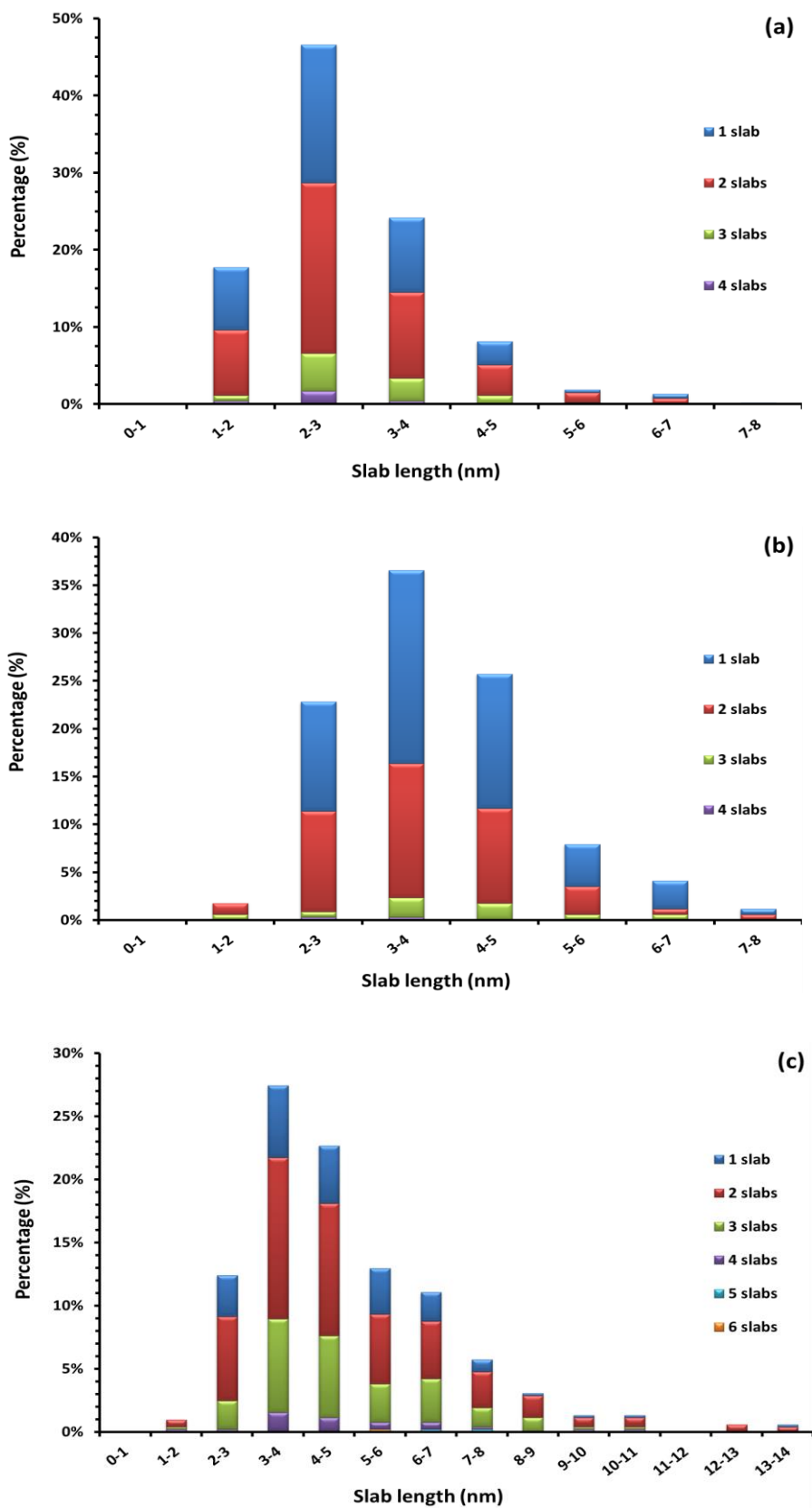


Figure 4.11. MoS₂ distribution by slab length of (a) 8.1% Mo/Al-3(S), (b) 8.3% K₂MoS₄/Al-3(S) and (c) 8.1% K₂MoO₄/Al-3(S)

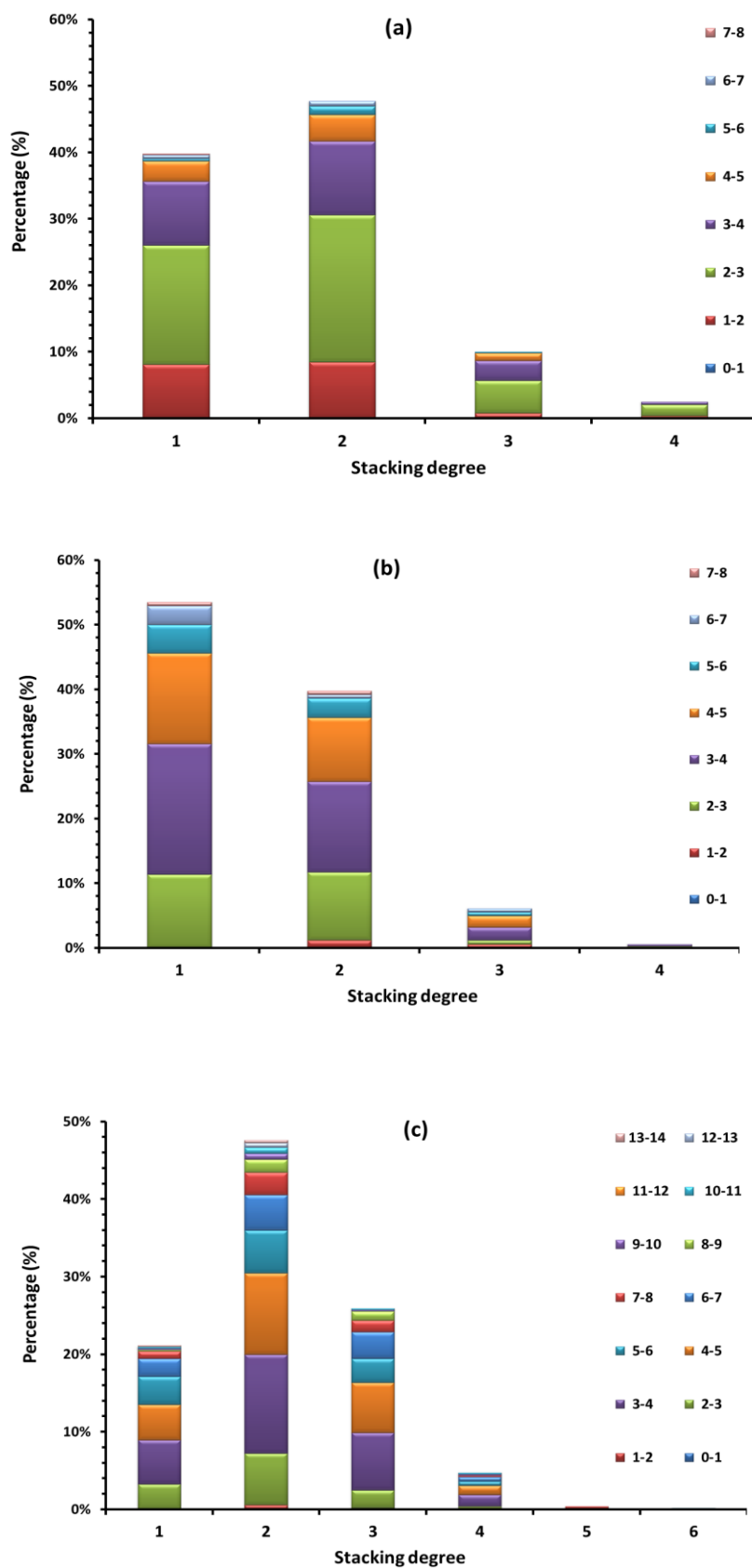


Figure 4.12. MoS₂ distribution by stacking degree of (a) 8.1% Mo/Al-3(S), (b) 8.3% K₂MoS₄/Al-3(S) and (c) 8.1% K₂MoO₄/Al-3(S)

4.2. K₂MoO₄-BASED CATALYSTS

After the study of the catalytic performance and its correlation with the presumed active phase in section 4.1 by using catalytic systems composed by Mo and K-Mo with the same Mo loading and using the same carrier, this section focusses in the improvement of the catalytic performance. With this purpose, we studied a series of catalysts prepared by using the precursor K₂MoO₄ at different Mo loadings (the maximum allowed loading, as a function of pore volume of support and the solubility of the impregnated salt) and on different carriers with different acidic-basic properties.

4.2.1. Catalytic test of sulfided K₂MoO₄-based

Table 4.5 shows the catalytic performance of K₂MoO₄-based solids for the synthesis of CH₃SH from syngas/H₂S mixture at 320 °C. The whole data comprising the three temperatures evaluated is included in annexes (annex 3).

Table 4.5. *Catalytic performance of K₂MoO₄-based catalysts in the reaction of syngas and H₂S*

CATALYST	X _{CO} (%)	Selectivity (%)			CH ₃ SH Productivity (g.h ⁻¹ .L ⁻¹)	CH ₃ SH Yield (%)
		CH ₃ SH	COS	CO ₂		
13,5% K ₂ MoO ₄ /Al-1 (S)	53,0	45,3	2,6	49,0	172,0	24,0
17,6% K ₂ MoO ₄ /Al-2 (S)	42,1	46,2	3,6	48,2	141,9	19,4
17,9% K ₂ MoO ₄ /Al-3 (S)	59,3	45,9	1,6	49,3	194,6	27,2
18,0% K ₂ MoO ₄ /Si-1 (S)	45,3	48,6	2,3	47,6	157,5	22,0
23,5% K ₂ MoO ₄ /Si-2 (S)	18,7	47,7	6,9	42,7	63,6	8,9
20,4% K ₂ MoO ₄ /Hap (S)	18,9	43,6	10,8	43,2	59,0	8,2
22,1% K ₂ MoO ₄ /HapNa (S)	21,3	44,0	10,3	42,5	66,9	9,4

REACTION CONDITIONS: 320 °C, CO:H₂:H₂S = 1:2:1, 1333,33 h⁻¹, 10 bar

Generally, as a function of the temperature, CO conversion is increased and the selectivities towards CH₃SH and CO₂ are not affected, meanwhile the selectivity towards COS decreases for this series of catalysts. The higher conversions are reached on aluminas and Si-1 supported catalysts while on Si-2 and Hap supported solids, the conversions are at least two

times lowers. This difference could be linked to the initial crystallites size of K₂MoO₄ phase on Hap, HapNa and Si-2 based catalysts because for these three solids the XRD patterns showed very well crystallized K₂MoO₄ phase. This observation supports again the fact that big crystallites are not active.

Regarding the selectivity, a similar trend is observed for the more active catalysts (those supported on aluminas and Si-1). CO converts about 46% in CH₃SH, about 2% in COS and about 48% in CO₂. For the Si-2 and Hap supported solids, a decrease in CO₂ selectivity (near to 5%) is observed. A slightly decrease in CH₃SH selectivity is also observed on Hap supported samples at expense of a higher COS selectivity. Among 1,5 and 3% of CH₄ is also observed over all the samples.

The observed tendencies are in agreement with the results obtained using K-promoted Mo-based reference catalysts. This suggests that COS is a primary product, coming from reaction (26) which then hydrogenated to CH₃SH and H₂O by reaction (27), and that CO₂ originates from water gas shift reaction (32) or by hydrolysis of COS (31) and CH₄ originates from the hydrogenation of CH₃SH [2], [13]. The different trends in selectivity observed for Si-2 solid and hydroxyapatite solids suggest an influence of the support since different properties were observed for these three different kinds of solids. Anyhow, a lower hydrogenation of COS to CH₃SH is detectable when K₂MoO₄ is supported on hydroxyapatite solids. The higher CH₃SH productivity reached is 194,6 g_{CH₃SH}.h⁻¹.L_{cat}⁻¹ with the solid 17.9% K₂MoO₄/Al-3. Thus, by increasing the Mo loading, the CH₃SH productivity is improved in 40%.

4.2.2. Characterization of sulfided K₂MoO₄-based catalysts

The characterization results of K₂MoO₄-based catalysts after sulfidation are presented in this subsection. Raman spectroscopy, X-ray photoelectron spectroscopy and high resolution transmission electron microscopy were used with this purpose.

4.2.2.1. Raman spectroscopy

Raman spectra of the catalysts after sulfidation are presented in figure 4.13. The lines in the region 350-500 cm⁻¹ are identified for all the catalysts, whereas broad lines at high wavenumbers (930-980 cm⁻¹) are also identified but only for some catalysts. The formation of MoS₂ is evidenced by the two intense lines at 375 and 400 cm⁻¹ [23–26]. The line at 375 cm⁻¹ is assigned to the Mo-S stretching modes while the one at 400 cm⁻¹ corresponds to the S-Mo-S stretching mode. The line positioned at 450 cm⁻¹ is attributed to a second order scattering as reported by Gutiérrez [12]. The Raman lines appearing at higher wavenumber, observed for few samples, are generally assigned to the presence of oxysulfide species (bridged species) or reduced molybdenum oxides species [26]. Anyhow, the presence of oxidic species may be due to the exposure to air of these samples.

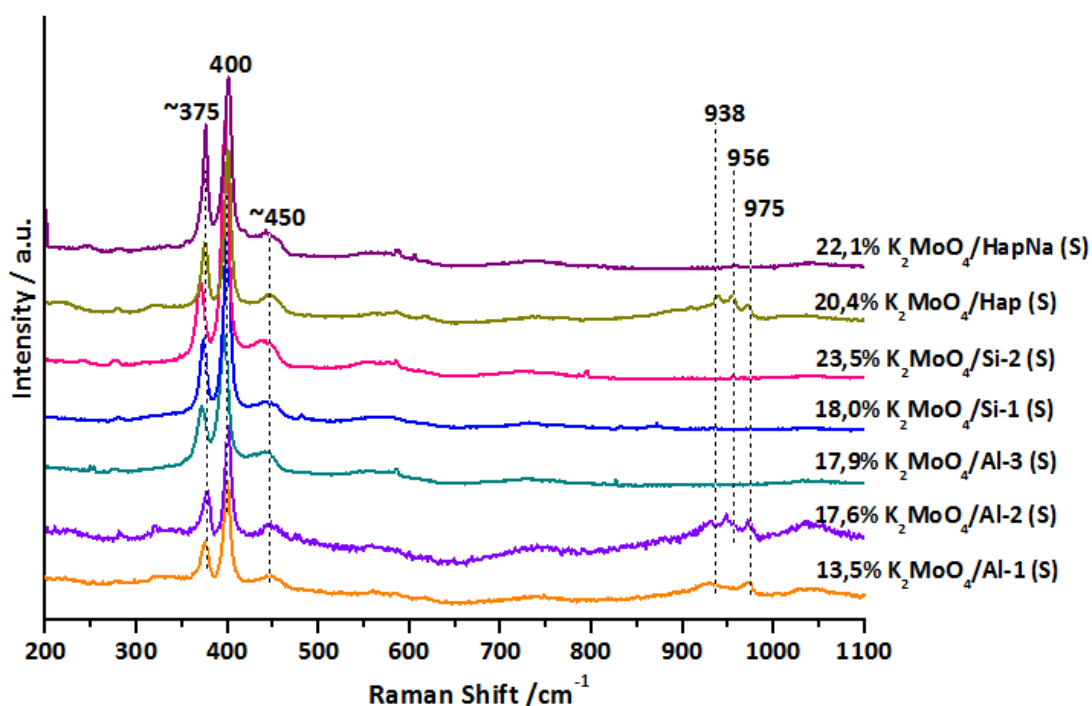


Figure 4.13. Raman spectra of sulfided K₂MoO₄-based catalysts

Raman spectroscopy was also used to carry out a study of the evolution of the catalysts surface during the pretreatment. The catalysts 17.9% K₂MoO₄/Al-3 was used for this study and the method of pretreatment used was the named METHOD S/RS described in chapter 2. For clarity reasons, the description of the pretreatment method used is showed in figure

4.14.

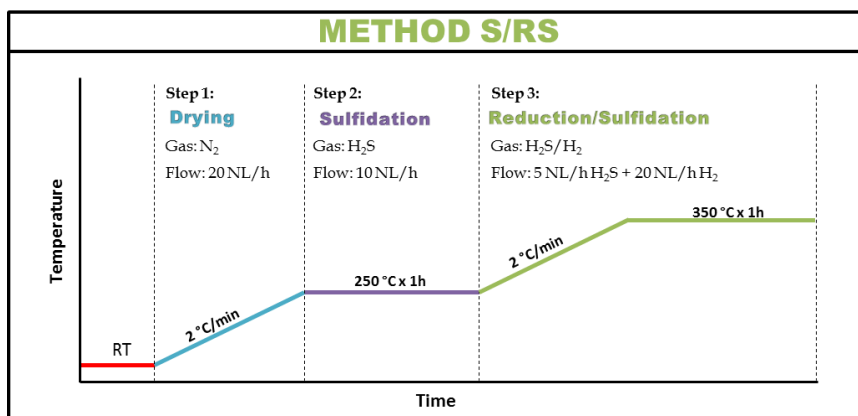


Figure 4.14. Pretreatment method S/RS

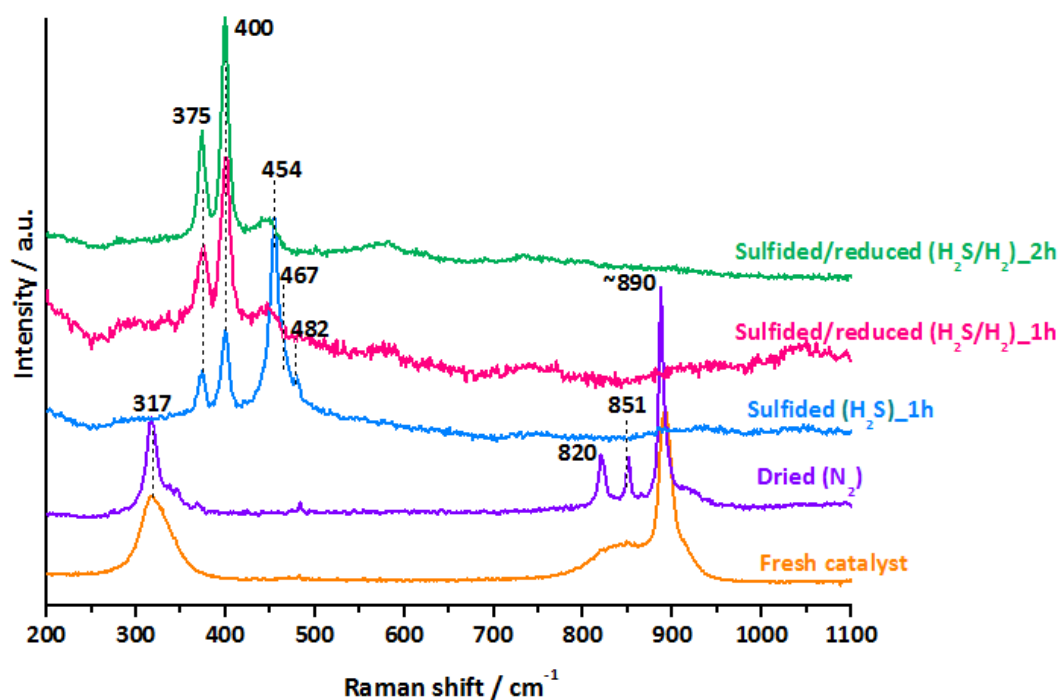


Figure 4.15. Evolution during the sulfidation of 17.9% K₂MoO₄/Al-3.

The obtained spectra are shown in figure 4.15. Fresh catalyst (1st spectrum from bottom to top) is shown as reference. As discussed in chapter 3, this sample exhibits lines at 893, 850, and 317 cm⁻¹ characteristic of K₂MoO₄ [12], [23]. The line at 893 cm⁻¹ is attributed to symmetric vibration of terminal Mo=O bonds, the line around 850 cm⁻¹ is assigned to asymmetric and symmetric stretches of the bridging Mo–O–Mo bond and finally the line at

317 cm⁻¹ is associated with the vibration mode of $\delta(\text{Mo}-\text{O})$. The 2nd spectrum from bottom to top corresponds to the dried catalyst which displays Raman lines at the same wavenumbers than the fresh catalyst but sharper, in fact, the broad line appearing in the fresh catalyst at 850 cm⁻¹, evolves into two lines situated at 851 and 821 cm⁻¹. These observations suggest that after drying, K₂MoO₄ species are more crystallized than on the fresh catalyst. After treatment with H₂S for 1h (3rd spectrum from bottom to top), a clear evolution is observed. The lines assigned to K₂MoO₄ disappear and five new lines at 375, 400, 454, 465 and 482 cm⁻¹ appeared. The lines at 375 and 400 cm⁻¹ are assigned to the formation of MoS₂ [25], [26] while the line at 454, 465 and 482 cm⁻¹ are attributed to K₂MoS₄ [27–29] as observed in the K₂MoS₄-based catalysts described in chapter 3. This result means that the starting species K₂MoO₄ evolves into K₂MoS₄ after reaction with H₂S and then, the formed K₂MoS₄ reacts further with H₂S to produce MoS₂, meaning that K₂MoS₄ is an intermediate in the sulfidation process. This argument is in agreement with the XPS results of 8.1% K₂MoO₄/Al-3 sulfided reference catalyst for which K₂MoS₄ was identified among the Mo species present. The 4th and 5th spectra (from bottom to top) correspond to the treatment with H₂S/H₂ mixture after one and two hours respectively (last step of sulfidation). The two spectra are very similar and show lines at 375 and 400 cm⁻¹ assigned to the Mo-S and S-Mo-S stretching modes respectively which correspond to the formation of MoS₂ as described earlier. The observation of the Raman spectra during sulfidation does not allow evidencing the formation of the K_xMoS₂ intercalated phase discussed for reference catalysts.

4.2.2.2. High resolution transmission electron microscopy (HRTEM)

Figure 4.16 shows the micrograph of MoS₂ crystallites on 17.9% K₂MoO₄/Al-3. The distribution of slabs length and number of fringes for this supported catalysts are indicated in figures 4.17 and 4.18, respectively. The observed images suggest the presence of long and stacked MoS₂ crystallites. In fact, for this solid, the slab length distribution is centered between 2 and 12 nm and with an average stacking degree between 1 and 4 (see figure 4.17 and 4.18). The distribution of crystallites length was shifted toward bigger particles (average length = 9 nm) as compared with the catalyst 8.1% K₂MoO₄/Al-3 (average length = 4.9 nm). Additionally, the 17.9% K₂MoO₄/Al-3 catalyst presents crystallites with a greater number of

fringes (average fringes = 2.7) than 8.1% K₂MoO₄/Al-3 (average fringes = 2.2). These results concerning the length and the number of fringes distributions suggest that the incorporation of Mo in a higher loading evolves to the presence of longer and stacked crystallites. The behavior of the high loaded K containing catalyst is clearly different compared to a highly loaded supported (Co)Mo HDS catalyst because so long and stacked MoS₂ slabs are generally not obtained on HDS-alumina supported catalysts (except when non-sulfided bulky oxide particles covered with stacked and long MoS₂ particles are formed). The unusual morphology of the MoS₂ phase in K-Mo catalysts can then be ascribed to the formation of very large and stacked K_xMoS₂ crystallites. The same trend (increase of MoS₂ length and staking) was already noticed in low loaded K₂MoO₄-based reference catalysts. But as for reference catalysts, it is not possible to discriminate between the MoS₂ and K_xMoS₂ phases observing the TEM images.

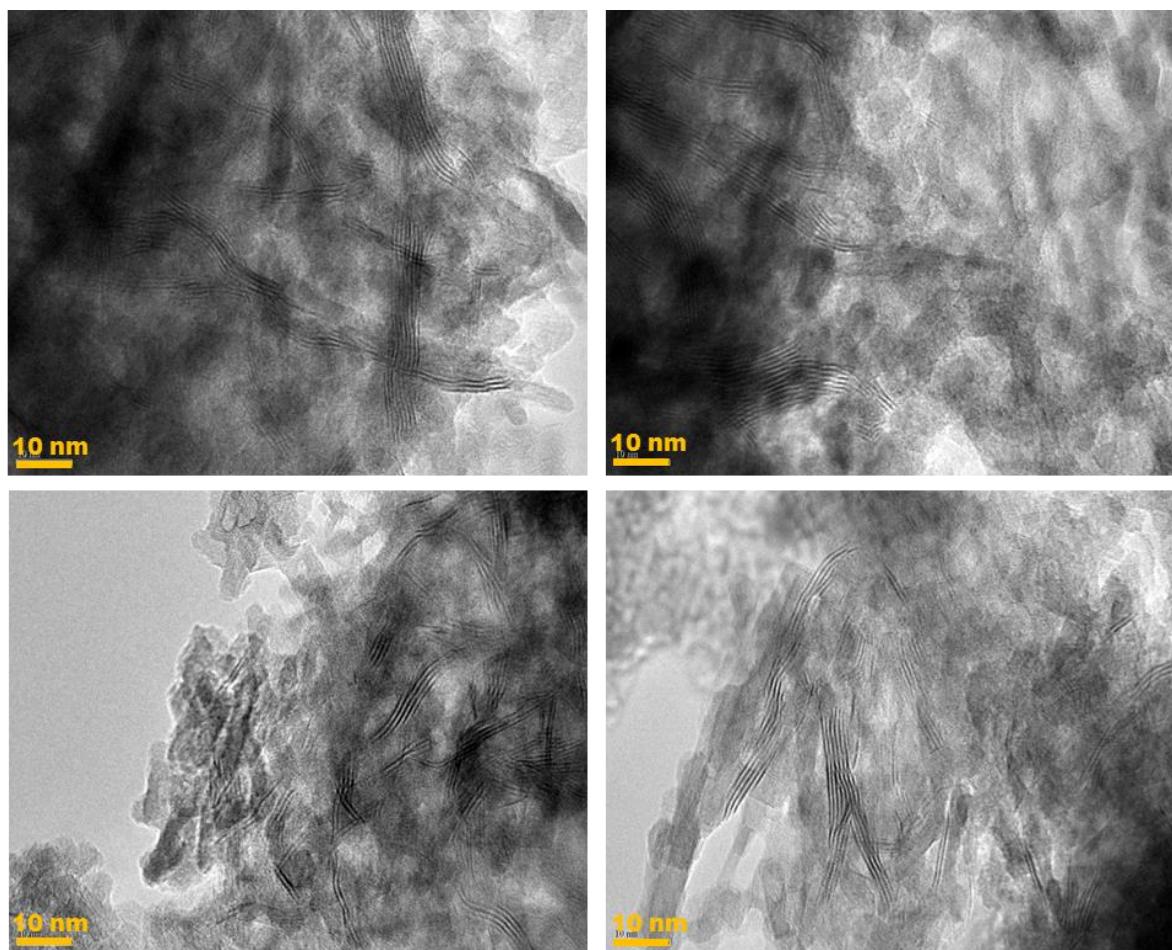


Figure 4.16. High resolution TEM images of 17.9% K₂MoO₄/Al-3

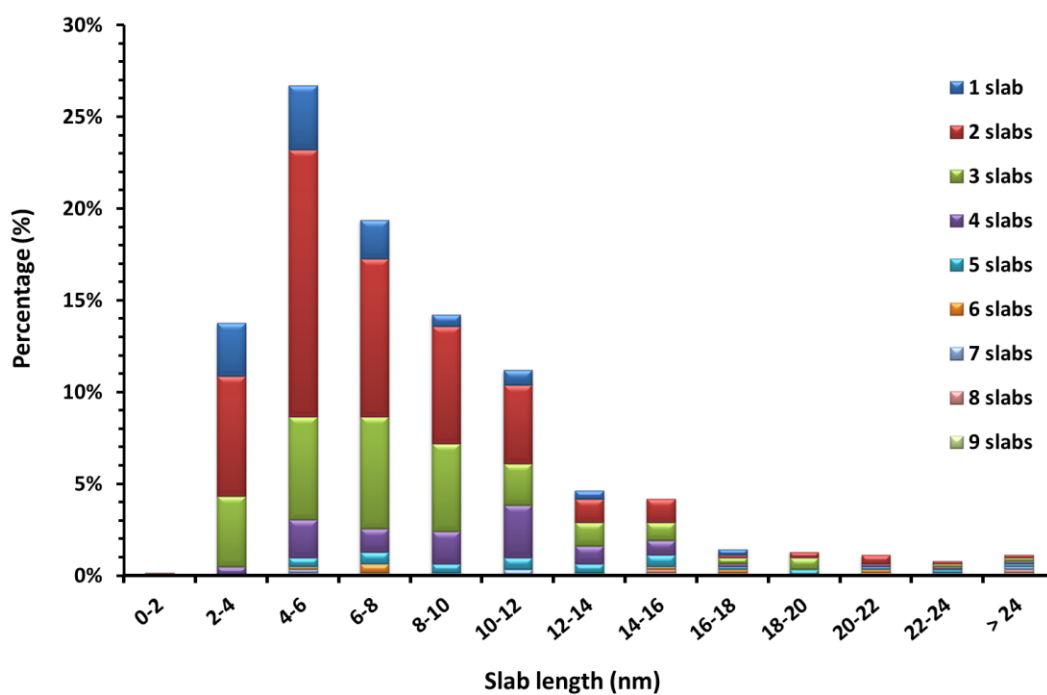


Figure 4.17. MoS₂ distribution by slab length of 17.9% K₂MoO₄/Al-3

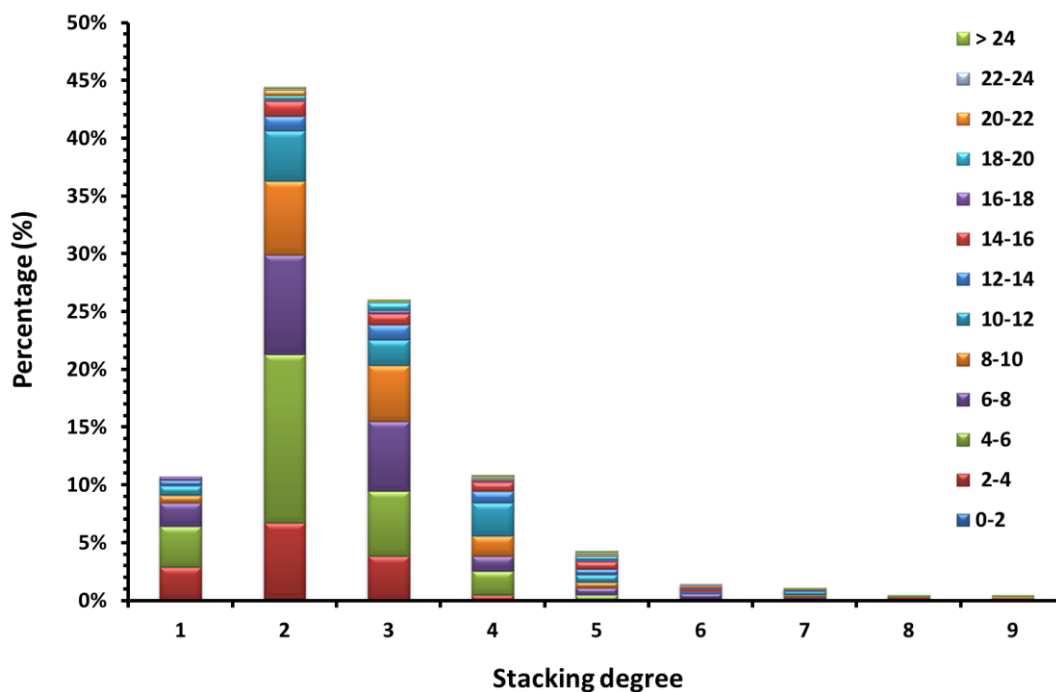


Figure 4.18. MoS₂ distribution by stacking degree of 17.9% K₂MoO₄/Al-3

Besides the formation of long and stacked MoS₂ slabs, the presence of big particles by HRTEM is also observed. Figure 4.19 shows some images of the observed particles. In order to determine the nature of these big crystallites, we calculate the interplanar spacing and a value equal to 5,1 Å was obtained; by reference to the literature (JCPDS 00-019-1001. See annex 5), this interplanar spacing could correspond to crystallized K₂MoS₄. However, Raman spectra of these sulfided catalysts do not exhibit lines corresponding to big crystallites of K₂MoS₄, which appears only as sulfidation intermediate. This discrepancy between the both techniques is not yet well understood.

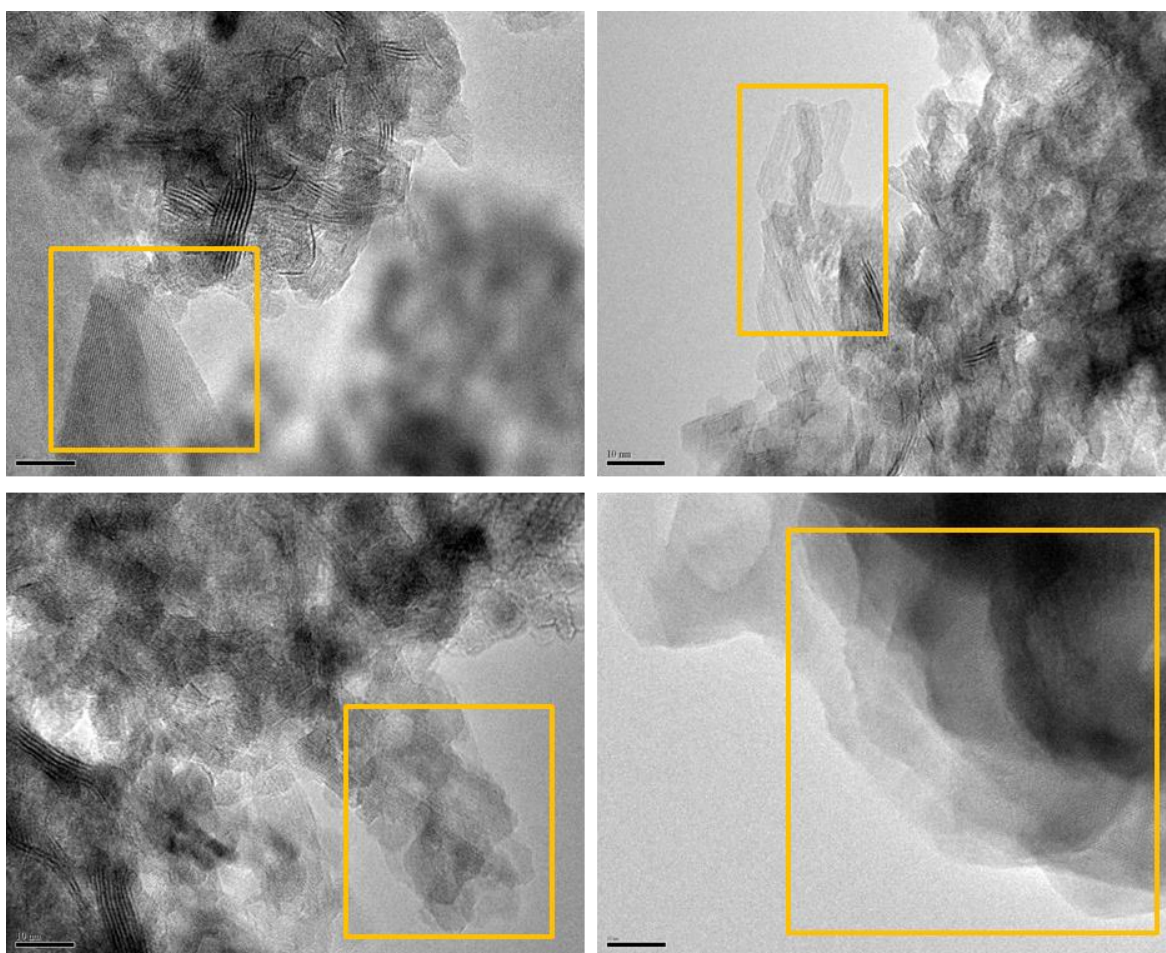


Figure 4.19. High resolution TEM images of 17.9% K₂MoO₄/Al-3 indicating the presence of big crystallites.

4.2.2.3. X-ray photoelectron spectroscopy (XPS)

The binding energies and At.% of Mo3d contributions of K₂MoO₄-based catalysts after sulfidation are reported in table 4.6.

As stated for 8.1%K₂MoO₄/Al-3 sulfided reference catalysts in the previous section, K₂MoO₄-based catalysts exhibit three Mo components positioned at 228.2±0.3, 229.1±0.2 and 230.1±0.2 eV attributed to K_xMoS₂, MoS₂ and K₂MoS₄ phases, respectively. The sample supported on Si-1 shows a different position regarding the component placing at higher binding energy. In fact, the third Mo component assigned to K₂MoS₄ for the other catalysts, is shifted towards higher binding energy (230.6 eV) indicating the existence of a different species in this sample. This species could be attributed either to Mo⁺⁵ surrounded by oxygen and sulfur atoms as observed for 8.1%Mo/Al-3 or Mo⁶⁺ in the form of oxysulfide (--S--Mo⁶⁺--O--) species in an oxidic-sulfidic surrounding as K₂MoO₂S₂ or K₂MoOS₃. Concerning the sulfur species, three contributions of S2s at about 226, 227 and 232 eV are observed and are assigned to sulfide S²⁻ present in MoS₂, sulfide S²⁻ present in K_xMoS₂ and sulfate species, respectively.

Table 4.6. Binding energies and relative at.% of Mo species of K₂MoO₄-based catalysts

CATALYST	Binding energy (eV) of Mo 3d _{5/2}			Relative at.% Mo		
	K-Mo ⁴⁺ (S)	Mo ⁴⁺ (S)	Mo ⁶⁺ (S)	K-Mo ⁴⁺ (S)	Mo ⁴⁺ (S)	Mo ⁶⁺ (S)
13.5% K ₂ MoO ₄ /Al-1(S)	228,4	229,3	230,2	64,6	23,1	12,3
17.6% K ₂ MoO ₄ /Al-2(S)	228,2	229,1	230,1	62,8	22,8	14,5
17.9% K ₂ MoO ₄ /Al-3(S)	228,2	229,2	230,1	52,7	24,3	23,0
18.0% K ₂ MoO ₄ /Si-1(S)	227,9	228,9	230,6	36,7	51,2	12,1
23.5% K ₂ MoO ₄ /Si-2(S)	227,9	228,9	229,9	40,5	45,8	13,7
20.4% K ₂ MoO ₄ /Hap(S)	228,1	229,1	230,3	53,8	21,7	24,5
22.1% K ₂ MoO ₄ /HapNa(S)	228,2	229,1	230,0	66,7	22,6	10,8

The predominant phase for alumina and hydroxyapatite solids (see table 4.6) is K_xMoS₂ which represent at least 50% of the Mo detected by XPS in these solids. The remaining percentage is shared between MoS₂ and K₂MoS₄, K₂MoS₄ being in most cases, the minority

species among the detected species. SiO₂ supported solids exhibit a different behavior. Indeed, MoS₂ phase predominates over K_xMoS₂ in these catalysts.

An important point to note is the fact that the differences between Mo bulk analyzed by ICP and Mo in the surface analyzed by XPS are very important. The atomic percentage of Mo in the bulk and that analyzed by XPS are listed in table 4.7. For most of the samples, the differences between the Mo determined by ICP and XPS are very high leading to a %Mo detected by XPS varying from 16.5 to 33.3%. As stated before, the difference between these two values is attributed to the formation of big particles, as observed on TEM images, instead small particles well dispersed on the surface of support. The presence of these big particles has already been noticed at the oxide state, indicating that their sulfidation do not lead to a high dispersed sulfide phase. Whatever the nature of the big crystallites, they are not detectable by XPS due to their big size and then it could be presumed that they are not active species.

Table 4.7. Comparison of bulk At.%Mo and XPS At.%Mo in sulfided K₂MoO₄-based catalysts

CATALYST	At.% Mo		%Mo detected by XPS
	XPS	Bulk	
13.5% K ₂ MoO ₄ /Al-1(S)	0,637	3,042	21,0
17.6% K ₂ MoO ₄ /Al-2(S)	1,454	4,361	33,3
17.9% K ₂ MoO ₄ /Al-3(S)	0,765	3,994	19,2
18.0% K ₂ MoO ₄ /Si-1(S)	3,009	5,145	58,5
23.5% K ₂ MoO ₄ /Si-2(S)	1,309	6,029	21,7
20.4% K ₂ MoO ₄ /Hap(S)	1,455	5,322	27,3
22.1% K ₂ MoO ₄ /HapNa(S)	0,942	5,702	16,5

4.2.2.4. Correlation between catalytic performance and active K_xMoS₂ phase

In order to correlate the Mo surface distribution to the catalytic performance as determined for sulfided reference catalysts, the curve %X_{CO}/n_{Mo} vs relative % of the phase K_xMoS₂ was plotted. The obtained curve is displayed in figure 4.20.

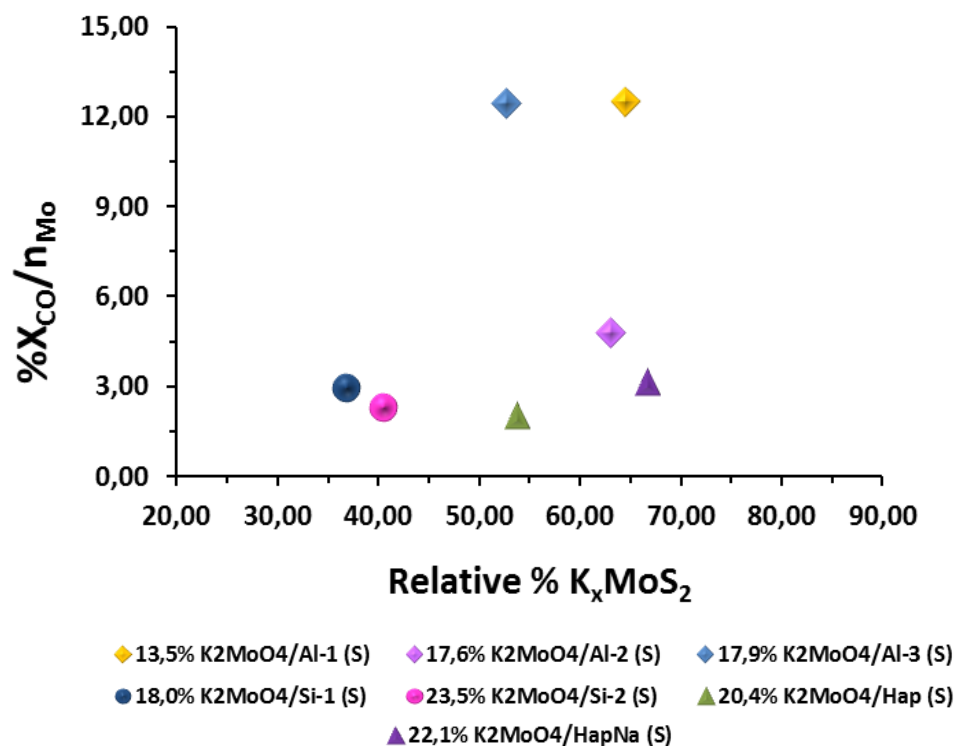


Figure 4.20. Correlation between catalytic performance and relative% of K_xMoS₂ phase in sulfided K₂MoO₄-based catalysts. %X_{CO} at 320 °C

The expected correlation was the increment of %X_{CO}/n_{Mo} as a function of the higher content of K-MoS₂. Not a linear correlation is observed for this series of catalysts. The deviation observed could be attributed to the fact that many variables are taken into account for this correlation. Indeed, trying to correlate solids prepared with different carriers with very different properties may result difficult. Nevertheless, as we assume that the big particles do not contribute to catalytic activity, all the catalytic systems evaluated can be largely improved if the formation of big particles can be avoided.

4.3. K₂MoS₄-BASED CATALYSTS

This section also focusses with the improvement of the catalytic performance. With this purpose, a series of catalysts prepared by using the precursor K₂MoS₄ at different Mo loadings and on different carriers with different properties is studied in this part. It is

important to highlight that for this series of catalysts, two different pretreatment methods were used. The pretreatment method named S/RS was used for the sulfidation of alumina-supported catalysts while the method R/SR was used for silica and hydroxyapatite-supported catalysts.

4.3.1. Catalytic test of sulfided K₂MoS₄-based catalysts

The catalytic performance of K₂MoS₄-based solids for the synthesis of CH₃SH from syngas/H₂S mixture at 320 °C is listed in table 4.8. The whole data comprising the three temperatures evaluated is included in annexes (annex 4).

Table 4.8. Catalytic performance of K₂MoS₄-based catalysts in the reaction of syngas and H₂S

CATALYST	X _{CO} (%)	Selectivity (%)			CH ₃ SH Productivity (g.h ⁻¹ .L ⁻¹)	CH ₃ SH Yield (%)
		CH ₃ SH	COS	CO ₂		
5,8% K ₂ MoO ₄ /Al1 (S)	38,0	38,5	4,5	49,0	104,5	14,6
8,1% K ₂ MoS ₄ /Al-2 (S)	32,6	41,9	6,1	41,9	97,7	13,7
8,3% K ₂ MoS ₄ /Al-3 (S)	47,6	41,3	3,2	48,5	140,7	19,7
8,4% K ₂ MoS ₄ /Si-1 (S)	27,8	41,5	7,0	47,4	88,4	11,7
12,1% K ₂ MoS ₄ /Si-2 (S)	29,0	45,1	5,2	47,6	93,5	12,4
9,9% K ₂ MoS ₄ /Hap (S)	8,3	40,5	29,5	26,7	24,1	3,4
11,1% K ₂ MoS ₄ /HapNa (S)	15,4	39,7	12,4	44,6	45,3	5,7

REACTION CONDITIONS: 320 °C, CO:H₂:H₂S = 1:2:1, 1333,33 h⁻¹, 10 bar

As observed for the K₂MoO₄-based catalysts, as a function of the temperature, CO conversion is increased while selectivities towards CH₃SH and CO₂ are not affected; by contrast, the selectivity towards COS decreases (exception for Hap-supported catalyst). In general, alumina supported catalysts are the most active. The higher conversion is reached with 8,3% K₂MoS₄/Al-3 catalyst (47.6%). Silica supported solids show conversions 1.7 times lower and hydroxyapatite-supported solids show conversions at least 3 times lower. Regarding the selectivity, a similar trend is observed for alumina, silica and HapNa-supported catalysts. CO converts about 40% in CH₃SH, from 3 to 7 % in COS and about 48% in CO₂. The

selectivity towards CH₄ is more noteworthy for these catalysts than for K₂MoO₄-based catalysts; selectivities up to 10% are reached at the higher temperatures evaluated. Hap supported solid exhibits a considerably lower selectivity to CO₂ and higher COS selectivity while CH₃SH selectivity is similar than alumina and silica-supported catalysts.

The observed tendencies are in agreement with the results obtained using K₂MoO₄-based catalysts. COS is an intermediate product coming from reaction (26) which then hydrogenated to CH₃SH and H₂O by reaction (27), and that CO₂ originates from water gas shift reaction (32) or by hydrolysis of COS (31) and CH₄ originate from the hydrogenation of CH₃SH [2], [13]. The trend in selectivity observed for Hap solid suggests that over this catalyst, the hydrolysis of COS and the water gas shift reaction to produce CO₂ are restrained. Thus, it could be supposed that an influence of the different support-properties play a role in this behavior. The higher CH₃SH productivity attained is 140,7 g_{CH₃SH}·h⁻¹·L_{cat}⁻¹ with the solid 8.3% K₂MoS₄/Al-3.

High-loaded K₂MoO₄-based catalysts contain about two times more Mo than K₂MoS₄-based catalysts. In order to determine the efficiency of both catalytic systems (K₂MoO₄ and K₂MoS₄), we calculate the CH₃SH productivity per mol of Mo, making in this form, both systems comparable. The CH₃SH selectivities in both catalytic systems, expressed in g_{CH₃SH}·h⁻¹·mol_{cat}⁻¹, are grouped in table 4.9. When comparing the low and high-loaded K₂MoO₄-based catalysts, it is remarkable the best performance of the low-loaded catalysts, putting in evidence that the presence of big particles, higher in the high loaded catalyst, leads to a low quantity of active phase which in turns leads to a less efficient catalytic system. Then, evaluating the influence of the precursor (K₂MoS₄ and K₂MoO₄), we observe that when using the thio-precursor a better catalytic performance is achieved. At the same time, alumina seems to be the more efficient support compared to silica and hydroxyapatite.

Table 4.9. Comparison of CH₃SH productivity per mol of Mo of K₂MoO₄ and K₂MoS₄-based catalysts

CATALYST	CH ₃ SH Productivity (g.h ⁻¹ .mol ⁻¹)	CATALYST	CH ₃ SH Productivity (g.h ⁻¹ .mol ⁻¹)
13.5% K ₂ MoO ₄ /Al ₂ O ₃ -1 (S)	153,6	5.8% K ₂ MoS ₄ /Al-1 (S)	248,5
17.6% K ₂ MoO ₄ /Al ₂ O ₃ -2 (S)	97,0	8.1% K ₂ MoS ₄ /Al-2 (S)	150,5
17.9% K ₂ MoO ₄ /Al ₂ O ₃ -3 (S)	141,4	8.3% K₂MoS₄/Al-3 (S)	346,0
18.0% K ₂ MoO ₄ /SiO ₂ -1 (S)	108,9	8.4% K ₂ MoS ₄ /Si-1 (S)	208,5
23.5% K ₂ MoO ₄ /SiO ₂ -2 (S)	30,8	12.1% K ₂ MoS ₄ /Si-2 (S)	134,2
20.4% K ₂ MoO ₄ /Hap (S)	31,3	9.9% K ₂ MoS ₄ /Hap (S)	40,1
22.1% K ₂ MoO ₄ /HapNa (S)	29,5	11.1% K ₂ MoS ₄ /HapNa (S)	102,1
8.1% K ₂ MoO ₄ /Al ₂ O ₃ -3 (S)	295,7		

REACTION CONDITIONS: 320 °C, CO:H₂:H₂S = 1:2:1, 1333,33 h⁻¹, 10 bar

4.3.2. Characterization of sulfided K₂MoS₄-based catalysts

Raman spectroscopy and X-ray photoelectron spectroscopy were used as techniques for the characterization of K₂MoS₄-based catalysts after sulfidation.

4.3.2.1. Raman spectroscopy

Figure 4.21 displays the Raman spectra of K₂MoS₄-based catalysts after sulfidation. The two intense lines around 376 and 400 cm⁻¹ confirm the formation of MoS₂ [23–26]. Few small Raman lines in the low-wavenumber region between 250 and 350 cm⁻¹ are also identified. These lines could be attributed to low amounts of species similar to the oxysulfide species observed during the sulfidation of classical Mo-based HDS catalysts. The Raman lines appearing at 960 and 589 cm⁻¹ in hydroxyapatite-based catalysts are characteristics of this compound and are assigned to the vibration mode of PO₄.

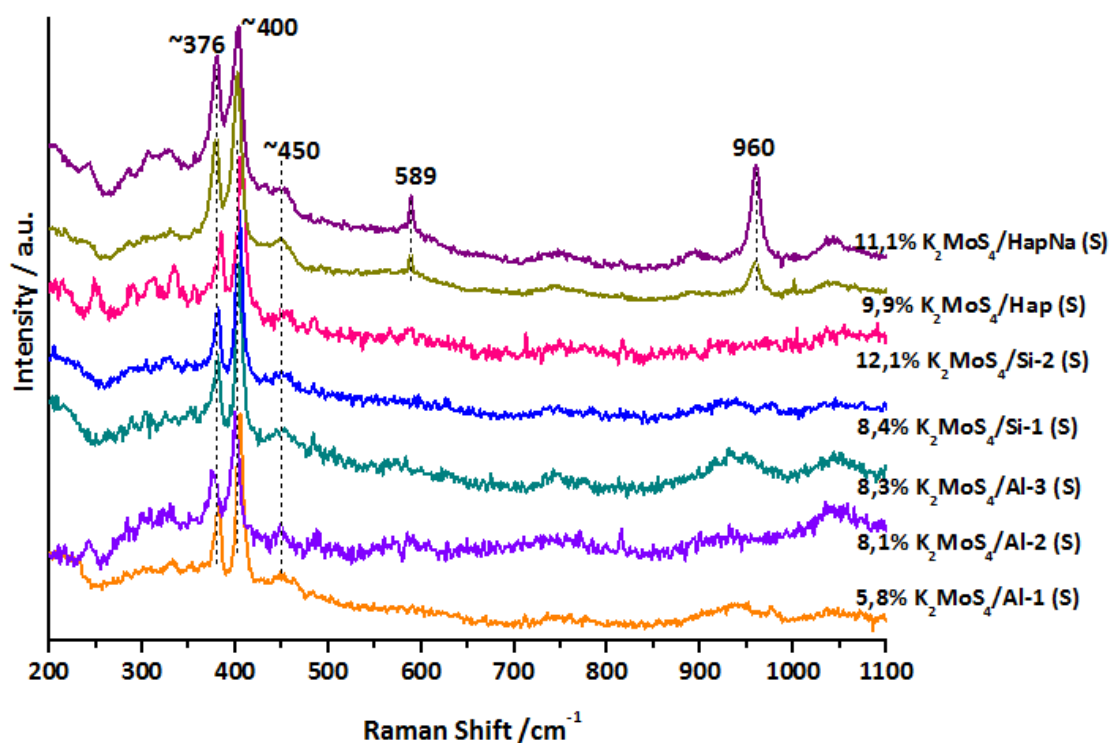


Figure 4.21. Raman spectra of sulfided K₂MoS₄-based catalysts

4.3.2.2. High resolution transmission electron microscopy (HRTEM)

The more active catalyst of this series (8.3% K₂MoS₄/Al-3) was analyzed by means of HRTEM. Besides the presence of MoS₂ layers observed (see figure 4.10-b), as displayed in figure 4.22, big crystallites were also observed. When calculating the interplanar spacing of some of these particles, the obtained value is 3,6 Å, a different value than that calculated and attributed to K₂MoS₄ in the sulfided 17% K₂MoO₄/Al-3 catalyst. Nevertheless, 3.6 Å could correspond to another interplanar spacing of K₂MoS₄ (see annex 5), indicating a different exposure of the crystallites in 8.3% K₂MoS₄/Al-3.

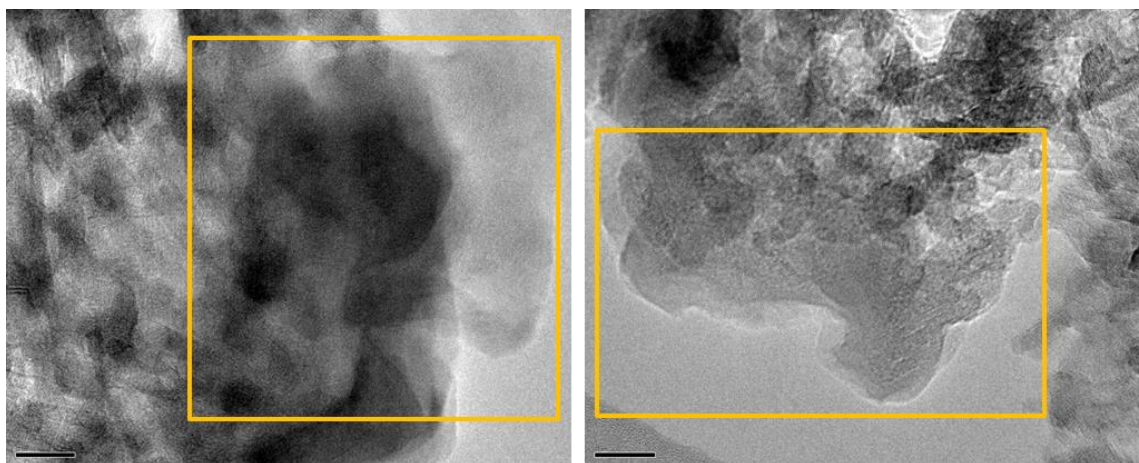


Figure 4.22. High resolution TEM images of 8.3% K₂MoS₄/Al-3 indicating the presence of big crystallites.

4.3.2.3. X-ray photoelectron spectroscopy (XPS)

Table 4.10 listed the binding energies and At.% of Mo contributions of K₂MoS₄-based catalysts after sulfidation.

Table 4.10. Binding energies and relative at.% of Mo species of K₂MoS₄-based catalysts

CATALYSEUR	Binding energy (eV) of Mo 3d _{5/2}			Relative at.% Mo		
	K-Mo ⁴⁺ (S)	Mo ⁴⁺ (S)	Mo ⁶⁺ (S)	K-Mo ⁴⁺ (S)	Mo ⁴⁺ (S)	Mo ⁶⁺ (S)
5,8% K ₂ MoS ₄ /Al-1 (S)	228,4	229,2	230,2	47,6	33,3	19,0
8,1% K ₂ MoS ₄ /Al-2 (S)	228,4	229,3	230,1	64,0	24,0	12,0
8,3% K ₂ MoS ₄ /Al-3 (S)	228,3	229,1	230,0	60,9	21,7	17,4
8,4% K ₂ MoS ₄ /Si-1 (S)	227,8	228,7	229,6	68,0	24,0	8,0
12,1% K ₂ MoS ₄ /Si-2 (S)	227,9	228,8	229,6	60,9	26,1	13,0
9,9% K ₂ MoS ₄ /Hap (S)	228,2	229,4	230,0	72,2	27,1	0,7
11,1% K ₂ MoS ₄ /HapNa (S)	228,2	229,4	230,0	74,7	24,2	1,2

K₂MoS₄-based catalysts exhibit three Mo components positioned at 228.1±0.3, 229.1±0.3 and 229.9±0.3 eV, attributed to K_xMoS₂, MoS₂ and K₂MoS₄ phases, respectively, as stated for K₂MoO₄-based catalysts and K-promoter reference catalysts. Concerning the sulfur species, three contributions of S2s at about 225.7±0.3, 227.4±0.3 and 231.7±0.3 eV are observed and

are assigned to sulfide S^{2-} present in MoS_2 , sulfide S^{2-} present in K_xMoS_2 and sulfate species, respectively. The distribution of the three Mo species identified is also exposed in table 4.10. K_xMoS_2 is the main phase, representing, for most of catalysts, among 60% and 75% of the Mo detected by XPS in these solids. Between 20 and 30 % correspond to the phase MoS_2 and the remaining percentage is attributed to the minority phase K_2MoS_4 .

But as we have seen before for K_2MoO_4 -based catalysts, not all the Mo atoms are detected by XPS. The atomic percentage of Mo in the bulk and that analyzed by XPS as well as the % Mo detected by XPS of K_2MoS_4 -based catalysts are listed in table 4.11. It is seen that the %Mo detected by XPS is very lower, between 13 and 25%, correlating very well with the presence of big crystallites over these solids such as evidenced by HRTEM. Thus, as indicated earlier, this non-dispersed phase probably does not participate in the catalytic performance.

Table 4.11. Comparison of bulk At.% Mo and XPS At.% Mo in sulfided K_2MoS_4 -based catalysts

CATALYSEUR	%At. Mo		%Mo detected by XPS
	XPS	Bulk	
5,8% K_2MoS_4 /Al-1 (S)	0,210	1,059	19,8
8,1% K_2MoS_4 /Al-2 (S)	0,246	1,822	13,5
8,3% K_2MoS_4 /Al-3 (S)	0,221	1,339	16,5
8,4% K_2MoS_4 /Si-1 (S)	0,267	1,671	16,0
12,1% K_2MoS_4 /Si-2 (S)	0,492	2,248	21,9
9,9% K_2MoS_4 /Hap (S)	0,457	2,113	21,6
11,1% K_2MoS_4 /HapNa (S)	0,454	1,786	25,4

4.3.2.4. Correlation between catalytic performance and active K_xMoS_2 phase

The fact that K_xMoS_2 is the main phase detected by XPS is in agreement with the performance of catalysts. In general, most of catalysts exhibited a good activity and productivity in methyl mercaptan which, as indicated earlier, is directly related to the presence of K_xMoS_2 . Nevertheless, not a direct correlation is obtained between these two parameters ($\%X_{CO}/n_{Mo}$ and at.% K_xMoS_2), as shown in figure 4.23. As discussed before, the

lack of correlation could be attributed to the fact that many supports with very different properties were used for preparation of these solids.

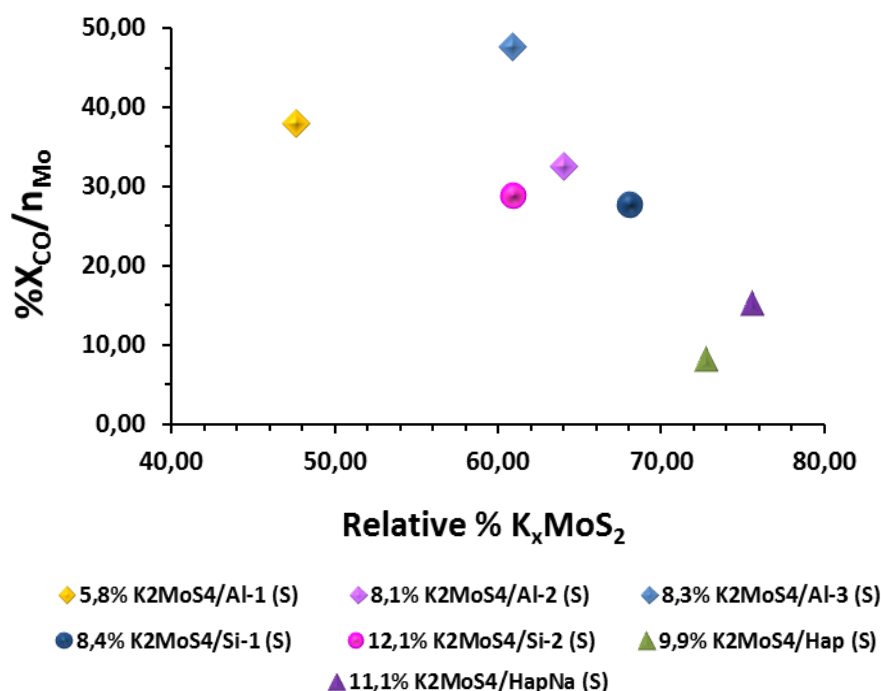


Figure 4.23. Correlation between catalytic performance and relative% of K_xMoS_2 phase in sulfided K_2MoS_4 -based catalysts. % X_{CO} at 320 °C

4.4. EFFECT OF Mo LOADING OVER A SERIES OF ALUMINA-SUPPORTED CATALYSTS

It was observed in the two later sections that either for K_2MoO_4 or K_2MoS_4 -based catalysts, it was not possible to correlate XPS results regarding the percentage of active phase K_xMoS_2 with the catalytic performance since, as we stated, different supports with very different properties were used and that the properties of the supports must have also some effect over the catalytic performance. In this regard, in this part, solids supported on the same carrier (Al-3) are compared. Figure 4.24 displays the graph obtained by plotting the CO conversion of low-loaded and high-loaded-molybdenum catalysts against the amount of K_xMoS_2 phase (nK_xMoS_2), knowing that the calculated amount of K_xMoS_2 phase take into account the relative% of K_xMoS_2 , the % of Mo detected by XPS, the wt.%Mo and the amount of catalyst charged into the reactor. A good correlation is conserved between these two

parameters. As expected, the solid 17.9%K₂MoO₄/Al-3 shows the higher CO conversion as a function of the higher $n_{K_xMoS_2}$, that is, by increasing the Mo loading, the amount of active phase charged in the reactor is increased as well which in turn favors the increase of CO conversion.

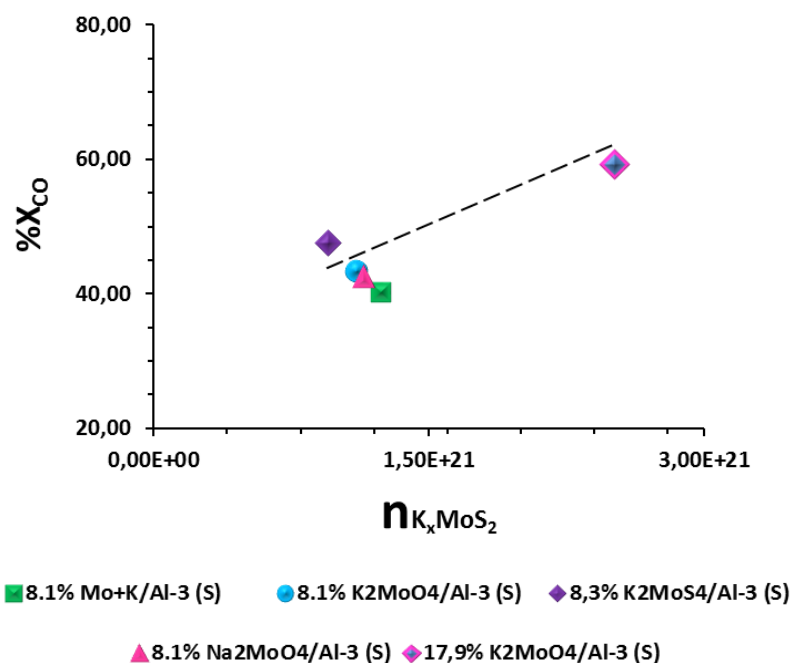


Figure 4.24. Correlation between catalytic performance and $n_{K_xMoS_2}$ in alumina supported catalysts. %X_{CO} at 320 °C.

By the other hand, when plotting the CO conversion per number of Mo atoms charged in the reactor per Mo percent detected by XPS ($\%X_{CO}/n_{Mo}$) against the relative% of active phase K_xMoS_2 (see figure 4.25), the general trend is the higher the relative% of K_xMoS_2 , the higher the $\%X_{CO}/n_{Mo}$. But the catalyst 17.9%K₂MoO₄/Al-3 is excluded of this trend, confirming that the “intrinsic performance” of the K_xMoS_2 phase depends on the loading of the catalyst. Otherwise, the high-loaded solid would be placed over the line followed by the other catalysts. This could be due to the different morphology of the K_xMoS_2 phase at low and high Mo loadings. Indeed, for high loaded catalysts, the K_xMoS_2 slabs are much larger than the ones observed for the low loaded solids. If we consider the classical HDS catalysts model for which the edges of the slabs are considered as the active sites, this large size is consistent with a lower number of active sites and thus for a lower activity per Mo atoms in K_xMoS_2 phase. The exact localization of these active sites is not clearly elucidated and future works

should be dedicated to the elucidation of this localization.

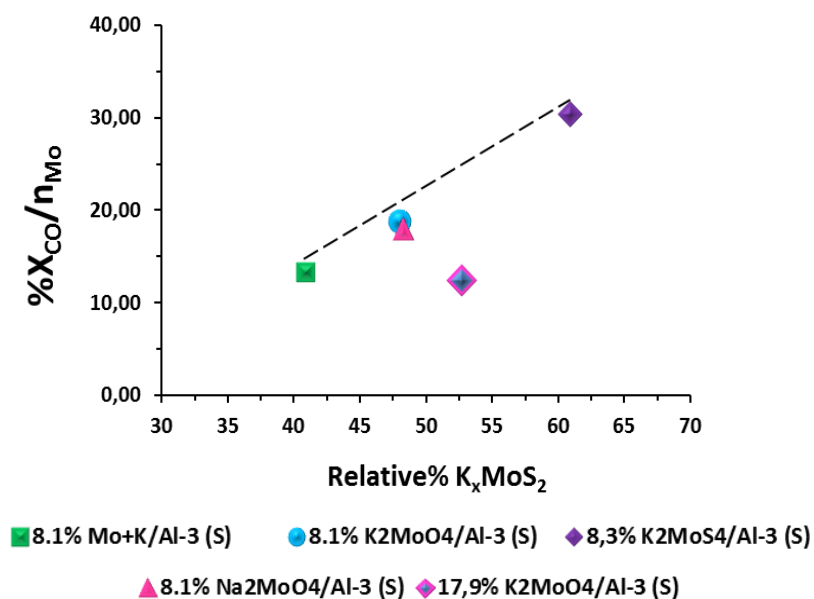


Figure 4.25. Correlation between catalytic performance and relative% of K_xMoS_2 in alumina supported catalysts. % X_{CO} at 320 °C.

4.5. EFFECT OF CATALYST PRETREATMENT OVER THE CATALYTIC ACTIVITY

This section has been destined to improvement of the catalytic performance by the evaluation of catalysts pretreated with different methods (for methods description, see chapter 2). With this purpose, the most active catalysts of each series were chosen (17.9% K₂MoO₄/Al-3 and 8.3% K₂MoS₄/Al-3). 17.9% K₂MoO₄/Al-3 solid was pretreated with the methods S/RS (pre-sulfidation step with pure H₂S followed by simultaneous reduction/sulfidation with a mixture H₂:H₂S), RS (reduction/sulfidation using a mixture H₂/H₂S) and RS+CO (pretreatment with the reaction mixture H₂S:H₂:CO=1:2:1). The same catalyst but calcined and pretreated with the method S/RS is also presented. 8.3% K₂MoS₄/Al-3 solid was treated as well with methods S/RS, RS, RS+CO and also with the method R/RS (reduction step using pure H₂ followed by simultaneous reduction/ sulfidation with a mixture H₂:H₂S).

4.5.1. Catalytic test

The catalytic results obtained for catalysts pretreated with different methods are grouped in

table 4.12.

Table 4.12. Catalytic performance of K₂MoO₄ and K₂MoS₄-based catalysts pretreated at different conditions

CATALYST	X _{CO} (%)	Selectivity (%)			CH ₃ SH Productivity (g.h ⁻¹ .L ⁻¹)
		CH ₃ SH	COS	CO ₂	
17,9% K ₂ MoO ₄ /Al-3 (S/RS)	59,3	45,9	1,6	49,3	194,6
17,9% K ₂ MoO ₄ /Al-3 (RS)	51,9	46,7	1,8	48,5	173,5
17,9% K ₂ MoO ₄ /Al-3 (RS+CO)	56,4	47,1	1,5	48,1	211,4
C-17,9% K ₂ MoO ₄ /Al-3 (S/RS)	56,6	45,1	5,7	45,6	195,6
8,3% K ₂ MoS ₄ /Al-3 (S/RS)	47,6	41,3	3,2	48,5	140,7
8,3% K ₂ MoS ₄ /Al-3 (R/RS)	29,0	34,0	6,4	48,9	68,2
8,3% K ₂ MoS ₄ /Al-3 (RS)	30,8	35,7	6,7	48,4	78,8
8,3% K ₂ MoS ₄ /Al-3 (RS+CO)	49,6	43,0	2,3	49,0	152,6

Beginning with K₂MoO₄-based catalysts, slight differences in conversion are observed. Among the studied solids, the catalyst pretreated with the method RS exhibits the lower CO conversion while that pretreated with the method S/RS displays the higher conversion. No significant differences in trend selectivity are observed. CH₃SH selectivity attains about 46%, CO₂ selectivity is near to 48% and COS and CH₄ selectivities are close to 2 and 5% respectively. The higher productivity in CH₃SH is reached with the catalyst pretreated with the method RS+CO (211.4 g_{CH₃SH}.h⁻¹.L_{cat}⁻¹) while the productivity reached for 17,9% K₂MoO₄/Al-3(S/RS) and 17,9% K₂MoO₄/Al-3(RS) are 194.6 g_{CH₃SH}.h⁻¹.L_{cat}⁻¹ and 173.5 g_{CH₃SH}.h⁻¹.L_{cat}⁻¹, respectively. No differences either on CO conversion or selectivities and productivity are detected between the dried and calcined catalysts pretreated with the method R/RS.

Regarding K₂MoS₄-based catalysts, different behaviors are observed. The catalysts pretreated with methods S/RS and RS+CO display the higher conversion (about 48%); by contrast, catalysts pretreated with methods R/RS and RS show a conversion about 20% lower (30%). CH₃SH selectivity and productivity as well are significantly lower when using

those two pretreatment methods. The catalysts lower selective in CH₃SH are at the same time more selective towards COS and CH₄. For this latter compound, selectivity surrounds 10% at the higher temperatures evaluated. CO₂ selectivity is maintained at 48%.

These results suggest that pretreatment methods have an influence over the catalytic performance of the evaluated catalysts. R/RS and RS are the less efficient pretreatment methods, especially when used to pretreat K₂MoS₄-based solids. Noticeably lower CO conversion and CH₃SH selectivity and productivity are attained when using these methods. RS+CO is no doubt the more effective method in terms of catalytic performance, being also interesting since less severe conditions (temperature) are used when applying this pretreatment method.

4.6. CONCLUSIONS

This chapter 4 is the central chapter of the thesis and deals with K-Mo-based catalysis for the synthesis of MeSH from syngas/H₂S mixture. The first part of this chapter present the results obtained using solids named reference catalysts. These solids were prepared using alumina as support and loaded with 8.1 Mo % and/or 6.1 K %. These two metals were impregnated on the support using K₂MoO₄ or K₂MoS₄ precursors but for comparison, a Mo/alumina and a Mo+K/alumina solid, were also studied; in the later solid, Mo and K were introduced separately. From the evaluation of catalytic performances and through careful characterizations performed by Raman, TEM and XPS, this study allowed us to propose an intercalated phase K_xMoS₂ as active phase in these sulfided KMo based catalysts. Indeed, a very good correlation has been obtained between the relative amounts of K_xMoS₂ and CO conversion taking into account the real quantity of molybdenum detected by XPS. In this case we assumed that non dispersed big particles, no detected by XPS, are not involved in the catalytic performances.

In the second part, high-loaded catalysts were prepared using different supports, three alumina, two silica and two hydroxyapatites. Even if it is difficult to understand the catalytic activity trends observed considering all the prepared catalysts because of the multiplicity of the supports, in K₂MoO₄ as well as in K₂MoS₄ sulfided catalysts, the intercalated phase is in

all cases evidenced by XPS. For this high loaded sulfided catalyst, an unusual morphology of the MoS₂ phase with highly stacked and large MoS₂ slabs was observed and probably attributed to the intercalated phase K_xMoS₂. Besides this phase, big crystallized particles were observed which explains the low quantity of molybdenum detected by XPS. The Mo atoms corresponding to these big particles are considered as not intervening in the catalytic performance. Considering only one support, i.e alumina, it has been shown that the conversion can be increased by increasing the amount of the K_xMoS₂ phase but that its “intrinsic” performance depends on the Mo loading and could be related to the different morphology observed assuming that the active sites could be placed on the edge of the MoS₂ slabs as in classical HDS catalysts. Dedicated works have to be done to elucidate this point. Another effect was observed. When comparing the CH₃SH productivity per Mo mol of low and high-loaded catalyst, it is remarkable the best performance of the low-loaded catalysts, putting in evidence that the presence of big particles, higher in the high-loaded catalyst, leads to a low quantity of active phase which in turns leads to a less efficient catalytic system.

CH₃SH productivity reported by Mo atom (from the global Mo content) shows that K₂MoS₄-based catalysts are more efficient compared with their counterparts K₂MoO₄-based catalysts. By these comparisons, the undesirable presence of big particles is also put in evidence. In addition, a higher CH₃SH productivity is attained if the feedstock (CO/2H₂/H₂S) is directly used to activate the catalyst.

4.7. REFERENCES

- [1] Y.-Q. Yang et al., "Process for the manufacture of methylmercaptan," U.S. Patent N° WO 2005/040082 A22005.
- [2] A. P. Chen, Q. Wang, Y. J. Hao, W. P. Fang, and Y.-Q. Yang, "Catalytic Synthesis of Methanethiol from H₂S-rich Syngas Over Sulfided SiO₂-supported Mo-based Catalysts," *Catalysis Letters*, vol. 121, no. 3–4, pp. 260-265, Nov. 2008.
- [3] G. Mul, I. E. Wachs, and A. S. Hirschon, "Catalytic synthesis of methanethiol from hydrogen sulfide and carbon monoxide over vanadium-based catalysts," *Catalysis Today*, vol. 78, no. 1–4, pp. 327-337, Feb. 2003.
- [4] J. Barrault, M. Boulinguez, C. Forquy, and R. Maurel, "Synthesis of methyl mercaptan from carbon oxides and H₂S whit tungsten-alumina catalysts," *Applied Catalysis*, vol. 33, pp. 309-330, 1987.
- [5] C. Roukoss, D. Laurenti, E. Devers, K. Marchand, L. Massin, and M. Vrinat, "Hydrodesulfurization catalysts: Promoters, promoting methods and support effect on catalytic activities," *Comptes Rendus Chimie*, vol. 12, no. 6–7, pp. 683-691, Jun. 2009.
- [6] J.-G. Choi and L. T. Thompson, "XPS study of as-prepared and reduced molybdenum oxides," *Applied Surface Science*, vol. 93, no. 2, pp. 143-149, Feb. 1996.
- [7] J. Iranmahboob, S. D. Gardner, H. Toghiani, and D. O. Hill, "XPS study of molybdenum sulfide catalyst exposed to CO and H₂," *Journal of Colloid and Interface Science*, vol. 270, pp. 123-126, 2004.
- [8] L. Portela, P. Grange, and B. Delmon, "XPS and NO adsorption studies on alumina-supported Co-Mo catalysts sulfided by different procedures," *Journal of Catalysis*, vol. 156, pp. 243-254, 1995.
- [9] D. Nikolova, R. Edreva-Kardjieva, G. Gouliev, T. Grozeva, and P. Tzvetkov, "The state of (K)(Ni)Mo/γ-Al₂O₃ catalysts after water–gas shift reaction in the presence of sulfur in the feed: XPS and EPR study," *Applied Catalysis A: General*, vol. 297, pp. 135-144, 2006.
- [10] L. Qiu and G. Xu, "Peak overlaps and corresponding solutions in the X-ray photoelectron spectroscopic study of hydrodesulfurization catalysts," *Applied Surface Science*, vol. 256, no. 11, pp. 3413-3417, Mar. 2010.
- [11] A. Griboval-Constant, J.-M. Giraudon, G. Leclercq, and L. Leclercq, "Catalytic behaviour of cobalt or ruthenium supported molybdenum carbide catalysts for FT reaction," *Applied Catalysis A: General*, vol. 260, no. 1, pp. 35-45, Mar. 2004.
- [12] O. Y. Gutiérrez, C. Kaufmann, A. Hrabar, Y. Zhu, and J. a. Lercher, "Synthesis of methyl mercaptan from carbonyl sulfide over sulfide K₂MoO₄/SiO₂," *Journal of Catalysis*, vol. 280, no. 2, pp. 264-273, Jun. 2011.
- [13] A. Chen, Q. Wang, Q. Li, Y. Hao, W. Fang, and Y.-Q. Yang, "Direct synthesis of methanethiol from H₂S-rich syngas over sulfided Mo-based catalysts," *Journal of Molecular Catalysis A: Chemical*, vol. 283, no. 1–2, pp. 69-76, Mar. 2008.

- [14] P. Afanasiev, "Synthetic approaches to the molybdenum sulfide materials," *Comptes Rendus Chimie*, vol. 11, no. 1–2, pp. 159-182, Jan. 2008.
- [15] C. M. Julien, "Lithium intercalated compounds: Charge transfer and related properties," *Materials Science and Engineering*, vol. 40, pp. 47-102, 2003.
- [16] E. Benavente, M. A. Santa Ana, F. Mendizabal, and G. Gonzalez, "Intercalation chemistry of molybdenum disulfide," *Coordination Chemistry Reviews*, vol. 224, pp. 87-109, 2002.
- [17] C. A. Papageorgopoulos and W. Jaegermann, "Li intercalation across and along the van der Waals surfaces of MoS₂ (0001)," *Surface Science*, vol. 338, pp. 83-93, 1995.
- [18] A. N. Enyashin and G. Seifert, "Density-functional study of Li_xMoS₂ intercalates (0 ≤ x ≤ 1)," *Computational and Theoretical Chemistry*, vol. 999, pp. 13-20, Nov. 2012.
- [19] C. Feng, J. Ma, H. Li, R. Zeng, Z. Guo, and H. Liu, "Synthesis of molybdenum disulfide (MoS₂) for lithium ion battery applications," *Materials Research Bulletin*, vol. 44, no. 9, pp. 1811-1815, Sep. 2009.
- [20] F. Wypych, T. Weber, and R. Prins, "Scanning Tunneling Microscopic Investigation of 1T-MoS₂," *Chemistry of Materials*, vol. 10, no. 3, pp. 723-727, Mar. 1998.
- [21] F. Wypych, T. Weber, and R. Prins, "Scanning tunneling microscopic investigation of K_x(H₂O)_yMoS₂," *Surface Science*, vol. 380, no. 1, p. L474-L478, 1997.
- [22] F. Wypych and R. Schollhorn, "1T-MoS₂, a New Metallic Modification of Molybdenum Disulfide," *J. Chem. Soc., Chem. Commun.*, no. 19, pp. 1386-1388, 1992.
- [23] Y. Hao, Y. Zhang, A. Chen, W. Fang, and Y.-Q. Yang, "Study on Methanethiol Synthesis from H₂S-Rich Syngas Over K₂MoO₄ Catalyst Supported on Electrolessly Ni-Plated SiO₂," *Catalysis Letters*, vol. 129, no. 3–4, pp. 486-492, Jan. 2009.
- [24] M. Viršek, A. Jesih, I. Milošević, M. Damjanović, and M. Remškar, "Raman scattering of the MoS₂ and WS₂ single nanotubes," *Surface Science*, vol. 601, no. 13, pp. 2868-2872, Jul. 2007.
- [25] E. Payen, S. Kasztelan, and J. Grimblot, "In situ Laser Raman Spectroscopy of the sulphiding of WO₃(MoO₃)/γAl₂O₃ catalysts," *Journal of Molecular Structure*, vol. 174, pp. 71-76, 1988.
- [26] G. L. Schrader and C. P. Cheng, "In Situ Laser Raman Spectroscopy of the Sulfiding of Mo/Al₂O₃ Catalysts," *Journal of Catalysis*, vol. 80, pp. 369-385, 1983.
- [27] A. Müller, N. Weinstock, and H. Schulze, "Laser-Raman-Spektren der Ionen MoS₄(2-), WS₄(2-), MoOS₃(2-) und WOS₃(2-) in wässriger Lösung sowie der entsprechenden kristallinen Alkalisalze," *Spectrochimica Acta*, vol. 28A, pp. 1075-1082, 1972.
- [28] A. Müller, E. J. Baran, and R. O. Carter, "Vibrational Spectra of Oxo-, Thio-, and Selenometallates of Transition Elements in the Solid State," *Vibrational spectra of transition element compounds*, vol. 3, pp. 81-139, 1975.
- [29] T. Weber, J. C. Muijsers, and N. J. W., "Structure of Amorphous MoS₃," *J. Phys. Chem.*, vol. 99, pp. 9194-9200, 1995.

CHAPTER 5

*Synthesis of MeSH from syngas/H₂S
mixture: Extension to tungsten based catalysts*

*Synthesis of MeSH from syngas/H₂S mixture: Extension to tungsten based catalysts:
Summary*

5.1. CHARACTERIZATION OF FRESH CATALYSTS.....	217
5.1.1. Characterization of K ₂ WO ₄ -based catalysts.....	217
5.1.1.1. Bulk composition and specific surface area.....	217
5.1.1.2. Raman spectroscopy.....	218
5.1.1.3. X-ray photoelectron spectroscopy (XPS).....	219
5.1.2. Characterization of K ₂ WS ₄ -based catalysts.....	221
5.1.2.1. Bulk composition and specific surface area.....	221
5.1.2.2. Raman spectroscopy.....	221
5.1.2.3. Wide angle powder XRD.....	222
5.1.2.4. X- ray photoelectron spectroscopy (XPS).....	224
5.2. CATALYTIC TEST OF W-BASED SOLIDS.....	225
5.3. CHARACTERIZATION OF SULFIDED CATALYSTS	228
5.3.1.1. Raman spectroscopy.....	228
5.3.1.2. X-ray photoelectron spectroscopy (XPS).....	229
5.4. CONCLUSIONS	233
5.5. REFERENCES	234

This chapter deals with catalytic systems similar to those studied in chapter 4 in which molybdenum is substituted by tungsten. Two catalytic systems are studied corresponding to K₂WO₄ and K₂WS₄ based catalysts. In the first part, the characterization of the fresh catalysts is presented. Catalytic performances in the reaction of the mixture CO+H₂+H₂S towards CH₃SH over the sulfided catalysts have been evaluated (second section) and are discussed in the third part taking into account the characterization of the sulfided catalysts.

5.1. CHARACTERIZATION OF FRESH CATALYSTS

Three K₂WO₄-based solids and three K₂WS₄-based solids supported on alumina (Al-3), silica (Si-1) and hydroxyapatite (Hap) were prepared. Elemental analysis, specific surface area BET, wide angle powder XRD, Raman and XPS spectra of these fresh catalysts are presented in this section.

5.1.1. Characterization of K₂WO₄-based catalysts

5.1.1.1. Bulk composition and specific surface area

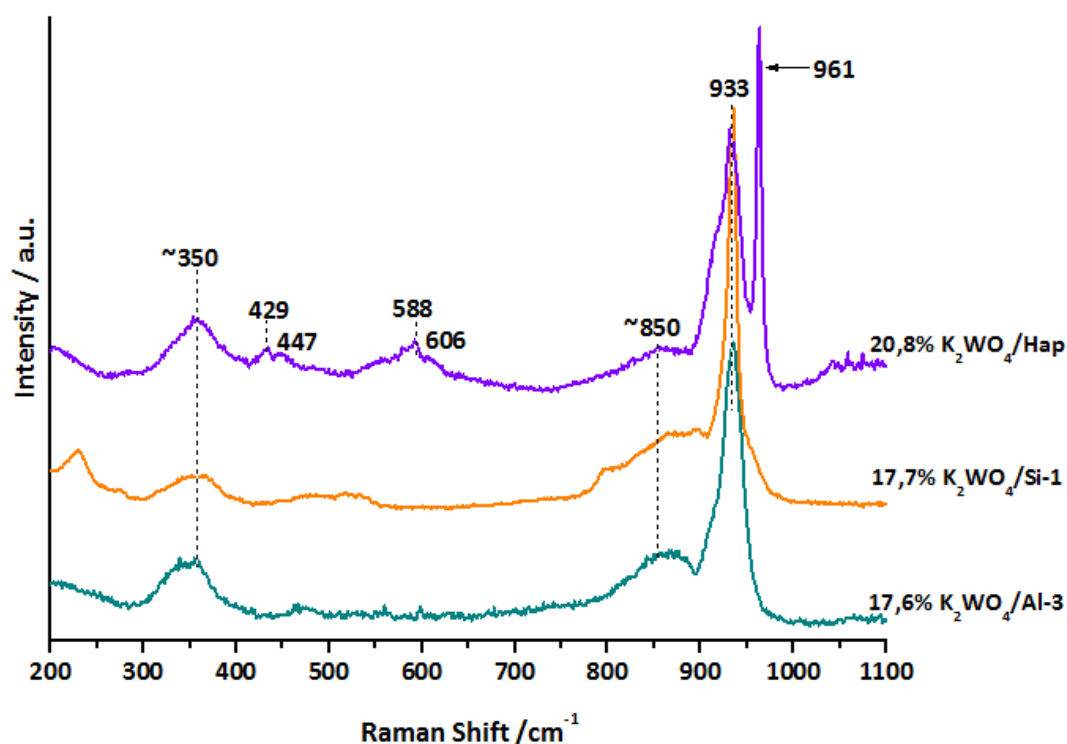
Bulk composition of solids determined by ICP is showed in table 5.1. Tungsten and potassium bulk compositions obtained by ICP analysis agree very well with the theoretical compositions. No more than 12% of difference is observed between the real and the theoretical values. K/W atomic ratio obtained by ICP is equal to 2, corresponding to the expected value in K₂WO₄ precursor. Catalysts specific surface areas listed in table 5.1 show an important decrease in the SSA compared to the initial area of support. About 50% of the support area is lost with the impregnation of K₂WO₄ on alumina and hydroxyapatite and 75% when silica is used as support, suggesting the presence of big crystallites inside the support matrix that induces pore blocking and thus a bad dispersion of the impregnated precursor.

Table 5.1. Bulk composition and specific surface area of K₂WO₄-based solids

CATALYST	Theoretical wt.%		ICP wt.%		K/W atomic ratio	Specific surface area (m ² .g ⁻¹)	Loss in specific surface area (%)
	W	K	W	K			
17.6% K ₂ WO ₄ /Al-3	17,6	7,5	15,4	6,7	2	147	47
17.7% K ₂ WO ₄ /Si-1	17,7	7,5	15,9	6,9	2	53	74
20.8% K ₂ WO ₄ /Hap	20,8	8,9	19,0	8,2	2	59	42

5.1.1.2. Raman spectroscopy

The Raman spectra of K₂WO₄-based catalysts are displayed in figure 5.1.

**Figure 5.1.** Raman spectra of K₂WO₄-based catalysts

The three Raman lines appearing at 933 cm⁻¹, about 850 cm⁻¹ and about 350 cm⁻¹, present on the three catalysts are characteristics of the monotungstate species WO₄²⁻ [1], [2]. For the monotungstate ion, the Raman line at 933 cm⁻¹ is attributed to symmetric stretch mode of

W=O, the line in the 880-820 cm⁻¹ region is due to the antisymmetric stretching mode and the line about 350 cm⁻¹ is assigned to the bending mode of WO₄ species. Raman lines observed in the Hap-supported solid at 961, 606, 588, 447 and 429 cm⁻¹ are attributed to the vibration (stretching and bending) modes of PO₄³⁻ ion.

The intensity and width on the main Raman line (933 cm⁻¹) is different for the three catalysts. In fact, the silica-supported catalyst exhibits the most intense and narrow peak, while the same peak in alumina and hydroxyapatite-supported solids is broader and less intense. This observation suggests a better crystallinity of the impregnated phase over silica than on alumina and hydroxyapatite which in turn suggests a lower dispersion of K₂WO₄ on silica support. These results agree very well with the loss in specific surface area (%) which was more important for the Si-supported catalyst.

5.1.1.3. X-ray photoelectron spectroscopy (XPS)

The analysis by XPS was carried out in order to obtain information about the distribution, oxidation state and dispersion of Mo species in the surface of catalysts. Figure 5.2 shows as example the spectrum of the W 4f level of the 17.6% K₂WO₄/Al-3 catalyst. A similar spectrum is obtained for silica and hydroxyapatite-supported solids.

The spectrum of the three samples in the W4f region displays the presence of three different components. The component positioned at lower binding energy (~33.5 eV) corresponds to the contribution of K3s which overlaps in the W4f region [3]. The K3s contribution in W4f line was calculated from K3p line area and systematically subtracted from W4f region for calculations. A component at higher binding energy (~41.5 eV) is also observed and corresponds to the contribution of the demi-orbital W5p_{3/2}. As well as for the K3s contribution, this component was not taken into account for the quantification of tungsten. Finally, we also observed two well resolved spectral lines at 35.7±0.2 and 37.8±0.2 eV assigned to the W 4f_{7/2} and W 4f_{5/2} spin-orbit components, respectively. These positions are characteristics of W⁶⁺ in oxidic environment [4–6], attributed to the presence of WO₄²⁻ ions with oxidation state +6 at the surface of the support in agreement with Raman analysis. The exact position of W⁶⁺ species in the three studied solids are listed in table 5.2.

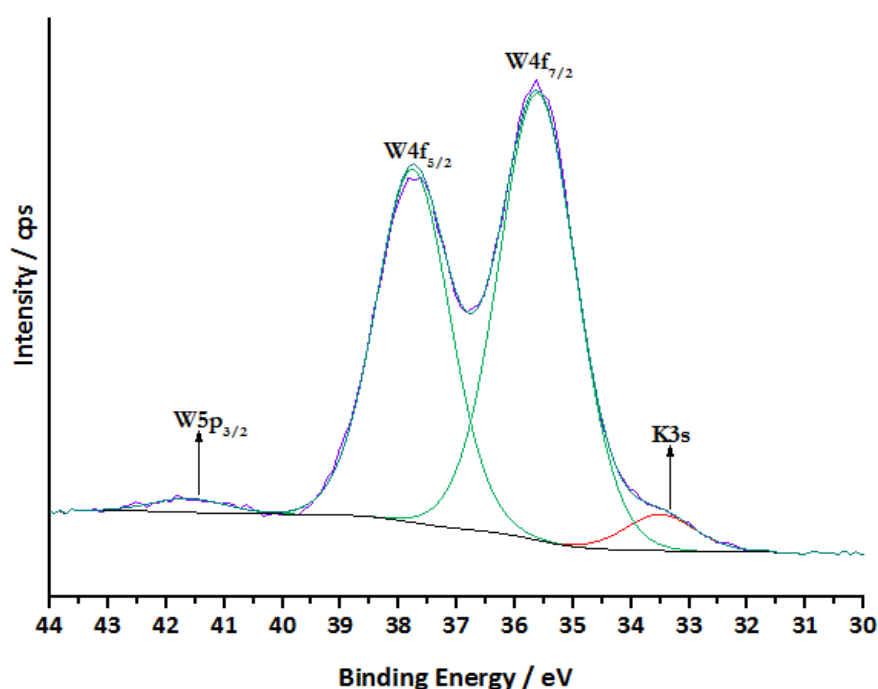


Figure 5.2. XPS spectra of W 4f level of 17.6% K₂WO₄/Al-3 catalyst

Table 5.2. Binding energy of W 4f level and At.% of W and K of K₂WO₄-based solids

CATALYST	Binding Energy (eV)		%At. W		%W detected by XPS
	W 4f _{7/2}	W 4f _{5/2}	XPS	Bulk	
17.6% K ₂ WO ₄ /Al-3	35,6	37,8	1,3	1,9	65
17.7% K ₂ WO ₄ /Si-1	35,9	38,1	0,8	2,0	37
20.8% K ₂ WO ₄ /Hap	35,7	37,9	1,0	2,9	35

The at.% of W obtained by means of XPS are shown in table 5.2. For comparison, the at.% of W in the bulk are also including. When comparing the surface and bulk analysis a significant difference among these two values is noticed. Only 65% of W is detected by XPS for the solid 17.6% K₂WO₄/Al-3 and about 35% for the Si and Hap supported solids. This result should indicate that W species are not sufficiently exposed at the surface to be detected which can be related to the presence of big crystallites on the surface of support. These results bear

out those obtained by Raman and BET analysis and show that the higher the crystallite size of K₂WO₄, the lower the %W detected by XPS.

5.1.2. Characterization of K₂WS₄-based catalysts

5.1.2.1. Bulk composition and specific surface area

The W and K bulk compositions of K₂WS₄-based samples determined by ICP are displayed in table 5.3. A maximum of 15% of difference between theoretical and real bulk composition are observed for supported solid. A good agreement between the theoretical (K/Mo=2) and real (ICP) K/W atomic ratio is observed.

Table 5.3. Bulk composition and specific surface area of K₂WS₄-based solids

CATALYST	Theoretical wt.%		ICP wt.%		K/W atomic ratio	Specific surface area (m ² .g ⁻¹)	Loss in specific surface area (%)
	W	K	W	K			
13.7% K ₂ WS ₄ /Al-3	13,7	5,8	11,4	4,9	2	154	45
13.8% K ₂ WS ₄ /Si-1	13,8	5,9	12,5	5,2	2	109	47
16.3% K ₂ WS ₄ /Hap	16,3	6,9	14,8	6,6	2	42	59

The specific surface area of solids is also listed in table 5.3. A substantial decrease in the initial area of support is observed, resulting in a loss in SSA in the order of 45-60% for all the samples analyzed. As can be observed, the loss in specific surface area (%) is higher as the wt.% Mo increases as observed on K₂WO₄-based solids.

5.1.2.2. Raman spectroscopy

The Raman spectra of fresh K₂WS₄-based solids are displayed in figure 5.3. Spectrum of the three evaluated samples exhibits lines at 485, 473, 459 and 454 cm⁻¹ attributed of potassium tetrathiotungstate. As reported in the literature [7], [8], the line at about 485 cm⁻¹ is

assigned to the symmetric (ν_1) vibration of the WS_4^{2-} anion and the lines at lower frequencies (473, 459 and 454 cm^{-1}) are attributed to antisymmetric (ν_3) vibrations of WS_4^{2-} ions. The presence of well-defined lines attributed to K_2WS_4 is indicative of the preservation of this species after impregnation. The lines on the three samples are intense and broad indicating that bulk particles with high crystallinity are formed whatever the support.

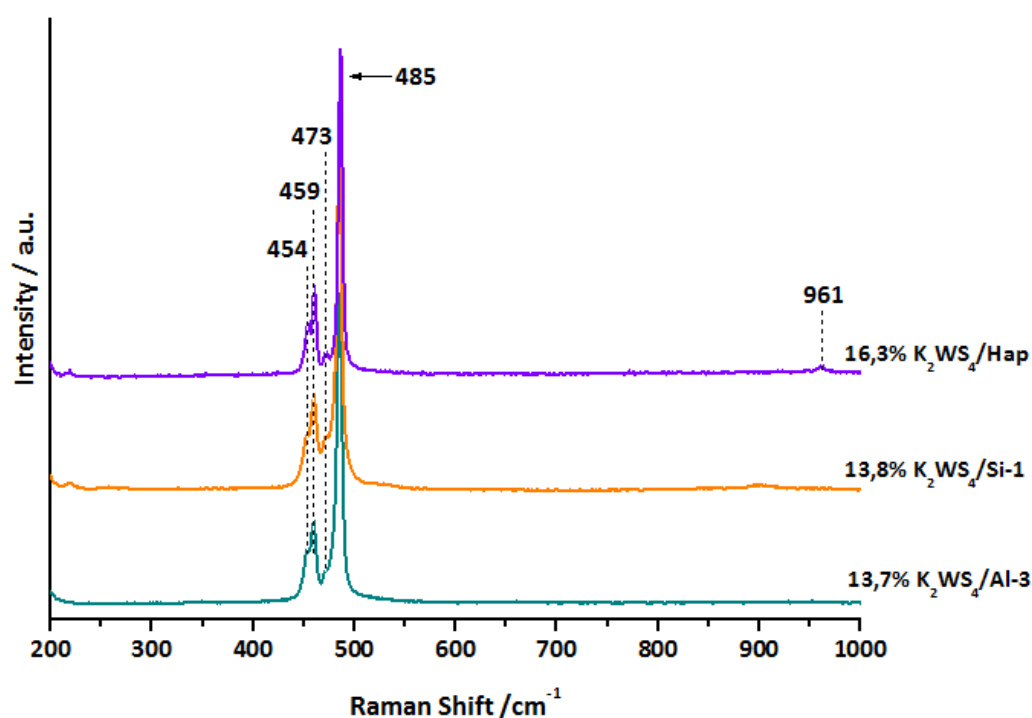


Figure 5.3. Raman spectra of K_2WS_4 -based catalysts

5.1.2.3. Wide angle powder XRD

Figure 5.4 displays the XRD patterns of the K_2WS_4 -based catalysts. The XRD patterns of the supports and the precursor salt impregnated K_2WS_4 are also included for reference. Besides the peaks assigned to alumina, silica and hydroxyapatite, peaks at $2\theta = 14.6, 17.6, 19.1, 24.0, 25.4, 29.4, 32.6, 35.5, 39.3, 41.5, 49.4, 51.2$ and 58.1° are identified and no other crystallized species are visible on the support; the detected peaks are characteristic of potassium tetrathiotungstate as reported in chapter 3, showing the crystallinity of this phase.

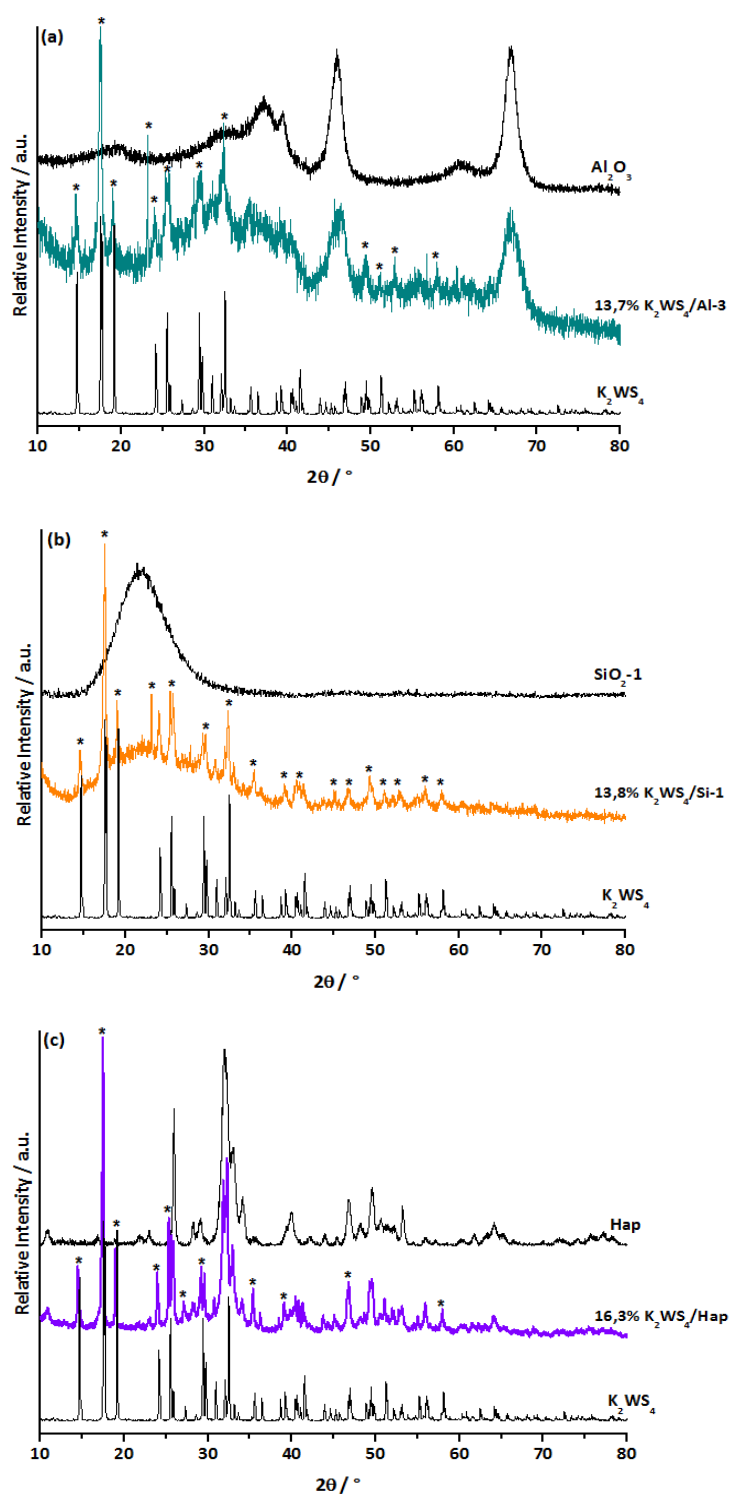


Figure 5.4. XRD patterns of (a) K_2WS_4/Al_2O_3 , (b) K_2WS_4/SiO_2 and (c) K_2WS_4/Hap . K_2WS_4 phase is represented by *.

This result is in agreement with those obtained by Raman spectroscopy considering that the precursor K_2WS_4 is preserved after impregnation and forms crystallized particles.

5.1.2.4. X-ray photoelectron spectroscopy (XPS)

XPS spectra of the core level W4f of K₂WS₄-based solids are very similar to those of K₂WO₄-based solids. The exact positions of the doublet W4f_{7/2} – W4f_{5/2} of the solids are presented in in table 5.4.

Table 5.4. Binding energy of W 4f level and At.% of W of K₂WS₄-based solids

CATALYSTS	Binding Energy (eV)		%At. W		%W detected by XPS
	W 4f _{7/2}	W 4f _{5/2}	XPS	Bulk	
13.7% K ₂ WS ₄ /Al-3	35,7	37,9	0,7	1,3	58
13.8% K ₂ WS ₄ /Si-1	35,9	38,0	0,2	1,4	16
16.3% K ₂ WS ₄ /Hap	35,9	38,0	1,0	1,9	51

The position of the W4f component observed in K₂WS₄-based solids suggests the presence of the oxidic component W⁶⁺ as present in K₂WO₄-based solids whereas the expected species were the W⁶⁺ species in a sulfided surrounding, whose characteristic photopeak should have been shifted to lower binding energy. Indeed, while references about the position of W4f level for K₂WS₄ species have not been found in the literature, Ye et al. [9] proposed that the component W4f_{7/2} of W⁶⁺ surrounded by sulfur in (NH₄)₂WS₄ is positioned at 33.9 eV shifted to lower binding energy compared to W⁶⁺ surrounding by oxygen.

Raman and XRD analysis have shown the preservation of K₂WS₄ species after impregnation. However the oxidation of K₂WS₄ at the surface of the catalyst is evidenced by XPS indicating a re-oxidation at the surface of the catalysts. It must be mentioned that even if catalysts were stored in vacuum, XPS analysis was carried out in a different time than Raman and XRD analyses, implying that an evolution of K₂WS₄ could occur while stored.

The comparison between surface and bulk analysis of W reveals that a significant part (about 50% for Al and Hap-supported solids and 75% for Si-supported solid) of the W present in the samples is not detected by XPS. As stated earlier, the agreement between surface and bulk

analysis is directly related to the presence of small particles and high dispersed materials, thus, in this case the existence of big and low dispersed particles is evidenced by the low quantity of W detected by XPS.

5.2. CATALYTIC TEST OF W-BASED SOLIDS

The catalytic performance of K₂WO₄ and K₂WS₄-based solids for the synthesis of CH₃SH from syngas/H₂S mixture are given in this section. All the catalysts were sulfided in situ prior to testing using the pretreatment method S/RS. 17.6% K₂WO(S)₄/Al-3 catalyst was pretreated at two different temperatures. In the last step of the sulfidation, a plateau at 350 °C for 1 hour under the mixture H₂/H₂S (80/20) is attained when using the method S/RS. Thus, for 17.6% K₂WO(S)₄/Al-3 solids, two temperatures were evaluated in this last step, 350 °C and 400 °C. The temperature of the last step of the sulfidation is shown into brackets, next to the name of the catalysts.

The catalytic performances of K₂WO₄-based solids at 320 °C are listed in figure 5.4. The full data comprising the three temperatures evaluated is included in annexes (annex 6). A similar trend to that reported for Mo-based catalysts is observed for this series of catalysts. As a function of the temperature, CO conversion is increased and the selectivities towards CH₃SH and CO₂ are slightly increased while the selectivity towards COS decreases. Silica and hydroxyapatite-supported solids are almost inactive in the reaction of syngas with hydrogen sulfide; the CO conversion reached for these samples is 2 and 4% respectively. The higher conversion is thus achieved on alumina-supported catalyst. As expected, CO conversion of the solid pretreated at 400 °C is higher than the conversion of the solid pretreated at 350 °C, meaning that the sulfidation of W species is accomplished in a higher extent at higher temperatures. Regarding the selectivities, even at low conversion, the solid 17.7% K₂WO₄/Si-1 is highly selective towards CO₂ (40%) and the remaining 60% is shared among CH₃SH and COS. In contrast, the solid 20.8% K₂WO₄/Hap is more selective towards COS (54%), followed by CO₂ (29%) and the low selectivity is towards CH₃SH (17%). 17.6% K₂WO₄/Al-3 catalyst, either at 350 or 400 °C exhibits the same trend in selectivity with about 46% in CH₃SH, 7% in COS and 47% in CO₂. In general, negligible amounts of CH₄, not higher

than 3% are also observed and no other by-products are detected as in the case of K-Mo-based catalysts.

Table 5.4. Catalytic performance of K₂WO₄-based catalysts in the reaction of syngas and H₂S

CATALYST	X _{CO} (%)	Selectivity (%)			CH ₃ SH Productivity (g·h ⁻¹ ·L ⁻¹)	CH ₃ SH Yield (%)
		CH ₃ SH	COS	CO ₂		
17.6% K ₂ WO ₄ /Al-3 (350 °C)	20	47	9	43	69	10
17.6% K ₂ WO ₄ /Al-3 (400 °C)	24	45	6	48	78	10
17.7% K ₂ WO ₄ /Si-1 (400 °C)	2	31	27	40	5	1
20.8% K ₂ WO ₄ /Hap (400 °C)	4	17	54	29	5	1

REACTION CONDITIONS: 320 °C, CO:H₂:H₂S = 1:2:1, 1333,33 h⁻¹, 10 bar

The observed tendencies are in agreement with the results obtained using Mo-based catalysts. As has been discussed in chapter 4, COS is a primary product (intermediary), coming from reaction (26) which can be later hydrogenated to CH₃SH and H₂O by reaction (27). CO₂ originates from water gas shift reaction (32) or by hydrolysis of COS (31) and CH₄ originate from the hydrogenation of CH₃SH [10–12]. As observed for K₂MoO₄-based solids, a low hydrogenation of COS to CH₃SH is noticeable when K₂WO₄ is supported on hydroxyapatite solids while when supported on silica and alumina, a high hydrogenation and/or hydrolysis of COS is observed. The higher CH₃SH productivity reached is 78,4 g_{CH₃SH}·h⁻¹·L_{cat}⁻¹ with the solid 17.6% K₂WO₄/Al-3 pretreated at 400 °C.

Table 5.5 listed the catalytic performances of K₂WS₄-based solids at 320 °C. The full data comprising the three temperatures evaluated is included in annexes (annex 6). No considerable differences are observed between this series of catalysts and K₂WO₄-based solids. Si and Hap-supported catalysts are as well inactive and only alumina supported catalyst shows a considerable CO conversion, being higher at the higher pretreatment temperature. Selectivities towards the main products CH₃SH, CO₂ and COS are similar to those observed for the K₂WO₄ series.

Table 5.5. Catalytic performance of K₂WS₄-based catalysts in the reaction of syngas and H₂S

CATALYST	X _{CO} (%)	Selectivity (%)			CH ₃ SH Productivity (g.h ⁻¹ .L ⁻¹)	CH ₃ SH Yield (%)
		CH ₃ SH	COS	CO ₂		
13.7% K ₂ WS ₄ /Al-3 (350 °C)	15	43	7	48	47	7
13.7% K ₂ WS ₄ /Al-3 (400 °C)	23	44	8	46	72	10
13.8% K ₂ WS ₄ /Si-1 (400 °C)	3	37	19	43	9	1
16.3% K ₂ WS ₄ /Hap (400 °C)	4	24	38	38	8	1

REACTION CONDITIONS: 320 °C, CO:H₂:H₂S = 1:2:1, 1333,33 h⁻¹, 10 bar

In order to compare the catalysts in terms of productivity, we estimated the productivity per mol of W metal. Table 5.6 collected the values of CH₃SH productivity of the more efficient catalysts of each series. Mo-based catalysts are also included for comparison.

Table 5.6. CH₃SH productivity of the more efficient Mo and W-based catalysts

CATALYST	CH ₃ SH Productivity (g.h ⁻¹ .mol _M ⁻¹)*
17.9% K ₂ MoO ₄ /Al-3 (S)	141,2
8.3% K ₂ MoS ₄ /Al-3 (S)	346,0
17.6% K ₂ WO ₄ /Al-3 (S)	144,0
13.7% K ₂ WS ₄ /Al-3 (S)	188,6
8.1% K ₂ MoO ₄ /Al ₂ O ₃ -3 (S)	295,7

REACTION CONDITIONS: 320 °C, CO:H₂:H₂S = 1:2:1, 1333,33 h⁻¹, 10 bar

* M = Mo or W

It seems noticeable the high efficiency of 8,3% K₂MoS₄/Al-3 which exhibits a productivity per mol of active metal 45% higher than the second best efficient catalyst (13.7% K₂WS₄/Al-3) which in turns is 24% more efficient than its counterpart 17.6% K₂WO₄/Al-3. These observations put in evidence the efficiency of the K-Mo(W)-S system compared with K-Mo(W)-O catalytic system. Other important consideration concerns the W-based solids. The pretreatment conditions for the sulfidation of these solids have not been optimized which means that by optimizing the pretreatment of such solids, the improvement of the

catalytic performance can be achieved as well. All these observations suggest that further improvement of catalysts to obtain higher CO conversion and CH₃SH selectivity and productivity are still possible.

5.3. CHARACTERIZATION OF SULFIDED CATALYSTS

Characterization results of W-based catalysts after sulfidation are presented in this section. Raman spectroscopy and x-ray photoelectron spectroscopy were used with this purpose. All the characterizations were carried out over the solids pretreated at 400 °C.

5.3.1.1. Raman spectroscopy

The Raman spectra of sulfided K₂WO₄-based solids are shown in figure 5.5. It can be noticed that each solid exhibits a different behavior. 20.8% K₂WO₄/Hap exposed Raman lines positioned at 485, 473, 459 and 454 cm⁻¹. These lines are characteristic of the species K₂WS₄ as showed in the previous section “characterization of fresh catalysts”. 17.7% K₂WO₄/Si-1 exhibits these lines as well but less resolved and broader and additionally two lines at 417 and 350 cm⁻¹ are observed. These two lines have been extensively reported as characteristic of WS₂ phase [13–15]. 17.6% K₂WO₄/Al-3 Raman spectrum presents only the two lines at 417 and 350 cm⁻¹ characteristic of WS₂ phase without lines corresponding to K₂WS₄. The Raman results suggest that during the pretreatment of the Hap-supported solid, the sulfidation is incomplete since only K₂WS₄ is observed; meaning that K₂WO₄ is sulfided towards the intermediate species K₂WS₄ without achieving the formation of WS₂. By the other hand, Si-supported solid shows the presence of both species, K₂WS₄ and WS₂, meaning that K₂WS₄ is only partially sulfided to the final species WS₂. 17.6% K₂WO₄/Al-3 catalyst exhibits only the lines corresponding to WS₂, meaning that K₂WS₄ reacts completely with the sulfidation mixture. These results are related to catalytic performance since catalysts where WS₂ is not detected or only partially detected by Raman are inactive catalysts. Catalyst where WS₂ is well observed leads to a significant increase in CO conversion and CH₃SH productivity.

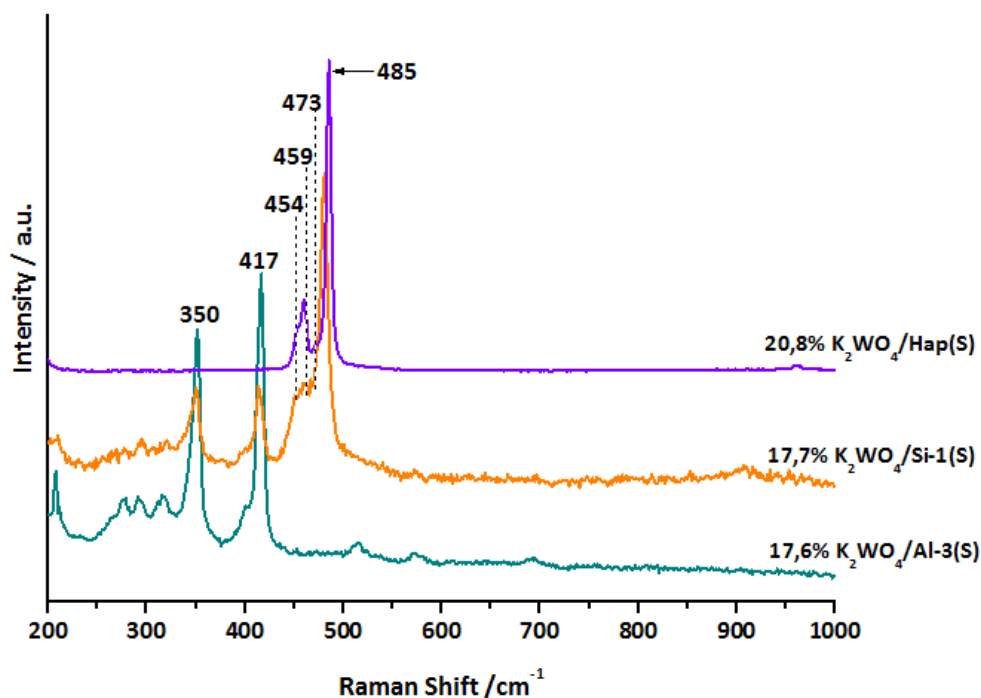


Figure 5.5. Raman spectra of sulfided K₂WO₄-based catalysts

5.3.1.2. X-ray photoelectron spectroscopy (XPS)

XPS analysis was made in order to estimate the surface composition and oxidation state of tungsten species in the sulfided catalysts. In figure 5.6 are displayed the decomposed W4f photopeaks of the three K₂WO₄-based catalysts as example.

By extrapolation of the decomposition results made for K-Mo-O(S)-based catalysts (chapter 4) and the decomposition of fresh tungsten-based solids and also sustained by the few literature references found for this type of catalysts, the decomposition of the W4f level of tungsten based catalysts was made as follow:

- The component positioned at 35.7±0.3 eV (position of the W4f_{7/2} demi-orbital) is assigned to W⁶⁺ in an oxidic environment [5], [6]. This position was observed in the fresh catalysts where only K₂WO₄ is present.
- The component placed at 33.9±0.3 eV is attributed to W⁶⁺ in a sulfidic surrounding, thus, K₂WS₄ species. No literature references were found regarding the position of this

component; nevertheless, Ye et al. [9] positioned the component W4f_{7/2} of the thio-compound (NH₄)₂WS₄ at 33.5 eV which matches well with the position found in this work.

- The component positioned at 31.8±0.3 eV is assigned to the reduced W⁴⁺ species linked to sulfur atoms. This species has been identified in the literature as belonging to WS₂ species [5], [6].

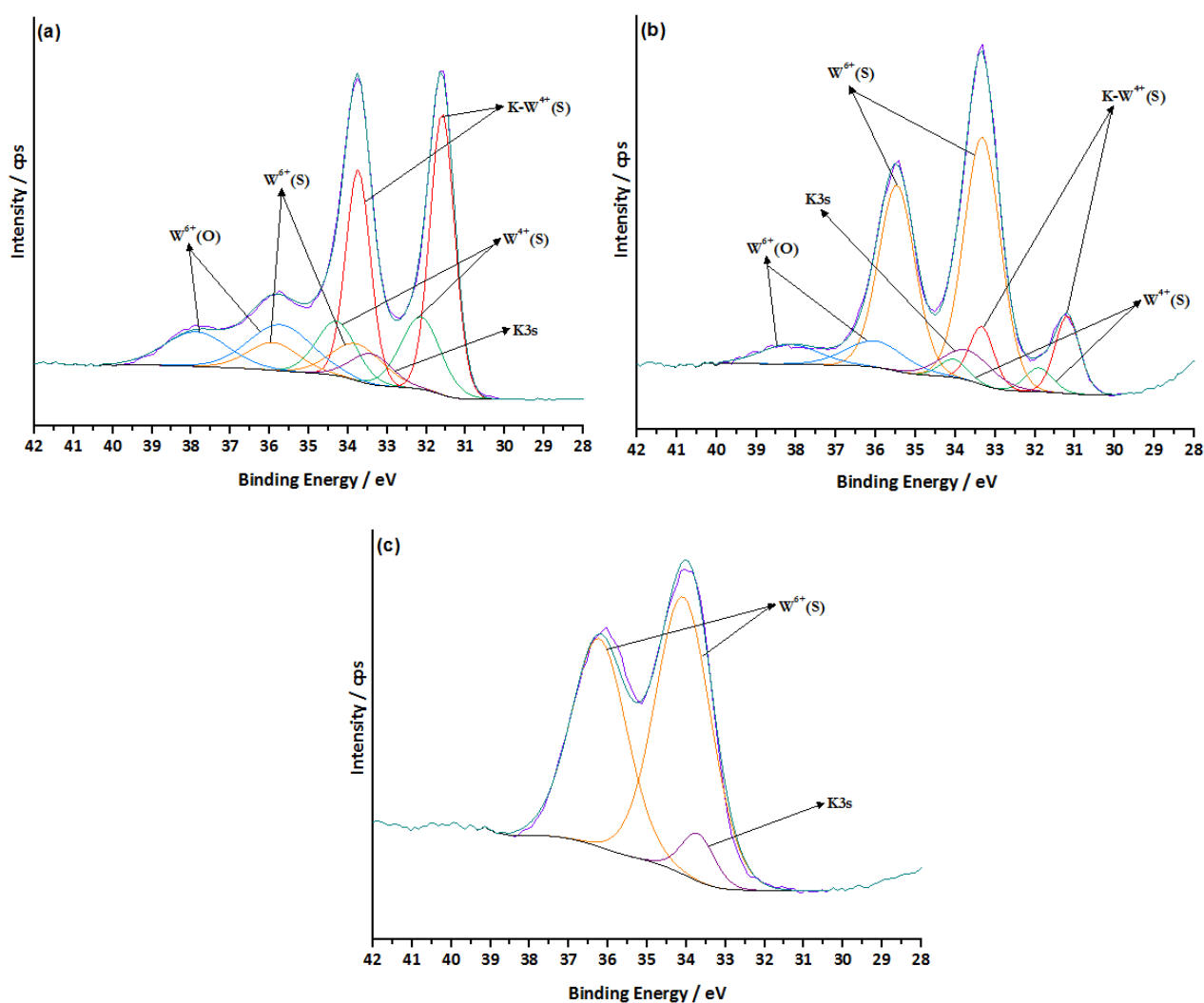


Figure 5.6. XPS spectra of W4f core level of (a) 17.6% K₂WO₄/Al-3, (b) 17.7% K₂WO₄/Si-1 and (c) 20.8% K₂WO₄/Hap

- The component positioned at 31.3±0.3 eV is assigned to a species WS₂ interacting with potassium. Indeed, if we take into account the decomposition of Mo-based materials

where a component positioned 0.8 eV at lower binding energy compared to the traditional MoS₂ phase was identified, it seems possible to make the same assumption for the W-based solids. In this case, the Δ BE between WS₂ and “K-WS₂” is lower (0.5-0.6 eV). It was found for K_xMoS₂ that the intercalation of the alkali metal induce structural and electronic changes by increasing the density on the sulfur atoms of the MoS₂ lattice [16], [17]. Thus, it is possible that the charge transfer between intercalate species (K⁺) and the host lattice (WS₂) is different (lower) compared to K_xMoS₂, meaning that a different shift in BE could be observed. Based on this statement, the component positioned at the lowest binding energy is assigned to the presence of K_xWS₂ species.

Table 5.7. Binding energies and relative at.% of W species of sulfided K-W-O(S)-based solids

CATALYST	Binding energy (eV) of W 4f _{7/2}				Relative at.% W			
	K-W ^{A+} (S)	W ^{A+} (S)	W ⁶⁺ (S)	W ⁶⁺ (O)	K-W ^{A+} (S)	W ^{A+} (S)	W ⁶⁺ (S)	W ⁶⁺ (O)
17.6% K ₂ WO ₄ /Al-3	31,6	32,1	33,8	35,7	47,5	19,6	12,9	20,0
17.7% K ₂ WO ₄ /Si-1	31,2	31,8	33,3	36,0	14,5	5,0	68,7	11,8
20.8% K ₂ WO ₄ /Hap	0,0	0,0	34,1	0,0	0,0	0,0	100,0	0,0
13.8% K ₂ WS ₄ /Si-1	31,2	31,7	33,3	35,4	31,6	19,2	46,1	3,1
16.3% K ₂ WS ₄ /Hap	31,6	0,0	33,9	0,0	8,9	0,0	91,1	0,0

The exact position and distribution of tungsten species in K-W-O(S)-based solids are listed in table 5.7. A very different distribution of W species is found depending on the support selected. Alumina supported catalyst exhibits the higher percent of K_xWS₂ phase (48%); the remainder is divided among the other three species WS₂, K₂WS₄ and K₂WO₄. Silica support solid shows a different distribution; in fact, the main species is K₂WS₄, either for K₂WO₄/Si or K₂WS₄/Si and the second more important component is K_xWS₂ phase. This result is in good agreement with those observed by Raman spectroscopy where the presence of both, K₂WS₄ and WS₂ were detected, bearing in mind that, in our work, no distinction between K_xWS₂ and WS₂ is possible by this technique. Hydroxyapatite based solid exhibits as well a different distribution; in 20.8% K₂WO₄/Hap, the unique observed species is K₂WS₄; in 16.3% K₂WS₄/Hap, the major species is K₂WS₄ (91%) together with a low amount of K_xWS₂ phase.

This result is as well consisting with Raman results since no other species than K_2WS_4 was detected by means of this technique. All these observations mean that the sulfidation is harder to achieve when hydroxyapatite or silica are used as supports which in turn may be related to the presence of big crystallites, evidenced by the large decrease of SSA, the low amount of W detected by XPS and the high crystallinity observed by XRD and Raman spectroscopy of Si and Hap-supported catalysts.

When correlating the relative % of K_xWS_2 phase as a function of the CO conversion, taking into account the number of atoms of tungsten charged in the reactor and detected by XPS, the plot showed in figure 5.7 was obtained. Thus, the straight line obtained shows a very good correlation between the two parameters involved. That is, the higher the relative percentage of K_xWS_2 phase, the higher the CO conversion, putting in evidence that the phase driving the catalytic performance is the one formed by the intercalation of potassium between the WS_2 layers, named K_xWS_2 . The extrapolation of Mo-based system to W-based system is well approached since the same phase, with the substitution of Mo by W, was found to be active in the reaction of syngas with hydrogen sulfide to produce methyl mercaptan. It is important to note that this line does not pass through the origin meaning that little conversion of CO can be obtained without the presence of K_xWS_2 phase as it has been observed for K/Al-3 catalyst (chapter 3).

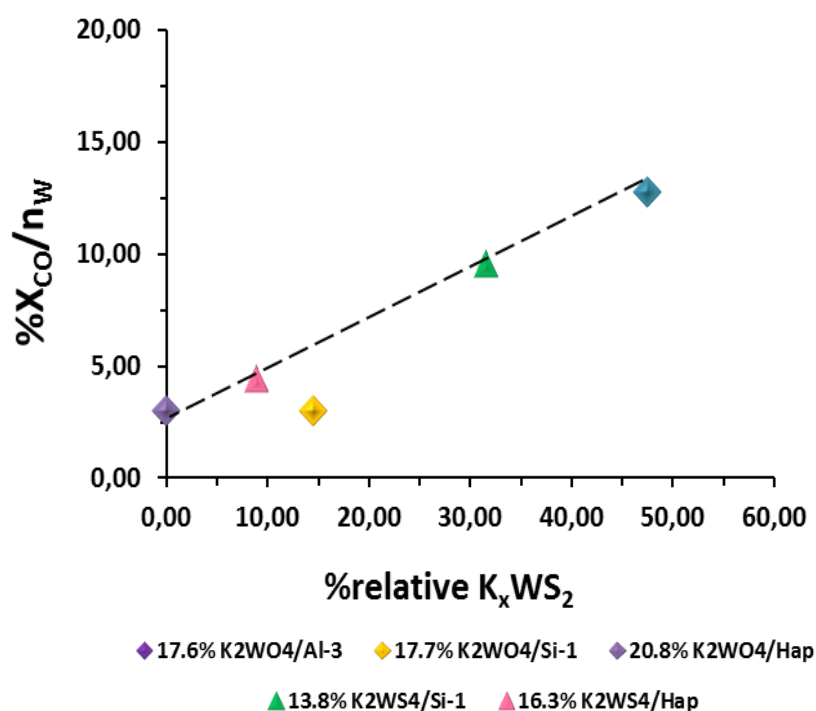


Figure 5.7. Correlation between catalytic performance and %relative of K_xWS₂ phase.
%X_{CO} at 320 °C

5.4. CONCLUSIONS

In this chapter, the study on K-Mo catalysts performed in chapters 3 and 4 has been extended to K-W system. The various analyses performed on fresh K₂WO₄ and K₂WS₄ alumina, silica and hydroxyapatite supported catalysts highlight the formation of bulk crystallites of K₂WO₄ and K₂WS₄ explaining the low quantity of tungsten species detected by XPS.

Catalytic performances have been evaluated and different CO conversions varying between 4 and 23 % were obtained, depending on the system used. These conversions appear lower than the K-Mo systems; nevertheless, expressed per tungsten atom, the efficiency of the K₂WS₄/Al-3 catalyst is put in evidence since an important CH₃SH productivity was reached, even if the K₂MoS₄/Al-3 system is still better (with productivity expressed per Mo atom).

With a very careful decomposition of W 4f core level and based on conclusions obtained from the XPS study of K-Mo sulfided catalysts, we proposed the formation of intercalated K_xWS_2 phase in sulfided K-W catalysts evidenced by a new component shifted towards lower binding energy than the usual WS_2 phase. The good correlation obtained between CO conversion (per W atom in the reactor) and the relative content of the intercalated K_xWS_2 phase allowed us to assume that this species is the active phase in the thiolation reaction from CO/H₂S/H₂.

5.5. REFERENCES

- [1] M. M. Ostromecki, L. J. Burcham, I. E. Wachs, N. Ramani, and J. G. Ekerdt, "The influence of metal oxide additives on the molecular structures of surface tungsten oxide species on alumina: I. Ambient conditions," *Journal of Molecular Catalysis A: Chemical*, vol. 132, no. 1, pp. 43-57, May 1998.
- [2] A. Erdöhelyi, R. Németh, A. Hancz, and A. Oszko, "Partial oxidation of methane on potassium-promoted WO₃/SiO₂ and on K₂WO₄/SiO₂ catalysts," *Applied Catalysis A: General*, vol. 211, pp. 109-121, 2001.
- [3] S. Bruyère, B. Domenichini, V. Potin, Z. Li, and S. Bourgeois, "WO_x phase growth on SiO₂/Si by decomposition of tungsten hexacarbonyl: Influence of potassium on supported tungsten oxide phases," *Surface Science*, vol. 603, no. 20, pp. 3041-3048, Oct. 2009.
- [4] L. Qiu and G. Xu, "Peak overlaps and corresponding solutions in the X-ray photoelectron spectroscopic study of hydrodesulfurization catalysts," *Applied Surface Science*, vol. 256, no. 11, pp. 3413-3417, Mar. 2010.
- [5] K. C. Wong, X. Lu, J. Cotter, D. T. Eadie, P. C. Wong, and K. A. R. Mitchell, "Surface and friction characterization of MoS₂ and WS₂ third body thin films under simulated wheel/rail rolling-sliding contact," *Wear*, vol. 264, no. 7-8, pp. 526-534, Mar. 2008.
- [6] F. Y. Xie et al., "XPS studies on surface reduction of tungsten oxide nanowire film by Ar⁺ bombardment," *Journal of Electron Spectroscopy and Related Phenomena*, vol. 185, no. 3-4, pp. 112-118, Apr. 2012.
- [7] A. Müller, N. Weinstock, and H. Schulze, "Laser-Raman-Spektren der Ionen MoS₄(2-), WS₄(2-), MoOS₃(2-) und WOS₃(2-) in wässriger Lösung sowie der entsprechenden kristallinen Alkalisalze," *Spectrochimica Acta*, vol. 28A, pp. 1075-1082, 1972.
- [8] A. Müller, E. J. Baran, and R. O. Carter, "Vibrational Spectra of Oxo-, Thio-, and Selenometallates of Transition Elements in the Solid State," *Vibrational spectra of transition element compounds*, vol. 3, pp. 81-139, 1975.
- [9] X. R. Ye, H. W. Hou, X. Q. Xin, and C. F. Hammer, "M-S (M=Mo, W) cluster compound films on copper surfaces," *Applied Surface Science*, vol. 89, no. 2, pp. 151-157, Jun. 1995.

- [10] A. P. Chen, Q. Wang, Y. J. Hao, W. P. Fang, and Y.-Q. Yang, "Catalytic Synthesis of Methanethiol from H₂S-rich Syngas Over Sulfided SiO₂-supported Mo-based Catalysts," *Catalysis Letters*, vol. 121, no. 3–4, pp. 260-265, Nov. 2008.
- [11] A. Chen, Q. Wang, Q. Li, Y. Hao, W. Fang, and Y.-Q. Yang, "Direct synthesis of methanethiol from H₂S-rich syngas over sulfided Mo-based catalysts," *Journal of Molecular Catalysis A: Chemical*, vol. 283, no. 1–2, pp. 69-76, Mar. 2008.
- [12] J. Barrault, M. Boulinguez, C. Forquy, and R. Maurel, "Synthesis of methyl mercaptan from carbon oxides and H₂S whit tungsten-alumina catalysts," *Applied Catalysis*, vol. 33, pp. 309-330, 1987.
- [13] M. Viršek, A. Jesih, I. Milošević, M. Damjanović, and M. Remškar, "Raman scattering of the MoS₂ and WS₂ single nanotubes," *Surface Science*, vol. 601, no. 13, pp. 2868-2872, Jul. 2007.
- [14] E. Payen, S. Kasztelan, and J. Grimblot, "In situ Laser Raman Spectroscopy of the sulphiding of WO₃(MoO₃)/γAl₂O₃ catalysts," *Journal of Molecular Structure*, vol. 174, pp. 71-76, 1988.
- [15] K. Shiva, R. H. S. S., H. B. Rajendra, A. J. Bhattacharyya, and C. N. R. Rao, "Employing synergistic interactions between few-layer WS₂ and reduced graphene oxide to improve lithium storage , cyclability and rate capability of Li-ion batteries," *Nano Energy*, pp. 1-7, 2013.
- [16] F. Wypych, T. Weber, and R. Prins, "Scanning Tunneling Microscopic Investigation of 1T-MoS₂," *Chemistry of Materials*, vol. 10, no. 3, pp. 723-727, Mar. 1998.
- [17] F. Wypych, T. Weber, and R. Prins, "Scanning tunneling microscopic investigation of K_x(H₂O)_yMoS₂," *Surface Science*, vol. 380, no. 1, p. L474-L478, 1997.

CONCLUSIONS AND PERSPECTIVES

The literature review on the production of methyl mercaptan from syngas/hydrogen sulfide is very limited. Most of the publications and patents are focused on the improvement of methyl mercaptan yield while they are much less addressed to the understanding of the nature of the active phase. This work has focused on both aspects. With this purpose, we used different catalytic systems in which potassium or sodium salts of tetraoxomolybdate(tungstate) or tetrathiomolybdate(tungstate) anions were impregnated on aluminas, silicas and hydroxyapatites supports.

The first part of this work (chapter 3) was devoted to the synthesis of the K_2MoS_4 and K_2WS_4 precursors (K_2MoO_4 and K_2WO_4 are commercial precursors) and to the Hap supports (SiO_2 and Al_2O_3 are commercial supports) and then to the preparation of the Mo-based fresh catalysts. All the solids were fully characterized, from the metal precursors and the supports to the final catalysts. So, K_2MoS_4 and K_2WS_4 were successfully synthesized. UV-Visible, Raman and XRD characterizations allowed us to determine the purity of these species indicating that no contamination with neighboring oxo-thio-compounds takes place. The homemade support hydroxyapatite was also successfully obtained. XRD pattern and Raman spectrum of this sample were in accordance with literature review. Fresh catalysts were characterized by means of elemental analysis (ICP), BET, XRD, Raman spectroscopy, XPS and SEM. In K_2MoO_4 and K_2MoS_4 -based catalysts, the preservation of the impregnated species was observed. But for most of the catalysts, we observed that these species precipitate inside the porosity during their incorporation, leading to crystallized species and giving rise to a significant difference between at.% of Mo in the bulk and at.% of Mo in the surface (XPS), Thus, a bad dispersion of the K(Na)Mo entities was obtained.

The second part (Chapter 4) was dedicated to the study of Mo sulfided catalysts, sulfidation being the classical activation procedure before catalytic test. In a first approach, we studied a series of reference alumina supported catalysts with the same Mo loading by varying various parameters: catalysts containing or not potassium, catalysts in which Mo and K are incorporated in different ways but maintaining the molar ratio $K/Mo=2$, catalysts with different alkali promoter (K or Na) and catalysts in which the precursor is incorporated in oxidic or pre-sulfided form (K_2MoO_4 and K_2MoS_4). Concerning the catalytic results, it was

observed that the simultaneous presence of Mo and K in the catalytic system allows achieving higher CO conversion and CH₃SH selectivity and a decrease in CO₂ selectivity, highlighting the favorable influence of the coexistence of both metals in the catalytic system. The incorporation of K and Mo coming from a unique precursor was beneficial when talking about catalytic performance but also must be advantageous when talking about time and costs of preparation of catalysts. It was remarkable that the use of potassium as promoter was more advantageous than using sodium since a higher CH₃SH selectivity and a lower CO₂ selectivity were achieved. By the other hand, when comparing 8.1% K₂MoO₄/Al-3 with its presulfided counterpart 8.3% K₂MoS₄/Al-3, the latter was a more active solid towards the production of CH₃SH. An extensive and careful study by XPS allowed us to propose an intercalated K_xMoS₂ phase as being the active phase in these sulfided KMo based catalysts. Indeed, a very good correlation has been obtained between the relative amount of K_xMoS₂ and CO conversion taking into account the real quantity of molybdenum detected by XPS. The study by HRTEM of these samples, suggested us that the presence of K has an effect over the slab length and stacking degree of MoS₂ layers and that is possibly due to the intercalation of K on MoS₂ phase; nevertheless, the exact location of the active sites still remains unclear. As for the fresh catalysts, the important amount of Mo undetected by XPS analysis was consistent with the formation of big crystallites. In this case we assume that these non-dispersed particles were not involved in the catalytic performances. The XPS characterization of high-loaded K₂MoO₄ and K₂MoS₄-based catalysts supported on alumina, silica and hydroxyapatite allowed us to evidence again the presence of the intercalated phase K_xMoS₂. However, it was difficult to obtain a direct correlation between the catalytic performance and this active phase because of the multiplicity of the support used. For the high-loaded sulfided catalyst, an unusual morphology of the MoS₂ phase with highly stacked and large MoS₂ slabs was observed by HRTEM and was supposed to be due to the intercalated phase K_xMoS₂. Besides this phase, big crystallized particles were also observed which explains the low quantity of molybdenum detected by XPS. When considering only one type of solid, i.e. K₂MoO₄/Al-3 catalyst, two effects were observed; when we compared the low and high-loaded K₂MoO₄-based catalysts, the best catalytic performance was obtained with the low-loaded catalysts, putting in evidence that the presence of big particles, higher in the high-loaded catalyst, leads to a low quantity of active phase which in

turns leads to a less efficient catalytic system. The other effect was regarding the active phase K_xMoS_2 ; in this sense, it was shown that the increase of the Mo loading induces an increase in the amount of the K_xMoS_2 phase in accordance with an optimization of the conversion. But the “intrinsic” performance of the K_xMoS_2 phase decrease with the Mo loading, which could be related to the different MoS_2 morphology (at low and high Mo loading).

The extension of KMo catalytic system to K-W catalytic systems was achieved successfully and allowed us to conclude that a similar phase than that observed in KMo systems is driving the catalytic performance. The amount of K_xWS_2 phase characterized by XPS showed a good correlation with CO conversion (per W atom in the reactor) of KW-based catalysts.

For further work, two major points that are obviously interconnected have to be considered: first, the understanding of the nature of the active phase (exact nature and localization of active sites, role of the support...) and second, the improvement of the catalytic performance (CO conversion, CH_3SH selectivity, decrease in CO_2 selectivity...). Thus many areas have to be explored based on the results obtained during this thesis.

Our study shows the negative effect of the presence of big crystallized particles. Taking into account these results, the catalyst preparation should be revisited in order to avoid as much as possible initial precipitation during the first preparation step of catalysts and thus to improve the dispersion of the KMo species. The use of more soluble precursors or different ways of preparation such as multiple impregnations could be considered.

Then, for improving our knowledge on active sites, it will be very interesting to perform a more systematic study in which the effect of the K/Mo (K/W) ratio and of the metal loading will be checked at the oxidic and sulfidic states for one alumina support. This study will help us to characterize active sites location and will also be useful to determine the most efficient catalyst composition regarding the activity and selectivity of the catalysts.

Then this study shall be extended to other supports in order to understand their role on the

dispersion of the active phase and to investigate the effect of their acid-basic properties. Indeed the first results we obtained have shown that the use of different supports led to different catalytic behaviors. Thus, we think that the effect of the support is also a way for improving catalysts performance.

This work also reveals that the pretreatment (i.e. sulfidation) can have a beneficial effect on the performance and is a way to obtain highly efficient catalysts. Consequently the study of this activation step should be very useful to understand the genesis of the active phase and to know how optimizing the nature and/or amount of the active phase.

Moreover, literature data indicate the efficiency of doping metals addition (Ni, Fe, Co, ...) in the catalyst formulation. This point will be very interesting to study regarding the nature of the active phase, keeping in mind our knowledge on hydrotreatment catalysts for which the "Co(Ni)Mo(W)S" phase is well known.

The composition of the gas mixture in the reactor inlet is also a parameter to study. Preliminary results show that the H₂/CO ratio significantly influences the CH₃SH and CO₂ selectivities. Furthermore this research is motivated by the possible use of a biosyngas for which the H₂/CO ratio is significantly lower than 2. Finally, in this bio-based products valorization context, the impact of impurities in the CO/H₂/H₂S mixture may be considered. Nevertheless, the major poison in bio-syngas is H₂S that is a reactant in our catalytic reaction to produce methyl mercaptan. COS also identified as a bio-syngas poison is produced during the reaction and acts as intermediate for the formation of CH₃SH. Other minor poison traces could be tested such as ammonia.

Another way of improvement could be the recycling the CO₂ formed during the reaction because a significant amount of CO₂ is formed. Results in the literature indicate that methyl mercaptan can be formed on tungsten-alumina catalysts from a CO₂/H₂/H₂S mixture, although the CO₂ conversion appears weaker than the CO conversion. CO₂ Recycling with a suitable catalyst thus appears as a potential way of improvement for the CH₃SH synthesis process.

ANNEXES

Study of surface composition by XPS of K_2MoS_4 precursor

Figure A.1 displays the photopeaks Mo3d/S2s of the solid K_2MoS_4 at fresh state. The analysis was mainly focused on the core levels of Mo3d/S2s with the goal to determine oxidation states and composition of the different species of Mo present.

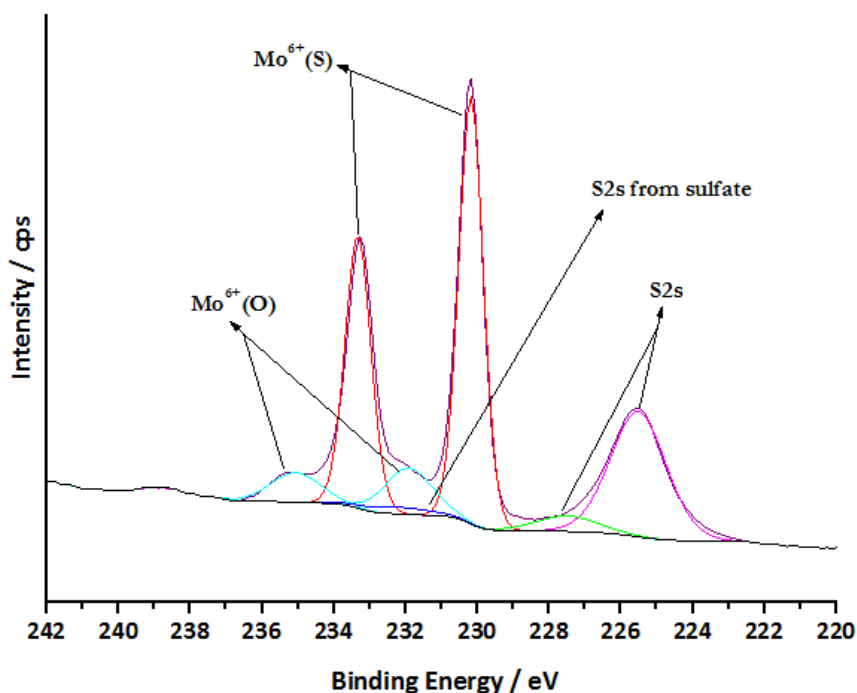


Figure A.1. XPS spectra of Mo3d-S2s core level of K_2MoS_4

Two Mo doublets are identified in the fresh K_2MoS_4 . The position of the peaks observed is listed in Table A.1. The first component placed at lower binding ($Mo3d_{5/2}=230.2$ eV) energy is assigned to Mo^{6+} species surrounded by sulfur atoms, thus this species corresponds to Mo in K_2MoS_4 compound. In contrast, the component positioned at higher binding energy ($Mo3d_{5/2}=231.9$ eV) was assigned to Mo^{6+} species in an oxidic environment, meaning that a portion of K_2MoS_4 is reoxidized to K_2MoO_4 which can be due possibly to the exposure to air of the sample. At any rate, the predominant species is the sulfided K_2MoS_4 , which represents more than 80% of the Mo existing in the compound.

Table A.1. Binding energies and percentage of Mo entities identified in K_2MoS_4

Binding Energy (eV)				Relative percentage of Mo species	
Mo ⁶⁺ (S)		Mo ⁶⁺ (O)		Mo ⁶⁺ (S)	Mo ⁶⁺ (O)
Mo 3d _{5/2}	Mo 3d _{3/2}	Mo 3d _{5/2}	Mo 3d _{3/2}		
230,2	233,3	231,9	235,1	82,6	17,4

Study of surface composition by XPS of K2p level of fresh and sulfided catalysts

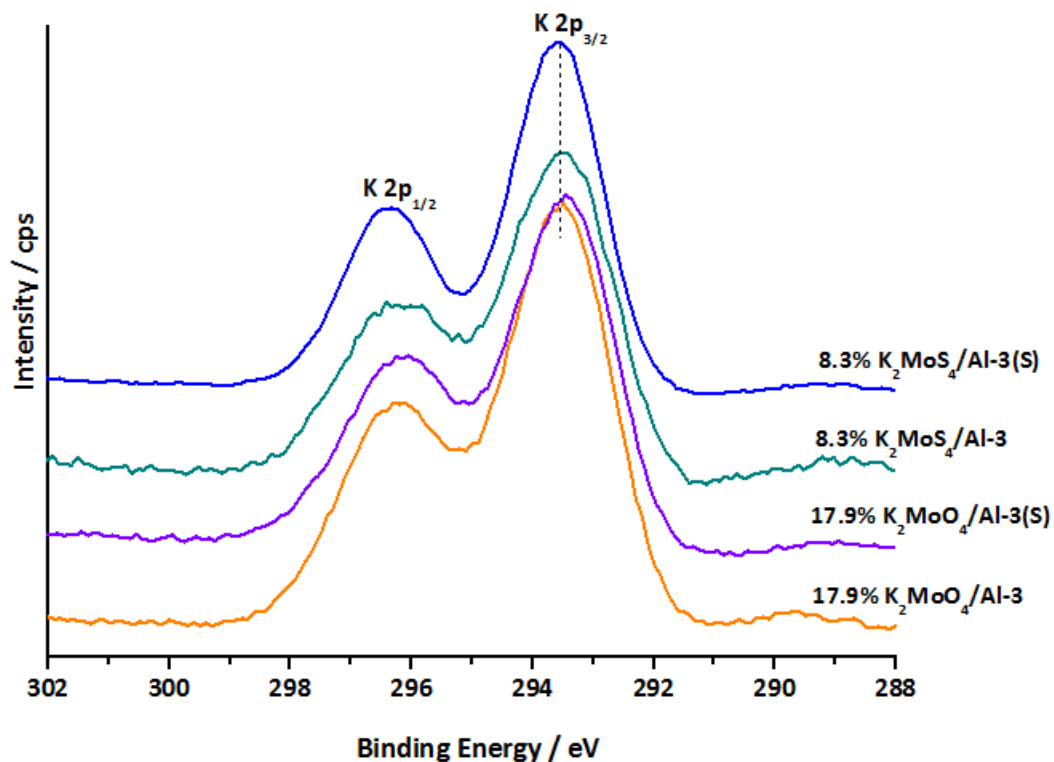


Figure A.2. XPS spectra of K2p core level of fresh and sulfided catalysts.

Figure A.2 shows the spectra of K2p core level of the catalysts 17.9% K₂MoO₄/Al-3 and 8.3% K₂MoS₄/Al-3 at fresh and sulfided state. No variation in the peak position is observed in catalysts before and after sulfidation.

Table A.2. Catalytic performance of K_2MoO_4 -based catalysts in the reaction of syngas and H_2S

CATALYST	CO Conversion (%)			Selectivity (%)									Productivity ($g \cdot h^{-1} \cdot L^{-1}$)									CH ₃ SH yield (%)		
				CH ₃ SH			COS			CO ₂			CH ₃ SH			COS			CO ₂					
	280 °C	300 °C	320 °C	280 °C	300 °C	320 °C	280 °C	300 °C	320 °C	280 °C	300 °C	320 °C	280 °C	300 °C	320 °C	280 °C	300 °C	320 °C	280 °C	300 °C	320 °C	280 °C	300 °C	320 °C
13.5% K_2MoO_4 /Al-1 (S)	32	44	53	46	46	45	6	3	3	48	49	49	104	146	172	16	14	12	98	142	170	15	20	24
17.6% K_2MoO_4 /Al-2 (S)	24	34	42	46	46	46	8	5	4	46	48	48	80	114	142	17	15	14	73	107	135	11	16	19
17.9% K_2MoO_4 /Al-3 (S)	38	51	59	47	47	46	3	2	2	49	50	49	129	172	195	12	10	8	123	166	191	18	24	27
18.0% K_2MoO_4 /Si-1 (S)	22	35	45	49	49	49	5	3	2	45	47	48	76	120	158	10	10	9	65	107	141	11	17	22
23.5% K_2MoO_4 /Si-2 (S)	6	11	19	54	49	48	20	11	7	26	38	43	23	61	64	10	40	12	10	28	52	3	6	9
20.4% K_2MoO_4 /Hap (S)	9	14	19	43	44	44	24	15	11	32	40	43	27	42	59	19	18	18	18	35	54	4	6	8
22.1% K_2MoO_4 /HapNa (S)	10	16	21	45	45	44	20	13	10	33	40	42	33	50	67	18	18	20	22	41	59	5	7	9

Table A.3. Catalytic performance of K_2MoS_4 -based catalysts in the reaction of syngas and H_2S

CATALYST	CO Conversion (%)			Selectivity (%)									Productivity ($g \cdot h^{-1} \cdot L^{-1}$)									CH ₃ SH yield (%)		
				CH ₃ SH			COS			CO ₂			CH ₃ SH			COS			CO ₂					
	280 °C	300 °C	320 °C	280 °C	300 °C	320 °C	280 °C	300 °C	320 °C	280 °C	300 °C	320 °C	280 °C	300 °C	320 °C	280 °C	300 °C	320 °C	280 °C	300 °C	320 °C	280 °C	300 °C	320 °C
5,8% K_2MoS_4 /Al-1 (S)	22	29	38	43	43	38	10	6	4	45	47	49	67	90	104	19	17	15	64	90	120	9	13	15
8,1% K_2MoS_4 /Al-2 (S)	19	26	33	43	42	42	12	8	6	43	46	42	59	80	98	21	19	18	53	80	89	8	11	14
8,3% K_2MoS_4 /Al-3 (S)	28	38	48	45	44	41	7	5	3	47	48	48	90	122	141	18	16	14	86	121	151	13	17	20
8,4% K_2MoS_4 /Si-1 (S)	16	22	28	39	41	42	15	10	7	44	46	47	47	68	88	23	21	19	49	70	92	6	9	12
12,1% K_2MoS_4 /Si-2 (S)	15	22	29	40	44	45	12	8	5	46	47	48	45	69	94	16	15	14	46	68	90	6	9	12
9,9% K_2MoS_4 /Hap (S)	10	7	8	44	36	40	23	34	30	33	22	27	30	18	24	20	22	22	21	10	15	4	3	3
11,1% K_2MoS_4 /HapNa (S)	8	11	15	33	38	40	26	18	12	41	45	45	20	32	45	20	19	18	23	34	47	3	4	6

JCDPS files of K_2MoS_4

00-019-1001

Status Primary QM: Blank (B) Pressure/Temperature: Ambient Chemical Formula: $K_2 Mo S_4$
 Empirical Formula: $K_2 Mo S_4$ Weight %: K25.86 Mo31.73 S42.41 Atomic %: K28.57 Mo14.29 S57.14
 Compound Name: Potassium Molybdenum Sulfide

Radiation: CuK α λ : 1.5418Å Filter: Ni Beta Intensity: Visual

SYS: Orthorhombic SPGR: Pnma (62)
 Author's Cell [AuthCell a: 9.36Å AuthCell b: 6.95Å AuthCell c: 12.13Å AuthCell Vol: 789.08Å³
 AuthCell Z: 4.00 AuthCell MolVol: 197.27]
 Author's Cell Axial Ratio [c/a: 1.296 a/b: 1.347 c/b: 1.745] Dcalc: 2.545g/cm³
 SS/FOM: F(21) = 1.5(0.099, 146)

Space Group: Pnma (62) Molecular Weight: 302.38
 Crystal Data [XtlCell a: 9.360Å XtlCell b: 12.130Å XtlCell c: 6.950Å XtlCell α : 90.00° XtlCell β : 90.00°
 XtlCell γ : 90.00° XtlCell Vol: 789.08Å³ XtlCell Z: 4.00]
 Crystal Data Axial Ratio [c/a: 0.743 a/b: 0.772 c/b: 0.573]
 Reduced Cell [RedCell a: 6.950Å RedCell b: 9.360Å RedCell c: 12.130Å RedCell α : 90.00°
 RedCell β : 90.00° RedCell γ : 90.00° RedCell Vol: 789.08Å³]

Crystal (Symmetry Allowed): Centrosymmetric

Pearson: oP28.00 Prototype Structure: $K_2 S O_4$ Prototype Structure (Alpha Order): $K_2 O_4 S$
 LPF Prototype Structure: $K_2 [S O_4], oP28,62$ LPF Prototype Structure (Alpha Order): $K_2 O_4 S$
 Subfile(s): Inorganic, Metals & Alloys, Primary Pattern Last Modification Date: 01/14/2012

References:

Type	Reference
Primary Reference	Clark, Doyle. J. Inorg. Nucl. Chem. 28, 381 (1966).
Unit Cell	Mulle. Z. Anorg. Allg. Chem. 288, 429 (1974).

Database Comments: Unit Cell Data Source: Powder Diffraction.

d-Spacings (21) - 00-019-1001 (Fixed Slit Intensity) - Cu K α 1.54056Å

2 θ	d(Å)	I	h	k	l	*	2 θ	d(Å)	I	h	k	l	*	2 θ	d(Å)	I	h	k	l	*
14.6537	6.040000	30	0	1	1		33.2791	2.690000	10	1	1	4		49.7271	1.832000	30	2	2	5	
17.5472	5.050000	100	1	1	1		35.4512	2.530000	30	2	2	2		51.1293	1.785000	10	5	1	1	
18.9060	4.690000	30	2	0	0		36.4949	2.460000	10	3	0	3		53.3103	1.717000	10	1	2	6	
24.2313	3.670000	30	2	1	1		39.3113	2.290000	30	0	1	5		56.4018	1.630000	60	2	4	0	
25.7264	3.460000	80	0	2	0		41.1858	2.190000	60	4	0	2		58.1535	1.585000	30	3	3	4	
29.5542	3.020000	80	3	0	1		45.4007	1.998000	10	0	3	3		60.5864	1.527000	10	5	2	3	
32.1719	2.780000	60	3	0	2		47.0450	1.930000	60	4	2	0		62.0728	1.494000	10	4	1	6	

Table A.4. Catalytic performance of KW-based catalysts in the reaction of syngas and H₂S

CATALYST	CO Conversion (%)			Selectivity (%)									Productivity (g.h ⁻¹ .L ⁻¹)									CH ₃ SH yield (%)		
				CH ₃ SH			COS			CO ₂			CH ₃ SH			COS			CO ₂					
	280 °C	300 °C	320 °C	280 °C	300 °C	320 °C	280 °C	300 °C	320 °C	280 °C	300 °C	320 °C	280 °C	300 °C	320 °C	280 °C	300 °C	320 °C	280 °C	300 °C	320 °C	280 °C	300 °C	320 °C
17.6% K ₂ WO ₄ /Al-3 (350 °C)	7	13	20	44	45	47	23	14	9	33	41	43	23	41	69	15	16	16	16	35	58	3	6	10
17.6% K ₂ WO ₄ /Al-3 (400 °C)	11	16	24	38	42	45	15	10	6	46	48	48	30	48	78	15	15	13	33	50	76	4	6	10
17.7% K ₂ WO ₄ /Si-1 (400 °C)	1	1	2	21	30	31	46	26	27	33	43	40	1	2	5	3	3	5	2	3	5	0	0	1
20.8% K ₂ WO ₄ /Hap (400 °C)	1	3	4	11	13	17	67	63	54	23	25	29	1	2	5	9	14	19	2	4	8	0	0	1
13.7% K ₂ WS ₄ /Al-3 (350 °C)	6	9	15	40	41	43	13	10	7	47	49	48	17	27	47	7	8	10	18	29	48	2	4	7
13.7% K ₂ WS ₄ /Al-3 (400 °C)	14	17	23	33	41	44	22	13	8	40	45	46	33	50	72	27	20	17	37	51	69	5	7	10
13.8% K ₂ WS ₄ /Si-1 (400 °C)	1	1	3	13	11	37	31	25	19	51	64	43	1	1	9	2	3	6	3	6	10	0	0	1
16.3% K ₂ WO ₄ /Hap (400 °C)	1	1	4	0	0	24	63	49	38	37	52	38	0	0	8	6	6	15	3	5	11	0	0	1

Résumé

La synthèse du méthylmercaptopan CH_3SH , précurseur de la méthionine, un acide aminé essentiel, est réalisée industriellement par réaction catalytique entre le méthanol et l' H_2S . Cette réaction est rapide et sélective mais l'emploi du méthanol lui-même synthétisé par étapes successives ($\text{CH}_4 + \text{H}_2\text{O} \longrightarrow \text{CO}/\text{H}_2 \longrightarrow \text{Méthanol}$) rend attractive une synthèse du méthylmercaptopan s'effectuant directement à partir d'un mélange CO/H_2 et H_2S . Jusqu'à présent, les recherches effectuées sur cette nouvelle voie de synthèse se sont plus particulièrement attachées à l'amélioration des performances catalytiques. Dans ce travail, nous avons cherché, tout en améliorant les performances catalytiques, à déterminer la nature de la phase active.

Des catalyseurs de type K-Mo(W) supportés sur alumine, silice et hydroxyapatite ont été utilisés dans ce travail. Différents teneurs en métaux et différents pré-traitements catalytiques ont été étudiés. La présence simultanée du potassium et du molybdène dans le système catalytique permet d'atteindre des valeurs importantes de conversion du CO et de sélectivité en CH_3SH , voire une diminution de la sélectivité en CO_2 . Dans notre étude, la productivité la plus élevée en méthylmercaptopan est obtenue avec un catalyseur $\text{K}_2\text{MoO}_4/\text{Al}_2\text{O}_3$ chargé à 17 % en Mo et atteint $211,4 \text{ g}\cdot\text{h}^{-1}\cdot\text{L}^{-1}$. La caractérisation par XPS a été largement mise à profit et a permis de mettre en évidence sur les catalyseurs la présence d'une nouvelle phase de type K_xMS_2 ($\text{M} = \text{Mo}$ or W) pour laquelle les ions potassium sont intercalés entre les feuillets de disulfure de molybdène (tungstène). La quantité de cette phase a été reliée à l'activité catalytique dans la réaction de synthèse du méthylmercaptopan à partir du mélange $\text{CO}/\text{H}_2/\text{H}_2\text{S}$ nous permettant de proposer cette phase intercalée comme phase active du catalyseur de thiolation.

Mots-clés: Composés organo-sulfurés, méthylmercaptopan, gaz de synthèse, disulfure de molybdène, Catalyseurs à base de Mo, Catalyseurs à base de W, Tetraoxomolybdate de potassium, Tetrathiomolybdate de potassium, hydroxyapatite.

Abstract

Methyl mercaptan (CH_3SH), widely used as raw material for the production of organosulfur compounds such as methionine, is commercially synthesized by the reaction of methanol with hydrogen sulfide. Although the formation of CH_3SH from $\text{CH}_3\text{OH}/\text{H}_2\text{S}$ route is a fast and selective reaction, a several-steps pathway is required for the synthesis of methanol ($\text{CH}_4 + \text{H}_2\text{O} \longrightarrow \text{Syngas} \longrightarrow \text{Methanol}$). In this regard, the one-step synthesis of methyl mercaptan from simple starting materials (syngas + hydrogen sulfide) is increasingly attractive for industrial application. So far, the disclosed researches in CH_3SH production by this route have been focused in the improvement of catalytic performances. In this work, the improvement of catalytic performances as well as the understanding of the nature of the active phase has been studied.

K-Mo(W)-based catalysts supported on alumina, silica and hydroxyapatite were used with this purpose. Different metal loading and catalytic pretreatment were evaluated. The simultaneous presence of Mo and K in the catalytic system allows achieving higher CO conversions and CH_3SH selectivity and a decrease in CO_2 selectivity. The higher CH_3SH productivity was achieved with a high loaded $\text{K}_2\text{MoO}_4/\text{Al}_2\text{O}_3$ catalyst ($211,4 \text{ g}\cdot\text{h}^{-1}\cdot\text{L}^{-1}$). With the study and analysis of a series of reference catalysts characterized by XPS, we evidenced the presence of a new phase named K_xMS_2 ($\text{M} = \text{Mo}$ or W) in which Mo(W) cations are intercalated between the MoS_2 layers. By correlating the amount of K_xMS_2 phase with the catalytic performances, we observed that the higher the amount of K_xMS_2 phase in the catalyst, the higher the CO conversion in the reaction of syngas with hydrogen sulfide to produce CH_3SH . Based on these statements we propose that K_xMS_2 is the active phase acting in the reaction of thiolation of syngas.

Key words: Organosulfur compounds, Methyl mercaptan, syngas, molybdenum disulfide, Mo-based catalysts, W-based catalysts, potassium tetraoxomolybdate, potassium tetrathiomolybdate, hydroxyapatite.